ULTRATHIN CONDUCTING POLYMER TRANSDUCERS: FABRICATION, CHARACTERIZATION, AND MODELING

by

Ngoc Tan Nguyen

M. Sc., Inje University, 2014
B. Eng. Danang University of Science and Technology, 2010

A THESIS SUBMITTED IN PARTIAL FULFILLMENT OF
THE REQUIREMENTS FOR THE DEGREE OF

DOCTOR OF PHILOSOPHY
in
THE FACULTY OF GRADUATE AND POSTDOCTORAL STUDIES
(Electrical &Computer Engineering)

THE UNIVERSITY OF BRITISH COLUMBIA
(Vancouver)

September 2018

© Ngoc Tan Nguyen, 2018

Université Polytechnique HAUTS-DE-FRANCE

Thèse de doctorat

Pour obtenir le grade de Docteur de

L'UNIVERSITÉ POLYTECHNIQUE HAUTS-DE-FRANCE

ET L'UNIVERSITÉ DE COLOMBIE BRITANNIQUE

Spécialité micro et nanotechnologies, acoustiques et télécommunications
Et Doctor of Philosophy in Electrical &Computer Engineering (PhD)

Présentée et soutenue par Ngoc Tan, NGUYEN.

Le 21/09/2018, à Villeneuve d'Ascq

Ecole doctorale :
Sciences Pour l'Ingénieur (SPI)

Equipe de recherche, Laboratoire :
Institut d'Electronique, de Micro-Electronique et de Nanotechnologie/Département d'Opto-Acousto-Electronique (IEMN/DOAE)

Transducteurs ultra fin à base de polymères conducteurs : fabrication, caractérisation et modélisation

Composition du jury

Président du jury
M. Edmond CRETU, Professeur de l'Université de Colombie Britannique, Vancouver

Rapporteurs
M. Alejandro A. FRANCO, Professeur des Universités, UPJV/ CNRS UMR 7314, Amiens.
M. Herbert SHEA, Professeur l'Université de EPFL, Neuchâtel.

Examinateurs
M. Mu CHIAO, Professeur de l'Université de Colombie Britannique, Vancouver
Mme. Ludivine FADEL, Professeur des Universités, IMS UMR 5218, Talence

Directeur de thèse

M. Éric CATTAN, Professeur des Universités, UPHF / IEMN, Valenciennes
M. Sébastien GRONDEL, Professeur des Universités, UPHF / IEMN, Valenciennes
M. John D.W. MADDEN, Professeur de l'Université de la Colombie Britannique, Vancouver

Membres invités
M. Cédric PLESSE, Maître de Conférence HDR, LPPI, Cergy Pontoise.

Abstract

Recently, ultrathin poly (3,4-ethylenedioxythiophene) (PEDOT) – based ionic actuators have overcome some initial obstacles to increase the potential for applications in microfabricated devices. While microfabrication processing of trilayer actuators that involve no manual handling has been demonstrated, their mechanical performances remain limited for practical applications.

The goal of this thesis is to optimize the transducers in thin films fabrication by micro technologies, fully characterize the electrochemomechanical properties of the resulting trilayers, and develop a model to simulate their bidirectional electromechanical ability (actuation and sensing).

At first, ultrathin PEDOT-based trilayer actuators are fabricated via the vapor phase polymerization of 3,4-ethylenedioxythiophene combining with the layer by layer synthesis process. This constitutes the first full characterization of ionic PEDOT-based microactuators operating in air of such a small thickness (17 µm) having bending deformation and output force generation of 1% and 12 µN respectively.

Secondly, electrical, electrochemical and mechanical properties of the resulting microactuators have been thoroughly studied. Non-linear characterization was extended to volumetric capacitance dependence on voltage window. Damping coefficient was characterized for the first time.

Thirdly, a nonlinear multi-physics model was proposed as a method of simulating actuator and sensor responses in trilayers, represented using a Bond Graph formalism, and was able to implement all of the characterized parameters. The concordance between the simulations and the measurements confirmed the accuracy of the model in predicting the non-linear dynamic behavior of the actuators. In addition, the information extracted from the model also provided an insight into the critical parameters of the actuators and how they affect the actuator efficiency, as well as the energy distribution.

Finally, a nouveau bidirectional electromechanical linear model was introduced to simulate the sensing ability of the trilayer transducer and was confirmed via experimental results in both frequency and time domains of a sinusoidal input displacement. The resulting actuators and the proposed models are promising for designing, optimizing, and controlling of the future soft microsystem devices where the use of polymer actuators should be essential.

<u>Keywords:</u> Electroactive polymer, conducting polymer transducers, interpenetrating networks, non-linear characterization, non-linear dynamic modeling, Bond Graph formalism.

Résumé

Récemment, les actionneurs ioniques ultra-minces à base de poly (3,4-éthylènedioxythiophène) (PEDOT) ont surmonté certains obstacles initiaux pour augmenter le potentiel d'applications dans les dispositifs microfabriqués. Bien que la microfabrication d'actionneurs à trois couches, n'impliquant aucune manipulation manuelle, ait été démontrée, leurs performances mécaniques restent limitées pour des applications pratiques. Le but de cette thèse est d'optimiser les transducteurs dans la phase de fabrication des couches minces en utilisant des micro technologies, de caractériser complètement les propriétés électrochimiques des transducteurs ainsi obtenus, et de développer un modèle pour simuler leurs capacités électromécaniques bidirectionnelles (actionnement et détection).

Tout d'abord, les actionneurs à trois couches ultra-minces à base de PEDOT sont fabriqués par polymérisation en phase vapeur de 3,4-éthylènedioxythiophène en réalisant un procédé de synthèse couche par couche. Le travail présenté constitue la première caractérisation complète de microactionneurs ioniques à base de PEDOT fonctionnant dans l'air d'une si faible épaisseur (17 µm) présentant une déformation en flexion et une génération de force de 1% et 12 µN respectivement. En effet, les propriétés électriques, électrochimiques et mécaniques des microactionneurs ont été minutieusement étudiées. La caractérisation non linéaire a été étendue à la dépendance de la capacité volumétrique sur une fenêtre de tension. Le coefficient d'amortissement a été caractérisé pour la première fois. Par ailleurs, un modèle multi-physique non linéaire a été proposé comme méthode de simulation des réponses en mode actionneur et capteur dans des couches multiples, représenté à l'aide d'un formalisme Bond Graph, et a été capable de mettre en œuvre tous les paramètres caractérisés. La concordance entre les simulations et les mesures a confirmé l'exactitude du modèle pour prédire le comportement dynamique non linéaire des actionneurs. En outre, les informations extraites du modèle ont également permis de mieux comprendre les paramètres critiques des actionneurs et leur incidence sur l'efficacité de l'actionneur et sur la distribution de l'énergie.

Enfin, un nouveau modèle linéaire électromécanique bidirectionnel a été introduit pour simuler la capacité de détection du transducteur à trois couches et a été confirmé par des résultats expérimentaux dans les domaines fréquentiel et temporel d'un déplacement d'entrée sinusoïdal. Les actionneurs résultants et les modèles proposés sont prometteurs pour la conception, l'optimisation et le contrôle des futurs dispositifs de microsystèmes souples dans lesquels l'utilisation d'actionneurs en polymère devrait être essentielle.

Keywords: ***Polymère électroactif, transducteurs polymères conducteurs, réseaux interpénétrés, caractérisation non linéaire, modélisation dynamique non linéaire, formalisme Bond Graph.***

Résumé Substantiel

Introduction

Les polymères conducteurs (CP) sont des polymères organiques conducteurs électricique. Depuis la découverte de conducteurs organiques polymères en 1977 (Chiang et al. 1977; Shirakawa et al. 1977), les connaissances dans ce domaine se sont considérablement développées. En particulier, le poly (3,4-éthylènedioxythiophène) (PEDOT) joue un rôle important dans les applications antistatiques, électriques et électroniques (Kirchmeyer et Reuter, 2005). L'idée d'utiliser des polymères conducteurs comme actionneurs pour la conversion directe d'énergie électrique en énergie mécanique, basée sur le processus d'oxydo-réduction entre les PC et les ions mobiles dans l'électrolyte, a été initialement proposée par Baughman (Baughman, 1996; Baughman, et al., 1991). De remarquables progrès ont été réalisés sur les actionneurs à base de PC par Pei et Inganäs, Smela et Inganäs, Otero et, récemment, par Vidal et al. (Maziz et al. 2014; Otero et al. 1992; Otero 2013; Pei et Inganäs 1993; Smela 2003; Vidal et al. 2006; Vidal et al. 2004). Ces actionneurs offrent des avantages par rapport aux autres types de muscles artificiels en proposant une combinaison de tension de fonctionnement faible (typiquement 1-2 V) et de biocompatibilité (Ateh et al. 2006; Cellot et al. 2015; Richardson-Burns, al. 2007), d'une plage de déformation importante allant de 1 à 10%, de force bloquante et de travail spécifique élevé. Ils peuvent être envisagés dans diverses applications, notamment les cathéters (Della Santa et coll. 1996; Jager 2002), l'affichage dynamique en braille (Runyan et Carpi 2011; Spinks et coll. 2003), les valves (Jager 2002) et la reconnexion des vaisseaux sanguins. (Mirfakhrai et al. 2007).

Récemment, le problème de la faible vitesse d'actionnement a été abordé par Maziz et al. (Maziz et al. 2016b; Maziz et al. 2014). Ils ont mis en évidence une vitesse de fonctionnement en kHz (à la résonance) des actionneurs à base de PEDOT, l'épaisseur totale de l'actionneur étant de plusieurs micromètres. Le Laboratoire de Physicochimie des Polymères et des Interfaces de l'Université de Cergy-Pontoise, l'Institut d'électronique de microélectronique et de nanotechnologie de l'Université Polytechnique des hauts de France et le laboratoire de mécatronique moléculaire de l'Université de Colombie Britannique ont une longue et fructueuse collaboration (depuis plus de 10 ans) sur les matériaux et dispositifs à base de polymères conducteurs (CP), ainsi que sur l'optimisation et la caractérisation, la modélisation et les applications de ces matériaux. Actuellement, l'un des principaux objectifs du groupe est de développer des microsystèmes à partir de transducteur polymère à base de PC. Comme cela a été évoqué, les transducteurs à base de CP sont aussi des candidats potentiels pour des applications à l'échelle microscopique (épaisseur de l'actionneur <20 µm) nécessitant une faible tension de fonctionnement, des contraintes élevées, un fonctionnement rapide à l'air libre et, en particulier, une compatibilité avec les techniques de microfabrication en salle blanche. Cependant, pour amener ces matériaux vers de nouveau procédé de fabrication comme proposé par Maziz et al. (Maziz, et al. 2016a) vers une production à grande échelle,

l'optimisation des techniques de fabrication, ainsi que la caractérisation complète et la modélisation de ces micro structures sont des étapes essentielles.

Le but de cette thèse est de fabriquer, caractériser les propriétés électro-chimico-mécaniques et de modéliser les transducteurs tricouches ultra-minces à base de PEDOT. La thèse est divisée en six chapitres. Un bref contenu de chaque chapitre est donné ci-dessous:

Chapitre 2:

Ce chapitre contient une brève introduction sur les mécanismes de fonctionnement des actionneurs à base de CP. Le processus de sélection des matériaux utilisés pour fabriquer la tri couche à base de CP dans cette étude sont décrits. Par la suite, les différentes méthodes de synthèse utilisées pour réaliser un polymère conducteur PEDOT sont brièvement passées en revue et la polymérisation en phase vapeur est sélectionnée pour le procédé de fabrication de l'électrode PEDOT, car elle permet de changer plus facilement l'épaisseur de l'électrode. Le processus de fabrication en trois couches est ensuite décrit et la structure obtenue est analysée avec un profilomètre, des techniques MEB et EDX afin de déterminer la rugosité et la structure exactes du tri couche. Les résultats de rugosité de surface montrent une asymétrie entre les deux électrodes de PEDOT, suggérant une différence de propriétés électriques des deux électrodes.

Chapitre 3:

Ce chapitre présente la caractérisation électro-chimico-mécaniques des tri couches obtenus comprenant les informations sur les méthodes de caractérisation et les résultats obtenus. Tout d'abord, les propriétés électrochimiques de la tri couche, telles que la conductivité électronique en fonction de l'état d'oxydation du PEDOT, la conductivité ionique et la capacité volumétrique des électrodes de PEDOT en fonction de la vitesse de balayage et de la tension, et la conductivité ionique du réseau semi-interpénétré NBR-PEO, sont déterminés. On mesure aussi le degré de déformation en flexion à partir duquel est calculé le couplage entre les domaines électrochimique et mécanique - un rapport déformation-charge empirique. Enfin, les propriétés mécaniques sont déterminées: le module de Young des électrodes PEDOT en fonction de l'état d'oxydation et de la structure en trois couches, le rapport d'amortissement, la densité en trois couches et les forces en fonction de la tension et de la fréquence sont déterminés.

Chapitre 4:

Le chapitre 4 est consacré à la modélisation des actionneurs à tri couches. Le formalisme Bond Graph est introduit et la raison de son utilisation expliquée. Un modèle électro-chimio-mécanique simple basé sur la théorie de poutres dynamiques d'Euler-Bernoulli est décrit. Ensuite, un modèle électro-chimio-mécanique dynamique non linéaire basé sur la méthode des éléments finis rigides dynamiques est présenté. Les propriétés des matériaux mesurés (chapitre 3) sont utilisées dans le modèle et les simulations sont comparées aux déviations d'actionneur observées de manière expérimentale au fil du temps. Le modèle proposé permet

d’extraire des informations sur les flux d’énergie à l’intérieur de la tri couche et d’évaluer les facteurs clés affectant les performances de l’actionneur (comme par exemple la déformation en sortie).

Chapitre 5:

Un modèle simple, comprenant à la fois la détection et l'actionnement, est proposé, démontrant l'avantage de la formulation Bond Graph dans les modes de fonctionnement électrique vers mécanique et mécanique vers électrique. Le modèle initial est basé sur l'utilisation aussi d’un rapport déformation sur charge comme coefficient de couplage empirique.

Chapitre 6:

Dans ce dernier chapitre, les conclusions de cette recherche sont résumées et les perspectives de travail à court et long terme sont développées.

Résultats

Tout d'abord, est décrit la fabrication d'une structure en trois couches d'un semi-NBR / PEO pris en sandwich entre deux électrodes PEDOT, réalisée par empilement par la technique dite couche par couche. La procédure de fabrication est résumée dans la figure 1.

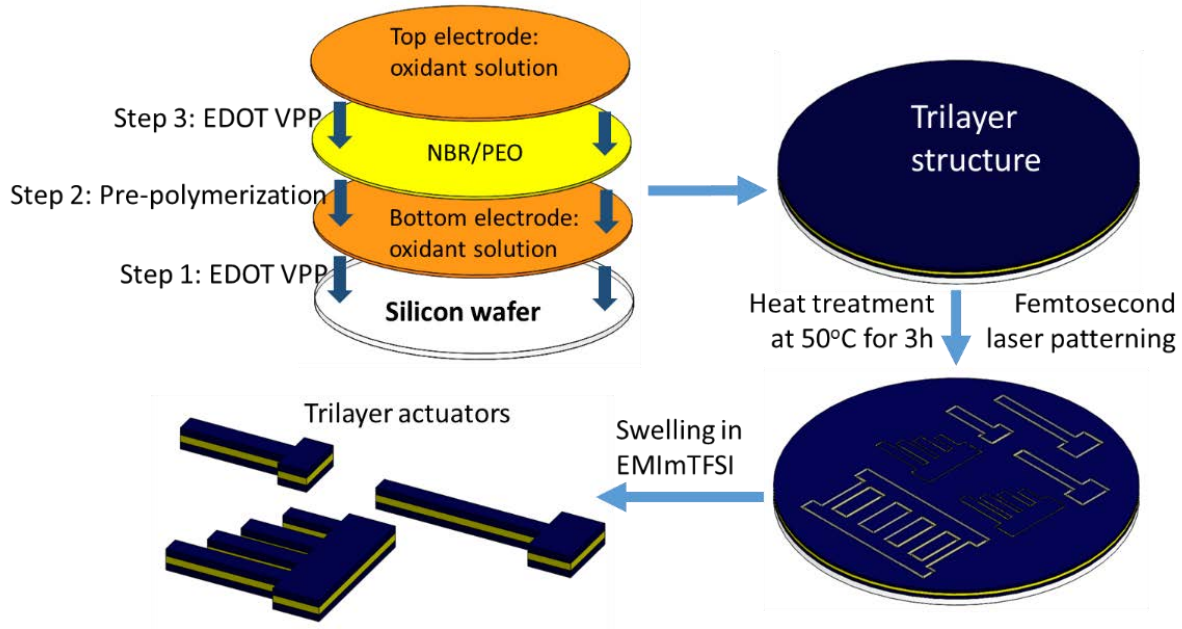


Fig.1 Procédé de fabrication d'un microactionneur montrant le processus multicouche suivi d'un micro-usinage au laser

En introduisant le PEO dans les trois couches, la conductivité ionique et l'adhésion mécanique entre ces couches augmentent. Cette méthode de fabrication nous a permis d’obtenir une épaisseur fine et contrôlable. Par rapport à de précédents travaux, des modifications notables ont été apportées : a) l’optimisation des électrodes de PEDOT entraînant l’augmentation du temps de polymérisation en phase vapeur de 30 à 50 minutes, b) l’utilisation d’une plaque chauffante sous atmosphère contrôlée (Sawatec HP-200) permettant un contrôle plus précis de la température et du vide pendant le polymérisation en phase vapeur, c) tout le processus

de fabrication a été effectué dans une salle blanche, ce qui garantit une reproductibilité accrue. Des lots d'échantillons tri couches ont été fabriqués et les mesures en déformation ont montré que les actionneurs fonctionnaient correctement. Le pourcentage de PEO dans la couche PEDOT est passé également à 10% par rapport aux 20% utilisés dans les travaux de A. Maziz (Maziz 2014). Ce pourcentage assure un équilibre entre une conductivité électronique élevée (environ 200 S / cm) et une densité de charge volumétrique élevée (entre 2,3 x 10^7 C / m^3 et 1,0 x 10^8 C / m^3) de la couche PEDOT. De plus, nous avons mis en évidence une légère asymétrie de rugosité de surface entre les couches PEDOT supérieure et inférieure (figure 2) qui a des conséquences sur les propriétés électriques des électrodes PEDOT et enfin sur les propriétés mécaniques (déplacement, force…) de l'actionneur.

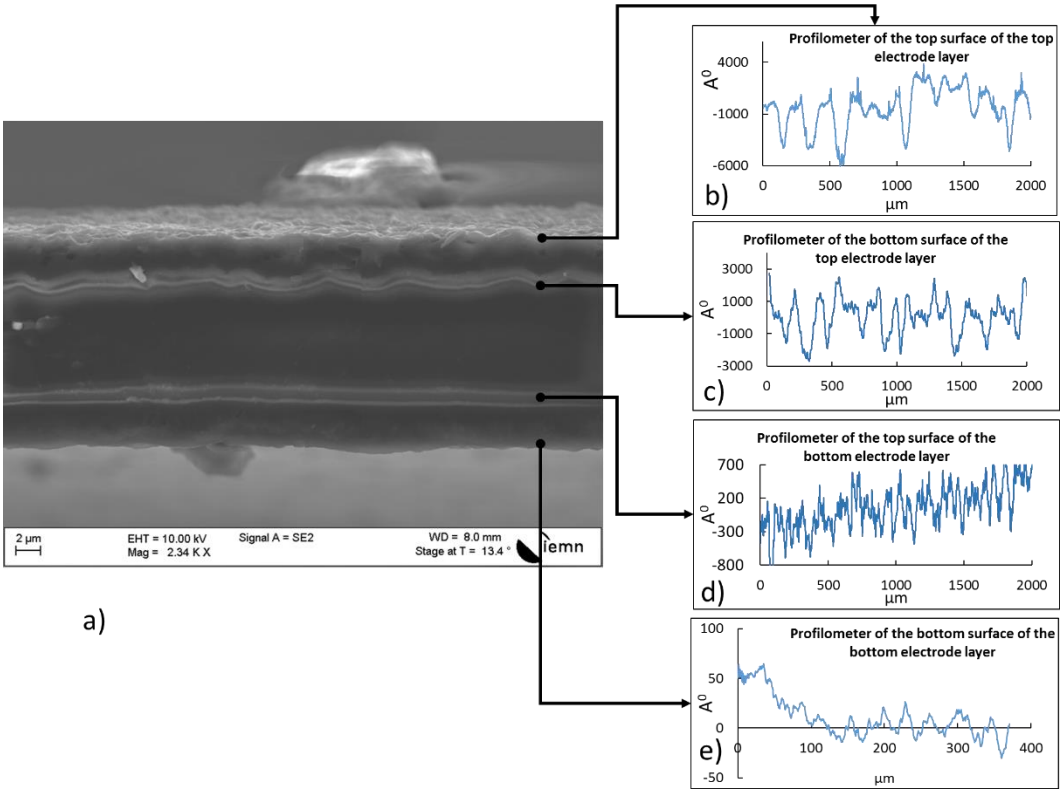


Fig.2 a) Image MEB de la coupe transversale de la tri couche non gonflé de liquide ionique, rugosité de la surface par profilomètrie de la surface supérieure de l'électrode supérieure, c) de la surface supérieure du polymère support d'électrolyte (NBR/POE) sur un bicouche PEDOT/SPE, d) de la surface supérieure de l'électrode inférieure, e) de la surface inférieure de l'électrode inférieure

Le procédé de polymérisation en phase vapeur de cette thèse utilise la solution oxydante conventionnelle constituée de 55% de Fe(TOs)3 dans du butanol. Cependant, la littérature a montré que ce pourcentage élevé produit une solution oxydante fortement acide et réactive, entraînant une polymérisation difficilement contrôlable et des défauts de structure du film déposé (Shi, et al. 2017). Des recherches sur l'optimisation du pourcentage de solution oxydante, ou l'ajout d'inhibiteurs de bases tels que la pyridine pour contrôler la vitesse de réaction, sont suggérées pour améliorer encore les propriétés électrochimiques de l'électrode en PEDOT. Ceci est envisagé dans le futur.

Deuxièmement, le transducteur à base de polymère conducteur résultant a été caractérisé. Ses propriétés électrochimiques, notamment la conductivité ionique des électrodes de PEDOT et de la couche polymère support d'électrolyte ainsi que la conductivité électronique du PEDOT en fonction de l'état d'oxydation et la capacité volumétrique du PEDOT avec sa dépendance en tension et avec la vitesse de balayage ont toutes été étudiées. De plus, les propriétés mécaniques telles que le module de Young du PEDOT en fonction de l'état d'oxydation, le module de Young de la couche polymère support d'électrolyte, le taux d'amortissement ont également été mesurés. Enfin, le couplage entre l'électrochimique et la mécanique représentant via un rapport empirique déformation/charge a été déterminé.

Le tableau ci-dessous résume les propriétés électriques, électrochimiques et mécaniques critiques des actionneurs tri couches. Ces valeurs obtenues permettent d'évaluer le modèle dynamique non linéaire établi et seront discutées dans le chapitre suivant.

En outre, ces paramètres obtenus nous fournissent un aperçu de la structure physique du système et du mécanisme de travail de l'actionneur. Plus important encore, les facteurs clés ayant une incidence sur le comportement d'actionnement sont tous déterminés, ce qui nous fournit les meilleures indications pour améliorer les performances de l'actionneur.

Table: Résumé des paramètres mesurés de l'actionneur ultramince tri couches

Conductivité électronique du PEDOT (S/cm)	Electrode supérieur de PEDOT: $-2.62U^3 + 2.76U^2 + 9.89U + 7.49$ Electrode inférieur de PEDOT: $-16.6U^3 + 1.1U^2 + 51.7U + 59.1$
Conductivité ionique des électrodes de PEDOT (S/m)	Electrode supérieur de PEDOT: 0.025 Electrode inférieur de PEDOT: 0.030
Capacité volumétrique des électrodes de PEDOT (F/m³)	$1.1 \times 10^6 U^6 - 1.9 \times 10^7 U^5 + 1.1 \times 10^8 U^4 - 2.8\ 10^8 U^3 + 3.4 \times 10^8 U^2 - 1.7 \times 10^8 U + 6.9 \times 10^7$
Conductivité ionique du NBR/PEO (S/m)	0.038
Rapport déformation/charge (m³/C)	$\alpha = 3.6 \pm 0.5 \times 10^{-10}$
Module Young du NBR/PEO (kPa)	329 ± 50
Module Young du tri couche (MPa)	$-0.09U^3 - 0.08U^2 - 0.26U + 9.54$
Module Young du PEDOT (MPa)	$-0.23U^3 - 0.19U^2 - 0.63U + 22.70$
Amortissement	0.39
Densité du matériau (kg/m³)	2000

Différence de déformation maximum (%)	0.56
Déformation linéaire (%)	1

Troisièmement, un modèle dynamique non linéaire et un modèle linéaire dynamique plus simple ont été proposés pour simuler l'actionnement de ces matériaux tri couches ultra-minces. Une comparaison entre ces deux modèles a montré que le modèle linéaire est plus simple à construire et que la caractérisation des paramètres requis est simple aussi. Cependant, il est plus approprié pour prédire de petits déplacements et l'on a des pertes de précision pour des déplacements et des tensions importants. Le modèle Bond Graph par mot pour les modèles linéaire et non linéaire est présenté dans la figure 3.

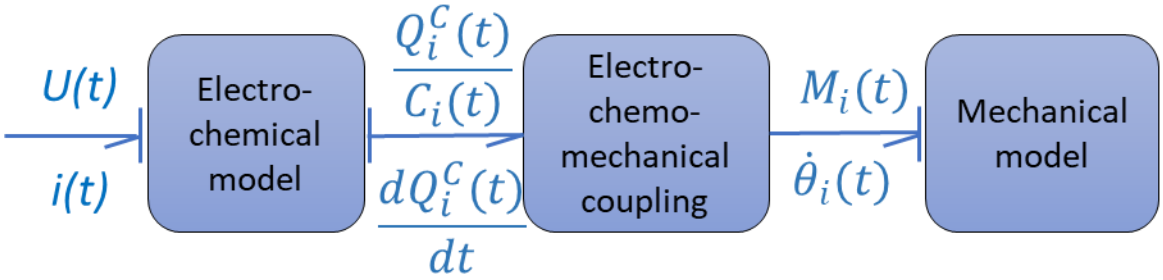


Fig.3 Actionneur tri couches modèle Bond Graph par mots.

Le modèle non linéaire proposé a montré des avancées par rapport aux travaux existants sur les actionneurs tri couches fonctionnant dans l'air en raison du fait qu'il permet de prédire avec précision un actionnement dynamique non linéaire en utilisant des propriétés électrochimiques et mécaniques non linéaires des matériaux: conductivités électriques et ioniques du PEDOT; valeurs de capacité volumétrique; et la variation du module de Young. De plus la prise en compte de la masse et l'amortissement associés à la poutre est aussi une nouveauté. De plus, toutes les caractéristiques physiques utilisées dans le modèle ont été mesurées. La figure 4 représente le modèle dynamique global non linéaire de l'actionneur à base de polymère conducteur.

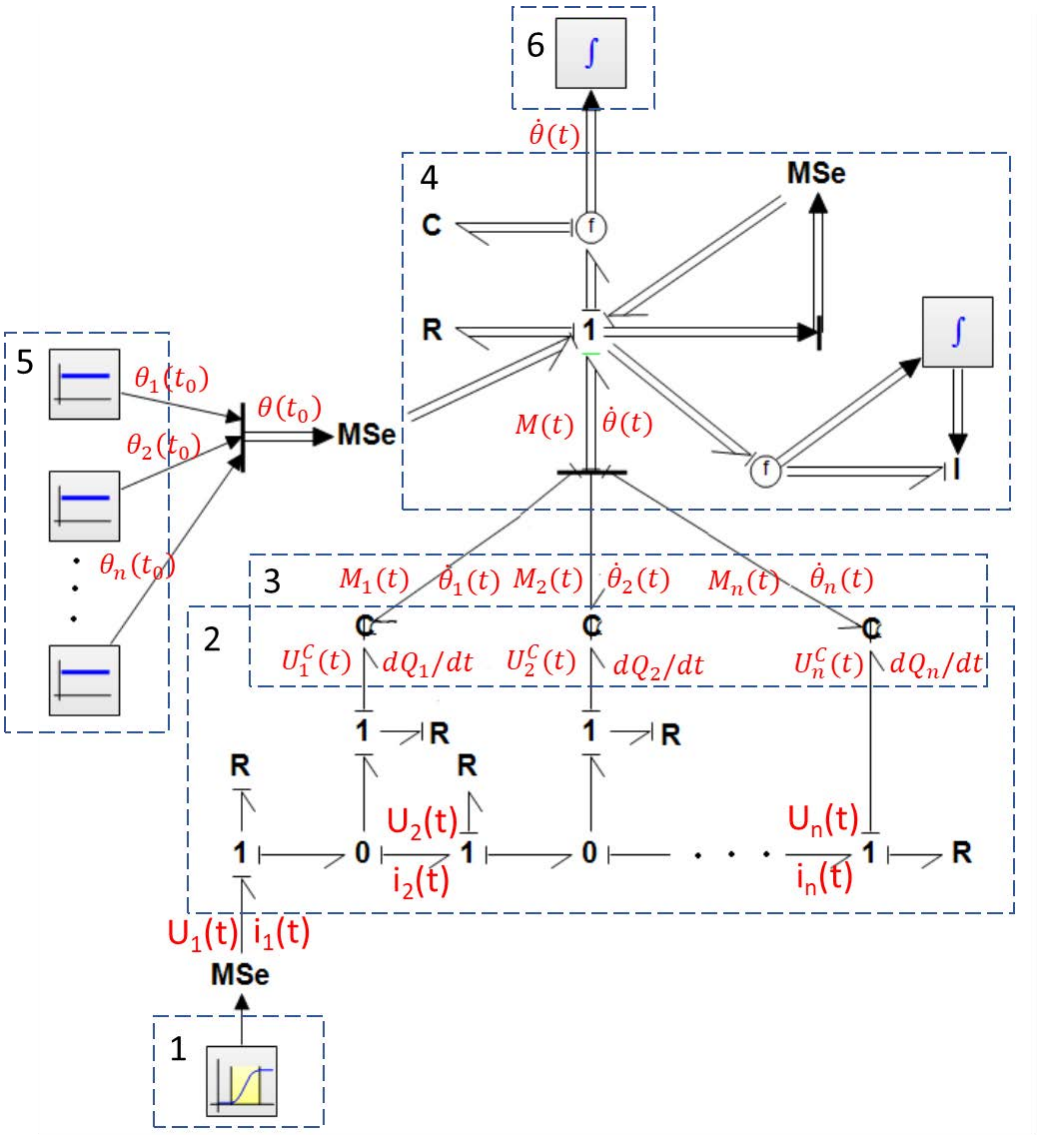


Fig.4 Modèle global de l'actionneur à base de polymère conducteur: 1. Source de tension, 2. Modèle électrochimique, 3. Couplage entre partie électrochimique et partie mécanique, 4. Modèle mécanique, 5. Conditions aux limites: contrainte initiale, 6. Déplacement de sortie.

La concordance entre la simulation et les résultats expérimentaux dans les domaines temporel et fréquentiel (illustrés dans la figure 5) confirme la capacité de prédire la flexion de l'actionneur tri couches.

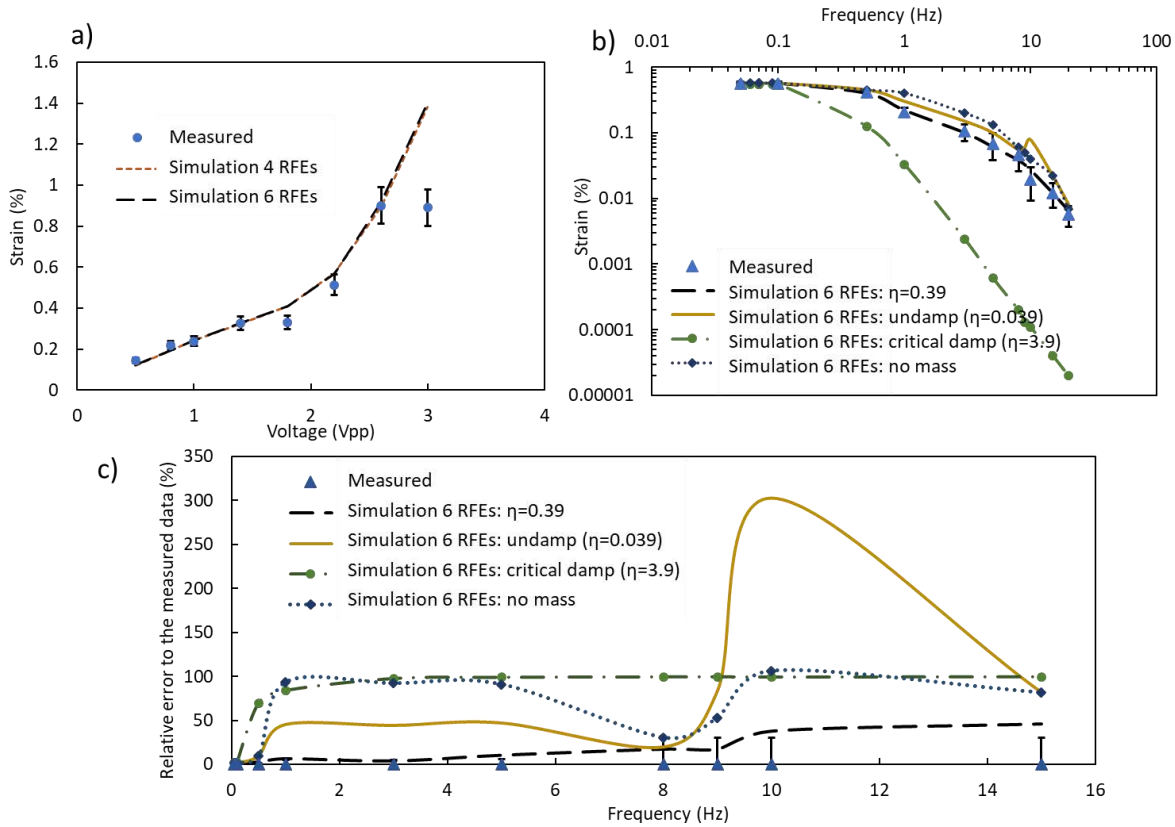


Fig.5 Comparaison entre les simulations et les expériences sur a) La déformation en fonction de l'amplitude de la tension appliquée à une fréquence constante de 0,1 Hz, b) La déformation en fonction de la fréquence de la tension appliquée à une valeur constante de ± 1,1 V c) L'erreur relative des simulations comparée aux données mesurées.

De plus, l'approche représentée en langage Bond Graph, offre un moyen simple d'accéder aux informations énergétiques (figure 6), d'évaluer les paramètres critiques affectant les performances de l'actionneur et de mieux comprendre les phénomènes qui se produisent dans l'actionneur.

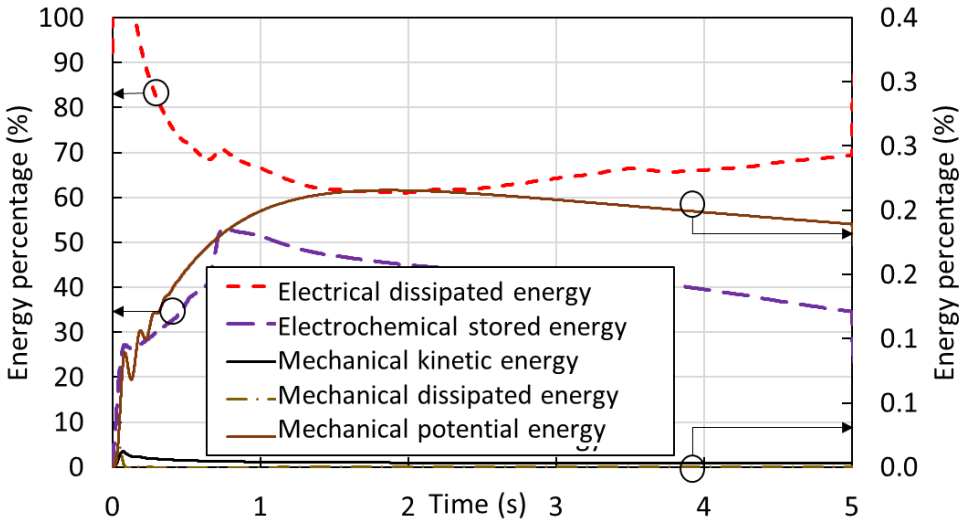


Fig.6 Couplage électrique / mécanique instantané.

De plus, le modèle peut également être utilisé pour optimiser la conception du transducteur avant sa fabrication. Le logiciel de simulation permet de faire varier les paramètres d'entrée, tels que les dimensions et les propriétés du matériau (conductivités, module de Young,…) sur des plages définies, afin de définir celle qui produira la réponse souhaitée. Ces valeurs serviront de guide au concepteur pour ajuster les propriétés du transducteur. L'outil peut également être utilisé pour déterminer les propriétés des matériaux qui limitent le plus la réponse afin de piloter le développement des matériaux ou de permettre l'évaluation de matériaux émergents. La figure ci-dessous donne une évaluation de la sensibilité à la différence de déformation, au module de Young, à la conductivité électrique PEDOT, à la conductivité ionique du polymère support d'électrolyte et à la longueur de l'actionneur. Les résultats sont montrés pour une basse fréquence (Fig. 7a) et une haute fréquence (Fig. 7b).

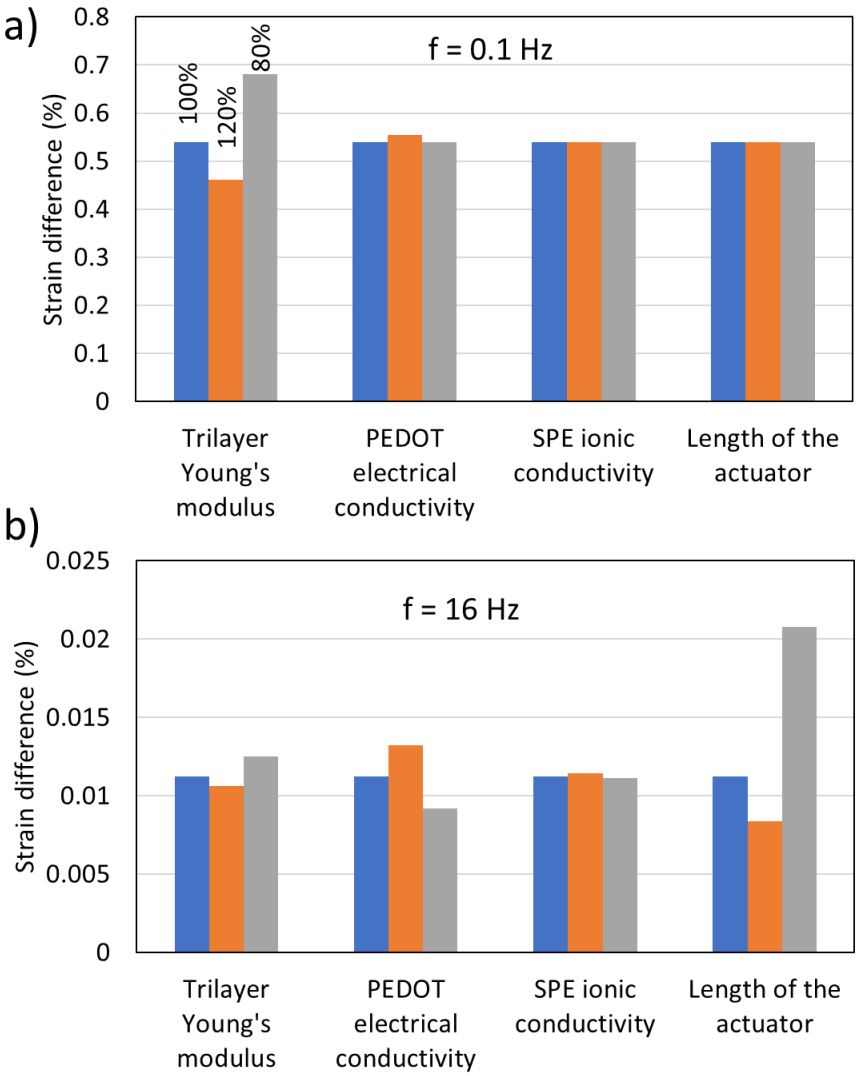


Fig.7 Facteurs clés affectant le déplacement de l'actionneur sous une tension carrée (Vpp = 2,4 V), a) à basse fréquence f = 0,1 Hz, et b) à haute fréquence f = 16 Hz. Pour chaque paramètre il y a trois colonnes qui, de gauche à droite représentent la valeur réelle (colonne bleue), l'effet lorsque la valeur est augmentée de 20% (colonne orange) et l'effet lorsque la valeur est réduite de 20% (colonne grise).

Par ailleurs, une relation simple entre une déformation manuelle et la tension de sortie aux bornes du transducteur a été proposé dans un modèle linéaire dans le but de créer un modèle unique permettant de fonctionner à la fois en mode d'actionnement et en mode de détection. Le rapport déformation/charge a été recaractérisé et la concordance entre la simulation et la mesure expérimentale de la tension de sortie a confirmé la capacité de prédire la fonction de détection de ces matériaux tri couche, malgré une petite erreur. Le modèle montre sa capacité à prédire assez bien la modification de tension électrique sous un déplacement pas à pas.

Conclusion

Les développements dans les transducteurs à base de polymères conducteurs opérant dans l'air ont permis de les rendre, entre autres, plus efficaces en termes de force générée, de déplacement et de fréquence de fonctionnement. Récemment, ils ont été fabriqués avec des épaisseurs acceptables pour une intégration potentielle dans des microsystèmes. Le but ultime est de disposer d'un matériau dont les propriétés sont bien connues et qui puisse être modélisé afin d'être prédictif dans la fabrication d'un microsystème souple comprenant des transducteurs souples. C'est pourquoi cette thèse s'est concentrée sur la caractérisation et la modélisation d'un certain type de transducteurs à base de polymères conducteurs. À notre connaissance, il s'agit du premier effort visant à caractériser et à modéliser de manière complète un tel transducteur tri couche très mince, dont l'épaisseur totale n'est que de 17 µm - après avoir été gonflé dans un liquide ionique.

La première étape de ce travail consistait à améliorer un processus de microfabrication compatible avec les salles blanches récemment mis au point pour les couches conductrices en polymère. Bien que le rendement de ces matériaux reste faible avec ce type de tri couche, les caractéristiques physiques pertinentes d'un transducteur performant ont été entièrement caractérisées, notamment les facteurs affectant le transport ionique et électronique, le couplage charge / déformation, les rigidités des matériaux et les amortissements. Lors de l'actionnement, une différence de déformation d'environ 1%, une force de blocage de 12 µN et une tension de détection de 0,7 mV ont été obtenues à partir d'un transducteur de longueur x largeur = 6 mm x 1 mm. Cette déflexion et cette tension de détection correspondent à la réponse attendue et qui a été aussi validée par un modèle non linéaire mis en place dans le cadre de cette thèse.

Le polymère conducteur PEDOT a été utilisé comme matériau actif en constituant les deux électrodes du transducteur. Étant donné que la polymérisation du 3,4-éthylènedioxythiophène (EDOT) est un processus complexe et sensible et que le PEDOT est un matériau présentant des propriétés électro-chimio-mécanique non linéaires, les processus de fabrication, de caractérisation et de modélisation ont été confrontés à divers problèmes. La résolution de ces problèmes a conduit aux principales contributions scientifiques et techniques décrites ci-dessous:

- L'amélioration du procédé de fabrication des transducteurs. Dans la configuration à trois couches, un semi-NBR / PEO est pris en sandwich entre deux électrodes PEDOT / PEO, produites par empilement couche par couche. Cette technique de fabrication permet d'ajuster l'épaisseur de chaque couche à notre guise. En outre, a été étudié l'asymétrie de rugosité de surface entre les couches PEDOT d'électrodes supérieure et inférieure, ce qui a des conséquences sur les propriétés électriques des électrodes de PEDOT et, enfin, sur les propriétés mécaniques (déplacement, force…) de l'actionneur.

- La caractérisation complète des propriétés électro-chimio-mécanique critiques des transducteurs tri couches a été effectuée. Les propriétés électrochimiques incluant la conductivité ionique des électrodes PEDOT et de la couche de polymère support d'électrolyte, la conductivité électronique du PEDOT en fonction de son état d'oxydation et la dépendance de la capacité volumétrique du PEDOT sur la fenêtre de potentielle ont toutes été étudiées. En outre, les propriétés mécaniques telles que le module de Young du PEDOT en fonction de l'état d'oxydation, le module de Young de la couche polymère support d'électrolyte et le taux d'amortissement ont aussi été mesurés. Enfin, le couplage électrochimique et mécanique a été évalué via un rapport empirique déformation-charge, la déformation linéaire a été déterminée et la force de blocage mesurée en fonction du potentiel appliqué.

- Le développement d'un modèle dynamique non linéaire - et d'une version beaucoup plus simple avec un modèle linéaire dynamique - capable de simuler l'actionnement de tri couches ultra-minces. Une comparaison entre ces deux modèles a montré que le modèle linéaire est simple à construire et qu'il est plus facile d'obtenir tous les paramètres requis. Il est plus approprié de prévoir dans ce cas de simuler de petits déplacements Il fournit une prévision moins précise que le modèle non linéaire pour des tensions appliquées plus importants produisant de grands déplacements. Le modèle non linéaire proposé montre des avancées intéressantes par rapport aux travaux existants sur les actionneurs tri couches en raison de sa capacité à prédire avec précision un actionnement dynamique non linéaire prenant en compte des propriétés électrochimiques et mécaniques non linéaires du matériau: conductivités électriques et ioniques du PEDOT; valeurs de capacité volumétrique; et la variation du module de Young. De plus, le modèle utilisé prend en compte aussi la masse et l'amortissement associés à la micro poutre de transducteur. Toutes les caractéristiques physiques utilisées dans le modèle ont été mesurées. La concordance entre la simulation et les résultats expérimentaux dans les domaines temporel et fréquentiel confirme la capacité de prédire la flexion de l'actionneur tri couches. En outre, l'approche est représentée dans un langage Bond Graph, offrant un moyen simple d'accéder aux informations énergétiques, d'évaluer les paramètres critiques affectant les performances de l'actionneur et de mieux comprendre les phénomènes qui se produisent dans l'actionneur ionique.

- Le développement d'un modèle linéaire unique fonctionnant à la fois en mode d'actionnement et en mode de détection. Une relation simple entre la déformation

provoquée mécaniquement et la tension de sortie a été utilisé dans le modèle simple linéaire. Le rapport déformation-charge a été re caractérisé en mode de détection et la concordance entre la simulation et la valeur expérimental de la tension de sortie a confirmé la capacité de prédire la fonction de détection tri couche, malgré une erreur faible. Une autre avancée de ce modèle est la possibilité de prédir le taux de décroissance de la tension de détection sous un déplacement pas à pas.

References

Ateh, D. D., H. A. Navsaria, and P. Vadgama
2006 Polypyrrole-based conducting polymers and interactions with biological tissues. J R Soc Interface 3(11):741-52.

Baughman, R. H.
1996 Conducting polymer artificial muscles. Synthetic Metals 78(3):339-353.

Baughman, R. H., et al.
1991 Micro Electromechanical Actuators Based on Conducting Polymers. *In* Molecular Electronics: Materials and Methods. P.I. Lazarev, ed. Pp. 267-289. Dordrecht: Springer Netherlands.

Cellot, G., et al.
2015 PEDOT:PSS Interfaces Support the Development of Neuronal Synaptic Networks with Reduced Neuroglia Response In vitro. Front Neurosci 9:521.

Chiang, C. K., et al.
1977 Electrical Conductivity in Doped Polyacetylene. Physical Review Letters 39(17):1098-1101.

Della Santa, A., A. Mazzoldi, and D. De Rossi
1996 Steerable microcatheters actuated by embedded conducting polymer structures. Journal of Intelligent Material Systems and Structures 7(3):292-300.

Jager, E.W., Immerstrand, C., Peterson, K.H. et al.
2002 The Cell Clinic: Closable Microvials for Single Cell Studies. Biomedical Microdevices 4(3):10.

Kirchmeyer, Stephan, and Knud Reuter
2005 Scientific importance, properties and growing applications of poly(3,4-ethylenedioxythiophene). Journal of Materials Chemistry 15(21):2077-2088.

Maziz, A., et al.
2016a Top-down Approach for the Direct Synthesis, Patterning, and Operation of Artificial Micromuscles on Flexible Substrates. ACS Appl Mater Interfaces 8(3):1559-64.

Maziz, Ali
2014 Microactionneurs à base de polymères conducteurs électroniques : Vers l'intégration aux microsystèmes par de nouveaux procédés d'élaboration, Laboratoire de Physico-chimie des Polymères et des Interfaces, Université de Cergy Pontoise.

Maziz, Ali, et al.
2016b Top-down Approach for the Direct Synthesis, Patterning, and Operation of Artificial Micromuscles on Flexible Substrates. ACS Applied Materials & Interfaces 8(3):1559-1564.

Maziz, Ali, et al.
2014 Demonstrating kHz Frequency Actuation for Conducting Polymer Microactuators. Advanced Functional Materials 24(30):4851-4859.
Mirfakhrai, Tissaphern, John D. W. Madden, and Ray H. Baughman
2007 Polymer artificial muscles. Materials Today 10(4):30-38.
Otero, T. F., et al.
1992 Electrochemomechanical properties from a bilayer: polypyrrole / non-conducting and flexible material — artificial muscle. Journal of Electroanalytical Chemistry 341(1):369-375.
Otero, Toribio F.
2013 Biomimetic Conducting Polymers: Synthesis, Materials, Properties, Functions, and Devices. Polymer Reviews 53(3):311-351.
Pei, Qibing, and Olle Inganäs
1993 Electrochemical applications of the bending beam method; a novel way to study ion transport in electroactive polymers. Solid State Ionics 60(1):161-166.
Richardson-Burns, S. M., et al.
2007 Polymerization of the conducting polymer poly(3,4-ethylenedioxythiophene) (PEDOT) around living neural cells. Biomaterials 28(8):1539-52.
Runyan, N. H., and F. Carpi
2011 Seeking the 'holy Braille' display: might electromechanically active polymers be the solution? Expert Rev Med Devices 8(5):529-32.
Shi, Wei, et al.
2017 Micron-thick highly conductive PEDOT films synthesized via self-inhibited polymerization: roles of anions. Npg Asia Materials 9:e405.
Shirakawa, Hideki, et al.
1977 Synthesis of electrically conducting organic polymers: halogen derivatives of polyacetylene, (CH). Journal of the Chemical Society, Chemical Communications (16):578-580.
Smela, E.
2003 Conjugated polymer actuators for biomedical applications. Advanced Materials 15(6):481-494.
Spinks, G. M., et al.
2003 Ionic Liquids and Polypyrrole Helix Tubes: Bringing the Electronic Braille Screen Closer to Reality. Proceedings of SPIE - The International Society for Optical Engineering, 2003. Vol. 5051, pp. 372-380.
Vidal, Frédéric, et al.
2006 Conducting IPN actuators: From polymer chemistry to actuator with linear actuation. Synthetic Metals 156(21–24):1299-1304.
Vidal, Frédéric, et al.
2004 Long-life air working conducting semi-IPN/ionic liquid based actuator. Synthetic Metals 142(1):287-291.

Lay Summary

This work constitutes the most thorough characterization and modeling to date of ionic conducting polymer-based actuators, applied to PEDOT microactuators operating in air. Non-linear characterization was extended to volumetric capacitance dependence on voltage window. Damping coefficient was characterized for the first time. These and other measured properties were included in a nonlinear multi-physics model that is demonstrated as an effective method for simulating actuation in trilayers. In addition, a new bidirectional electromechanical linear model was introduced to simulate both the actuation and sensing ability of the trilayer transducer.

Preface

This dissertation is formatted in accordance with the regulations of the University of Polytechnique Haut-de-France and submitted in partial fulfillment of the requirements for a PhD degree awarded jointly by the University of Polytechnique Haut-de-France and the University of British Columbia. Versions of this dissertation will exist in the institutional repositories of both institutions.

All aspects of the material appearing in this thesis have been originally written by the author unless otherwise stated.

This work has been done in the IEMN-DOAE laboratory and in Molecular Mechatronics Lab under the supervision of Prof. Eric Cattan, Prof. Sébastien Grondel, and Prof. John D. W. Madden.

A version of chapter 2 has been published. [T.N. Nguyen], K. Rohtlaid, C. Plesse, G.T.M. Nguyen, C. Soyer, S. Grondel, E. Cattan, J.D.W. Madden, F. Vidal, Ultrathin electrochemically driven conducting polymer actuators: fabrication and electrochemomechanical characterization, Electrochimica Acta, 265(2018) 670-80. All of the fabrication and characterization have been performed with the supervision of Prof. Eric Cattan, Prof. John D. W. Madden, and Prof. Frédéric Vidal. Dr. Cédric Plesse, Dr. Giao T.M. Nguyen, Dr. Caroline Soyer, Prof. Sébastien Grondel helped to reviewed the results and revise the manuscript. I conducted the PEDOT-based trilayer fabrication process and the trilayer characterization including geometries and surface roughness, electrochemical and mechanical properties. The sections on “PEDOT electrode fabrication” and “Optimization of electrochemical properties of PEDOT electrodes” was written by K. Rohtlaid.

A version of chapter 3 and 4 has been submitted. [T.N. Nguyen], Y. Dobashi, C. Soyer, C. Plesse, G.T.M. Nguyen, F. Vidal, E. Cattan, S. Grondel, J.D.W. Madden, Non-linear dynamic modeling of ultrathin conducting polymer actuators including inertial effects, Smart Materials and Structures, May 2018. All the experiments and simulations were conducted by the author under the supervision of Prof. Eric Cattan, Prof. John D. W. Madden, and Prof. Sébastien Grondel. Yuta Dobashi helped to setup the experiments.

The section 4.3 of chapter 4 was presented SPIE conference on electroactive polymer actuators and devices, 2017 (N.T. Nguyen, C. Plesse, F. Vidal, C. Soyer, S. Grondel, J.D.W. Madden, E. Cattan, Microfabricated PEDOT trilayer actuators: synthesis, characterization, and modeling, SPIE Smart Structures and Materials + Nondestructive Evaluation and Health Monitoring, SPIE2017, p. 13).

Table of Contents

Abstract iii
Résumé iv
Résumé Substantiel v
Lay Summary xviii
Preface xix
Table of Contents xx
List of Figures xxiii
List of Tables xxix
Abbreviations xxx
Acknowledgements xxxi
Dedication xxxii
Chapter 1: Introduction 1
1.1 Mammalian muscles 2
1.2 Artificial muscles 2
1.3 Motivation and problem statement 9
1.4 Thesis structure 9
Chapter 2: PEDOT-based trilayer fabrication process 16
2.1 Introduction 17
2.2 The selection of materials for CP-based trilayer actuators 22
2.2.1 Electrodes of the microactuators 22
2.2.2 Solid polymer electrolyte layer 22
2.2.3 The electrolyte 24
2.2.4 Microactuator fabrication technique 26
2.3 Materials 26
2.4 PEDOT synthesis route 27
2.5 PEDOT-based trilayer fabrication process 30
2.5.1 Trilayer fabrication process 30
2.6 PEDOT-based trilayer patterning 33
2.6.1 Fabrication of samples for the characterization process 35
2.7 Analysis of the texture of the trilayer structure 36
2.8 Conclusion 39
Chapter 3: Electrochemomechanical characterization of the trilayer structure 45

3.1 Introduction 46
3.2 Electro-chemical properties 48
3.2.1 Ionic conductivity of the SPE and PEDOT layers 49
3.2.2 Electrical conductivity of the PEDOT electrodes 52
3.2.3 Volumetric capacitance of the PEDOT electrodes 55
3.2.4 Possible short circuit between two PEDOT layers 58
3.3 Mechanical properties 59
3.3.1 Youngs moduli of the SPE layer and of the trilayer actuator 59
3.3.2 Damping ratio 62
3.3.3 Blocking force characterization 63
3.4 Empirical strain-to-charge ratio 64
3.4.1 Strain to charge ratio 64
3.4.2 Linear strain 67
3.5 Conclusion 69
Chapter 4: Linear dynamic and nonlinear dynamic model to predict PEDOT-based trilayer actuation behavior 73
4.1 Motivation 74
4.1.1 Objectives 74
4.1.2 Proposed methodology 74
4.2 State of art 74
4.2.1 A summary of Black box, white box, grey-box models for CP actuators 75
4.2.1.1 Black-box model 75
4.2.1.2 Grey-box model 75
4.2.1.3 White-box model 78
4.2.2 Why the choice of the Bond Graph language? 80
4.3 Dynamic Bond Graph modeling 84
4.3.1 Actuation description 84
4.3.2 Word Bond Graph model 86
4.3.3 BG submodels 87
4.3.3.1 Electrical model 87
4.3.3.2 Electromechanical coupling 92
4.3.3.3 Mechanical model 93
4.3.4 BG global models 99
4.4 Simulation tests 101

4.4.1 Software implementation 101
4.4.2 Comparison between the linear and nonlinear simulations 102
4.5 Comparison to experimental tests 106
4.5.1 Time domain responses 106
4.5.2 Frequency responses 110
4.6 Parameter sensitivity and power performance analysis 113
4.7 Conclusion 117
Chapter 5: Sensing ability and sensing model of the PEDOT-based trilayer actuators 112
5.1 Introduction 123
5.2 Theories on the mechanoelectrical effects 123
5.3 Sensing modeling 129
5.3.1 Mechanoelectrical coupling 129
5.3.2 Global model 131
5.4 Experimental setup 131
5.5 Results 134
5.5.1 Comparison between the model simulation and experimental results 134
5.6 Discussion 139
5.6.1 Force in response to a step displacement 141
5.7 Conclusion 142
Chapter 6: Conclusion and outlook 145
Appendix 149
A.2 Chapter 2: PEDOT-based trilayer fabrication process 149
A.2.1 Optimization of electrochemical properties of PEDOT electrodes 149
A.2.2 Surface measurement method 153
A.3 Chapter 3: Electrochemomechanical characterization of the trilayer structure 154
A.3.1 Qualitative explanation the apparent capacitance of the PEDOT electrodes at extreme low scan rate 154
A.4 Chapter 4: Linear dynamic and non-linear dynamic model to predict PEDOT-based trilayer actuation behavior 155
A.4.1 The coupling matrix derivation method 155
A.5 Chapter 5: Sensing ability and sensing model of the PEDOT-based trilayer actuators 156
A.5.1 A possible qualitative sensing model 156

List of Figures

Chapter 1: Introduction

Fig. 1. Dependence of blocking stress on actuation strain for various artificial muscles. Abbreviations: PVDF - piezoelectric polymer [32], PZT - piezoelectric ceramic [33], TE 100K - Thermal expansion actuators 100K [34], SMA – shape memory alloy [35], CP – conducting polymer [36], IPMC – ionic polymer metal composite [37], PZT-PT – piezoelectric single crystal [33], P(VDF-TrFE) – relaxor ferroelectric polymer [38], DEA – dielectric elastomer [35], PAM – pneumatic artificial muscle [19], Gels – Gel actuators [39], NM – natural muscle [1]. 4
Fig. 2. Dependence of specific work on actuation strain for various artificial muscles. 5
Fig. 3. Chemical structures of some typical conducting polymers. 8

Chapter 2: PEDOT-based trilayer fabrication process

Fig. 1. Actuation mechanism of conducting polymer actuators: a) anion driven mechanism, b) cation driven mechanism [6] (Reprinted with permission from Springer Nature). The ovals represent positive electronic charge on the backbone. 17
Fig. 2. Cation driven actuation in a PEDOT-based actuator. 18
Fig. 3. Bending actuation mechanism of PEDOT-based trilayer actuators. The anode contracts due to ion expulsion and the cathode expands due to cation incorporation, leading to bending. 18
Fig. 4. A possible model taking into account two electrochemical doping process: some ions (II), deeply trapped near the polymer chains are released at only very low potentials. Other ions (I) are shallowly trapped, they form a double layer at a certain distance from the chain. (Reproduced with permission from [10], The Electrochemical Society.) 19
Fig. 5. a) Schematic of a micropump driven by a PPy-based CP actuator [12] (Reprinted with permission from John Wiley and Sons), b) A diagram pump: the mechanism of flap check valves and a bottom view of the assembled micropump [13] (Reprinted with permission from Elsevier), c) Micro autofocus lens actuator that uses bending conducting polymer actuators [14] (Reprinted with permission from Elsevier), d) A prototype of a robotic fish [15] (Reprinted with permission from IOP Publishing) 20
Fig. 6. a) A schematic drawing of a closable microvials [16] (Reprinted with permission from Springer Nature), b) A sequence of pictures (left) showing the grabbing and lifting of a 100 µm glass bead and schematic drawings of the motion (right) [17] (Reprinted with permission from The American Association for the Advancement of Science) 21
Fig. 7. Schematic of a) full-IPN and b) semi-IPN where the pink, blue, and empty dot represent for the crosslinking between two polymer chains. 23

Fig. 8. a) properties of ionic liquids incorporated in NBR/PEO matrix, and b) strain differences calculated for PEDOT-NBR/PEO-PEDOT actuator swollen with different ionic liquids [42] (Reprinted with permission from Elsevier). 25
Fig. 9. Molecular formula of a) the precursor PEGM, b) PEDGM, c) the linear chain NBR, d) the initiator DCPD, and e) the ionic liquid EMITFSI [46] (Reprinted with permission from American Chemical Society, 2008.) 27
Fig. 10. Oxidation of EDOT with iron (III) p-toluene sulfonate 28
Fig. 11. Fabrication process of PEDOT electrodes [51] 28
Fig. 16. Relation between the rotational speed of the spin-coater for deposition of the oxidant solution on a silicon wafer and the thickness of the PEDOT electrode, where the mPEG content is 10% of oxidant solution 30
Fig. 13. Microactuator fabrication process showing the multilayer process followed by laser micromachining 31
Fig. 14. Relationship between rotation speed of spin-coater for deposition of NBR/PEO and its resulting thickness 32
Fig. 15. Trilayer structures during washing step in methanol, the rotational coating speeds of PEDOT:NBR/PEO:PEDOT are a) 1000:2000:1000 b) 1500:2000:1500 c) 2500:2000:2500 d) 3000:2000:3000; the acceleration and coating duration are constant at 1000 rpm s^{-1} and 30 s, respectively. Les coloration is seen during washing for the fast spun, thin layers of oxidant solution, indicating less weakly polymerized EDOT. 33
Fig. 16. a) The wafer after drying process, the white trace on the top right indicating the area has been peeled off for characterization: EDX and SEM, b) the resulting trilayer actuator after laser patterning process, the dimensions of the trilayer are length x width = 5 mm x 1 mm c) SEM images of the trilayer after swollen in EMITFSI 35
Fig. 17. a) The EDX of the trilayer structure, b) The anticipated morphology of the trilayer structure PEDOT:NBR/PEO:PEDOT 37
Fig. 18. a) SEM image of the trilayer cross section in dry state, profilometer surface roughness of the b) top surface of the top electrode layer, c) top surface of the SPE of a bilayer PEDOT/SPE, d) top surface of the bottom electrode layer, e) bottom surface of the bottom electrode layer 38

Chapter 3: Electrochemomechanical characterization of the trilayer structure

Fig. 1. Actuator behavior under a step voltage a) The applied step voltage and the response current, b) Bending response of the actuator, c) A picture of the bending actuator (length x width x thickness = 4 mm x 1 mm x 0.017 mm), the + and – indicate the polarity of the applied voltage. 47
Fig. 2. a) EIS measurement using 4-point setup, b) NBR/PEO layer, bottom bilayer, and top bilayer configuration, and c) a zoomed image of an area in the red rectangular A-A and its equivalent circuit showing the current direction at low and high operating frequency. 50

Fig. 3. Impedance values obtained from EIS measurements of a pure EMImTFSI, a top bilayer of NBR/PEO-PEDOT, a bottom bilayer of PEDOT-NBR/PEO, and a single NBR/PEO layer. 51
Fig. 4. Three-electrode system for setting the oxidation state of the PEDOT and for cyclic voltammetry analysis. 53
Fig. 5. A built in-house four-line probe to measure the electronic conductivity of the PEDOT electrodes, where the distance between two copper lines is d = 2 mm. 54
Fig. 6. PEDOT electrical conductivity as a function of oxidation state: a) on the bottom PEDOT surface of the trilayer structure, b) on the top PEDOT surface of the trilayer structure 55
Fig. 7. a) Cyclic voltammograms of PEDOT electrodes obtained in neat EMImTFSI within a potential window of -0.6 V to +0.7 V with different scan rates: b) Volumetric capacitance of PEDOT electrodes as function of the scanning rate. 56
Fig. 8. Volumetric capacitance as a function of the voltage window from 0.5 Vpp to 3.3 Vpp. 57
Fig. 9. The current response to an input step voltage at low frequency (f = 0.005 Hz) 59
Fig. 10. Young's moduli of the NBR-PEO layer alone - and of a trilayer structure as a function of oxidation state - were measured using a Bose Electroforce 3000 dynamic mechanical analyzer 60
Fig. 11. Young's modulus of the trilayer actuator and the PEDOT layer as a function of applied voltage. 61
Fig. 12. Experimental setup to measure the damping ratio of the trilayer actuator and the blocking force 62
Fig. 13. Beam vibrating as function of time. 62
Fig. 14. Force generated as a function of the magnitude and the frequency of the applied voltage from a trilayer actuator of length x width x thickness: 6 mm x 1 mm x 0.017 mm. 63
Fig. 15. Actuator at the a) neutral state where the bending radius is equal r_0 = 12 mm, and b) excited state where the bending radius is r_t = 2.8 mm. The orange square on the background of the pictures has the dimension of 1 x 1 mm. 64
Figure 16. Current and charge response to a triangular input voltage. 65
Fig. 17. Charge density and strain of the trilayer actuator as a function of time under a triangular wave voltage excitation 65
Fig. 18. Uniaxial deformation of the trilayer actuator under a step voltage 67

Chapter 4: Linear dynamic and nonlinear dynamic model to predict PEDOT-based trilayer actuation behavior

Fig. 1. a) The equivalent electrical circuit of the diffusive elastic model, which includes: a double layer capacitance C, electrolyte resistance R, and the impedance associated with ionic charge transport dominated by diffusivity Z_D, b) Example of an equivalent electrical circuit including a finite diffusion element C_{jk} and R_{ijk}, a resistance R_{ej}, and capacitance at the interface between the solution and the polymer 76

Fig. 2. a) a CP actuator in neutral state and its dimensions (shown in the magnified section in the middle), and b) a voltage excitation induces a tips displacement w(L, t) and an angular rotating angle $\theta(x,t)$ of the actuator, which is equivalent to an external force F(L, t) or a moment M(x, t), respectively. The Young's moduli of the PEDOT electrodes and the NBR/PEO layer are E_P and E_S, respectively. 85
Fig. 3. Trilayer actuator Words BG model.....86
Fig.4. a) 2D diffusion transmission line across the thickness and the length of a trilayer actuator, and simplified electrochemical model of the trilayer actuator for b) nonlinear model, and c) linear model 90
Fig. 5. BG representation of a) the nonlinear electrochemical model, b) the linear electrochemical model. 91
Fig. 6. Coupling between electrical sub-system and mechanical sub-system. 92
Fig. 7. Rigid Finite Element Model (RFEM) of a trilayer actuator, in which it is divided into (n+1) rigid elements: from RFE_0 to RFE_n, the elements each have a mass and are linked by a spring-damper element SDE_1 to SDE_n, shown in their initial positions. The integrated coordinator includes X_0 axis along the length of the actuator, X_1 axis perpendicular to the X_0 and X_2 axis perpendicular to the X_0X_1 surface. 94
Fig. 8. Trilayer actuator in a bent state. The bending angle between the element (i-1) and the element i is θi.....95
Fig. 9. Mechanical BG model.....97
Fig. 10. BG representation of the mechanical model of the trilayer actuator, the block 1 (red color) indicates the point force F(L, t) obtaining from the electromechanical coupling matrix applying to the free end of the beam, the block 2 (green color) presents the boudary condition where one end of the beam is fixed, the block 3 (pink color) is a BG presentation of the equation (25), and finally the block 4 (orange color) introduces the method to extract the tips displacement of the beam w(L, t). 99
Fig. 11. CP actuator global model: 1. Voltage source, 2. Electrochemical model, 3. Coupling between electrochemical and mechanical part, 4. Mechanical model, 5. Boundary conditions: initial stress, 6. Displacement output. 100
Fig. 12. Linear BG global model of CP actuators, where a source of voltage is employed as the input and the tips displacement of the beam is the output of the model. 101
Figure 13. Interface of 20-sim simulation software 102
Fig. 14. Comparison between the output current of the linear model and nonlinear (6 RFEs) responses to a step voltage of 2 V_{pp} at f = 0.1 Hz 104
Fig. 15. Comparison between the linear model and the nonlinear model in bending displacement of the actuator in response to the step input voltage with various magnitudes 105

Fig. 16. Trilayer actuator under voltage excitation: a) Top PEDOT electrode voltage: -1.1 V, Bottom PEDOT electrode: 1.1 V, b) neutral state, c) Top PEDOT electrode: 1.1 V, Bottom PEDOT electrode: -1.1 V.....107
Fig. 17. a) Triangular wave and rectangular wave applied voltage, b) Measured and simulation current response.....108
Fig. 18. Modeled voltage drops along the length of the beam due to the existence of electrical resistance of PEDOT electrodes. The black curve is the voltage seen at the fixed end of the cantilever where electrical contact is made. The dashed green line is the predicted voltage as seen at 0.9 of the length, and the others are in between. 109
Fig. 19. Comparison between the simulations and the experiments on the strain as a function of the magnitude of applied voltage at a constant frequency of 0.1 Hz 110
Fig. 20. a) Comparison between the simulations and the experiments on the strain as a function of the frequency of applied voltage at a constant magnitude of ±1.1 V, b) The relative error of the simulations compared to the measured data. 111
Fig. 21. Comparison between the experiment and the simulation in terms of the dynamic mechanical behavior of the beam subjected to a voltage excitation of 2.2 Vpp at 0.1 Hz...112
Fig. 22. Key factors affecting the actuator displacement under a square wave voltage (Vpp = 2.4 V), a) at low frequency f = 0.1 Hz, and b) at high frequency f = 20 Hz. For each parameter, three columns from left to right represent for its real value (blue column), its value increased by 20% (orange column), and its value reduced by 20% (grey column).....113
Fig. 23. Evolution of energy over half a period of applied voltage: a) In the electrochemical part, b) In the mechanical part. 115
Fig. 24. Instantaneous electrical to mechanical coupling.....116

Chapter 5: Sensing ability and sensing model of the PEDOT-based trilayer actuators

Fig. 1. a) Schematic of CP free-standing film sensing mechanism before and after subjected to a linear force, and b) Schematic of a bending trilayer sensor [4] 123
Fig. 2. Effect of counter-ion and redox state on the voltage output of polypyrrole mechanical sensor [2] (Reprinted with permission from John Wiley and Sons) 125
Fig. 3. Schematic diagram illustrating the net ion transport expected in both the "Deformation Induced Ion Flux" model and based on elastic energy considerations [2] (Reprinted with permission from John Wiley and Sons). In the first case compression of the polymer leads to an increase in ion concentration within the polymer, and a net flux of ions out. In the second, it is the compressive stress that squeezes ions out. 126
Fig. 4. Experimental scheme and induced voltage mechanism of a thin ionic conducting polymer film under an applied stress [10].....127
Fig. 5. Schematic experiments and comparison of output voltage in two different trilayer configurations: Gold-NBR/PEO-Gold, and PEDOT-NBR/PEO-PEDOT with the dimension of L = 15mm, b = 5mm, h_t = 0.17 mm at various EMITFSI-PC concentrations, under a 2% applied

strain [11] (Retrieved from https://tel.archives-ouvertes.fr/tel-01413677. By permission from author.). In this case a positive voltage suggests anion motion. 128
Fig. 6. Global Word BG model, where (1) and (3) represent the input voltage and the tip displacement, respectively, as the trilayer structure in actuation mode; the (4) and (5) are the input displacement and the voltage output, respectively, when the trilayer is operated as a sensor, (2) is the global BG model 131
Fig. 7. a) Experimental setup to measure the voltage response to a sinusoidal displacement, and b) An output voltage response to an input displacement of the magnitude of 2 mm and frequency of 3 Hz on a trilayer of 7 mm x 1 mm x 0.017 mm. 133
Fig. 8. Experimental setup to measure the decaying of blocking force of the actuator in response to a step displacement 134
Fig. 9. a) Schematic of a trilayer transducer under a displacement excitation and the produced voltage polarity b) Voltage magnitude and the strain-to-charge ratio as a function of frequency when the magnitude of the sinusoidal displacement is constant at 2mm, c) Comparison between the simulation and the experiment of the magnitude of output voltage 136
Fig. 10. a) Voltage magnitude and the strain-to-charge ratio as a function of magnitude when the frequency of displacement is constant at 3 Hz, b) Comparison between simulation and experiment of the magnitude of output voltage 138
Fig. 11. Comparison between the simulation and measured voltage responding to an applied step displacement 139
Fig. 12. a) Experiment of applying step displacement, and b) The decay of force response of the beam as a function of time. 142

List of Tables

Chapter 2: PEDOT-based trilayer fabrication process

Table 1. Summary some important properties of three different PEO-based IPNs.....24
Table 2. Summary the sample configuration for different characterizations 35

Chapter 3: Electrochemomechanical characterization of the trilayer structure

Table 1. Thickness in swollen state and ionic conductivity of the NBR/PEO alone, top bilayer, and bottom bilayer 52
Table 2. Summary strain-to-charge ratio for different materials and actuator configuration66
Table 3 Summary of measured parameters of the ultrathin trilayer actuator 68

Chapter 4: Linear dynamic and nonlinear dynamic model to predict PEDOT-based trilayer actuation behavior

Table 1. Summarize on various model approaches of CP-based actuators 81
Table 2. Notations for continuous, lumped, and distributed modeling approaches 85
Table 3 Summary of derived parameters for the linear model.....101
Table 4. Pros and cons of the linear model in comparison to the nonlinear model 103

Abbreviations

BG	Bond Graph
CP	conducting polymer
CV	cyclic voltammetry
EAP	electroactive polymer
EDOT	3,4-ethylenedioxythiophene
EDX	energy-dispersive X-ray spectroscopy
EIS	electrochemical impedance spectroscopy
EMITFSI	1-ethyl-3-methylimidazolium bis(trifluoromethanesulfonyl)imide
IPMC	ionic polymer-metal composite
IPN	interpenerating network
LbL	Layer by Layer
NBR	nitrile butadiene rubber
PEDOT	poly(3,4-ethylenedioxythiophene)
PEDOT:PSS	poly(3,4-ethylenedioxythiophene): poly(styrene sulfonate)
PEGDM	poly(ethylene glycol) dimethacrylate
PEGM	poly(ethylene glycol) methyl ether methacrylate
PEO	polyethylene oxide
PPy	polypyrrole
PVDF	polyvinylidene difluoride
RFE	rigid finite element
RFEM	rigid finite element method
SDE	spring damper element
SEM	scanning electron microscopy
sIPN	semi interpenerating network
SPE	solid polymer electrolyte
VPP	vapor phase polymerization

Acknowledgements

Financial support for my study was generously provided by the European Union's Horizon 2020 research and innovation programme under the Marie Skłodowska-Curie grant agreement No 641822 (http://micact.eu), National Research Agency (ANR) under program PIA EQUIPEX LEAF (ANR-11-EQPX-0025), RENATECH and MICRO-TIP projects.

This study could not be finished without collaboration and support of my supervisors, my colleagues, and my family.

First of all, I gratefully acknowledge my supervisors: Prof. Eric Cattan, Prof. Sébastien Grondel, and Prof. John D.W. Madden for their enduring patience and thoughtful advices, for granting me the freedom to pursue my ideas, and for giving me the opportunity to interact with experts of electroactive polymer community.

I would like to acknowledge the LPPI team: Prof. Frédéric Vidal, Dr. Cédric Plesse, Dr. Giao Nguyen, and Kätlin Rohtlaid for giving me the opportunity to visit their lab, to discuss the challenges arising in transducers' fabrication process, and to collaborate with me on some parts of the thesis.

Thank you to my past and present colleagues in MAMINA group in IEMN, Dr. Caroline Soyer, Dr. Damien Faux, Mohamed Bentefrit, Lauréline Seurre, and in Molecular Mechatronics Laboratory in UBC, Dr. Ali Mahmoudzadeh, Yuta Dobashi, Saquib Sarwar, Claire Preston, and Saeedeh Ebrahimi for their great friendship and help.

Finally, thanks to my loving wife Minh Quan and my daughter Minh Anh, who always had faith in me through the most difficult time of my life. I owe special gratitude to my Mother and my Brother for their unconditional love and support, encouragement, patience, without which this work would not have been possible. You have been supported me in one way or another along the way.
Thank you all.

Dedication

I dedicate this thesis

To the memory of my late Father.

Chapter 1: Introduction

Contents

1.1 Mammalian muscles 2
1.2 Artificial muscles 2
1.3 Motivation and problem statement 9
1.4 Thesis structure 9

This chapter reviews the motivation for the work and outlines the structure of the thesis. At first, a brief review on mammalian muscles is given. Then contractile materials, known as artificial muscles, are described. Particular attention is paid to conducting polymer actuators and sensors, which are the subjects of this thesis.

1.1 Mammalian muscles

Mammalian muscles are highly optimized systems as their structure are considered to be the same for all animals. They are driven by a complex mechanism where a chemical reaction drives reversible hydrogen bonding between proteins actin and myosin, sliding them past each other to produce strain. Mammalian muscle performance has been reported reach a peak stress of 150-300 kPa at a strain of about 25% and the maximum power output is 150-225 W/kg. At low and intermediate operating frequencies, natural muscle has the average power of 50 W/kg the energy density of 20-70 J/kg [1]. Because of their micro fiber structure, natural muscles are easy to scale. However, the biggest challenge is the requirement of a complex accompanying system to feed and keep them alive. This issue has driving the researchers to keep searching possible materials and structures, which can replicate natural muscles.

1.2 Artificial muscles

Actuating materials, or “artificial muscles” have long been of interest. A growing interest in artificial muscles has been observed over two last decades. Aiming to develop a soft robotic programmable motion has driven researchers around the world to experiment with a variety of materials and designs. The designed robots were expected to mimic the bending and flexing in a way that can interact more naturally with living organisms. These are materials or devices having the ability to reversibly contract, expand, or rotate within one component under an external stimulus [2], and promise compact, lightweight means to mechanically power everything from robots, exoskeletons, and medical prosthetics to micro-fluidic circuits and micro-tools. Different materials have been developed for artificial muscles including shape memory alloys (SMAs) [3], electroactive polymers (EAPs) [4], and piezoelectric and dielectric materials [5]. Like natural muscles, artificial muscles are characterized by a reciprocating or oscillatory types of motion that may be evident as linear [6, 7], bending [8-12], torsional [13] [14, 15] [3]or torsional induced linear actuation [16] and a combination of these processes [5]. Based on the actuation mechanism, these artificial muscles can be classified into four categories: pneumatic, thermal, ionic-based, and electric field driven actuation - wherein the actuation is due to Coulombic forces. The relation between blocking stresses and actuation strains for a variety of the artificial muscles can be found in the Fig. 1.

Pneumatic artificial muscle (PAM), so-called McKibben Artificial Muscle, Fluidic Muscle, or the Biomimetic Actuator [17], is an actuator, which is shortened in the actuating length when it is pressurized [18]. The common structure of a PAM is a long and hollow cylinder made of

synthetic or natural rubber, wrapped inside a braided mesh shell built at a predetermined angle. The working mechanism of the PAM relies on the supply of compressed-air to the interior of the cylinder, which contracts in length and expands radially. Upon the air being released, the mesh plays a role as a spring that restores the cylinder to its original form. The most significant advantage of PAM in control applications is that only pressure parameter needs to be controlled [19]. In addition, PAMS are also lightweight, easy to fabricate, and have load-length curves similar to human muscle [20, 21]. However, PAMs are not very accurate, have a low force output, and require lot of additional equipment such as: a source of pressurized air, a feedback sensor, and a solenoid for controlling flow. These deficiencies motivate research on alternatives to PAMs going forward.

In the class of thermal actuation, shape memory alloys (SMAs) are the well-known actuators, which belong to the class of shape memory materials. They are metallic alloys having the ability to return to their original shape when subjected to a temperature or magnetic field memorization process between two transformation phases [22-25]. Under some certain conditions, superelasticity or visco-elasticity are also commonly observed [24]. The SMAs have been used in various fields such as automotive, aerospace, robotics, and biomedical applications [26-28]. They have been proven to provide unique characteristics such as bio-compatibility, high stress, high work per volume and work density (for NiTi SMA type: 200 MPa, 10%, 100 J/cm^3, 15 kJ/kg) [29]. However, they also have several disadvantages such as low accuracy, limited strain, fatigue, stability, and low energy efficiency [30, 31]. Therefore, intensive work is required to enhance the performance of SMAs.

Recently, new members of the thermal actuation family have been warmly welcomed. Lima *et al.* [15] have introduced hybrid yarn actuators in which a guest material is incorporated into the pore space between multi-walled carbon nanotube bundles. The actuators produce a torsional rotation and contraction performance when an electrical, chemical, or photonic excitation is induced on the host material, resulting in a dimension change of the guest and the yarn. Later on, Haines *et al.* [16] demonstrated that inexpensive high-strength polymer fibers used for fishing line and sewing thread can be used for tensile and torsional muscles. These fishing line artificial muscles produce a large stroke (up to 49%), and high stress. Considering they are of the same length and weight, these fishing line can lift a loads over 100 times larger compare to that of human.

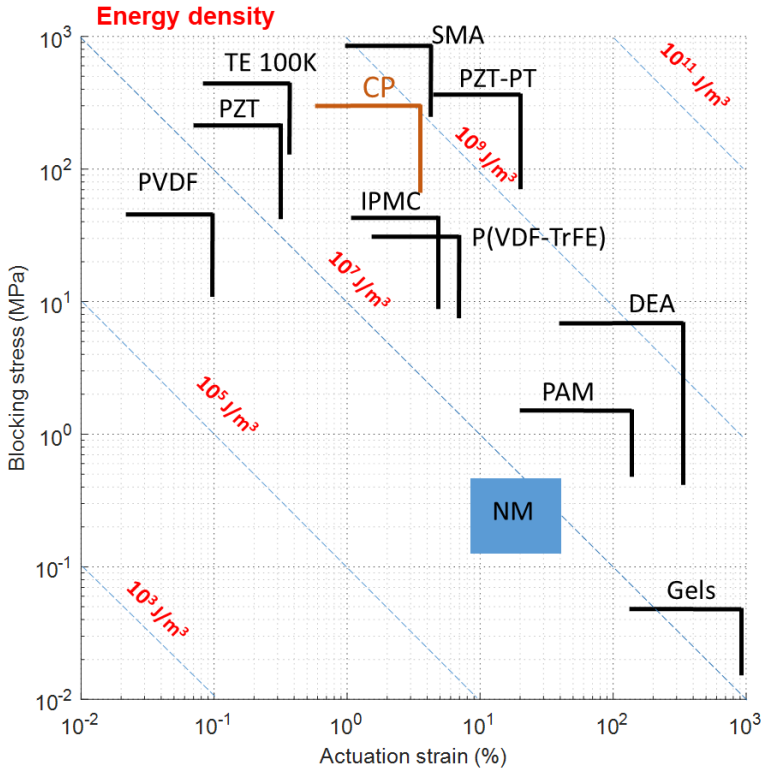


Fig. 1. Dependence of blocking stress on actuation strain for various artificial muscles. Abbreviations: PVDF - piezoelectric polymer [32], PZT - piezoelectric ceramic [33], TE 100K - Thermal expansion actuators 100K [34], SMA – shape memory alloy [35], CP – conducting polymer [36], IPMC – ionic polymer metal composite [37], PZT-PT – piezoelectric single crystal [33], P(VDF-TrFE) – relaxor ferroelectric polymer [38], DEA – dielectric elastomer [35], PAM – pneumatic artificial muscle [19], Gels – Gel actuators [39], NM – natural muscle [1].

Electric field actuation includes piezoelectric and dielectric elastomer actuation (DEAs). Piezoelectric materials are known as materials that undergo a small reversible change in dimensions when subjected to an electric field. An electric polarization is developed when they are strained [33]. Piezoelectricity can be used in various applications such as sound production and detection, microbalances, and ultrafine focusing of optical assemblies. In addition, it is a basic component in various scientific devices, such scanning probe microscopes [40], the ignition source for cigarette lighters, and the time reference source in quartz watches [41]. The most common type of piezo ceramic is lead zirconate titanate known as PZT. However, it is known as a brittle material causing limitations in the applications where high strain is required.

For applications requiring deformable materials researchers have developed flexible material which can withstand a large amount of strain [35]. DEAs are made of thin film of electrically insulating elastomeric materials, which are coated on both sides with the electronically conducting compliant electrodes. When a voltage is applied to the electrodes, the films

expand in area and compress in thickness. DEAs are a promising EAP technology that can be applied in various technologies, such as actuators, strain sensors, and electrical generators used to harvest mechanical energy [29, 42, 43]. However, the widespread adoption of DEAs has been challenged by early breakdown and the high electric field requirements, and large support frames to hold the DEA membranes [29]. The miniaturization to the micro scale of the DEA fabrication process has recently been investigated. A thin film of 5 µm was fabricated and stacked on the top of each other up to 50 layers to increase the total height of the system to obtain usable displacement and reduce the controlling voltage down to 150 V [44-46], which still remains high and be restricted for the human affinity applications.

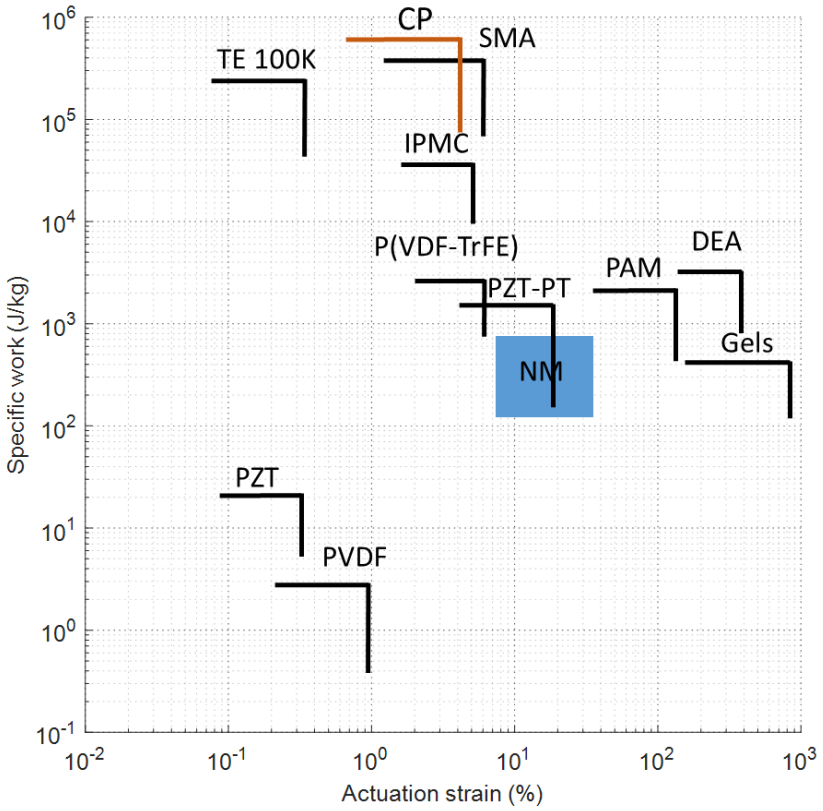


Fig. 2. Dependence of specific work on actuation strain for various artificial muscles.

Gels, ionic polymer-metal composites (IPMCs), carbon nanotubes (CNTs), and conducting polymers fall under the ionic-based classification. Gels are found in manufactured foods, cosmetics, and in medical creams [47, 48]. They can be extremely soft, biocompatible and biodegradable [49, 50]– all properties of interest for medical and *in vivo* applications. Basically, ionic gels contain a crosslinked polymer in an electrolyte solution (it can be water-based or organic solvent). As actuators, gels are exciting because of the very large dimensional changes they can produce (more than 40% in strain) [32], albeit at blocking forces (maximum pressure at 0.3 MPa). Depending on types of stimulus signal, gel actuators can be classified into temperature-responsive gels [51], photoresponsive gels [52], chemical driven gels [53],

and electrically driven gels where an electric field can induce a flow of positively charged surfactant binding to one side of the gel [54]. Gels also have a great potential as sensors. But the actual uses of gels are somewhat restricted. Gel actuators have very low blocking force due to their low modulus (normally < 4 MPa) [47]. In addition, delivery of chemical energy requires pumping systems, which may add to the weight and complexity. The other limitations of gel actuators are low response speed - which is due to diffusion rates - and drying out of hydrogels when they are used outside of a wet environment. Recent work by Spinks in which gels are used as the swelling element in McKibben actuators (PAMs that swell with gel instead of air) show large strains (9%) and relatively high forces (2 N) when heated or swollen in the hot water, but remain slow [55].

Carbon nanotubes (CNTs), which were discovered in 1991 by Iijima [56], have attracted a lot of interest thanks to their intrinsic electrical and mechanical properties. An individual CNT possesses a high Young's modulus of approximately 1 TPa, maximum tensile strength of 100 GPa, and a conductivity of 10^6 – 10^7 S/m [57]. In addition, CNTs can be incorporated with different guest materials to form composite materials and benefit from those. Although the mechanical strength of an individual CNT is extremely high, the effective strength of CNT bundles is pretty low because of weak shear interactions between adjacent shells and tubes [58]. CNTs alone have been used in tensile and torsional actuators [14, 59, 60] where the working mechanism is based on the formation of a double layer capacitance to balance the charges injected by an applied potential – with the formation of this double layer also appearing to push nanotubes apart [60, 61]. Due to their high stiffness, the obtained strain is pretty small, ~ 0.07 % [59]. However, the high porosity and fast ion diffusion are the main contribution to a high strain rate of 19 % s^{-1} [62]. CNTs remain expensive to mass produce [63, 64] which has limited their widespread applications in artificial muscles and other applications to date.

IPMCs, which are structured of an ionic conducting polymer sandwiched by two metal electrodes, are one of the promising electroactive polymers (EAP) for soft actuators and sensors. Their actuation mechanism is based on mobile cations accompanied by water (or solvent) flow. An electric field induces a change in ion concentration, which attracts water molecules (or other solvent) to one side of the polymer, causing a deflection of the total structure toward one of the metal electrodes – and away from the side that swells. IPMCs offer a huge advantages that attract the use in various biomedical and human interface applications such as, low driving voltage (1 – 3 V), quite high frequency response up to several hundred hertz [65, 66], large displacement (maximum strain 3%), softness (maximum pressure 30 MPa) [37], ready manufacturing into a wide range of shapes, operation in wet conditions (water, solutions) as well as dry (open air) conditions [67-69]. IPMCs also exhibit sensing properties - generating an electric current in response to bending moments imposed on them. However, a big drawback of IPMCs is a slow relaxation due to the backward

movement of water molecules out of the cation-rich areas. They also require a constant applied voltage and some power to maintain their operating position [70]. Recently, ionic liquid was incorporated into the IPMCs instead of solvent, to reduce the relaxation and increase the operating lifetime of the actuators - at the cost of very low response speeds [71-74].

Conducting polymers (CPs) are organic polymers that conduct electricity. Since the discovery of polymeric organic conductors in 1977 [75, 76], knowledge in this field has grown dramatically. Based on the heteroatoms present in the structure, conducting polymers can be classified into three types: i) no heteroatom such as poly(acetylene)s (PA), and poly(p-phenylene vinylene) (PPV), ii) nitrogen containing such as poly(pyrrole)s (PPy), and polyanilines (PANI), and iii) sulfur-containing such as poly(thiophene)s (PT), poly(3,4-ethylenedioxythiophene) (PEDOT), and poly(p-phenylene sulfide) (PPS). Molecular structure of some popular conducting polymers is described in Fig. 3. PEDOT holds an important role in anti-static, electric and electronic applications [77]. The idea of using conducting polymers as actuators for the direct conversion of electrical energy to mechanical energy, based on the redox process between the CPs and the mobile ions in electrolyte, was initially proposed by Baughman [8, 78]. Remarkable progress in conducting polymer actuators has been reported by Pei and Inganäs, Smela and Inganäs, Otero, and, recently, by Vidal *et al.* [11, 12, 79-83]. These actuators have offered advantages over other types of artificial muscles by offering a combination of low operating voltage (typically 1-2 V), biocompatibility [84-86], large strain range from 1 up to 10 %, high blocking force and high specific work (Fig. 1 and Fig. 2). They can be found in various potential applications including catheters [87, 88], dynamic Braille display [89, 90], valves [88], and blood vessel reconnection [61].

CP actuators suffer from very low efficiency (less than 1%) and electrochemical coupling under 1% [5], however the operating efficiency can be improved by recover the stored energy under the form of electrochemical, mechanical elastic and potential energy. In addition, the actuation response is normally slow since their working mechanism relies on ion migration. Recently, the problem of low actuation speed has been addressed by Maziz *et al.* [83, 91]. They have demonstrated a kHz operating speed (at resonance) of PEDOT-based actuators, where the total thickness of the actuator is several micrometers. Later on, they showed that this actuator is compatible with a microfabrication process that includes: i) compatibility with photolithography process and plasma etching [92, 93] ii) the layer-by-layer technique combined with the vapor phase polymerization to fabricate thin actuators, ii) integration the electrical contact onto the electrodes and patterns them into desired shape with high precision [91, 92]. In the remainder of the thesis, this fabrication technique and the subsequent developments are built upon.

Considering CP-based transducers and IPMCs, they both show quite similar advantages, as reported previously, and can both be adapted to similar applications. In term of working

mechanism, they are based on ion movements due to the redox reactions in the first case, and mobile cations accompanied by water (or solvent) flow in the second case. These result in a contraction or an expansion of the CP electrode or an osmotic pressure gradient towards the negative electrode of IMPC. However, while the modelization of IPMCs was well established, the working mechanism of CP-based actuators is still unclear.

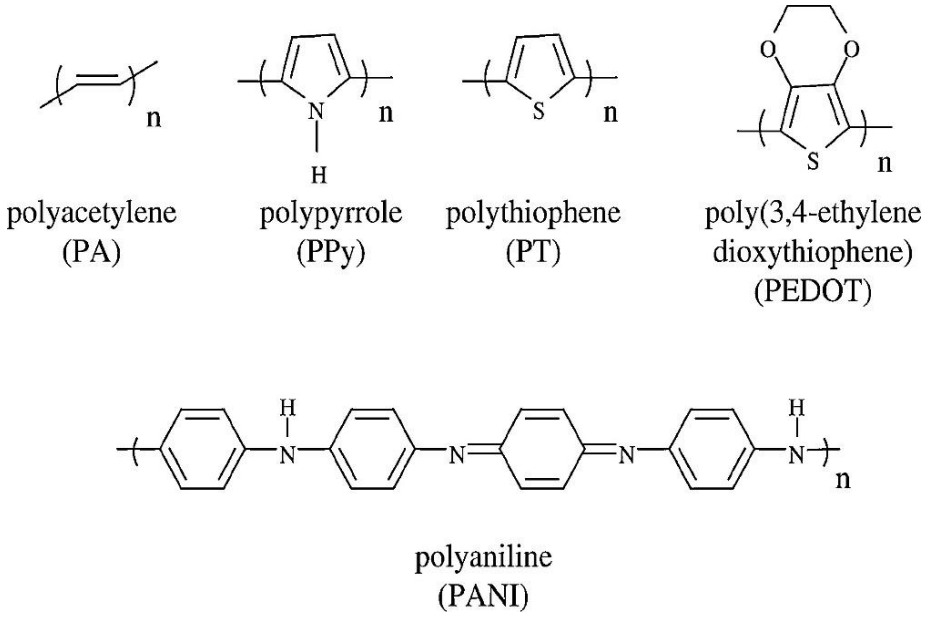


Fig. 3. Chemical structures of some typical conducting polymers.

The Laboratoire de Physicochimie des Polymères et des Interfaces at the University of Cergy-Pontoise, the Institut d'électronique de microélectronique et de nanotechnologie at the University of Valenciennes et du Hainaut Cambrésis, and the laboratory of Molecular Mechatronics at the University of British Columbia have had a long (more than 10 years) and fruitful collaboration on conducting polymer (CP) materials and devices, including optimization and characterization, modeling, and applications of the materials. Currently, one of the main goals of the group is to develop microsystems from CP materials. CP actuators, as demonstrated previously, are potential candidates for microscale applications (thickness of the actuator < 20 μm), where a low operating voltage, high strain, fast operation in open air, and especially a compatibility with clean room techniques are required. However, to bring this material and the new fabrication method proposed by Maziz *et al.* [36] from the lab into large scale manufacturing and production, the optimization on the fabrication techniques, as well the full characterization and modeling of this ultrathin structure are the essential steps.

1.3 Motivation and problem statement

The goal of this thesis is to fabricate, characterize electro-chemo-mechanical properties, and to model the ultrathin PEDOT-based trilayer transducers.

For this purpose, a versatile fabrication technique, which offers high precision and reliability, is required to produce a good trilayer. The layer-by-layer fabricating technique, which is compatible with the photolithography process including plasma dry etching, is selected to fabricate the trilayer structure. Characterization methods have been developed to respond to measurements made on very thin films to understand their transducer mechanisms. The characterization process of the trilayer transducers may also bring some difficulties, and since these trilayers are thin and easy to damage under mechanical stress. In addition, properties can be varied with oxidation state.

Ultimately, to fully exploit the thin trilayer structures, modeling is required to predict behavior of micro-actuators and micro-sensors, to optimize their design before mass production and finally to understand and control device operation. As demonstrated previously, the actuation mechanism of the PEDOT-based actuators is a complex process, that involves electrical stimulation, redox reactions, and induces mechanical strain. These can challenge the modeling process, where a complex model including different domains is needed.

Within this thesis, these challenges on the layer-by-layer fabrication technique and the characterization as well as the modeling process of the resulting trilayer transducers will be confronted and the outcome will be drawn.

1.4 Thesis structure

The thesis is divided in six chapters. The brief content of each chapter is drawn as below:

Chapter 2:

Within this chapter, a brief introduction on working mechanism of CP-based actuators is given. The process of selection of the materials used to fabricate the CP-based trilayer in this study is described. Later on, different synthesis methods used to synthesize PEDOT conducting polymer are briefly reviewed and the vapor phase polymerization is selected for the PEDOT electrode fabrication process since it allows an easier means to change the electrode's thickness. The trilayer fabrication process is then described and the obtained trilayer is analyzed with profilometer, SEM and EDX techniques to determine the exact surface roughness and structure of the trilayer. The roughness surface results show an asymmetric between the two PEDOT electrodes suggesting a difference in electrical properties of the two electrodes.

Chapter 3:

This chapter presents the electrochemomechanical characterization of the resulting trilayers, including characterization techniques and the obtained results. At first, the electro-chemical properties of the trilayer, such as the electronic conductivity as the function of oxidation state of PEDOT, the ionic conductivity, and the volumetric capacitance of PEDOT electrodes as a function of the scanning rate and the voltage window, and the ionic conductivity of NBR-PEO semi interpenetrating network, are determined. The degree of bending is measured, from which the coupling between the electro-chemical and the mechanical domains - an empirical strain-to-charge ratio - is computed. Finally, the mechanical properties: Young's modulus of the PEDOT electrodes as a function of oxidation state, and of the trilayer structure, the damping ratio, the trilayer density and the forces as a function of voltage and frequency are determined.

Chapter 4:

Chapter 4 is devoted to the modeling of the trilayer actuators. The Bond Graph formalism is introduced, and the reason for its use explained. A simple electro-chemo-mechanical model based on Euler-Bernoulli dynamic beam theory is described. Later, a non-linear dynamic electro-chemo-mechanical model based on the dynamic rigid finite element method is introduced. The measured material properties (Chapter 3) are used in the model, and the simulations are compared with experimentally observed actuator deflections through time. The proposed model enables to extract the information on the energy flows inside the trilayer and evaluate the key factors affecting the actuator's performance (strain output).

Chapter 5:

A simple model including both sensing and actuation is proposed, demonstrating the advantage of the Bond Graph formulation in running in both forward (electrical to mechanical) and backward (mechanical to electrical) modes. The initial model is based on using the strain to charge ratio as an empirical coupling coefficient.

Chapter 6:

In this last chapter, the findings of this investigation are summarized and the most conclusions are drawn. Furthermore, the prospects for ongoing work are developed.

[1] G.H.R. Pollack, Frederick B.; Blyakhman, Felix A.; Yakovenko, Olga V.; Dunaway, Dwayne L., Natural Muscle as a Biological System, in: Y. Bar-Cohen (Ed.) Electroactive Polymer (EAP) Actuators as Artificial Muscles: Reality, Potential, and Challenges, SPIE, USA, 2004.
[2] S.M. Mirvakili, Niobium Nanowire Yarns and Their Application as Artificial Muscle: University of British Columbia; 2013.
[3] K.P. Jamie, H. Elliot, J.W. Robert, A novel low-profile shape memory alloy torsional actuator, Smart Materials and Structures, 19(2010) 125014.
[4] Y. Bar-Cohen, Electroactive Polymers as Artificial Muscles: A Review, Journal of Spacecraft and Rockets, 39(2002) 822-7.
[5] J.D.W. Madden, N.A. Vandesteeg, P.A. Anquetil, P.G.A. Madden, A. Takshi, R.Z. Pytel, S.R. Lafontaine, P.A. Wieringa, I.W. Hunter, Artificial muscle technology: Physical principles and naval prospects, IEEE Journal of Oceanic Engineering, 29(2004) 706-28.
[6] A.D. Santa, D.D. Rossi, A. Mazzoldi, Characterization and modelling of a conducting polymer muscle-like linear actuator, Smart Materials and Structures, 6(1997) 23.
[7] A. Fannir, Actuators based on conducting polymers with a linear deformation in open air and compatible with a space environment: Université de Cergy Pontoise; 2017.
[8] R.H. Baughman, L.W. Shacklette, R.L. Elsenbaumer, E.J. Plichta, C. Becht, Micro Electromechanical Actuators Based on Conducting Polymers, in: P.I. Lazarev (Ed.) Molecular Electronics: Materials and Methods, Springer Netherlands, Dordrecht, 1991, pp. 267-89.
[9] J.D. Madden, P.G. Madden, I.W. Hunter, Polypyrrole actuators: modeling and performance, 2001, pp. 72-83.
[10] P.G.A. Madden, Development and Modeling of Conducting Polymer Actuators and the Fabrication of a Conducting Polymer Based Feedback Loop: MASSACHUSETTS INSTITUTE OF TECHNOLOGY; 2003.
[11] E. Smela, Conjugated polymer actuators for biomedical applications, Advanced Materials, 15(2003) 481-94.
[12] T.F. Otero, E. Angulo, J. Rodríguez, C. Santamaría, Electrochemomechanical properties from a bilayer: polypyrrole / non-conducting and flexible material — artificial muscle, Journal of Electroanalytical Chemistry, 341(1992) 369-75.
[13] K.J. Gabriel, W.S.N. Trimmer, J.A. Walker, A micro rotary actuator using shape memory alloys, Sensors and Actuators, 15(1988) 95-102.
[14] J. Foroughi, G.M. Spinks, G.G. Wallace, J. Oh, M.E. Kozlov, S. Fang, T. Mirfakhrai, J.D.W. Madden, M.K. Shin, S.J. Kim, R.H. Baughman, Torsional Carbon Nanotube Artificial Muscles, Science, 334(2011) 494.
[15] M.D. Lima, N. Li, M. Jung de Andrade, S. Fang, J. Oh, G.M. Spinks, M.E. Kozlov, C.S. Haines, D. Suh, J. Foroughi, S.J. Kim, Y. Chen, T. Ware, M.K. Shin, L.D. Machado, A.F. Fonseca, J.D.W. Madden, W.E. Voit, D.S. Galvão, R.H. Baughman, Electrically, Chemically, and Photonically Powered Torsional and Tensile Actuation of Hybrid Carbon Nanotube Yarn Muscles, Science, 338(2012) 928.
[16] C.S. Haines, M.D. Lima, N. Li, G.M. Spinks, J. Foroughi, J.D. Madden, S.H. Kim, S. Fang, M. Jung de Andrade, F. Goktepe, O. Goktepe, S.M. Mirvakili, S. Naficy, X. Lepro, J. Oh, M.E. Kozlov, S.J. Kim, X. Xu, B.J. Swedlove, G.G. Wallace, R.H. Baughman, Artificial muscles from fishing line and sewing thread, Science, 343(2014) 868-72.
[17] E.T. Roche, R. Wohlfarth, J.T.B. Overvelde, N.V. Vasilyev, F.A. Pigula, D.J. Mooney, K. Bertoldi, C.J. Walsh, A Bioinspired Soft Actuated Material, Advanced Materials, 26(2014) 1200-6.
[18] G. Andrikopoulos, G. Nikolakopoulos, S. Manesis, A Survey on applications of Pneumatic Artificial Muscles, 2011 19th Mediterranean Conference on Control & Automation (MED)2011, pp. 1439-46.
[19] C. Ching-Ping, B. Hannaford, Measurement and modeling of McKibben pneumatic artificial muscles, IEEE Transactions on Robotics and Automation, 12(1996) 90-102.
[20] S.C. Obiajulu, E.T. Roche, F.A. Pigula, C.J. Walsh, Soft Pneumatic Artificial Muscles With Low Threshold Pressures for a Cardiac Compression Device, (2013) V06AT7A009.

[21] M. Doumit, A. Fahim, M. Munro, Analytical Modeling and Experimental Validation of the Braided Pneumatic Muscle, IEEE Transactions on Robotics, 25(2009) 1282-91.
[22] P.S. Lobo, J. Almeida, L. Guerreiro, Shape Memory Alloys Behaviour: A Review, Procedia Engineering, 114(2015) 776-83.
[23] J. Mohd Jani, M. Leary, A. Subic, M.A. Gibson, A review of shape memory alloy research, applications and opportunities, Materials & Design (1980-2015), 56(2014) 1078-113.
[24] W.M. Huang, Z. Ding, C.C. Wang, J. Wei, Y. Zhao, H. Purnawali, Shape memory materials, Materials Today, 13(2010) 54-61.
[25] A. Nespoli, S. Besseghini, S. Pittaccio, E. Villa, S. Viscuso, The high potential of shape memory alloys in developing miniature mechanical devices: A review on shape memory alloy mini-actuators, Sensors and Actuators A: Physical, 158(2010) 149-60.
[26] J. Van Humbeeck, Non-medical applications of shape memory alloys, Materials Science and Engineering: A, 273-275(1999) 134-48.
[27] L. Sun, W.M. Huang, Z. Ding, Y. Zhao, C.C. Wang, H. Purnawali, C. Tang, Stimulus-responsive shape memory materials: A review, Materials & Design, 33(2012) 577-640.
[28] M. Sreekumar, T. Nagarajan, M. Singaperumal, M. Zoppi, R. Molfino, Critical review of current trends in shape memory alloy actuators for intelligent robots, Industrial Robot, 34(2007) 285-94.
[29] P. Brochu, Q. Pei, Advances in Dielectric Elastomers for Actuators and Artificial Muscles, Macromolecular Rapid Communications, 31(2010) 10-36.
[30] K. Marjaana, L. Tomi, Long-term behaviour of binary Ti–49.7Ni (at.%) SMA actuators—the fatigue lives and evolution of strains on thermal cycling, Smart Materials and Structures, 19(2010) 115019.
[31] T.W. Duerig, D. Stöckel, A. Keeley, Actuator and Work Production Devices, Engineering Aspects of Shape Memory Alloys, Butterworth-Heinemann1990, pp. 181-94.
[32] R. Pelrine, R. Kornbluh, J. Joseph, R. Heydt, Q. Pei, S. Chiba, High-field deformation of elastomeric dielectrics for actuators, Materials Science and Engineering: C, 11(2000) 89-100.
[33] A.J. Moulson, J.M. Herbert, Piezoelectric Ceramics, Electroceramics, John Wiley & Sons, Ltd2003, pp. 339-410.
[34] J.E. Huber, N.A. Fleck, M.F. Ashby, The selection of mechanical actuators based on performance indices, Proceedings of the Royal Society of London Series A: Mathematical, Physical and Engineering Sciences, 453(1997) 2185.
[35] R.D. Kornbluh, R. Pelrine, Q. Pei, S. Oh, J. Joseph, Ultrahigh strain response of field-actuated elastomeric polymers, SPIE's 7th Annual International Symposium on Smart Structures and Materials, SPIE2000, p. 14.
[36] A. Maziz, C. Plesse, C. Soyer, E. Cattan, F. Vidal, Top-down Approach for the Direct Synthesis, Patterning, and Operation of Artificial Micromuscles on Flexible Substrates, ACS Appl Mater Interfaces, 8(2016) 1559-64.
[37] S. Mohsen, J.K. Kwang, Ionic polymer–metal composites: IV. Industrial and medical applications, Smart Materials and Structures, 14(2005) 197.
[38] F. Xia, Z.Y. Cheng, H.S. Xu, H.F. Li, Q.M. Zhang, G.J. Kavarnos, R.Y. Ting, G. Abdul-Sadek, K.D. Belfield, High Electromechanical Responses in a Poly(vinylidene fluoride–trifluoroethylene–chlorofluoroethylene) Terpolymer, Advanced Materials, 14(2002) 1574-7.
[39] C.W. Peak, J.J. Wilker, G. Schmidt, A review on tough and sticky hydrogels, Colloid and Polymer Science, 291(2013) 2031-47.
[40] J.A. Christman, R.R. Woolcott, A.I. Kingon, R.J. Nemanich, Piezoelectric measurements with atomic force microscopy, Applied Physics Letters, 73(1998) 3851-3.
[41] E.R. Keeler, Electronic watch counting circuit, in: US (Ed.), Timex Corp US, 1968.
[42] C. Federico, A. Iain, B. Siegfried, F. Gabriele, G. Giuseppe, G. Massimiliano, G. Christian, J.-M. Claire, K. William, K. Guggi, K. Matthias, K. Roy, L. Benny, M. Marc, M. Silvain, N. Stephan, O.B. Benjamin, P. Qibing, P. Ron, R. Björn, R. Samuel, S. Herbert, Standards for dielectric elastomer transducers, Smart Materials and Structures, 24(2015) 105025.

[43] S. Rosset, H.R. Shea, Small, fast, and tough: Shrinking down integrated elastomer transducers, Applied Physics Reviews, 3(2016) 031105.
[44] P. Lotz, M. Matysek, H.F. Schlaak, Fabrication and Application of Miniaturized Dielectric Elastomer Stack Actuators, IEEE/ASME Transactions on Mechatronics, 16(2011) 58-66.
[45] D. Gatti, H. Haus, M. Matysek, B. Frohnapfel, C. Tropea, H.F. Schlaak, The dielectric breakdown limit of silicone dielectric elastomer actuators, Applied Physics Letters, 104(2014) 052905.
[46] S.-A. Susana, K. Florian, M. Holger, F.-Z. Florentine, F.S. Helmut, A novel application of dielectric stack actuators: a pumping micromixer, Smart Materials and Structures, 27(2018) 074008.
[47] P. Calvert, Hydrogels for Soft Machines, Advanced Materials, 21(2009) 743-56.
[48] P. Calvert, Gel Sensors and Actuators, MRS Bulletin, 33(2011) 207-12.
[49] L. Taylor Danielle, M. in het Panhuis, Self-Healing Hydrogels, Advanced Materials, 28(2016) 9060-93.
[50] C.J. Ferris, K.G. Gilmore, G.G. Wallace, M. in het Panhuis, Biofabrication: an overview of the approaches used for printing of living cells, Applied Microbiology and Biotechnology, 97(2013) 4243-58.
[51] L.-W. Xia, R. Xie, X.-J. Ju, W. Wang, Q. Chen, L.-Y. Chu, Nano-structured smart hydrogels with rapid response and high elasticity, 4(2013) 2226.
[52] F. Carpi, Electromechanically active polymers : a concise reference, Cham: Springer; 2016.
[53] Q. Zhao, J.W.C. Dunlop, X. Qiu, F. Huang, Z. Zhang, J. Heyda, J. Dzubiella, M. Antonietti, J. Yuan, An instant multi-responsive porous polymer actuator driven by solvent molecule sorption, Nature Communications, 5(2014) 4293.
[54] Y. Osada, H. Okuzaki, H. Hori, A polymer gel with electrically driven motility, Nature, 355(1992) 242.
[55] D. Sangian, S. Naficy, G.M. Spinks, Thermally activated paraffin-filled McKibben muscles, Journal of Intelligent Material Systems and Structures, 27(2016) 2508-16.
[56] S. Iijima, Helical microtubules of graphitic carbon, Nature, 354(1991) 56.
[57] A. Eatemadi, H. Daraee, H. Karimkhanloo, M. Kouhi, N. Zarghami, A. Akbarzadeh, M. Abasi, Y. Hanifehpour, S.W. Joo, Carbon nanotubes: properties, synthesis, purification, and medical applications, Nanoscale Research Letters, 9(2014) 393-.
[58] T. Filleter, R. Bernal, S. Li, H.D. Espinosa, Ultrahigh Strength and Stiffness in Cross-Linked Hierarchical Carbon Nanotube Bundles, Advanced Materials, 23(2011) 2855-60.
[59] R.H. Baughman, C. Cui, A.A. Zakhidov, Z. Iqbal, J.N. Barisci, G.M. Spinks, G.G. Wallace, A. Mazzoldi, D. De Rossi, A.G. Rinzler, O. Jaschinski, S. Roth, M. Kertesz, Carbon Nanotube Actuators, Science, 284(1999) 1340.
[60] T. Mirfakhrai, O. Jiyoung, K. Mikhail, F. Eddie Chi Wah, Z. Mei, F. Shaoli, H.B. Ray, D.W.M. John, Electrochemical actuation of carbon nanotube yarns, Smart Materials and Structures, 16(2007) S243.
[61] T. Mirfakhrai, J.D.W. Madden, R.H. Baughman, Polymer artificial muscles, Materials Today, 10(2007) 30-8.
[62] J.D.W. Madden, J.N. Barisci, P.A. Anquetil, G.M. Spinks, G.G. Wallace, R.H. Baughman, I.W. Hunter, Fast Carbon Nanotube Charging and Actuation, Advanced Materials, 18(2006) 870-3.
[63] J. Lee, T. Aida, "Bucky gels" for tailoring electroactive materials and devices: the composites of carbon materials with ionic liquids, Chemical Communications, 47(2011) 6757-62.
[64] M. Tunckol, J. Durand, P. Serp, Carbon nanomaterial–ionic liquid hybrids, Carbon, 50(2012) 4303-34.
[65] J.D. Carrico, M. Fleming, M.A. Tsugawa, K.K. Leang, Chapter 11 Precision Feedback and Feedforward Control of Ionic Polymer Metal Composite Actuators, Ionic Polymer Metal Composites (IPMCs): Smart Multi-Functional Materials and Artificial Muscles, Volume 1, The Royal Society of Chemistry2016, pp. 354-85.
[66] F. Carpi, Electromechanically active polymers, 1st ed., Place of publication not identified: Springer; 2016.

[67] K.J. Kim, S. Tadokoro, Electroactive polymers for robotic applications : artificial muscles and sensors, London: Springer; 2007.
[68] F. Carpi, E. Smela, Biomedical applications of electroactive polymer actuators, Chichester, West Sussex: John Wiley & Sons; 2009.
[69] C. Jo, D. Pugal, I.-K. Oh, K.J. Kim, K. Asaka, Recent advances in ionic polymer–metal composite actuators and their modeling and applications, Progress in Polymer Science, 38(2013) 1037-66.
[70] S. Nemat-Nasser, Micromechanics of actuation of ionic polymer-metal composites, Journal of Applied Physics, 92(2002) 2899-915.
[71] M. Safari, L. Naji, R.T. Baker, F.A. Taromi, The enhancement effect of lithium ions on actuation performance of ionic liquid-based IPMC soft actuators, Polymer, 76(2015) 140-9.
[72] J.-W. Lee, S.M. Hong, C.M. Koo, High-performance polymer ionomer–ionic liquid membrane IPMC actuator, Research on Chemical Intermediates, 40(2014) 41-8.
[73] B.J. Akle, M.D. Bennett, D.J. Leo, High-strain ionomeric–ionic liquid electroactive actuators, Sensors and Actuators A: Physical, 126(2006) 173-81.
[74] M.D. Bennett, D.J. Leo, Ionic liquids as stable solvents for ionic polymer transducers, Sensors and Actuators A: Physical, 115(2004) 79-90.
[75] H. Shirakawa, E.J. Louis, A.G. MacDiarmid, C.K. Chiang, A.J. Heeger, Synthesis of electrically conducting organic polymers: halogen derivatives of polyacetylene, (CH), Journal of the Chemical Society, Chemical Communications, (1977) 578-80.
[76] C.K. Chiang, C.R. Fincher, Y.W. Park, A.J. Heeger, H. Shirakawa, E.J. Louis, S.C. Gau, A.G. MacDiarmid, Electrical Conductivity in Doped Polyacetylene, Physical Review Letters, 39(1977) 1098-101.
[77] S. Kirchmeyer, K. Reuter, Scientific importance, properties and growing applications of poly(3,4-ethylenedioxythiophene), Journal of Materials Chemistry, 15(2005) 2077-88.
[78] R.H. Baughman, Conducting polymer artificial muscles, Synthetic Metals, 78(1996) 339-53.
[79] Q. Pei, O. Inganäs, Electrochemical applications of the bending beam method; a novel way to study ion transport in electroactive polymers, Solid State Ionics, 60(1993) 161-6.
[80] T.F. Otero, Biomimetic Conducting Polymers: Synthesis, Materials, Properties, Functions, and Devices, Polymer Reviews, 53(2013) 311-51.
[81] F. Vidal, C. Plesse, D. Teyssié, C. Chevrot, Long-life air working conducting semi-IPN/ionic liquid based actuator, Synthetic Metals, 142(2004) 287-91.
[82] F. Vidal, C. Plesse, G. Palaprat, A. Kheddar, J. Citerin, D. Teyssié, C. Chevrot, Conducting IPN actuators: From polymer chemistry to actuator with linear actuation, Synthetic Metals, 156(2006) 1299-304.
[83] A. Maziz, C. Plesse, C. Soyer, C. Chevrot, D. Teyssié, E. Cattan, F. Vidal, Demonstrating kHz Frequency Actuation for Conducting Polymer Microactuators, Advanced Functional Materials, 24(2014) 4851-9.
[84] G. Cellot, P. Lagonegro, G. Tarabella, D. Scaini, F. Fabbri, S. Iannotta, M. Prato, G. Salviati, L. Ballerini, PEDOT:PSS Interfaces Support the Development of Neuronal Synaptic Networks with Reduced Neuroglia Response In vitro, Front Neurosci, 9(2015) 521.
[85] S.M. Richardson-Burns, J.L. Hendricks, B. Foster, L.K. Povlich, D.H. Kim, D.C. Martin, Polymerization of the conducting polymer poly(3,4-ethylenedioxythiophene) (PEDOT) around living neural cells, Biomaterials, 28(2007) 1539-52.
[86] D.D. Ateh, H.A. Navsaria, P. Vadgama, Polypyrrole-based conducting polymers and interactions with biological tissues, J R Soc Interface, 3(2006) 741-52.
[87] A. Della Santa, A. Mazzoldi, D. De Rossi, Steerable microcatheters actuated by embedded conducting polymer structures, Journal of Intelligent Material Systems and Structures, 7(1996) 292-300.
[88] E.W. Jager, Immerstrand, C., Peterson, K.H. et al. , The Cell Clinic: Closable Microvials for Single Cell Studies, Biomedical Microdevices, 4(2002) 10.

[89] G.M. Spinks, G.G. Wallace, J. Ding, D. Zhou, B. Xi, J. Gillespie, Ionic Liquids and Polypyrrole Helix Tubes: Bringing the Electronic Braille Screen Closer to Reality, Proceedings of SPIE - The International Society for Optical Engineering2003, pp. 372-80.
[90] N.H. Runyan, F. Carpi, Seeking the 'holy Braille' display: might electromechanically active polymers be the solution?, Expert Rev Med Devices, 8(2011) 529-32.
[91] A. Maziz, C. Plesse, C. Soyer, E. Cattan, F. Vidal, Top-down Approach for the Direct Synthesis, Patterning, and Operation of Artificial Micromuscles on Flexible Substrates, ACS Applied Materials & Interfaces, 8(2016) 1559-64.
[92] A. Khaldi, A. Maziz, C. Plesse, C. Soyer, D. Teyssié, F. Vidal, E. Cattan, Patterning innovative conducting interpenetrating polymer network by dry etching, IEEE/ASME International Conference on Advanced Intelligent Mechatronics, AIM2014, pp. 1424-9.
[93] A. Khaldi, C. Plesse, C. Soyer, E. Cattan, F. Vidal, C. Legrand, D. Teyssié, Conducting interpenetrating polymer network sized to fabricate microactuators, Applied Physics Letters, 98(2011) 164101.

Chapter 2: PEDOT-based trilayer fabrication process

Contents

2.1 Introduction 17
2.2 The selection of materials for CP-based trilayer actuators 22
2.2.1 Electrodes of the microactuators 22
2.2.2 Solid polymer electrolyte layer 22
2.2.3 The electrolyte 24
2.2.4 Microactuator fabrication technique 26
2.3 Materials 26
2.4 PEDOT synthesis route 27
2.5 PEDOT-based trilayer fabrication process 30
2.5.1 Trilayer fabrication process 30
2.6 PEDOT-based trilayer patterning 33
2.6.1 Fabrication of samples for the characterization process 35
2.7 Analysis of the texture of the trilayer structure 36
2.8 Conclusion 39

2.1 Introduction

The actuation mechanism of conducting polymer (CP) actuators is based on their reversible redox chemistry. The actuation is obtained when the CP is oxidized or reduced electrochemically [1]: ions and solvent molecules, coming from a surrounding electrolyte, are inserted or expelled from the CP in order to ensure the overall electroneutrality, which results in a variation of the CP volume, or in short, the CP actuator responds to the consumed charge. The degree of oxidation of the CPs, or in other words, the density of the polarons that carry electronic charge in conducting polymers, can be controlled by the applied voltage. These ion movements are principally responsible for the volume changes and, thus, the actuation response that is referred to as electro-chemo-mechanical deformation.

Fig. 1 shows two models of operating mechanism of actuation in CPs [2, 3]. By electrochemical reduction, the CPs experience two paths that depend on the size of doping anions. When small anion like ClO_4^- is involved, the anion moves out from the bulk of CPs into electrolyte during electrochemical reduction. In this path, the CPs is shrunk in reduced state and the actuation is named anion driven, as shown by Fig. 1a. Otherwise, when a large negative cluster like 1-Ethyl-3-methylimidazolium (EMI^+) bis-trifluoromethan sulfonylimide ($TSFI^-$) is used, it is twisted and immobilized in polymer network [4]. In this cation-driven path, the CPs are reduced by insertion of cations (Li^+, or EMI^+ for example) from the electrolyte, and then swollen by the additional cations [5], as described in Fig. 1b.

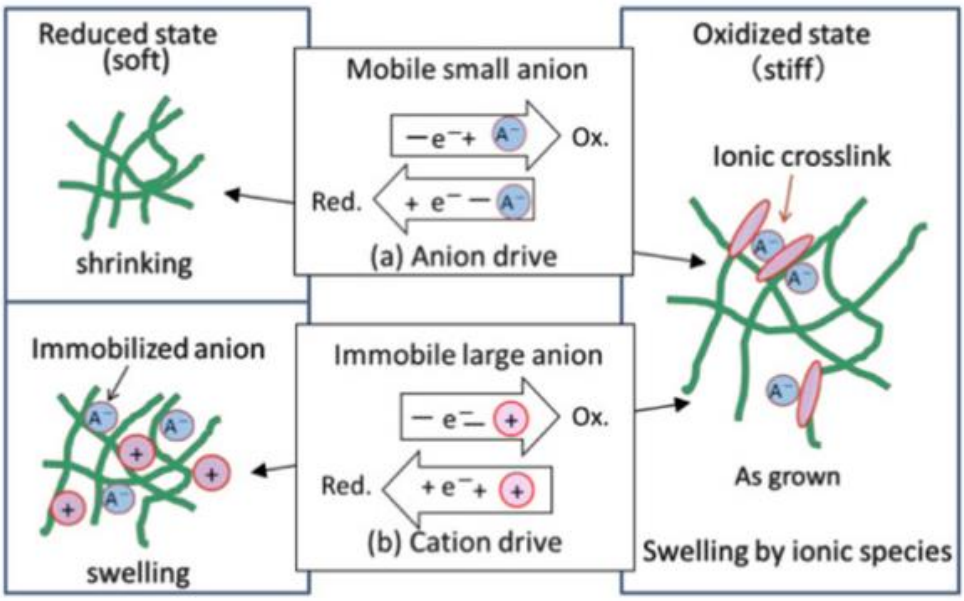


Fig. 1. Actuation mechanism of conducting polymer actuators: a) anion driven mechanism, b) cation driven mechanism [6] (Reprinted with permission from Springer Nature). The ovals represent positive electronic charge on the backbone.

The cation driven reaction of PEDOT, one of the most widely studied conjugated polymers, is described in Fig. 2. Providing an ionically conducting medium is available, PEDOT can be used

as the active component in CP actuators. To operate in air, CP actuators are usually built using a solid polymer electrolyte (SPE) film sandwiched between two PEDOT electrodes (PEDOT//SPE//PEDOT) [7-9], as demonstrated in Fig. 3. The SPE layer plays a role as an ion reservoir as well as a supporting structure deciding the mechanical strength of actuator. When two CP electrodes are subjected to an applied voltage (typically smaller than ±2 V), one CP layer will be reduced leading to an increase in volume whereas the other layer will be oxidized and shrunk in volume. Finally, the bending movement is induced.

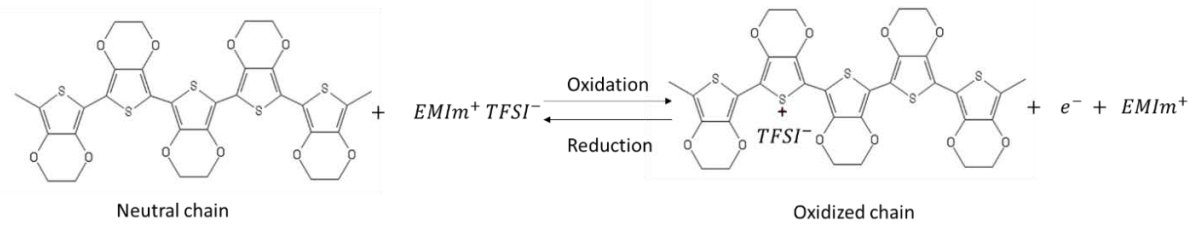


Fig. 2. Cation driven actuation in a PEDOT-based actuator.

The expansion and speed of the actuation of CP actuators are affected by the electrochemomechanical properties of the polymer, the diameter and the speed of the ions moving into and out of the polymer, as well as the SPE's ability to facilitate ion movement. These key factors will be discussed in detail in chapters 4.

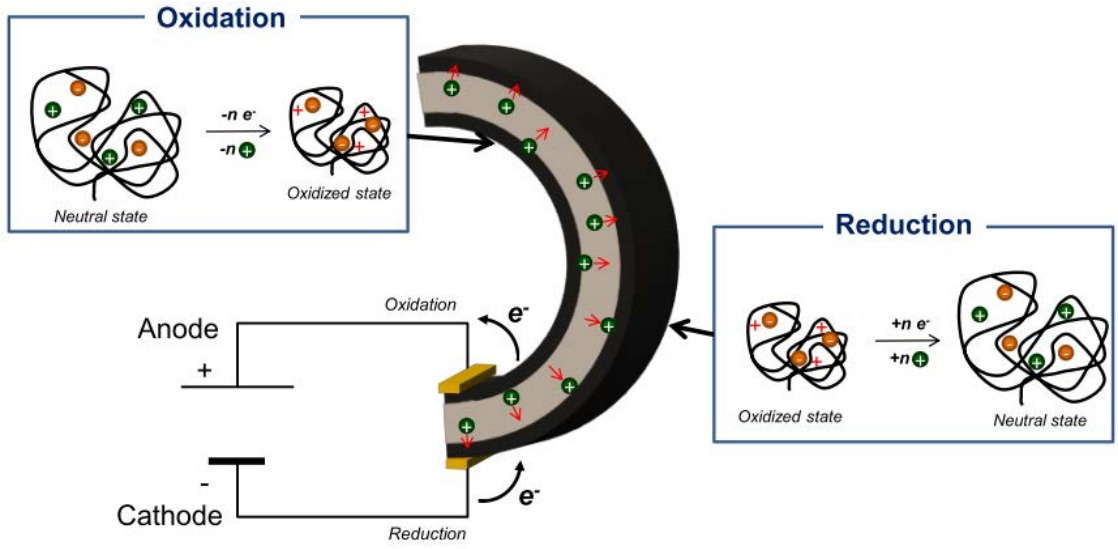


Fig. 3. Bending actuation mechanism of PEDOT-based trilayer actuators. The anode contracts due to ion expulsion and the cathode expands due to cation incorporation, leading to bending.

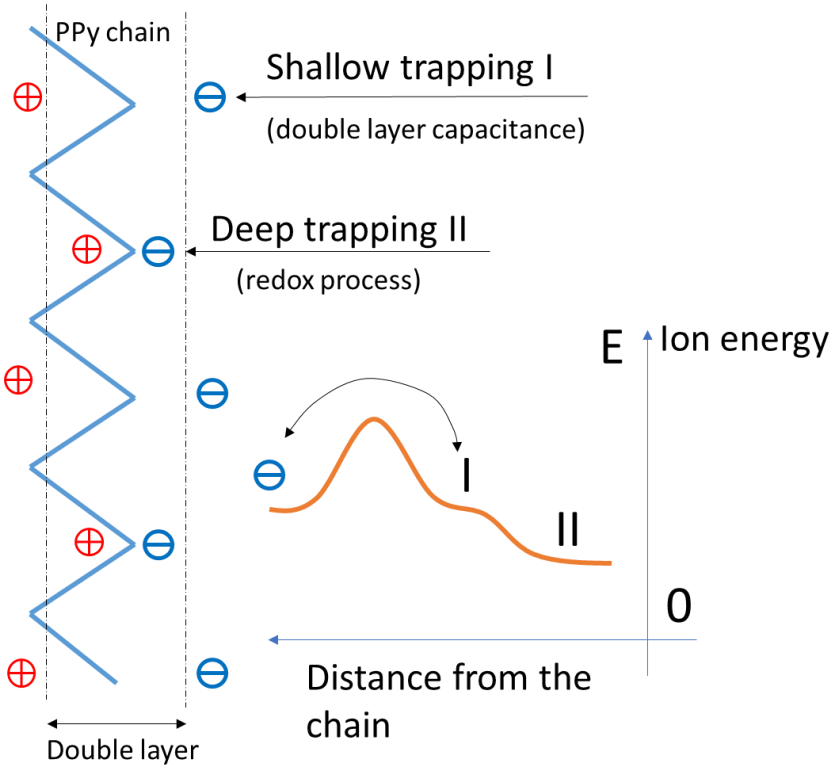


Fig. 4. A possible model taking into account two electrochemical doping process: some ions (II), deeply trapped near the polymer chains are released at only very low potentials. Other ions (I) are shallowly trapped, they form a double layer at a certain distance from the chain. (Reproduced with permission from [10], The Electrochemical Society.)

In addition to the redox process happening in the CP electrodes as mentioned above, another possible contribution to the bending of the actuator comes from the forming of double layer between the electrolyte and the CP's nanostructure [10, 11]. Fig. 4 shows a two-step doping process of polypyrrole conducting polymer thin film in lithium perchlorate in propylene carbonate (1M). At low potential in redox process, the ionic double capacitance layer is formed at the surface of the polymer chains arising from the accumulation near this chain of the weakly trapped ions. When the applied potential reaches the oxidation potential of the CP, a certain amount of ions approaches the polymer chains which are switched in their oxidation state [10]. However, the identification of the percentage of this contribution into the actuation mechanism remains open.

There were efforts to make use of CP actuators in different applications. Naka *et al.* have developed a micropump driven by a PPy-based conducting polymer soft actuators [12]. The micropump can transport fluids in one direction without backflow by means of two soft actuators – consisting of a pair of conducting polymer driven bending structures - that open and close (Fig. 5a). At a bigger scale, Fang *et al.* [13] introduced a diaphragm pump based on circular CP actuators. The flow rate achieved with the diaphragm pump is 1260 µL/min, which is achieved when the operating frequency is about 0.5 Hz.

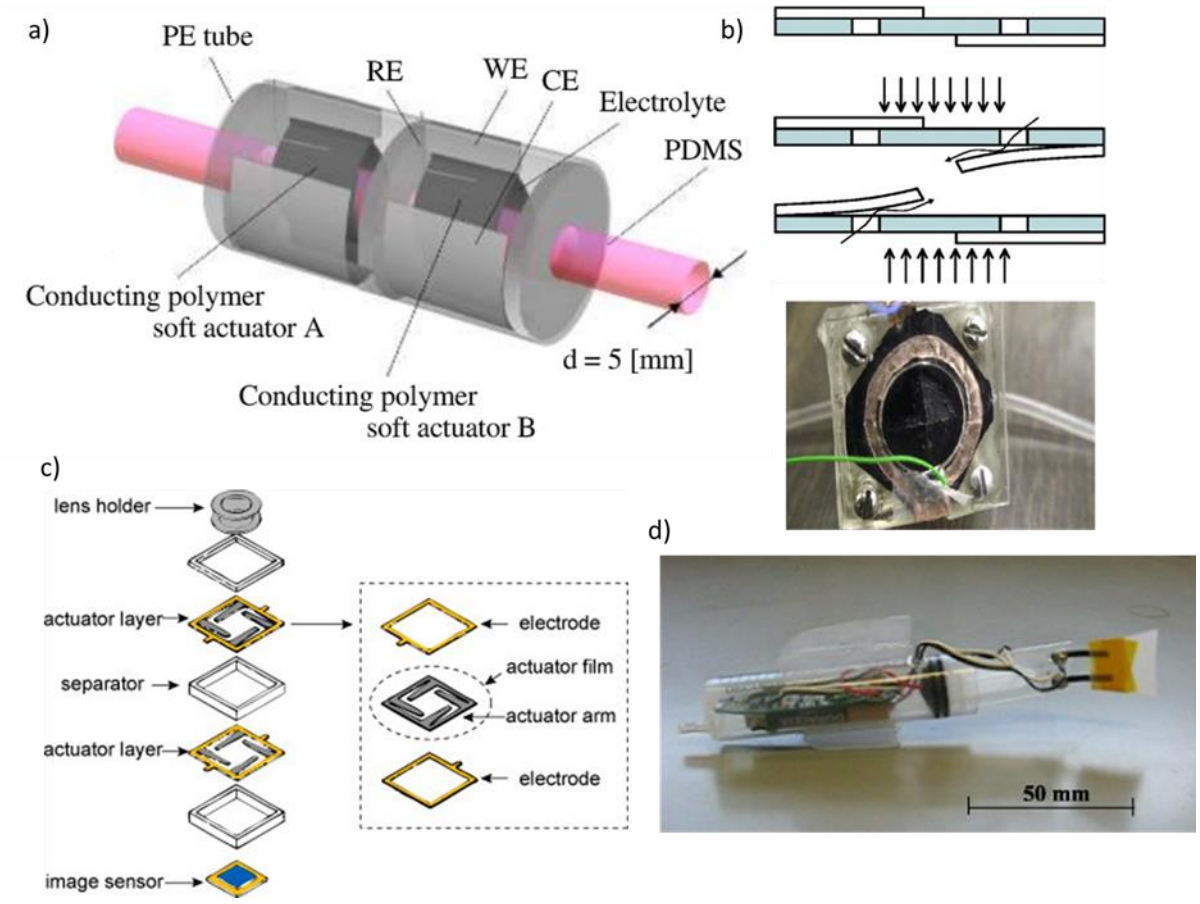


Fig. 5. a) Schematic of a micropump driven by a PPy-based CP actuator [12] (Reprinted with permission from John Wiley and Sons), b) A diagram pump: the mechanism of flap check valves and a bottom view of the assembled micropump [13] (Reprinted with permission from Elsevier), c) Micro autofocus lens actuator that uses bending conducting polymer actuators [14] (Reprinted with permission from Elsevier), d) A prototype of a robotic fish [15] (Reprinted with permission from IOP Publishing)

An autonomously powered and controlled robotic fish is shown in Fig. 5d. This robot has an active flexural joint tail fin, which can be activated through polypyrrole (PPy) based actuator developed by McGovern *et al.* [15]. The authors demonstrated an ability to control wirelessly in real time the robotic fish, and a directional control. The highest speed of the fish was approximately 33 mm/s corresponding to a flapping frequency of 0.6 – 0.8 Hz.

Fig. 5c shows micro autofocus lens actuators using a trilayer actuator structuring of a polyvinylidene difluoride (PVDF) membranes sandwiched between two layers of a poly ethylenedioxythiophene/poly (styrene sulfonic acid) (PEDOT/PSS) [14]. The actuator was fabricated by casting for easily producing bending conducting polymer actuators with high mechanical strength.

Jager implemented several designs aimed at medical applications. A closable microvial for single cell studies (Fig. 6a) [16] was fabricated from two polypyrrole/Au microactuators. It might also act as a microrobot for handling micrometer-size objects (including cells) in

aqueous solution [17]. In an effort to individually control the microactuators and avoid the short circuiting due to electrical connections, a microactuator fabrication method was developed, where CP actuators were patterned using microfabrication technology including photolithography [18].

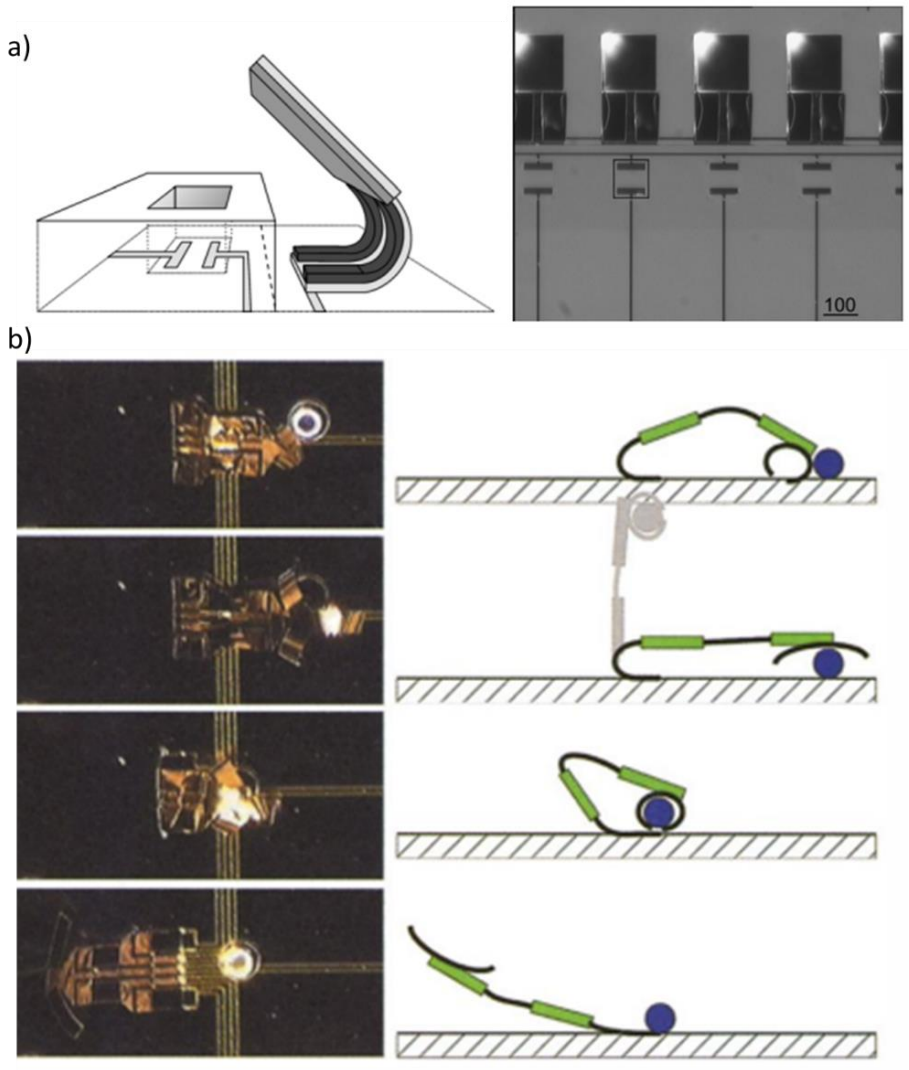


Fig. 6. a) A schematic drawing of a closable microvials [16] (Reprinted with permission from Springer Nature), b) A sequence of pictures (left) showing the grabbing and lifting of a 100 µm glass bead and schematic drawings of the motion (right) [17] (Reprinted with permission from The American Association for the Advancement of Science)

Wolff and Beiski proposed and patented a controllable drug delivery system where a polypyrrole actuator was used in different microvalve configurations, that can be inserted into the oral cavity of an adult human, for example as part of a dental prosthesis [19]. The two biggest advantages of this drug delivery system are a novel route for drug delivery via the buccal mucosa, and a controllable and miniaturized drug delivery system that is the size of two teeth.

In conclusion, conducting polymer- based actuators have received significant attention because they offer lot of advantages over other electroactive polymers such as dielectric elastomers and piezoelectric polymers. CP-based actuators have been known for their highly reversible, fast switching redox processes [20]. Also, they are lightweight, biocompatible, produce high stress (~ 10 MPa) [21], high power/weight ratio [22], significant strain (up to 1%), require low operating voltages (typically < 2 Vpeak-peak (Vpp)) [23] in solutions or in open-air condition [24], can be electronically controlled with high frequency response (50 Hz or more) and are potentially suitable for microscale applications [24, 25].

In this chapter, we will introduce the selection process of the materials from the type of conducting polymer, the solid polymer electrolyte, and the electrolyte, which are suitable for the microactuator fabrication process. And then, we propose the materials to be used and describe the Vapour Phase Polymerization (VPP) synthesis of PEDOT electrodes to provide highly electroactive electrodes, suitable for effective microactuators. Monolayers of PEDOT, bilayers of NBR-PEO/PEDOT have been also prepared for specific measurements. Trilayer microbeams of the actuators will be prepared using the Layer-by-Layer (LbL) approach and patterned by femtosecond laser. In the final step, the geometric properties of the resulting devices are then characterized.

2.2 The selection of materials for CP-based trilayer actuators

2.2.1 Electrodes of the microactuators

Polypyrrole (PPy) and PEDOT are the most popular materials to prepare CP-based actuators. PPy-based actuators have been known for their high actuation speeds, large strains, and acceptability for various applications. However, their notable disadvantages are high rigidity, low ionic conductivity, and suffering a considerable damage in over-oxidation. Whereas, PEDOT-based actuators have been described as thermally and chemically stable actuators. PEDOT itself shows high electrochemical stability and good conductivity [8, 26-28]. In comparison to PPy, PEDOT is typically a higher conductivity material, which can reduce the voltage drop along the length of the actuator and increase the actuation efficiency in general. In addition, PEDOT and its based devices can be adapted to various fabrication processes, for example spin coating process. These are the reasons why PEDOT is chosen as the CP material used for the electrodes of the actuators in this study.

2.2.2 Solid polymer electrolyte layer

The performance of CP-based actuators does not depend only on the CP performance but also on the SPE layer. The electrolyte medium providing the ions necessary to the redox process has a great effect on electromechanical response of the actuators. Low ionic conductivity of the SPE layer will lead to a slower response and higher energy loss, which is further investigated in section 4.3.2. And a stiffer SPE reduces the magnitude of the actuation.

Since the CP materials are often brittle, the mechanical toughness and stretchability of the actuators is mainly dependent on the SPE layer.

Therefore, a full interpenetrating polymer network (full-IPN) or a semi interpenetrating polymer network (sIPN) is employed to meet the requirement of both ionic conductivity and mechanical properties.

IPNs were discovered in the 1960s. Several group of researchers [29, 30] found out that if two immiscible polymers were formed into an IPN, the glass-transition temperatures of these polymers were shifted towards each other, resulting from an increase in the miscibility of these polymers caused by the presence of cross-links. Based on the chemical bonding and rearrangement pattern, IPN can be classified into: sIPN and full-IPN in terms of structure, or sequential IPN and simultaneous IPN regarding their synthesis pathway.

In a full-IPN, shown in Fig. 7a, two polymers are present as cross-linked networks, however there is negligible bonding between these polymers. These can be prepared sequentially or simultaneously.

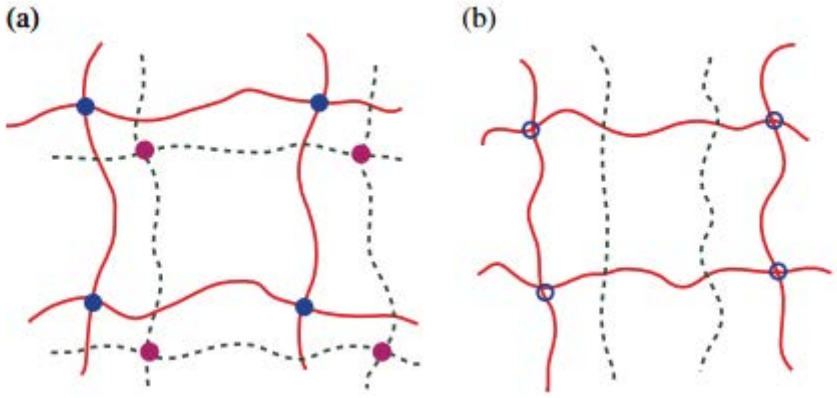


Fig. 7. Schematic of a) full-IPN and b) semi-IPN where the pink, blue, and empty dot represent for the crosslinking between two polymer chains.

In a sIPN, only one cross-linked polymer is present as a host network (Fig. 7b). In comparison to a full IPN, this can enhance the miscibility of the linear polymer in the hosted matrix. However, the mobility of the linear polymer increases the ability of the phase segregation when two components are not thermodynamically compatible. Applications of IPNs related to this work are as solid polymer electrolytes for fuel cell and as soft mechanical actuators [28, 31, 32].

Different partner materials used to fabricate an “ideal” IPN for actuator applications have been investigated. Poly(ethylene oxide) (PEO) is normally the first candidate in an IPN since it is well known for its high ionic conductivity property, which can reach 0.1 S/cm when incorporating the ionic liquid EMITFSI at ambient temperature [33]. The synthesis of this PEO network is via free radical copolymerization of poly(ethylene glycol) methyl ether

methacrylate and poly(ethylene glycol) dimethacrylate. However, PEO films show poor mechanical properties and weak dimensional stability [34]. Adding a second networkto PEO [35], namely hydroxytelechelic polybutadiene (HTPB) [36], or polytetrahydrofurane (PTHF) [37], or nitrile butadiene rubber (NBR) [32], was proposed to improve the mechanical properties.

Table 1 describes the most important parameters of HTPB/PEO, PTHF/PEO, and NBR/PEO IPNs. As can be seen, among the three types of IPNs, NBR/PEO IPN shows quite good ionic conductivity, high strain at break, small Young's moduli, and can operate very high frequency (in kHz range). In addition, the NBR/PEO IPN had shown its compatibility with the reactive ionic etching process, which is an indispensable step in photolithography for patterning the microbeam. These properties make NBR/PEO become a promising candidate for the lithography process and microactuator system.

Table 1. Summary some important properties of three different PEO-based IPNs

	HTPB/PEO	**PTHF/PEO**	**NBR/PEO**
Ionic conductivity (S/m) (incorporated with EMITFSI)	0.25 [38]	0.04 [37]	0.1 [33]
Elongation at break in dry state (%)	N/A	110 [37]	150 [33]
Young's moduli (MPa)	1.2 [38]	6 [37]	0.8 [33]
Maximum operating frequency (Hz)	18 [37]	125 [37]	900 [39]
Durability (cycles)	3.5 x 10^6 [28]	N/A	N/A

2.2.3 The electrolyte

A variety of types of electrolytes have been used to incorporate in microactuators. Solutions of lithium perchlorate ($LiClO_4$) and lithium bis(trifluoromethanesulfonyl)imide (LiTFSI) in propylene carbonate (PC) are the powerful tools for microactuators since they display a high ionic conductivity and can be tuned by changing their concentration in PC. However, one of their notable drawbacks is volatility, which quickly reduces the actuator performance after a short amount of time of continuous operation. Encapsulation of the actuators is necessary for a long-term functioning.

Ionic liquids can get over these problems since they have a large window of electrochemical stability, high thermal stability, and non-volatility, so thereby non-flammability [40, 41]. However, due to a high viscosity, the conductivity of ionic liquids in general is not as high as solvent based electrolyte. 1-ethyl-3-methylimidazolium bis(tri- fluoromethylsulfonyl)imide (EMITFSI), 1-allyl-3-methylimidazolium bis(trifluoromethylsulfonyl) imide (AMITFSI), 1-butyl-3- methylimidazolium bis(trifluoromethylsulfonyl)imide (BMITFSI), 1-methyl-1-propylpiper-idinium bis(trifluoromethylsulfonyl)imide (MPPPTFSI), 1-ethyl-3-methylimidazolium bis(fluor-

osulfonyl)imide (EMIFSI), 1- butyl-1-methylpyrrolidinium bis(fluorosulfonyl)imide ($Pyr_{14}FSI$), 1-butylpyridinium tetra-fluoroborate ($BuPyBF_4$), and 1-ethyl-3-methylimidazolium tetrafluoroborate ($EMIBF_4$) are the most commonly used to incorporate into SPE layers in microactuators. Fig. 8 shows the properties of variety of ionic liquids and the strain difference their produce when they are incorporated in PEDOT-NBR/PEO-PEDOT actuators. The EMITFSI displays a medium ionic conductivity, quite high maximum swelling, and highest strain difference.

These are the reason why EMITFSI is chosen as the electrolyte to incorporate to the microactuators in our study.

a)

Ionic liquid	Ionic conductivity of neat ionic liquid (mS/cm)	Viscosity of neat ionic liquid (mPa s)	Ionic conductivity of the host matrix (mS/cm)	Maximum swelling of the matrix (corresponding to final ionic liquid content)
EMIFSI	16.5	24.5	3.3	266% (73%)
$EMIBF_4$	14	37	2	103% (51%)
AMITFSI	7.35	31	1.3	262% (72%)
$Pyr_{14}FSI$	4.1	65.9	1.2	214% (68%)
EMITFSI	8.58	34.1	1	249% (71%)
BMITFSI	3.9	50	0.7	259% (72%)
$BuPyBF_4$	2.42	163.3	0.54	115% (54%)
MPPPTFSI	1.51	117	0.36	168% (62%)

b)

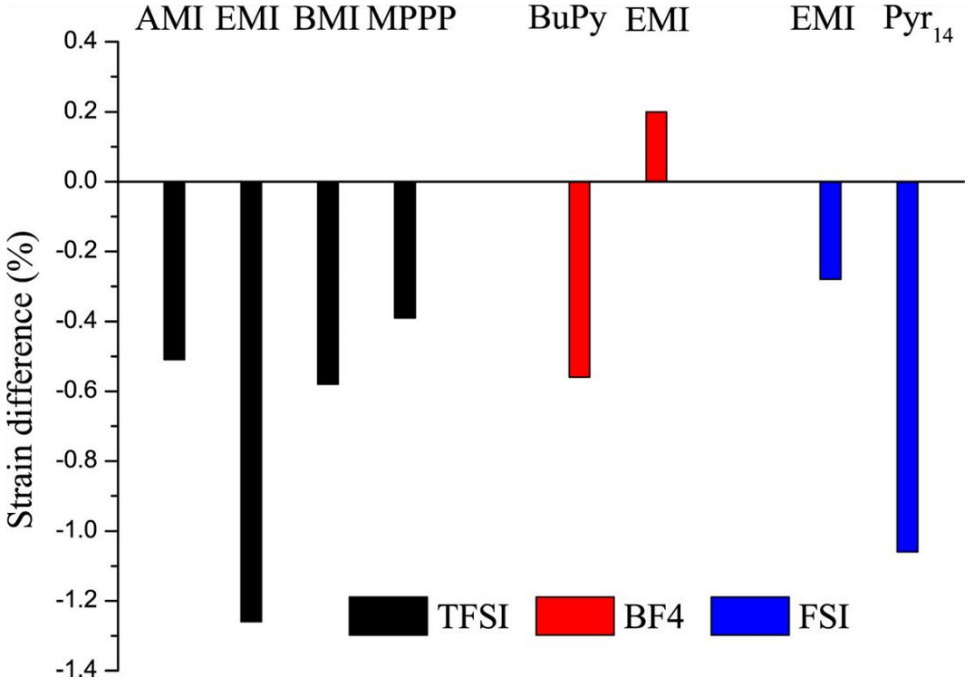


Fig. 8. a) properties of ionic liquids incorporated in NBR/PEO matrix, and b) strain differences calculated for PEDOT-NBR/PEO-PEDOT actuator swollen with different ionic liquids [42] (Reprinted with permission from Elsevier).

2.2.4 Microactuator fabrication technique

For microscale actuators, the thickness must be less than 20 µm to be compatible with, in particular, etching processes, which is the reason why the layer-by-layer (LbL) approach has been developed recently [43]. The bending microactuators were fabricated by sequentially stacking layers using a layer-by-layer polymerization of conducting polymer electrodes and a SPE. Each layer was deposited by spin-coating to accurately control the thicknesses. PEDOT can be fabricated in-situ via electropolymerization [44] or via vapor phase polymerization (VPP) [45] (see 2.4). In this work the first and last layers of the actuators were obtained using VPP of 3,4-ethylenedioxythiophene (EDOT). The intermediate SPE layer was synthesized as a semi-IPN combining a poly(ethylene oxide) (PEO) network for ionic conductivity and nitrile butadiene rubber (NBR) for mechanical strength [9, 27] (described in 2.5).

For the LbL process, while the proof of concept has been demonstrated previously, the resulting performances remained relatively poor (0.13% strain and 0.75 µN of generated force) [43] mainly due to the low electroactivity of PEDOT electrodes obtained by VPP. The process can also be difficult, given the fine dimensions required, and yields are low. Often it takes many attempts to achieve one or two successful samples. Practical use of such microactuators and integration into innovative microelectromechanical systems require improved performance in mechanical response, and ideally also in yield. In this thesis we show good electrical and mechanical response, and the process has been improved. Further work will still be required to increase yield – perhaps through some optimization of the chemistry.

2.3 Materials

Poly(ethylene glycol) methyl ether methacrylate (PEGM, M_n = 500 g mol^{-1}), poly(ethylene glycol) dimethacrylate (PEGDM, M_n = 750 g mol^{-1}), cyclohexanone (>99.8%) and 3,4-ethylenedioxythiophene (EDOT, distilled under reduced pressure) were obtained from Sigma Aldrich. Iron(III) p-toluene sulfonate Clevios™ CB 55 V2 (55 wt% in butanol, $Fe(OTs)_3$ in BuOH) was purchased from HERAEUS. 1-butanol (99%), initiator dicyclohexyl peroxydicarbonate (DCPD), 1-ethyl-3-methylimidazolium bis(trifluoromethanesulfonyl)imide (EMITFSI 99.9%) and nitrile butadiene rubber (NBR), were used as supplied from Alfa Aesar, Groupe Arnaud, Solvionic and LANXESS, respectively. The molecular structure of these materials are described in Fig. 9.

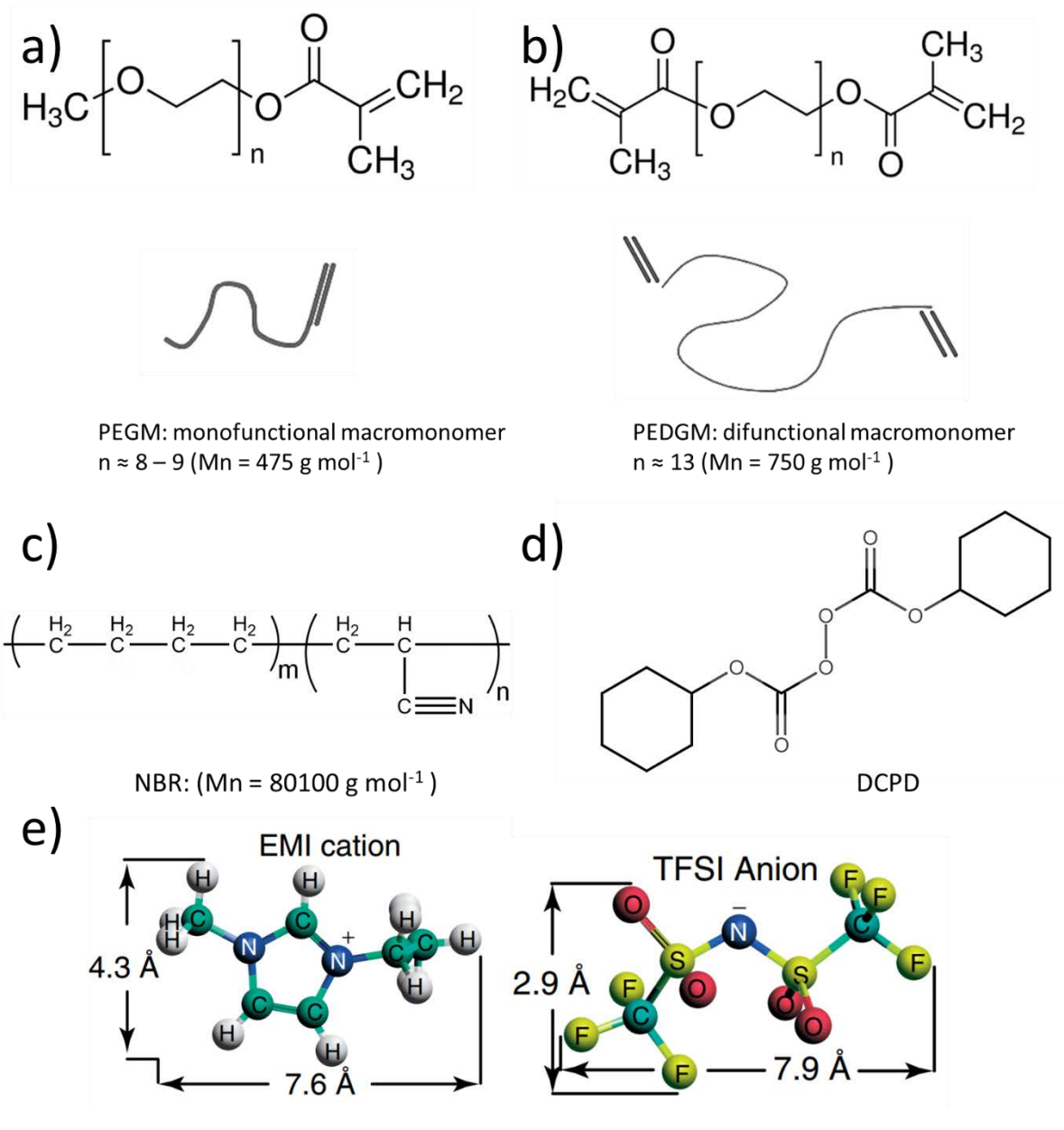


Fig. 9. Molecular formula of a) the precursor PEGM, b) PEDGM, c) the linear chain NBR, d) the initiator DCPD, and e) the ionic liquid EMITFSI [46] (Reprinted with permission from American Chemical Society, 2008.)

2.4 PEDOT synthesis route

The PEDOT polymerization occurs through a three step mechanism (Fig. 10). The reaction is initiated by an $Fe(OTs)_3$, which generates a radical cation Fe^{3+}. Radical termination of two activated EDOT monomers provides carbon–carbon coupling. Typically, the anion $(OTs)^-$ acts as a dopant to the polymer, stabilizing the positive charge on the sulfur. π-conjugation refers to the alternating single and double bonds of the EDOT oligomers that typically result from this synthesis process. This π-conjugation delocalizes the electrons and decreases the oxidation potential. Consequently, existing PEDOT chains develop faster than new ones are created since oligomers are more easy to oxidize than the monomers. The neutral PEDOT

chains are oxidized and a positive charge along the backbone with the ratio of every three or four chain segments per charge is created. A “dopant” anion is electrostatically attracted to the polymer and balances the charge [47]. The oxidation strength of the oxidant plays an important role in PEDOT polymerization. At one hand, it must be high enough to drive the reaction, but on the other hand it should be low enough to avoid unwanted bonding split in the monomer leading to imperfection bonds, which can disrupt conjugation and reduce conductivity [48, 49].

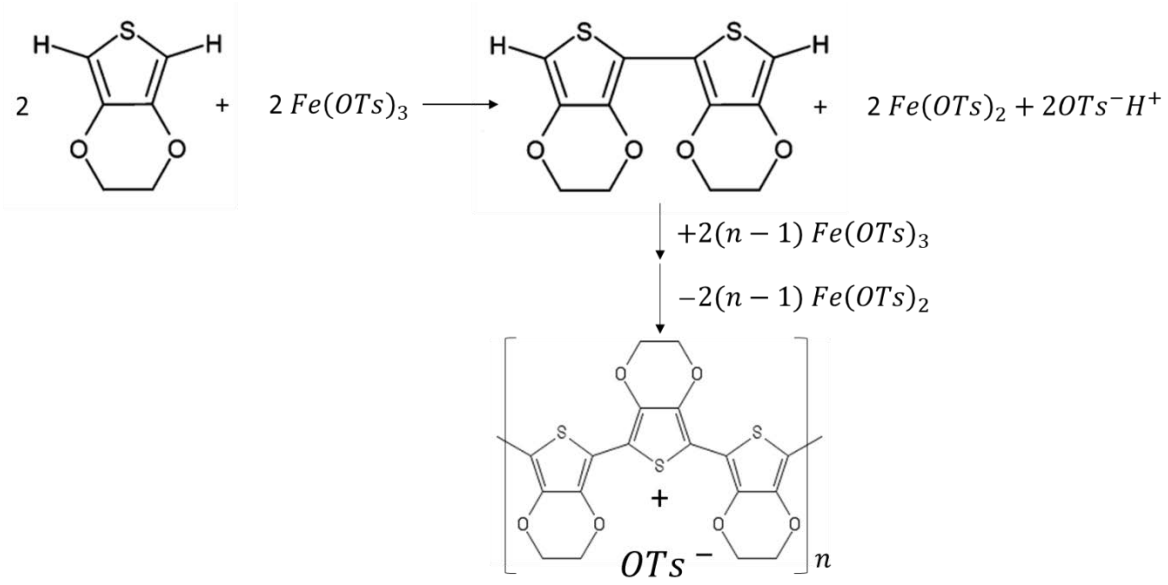


Fig. 10. Oxidation of EDOT with iron (III) p-toluene sulfonate

The fabrication process of the PEDOT electrodes was performed as described in the work of Maziz [50] and is depicted in Fig. 11.

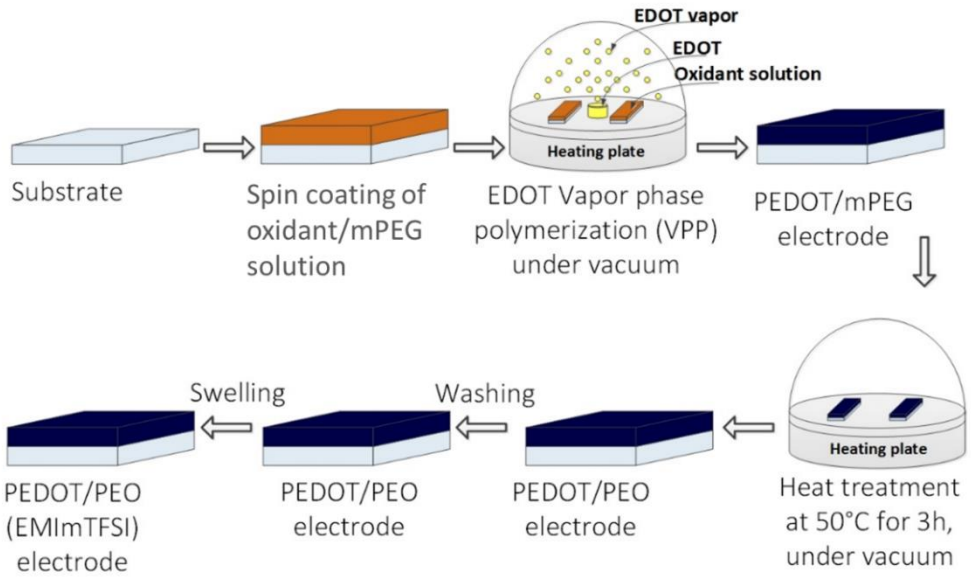


Fig. 11. Fabrication process of PEDOT electrodes [51]

The PEDOT electrode layers were obtained from EDOT VPP, first described by Winther-Jensen [45]. The VPP of EDOT was carried out with a direct chemical oxidation using the commercial solution of Iron(III) tosylate $Fe(OTs)_3$ (55 wt% in butanol). In a departure from Winther-Jensen, PEO precursors (mPEG) composed of 50 wt% of PEGM and 50 wt% of PEGDM were added as a monomer and a crosslinker, respectively, to the $Fe(OTs)_3$ solution. Additionally, DCPD (3 wt% vs mPEG) as the radical initiator for mPEG polymerization was introduced to the solution. The latter was then stirred until dissolution and degassed. The oxidant solution was then spin-coated with different rotational speeds from 1000 rpm to 3500 rpm (the acceleration and duration were held constant at 1000 rpm s^{-1}, and 30 s, respectively) onto a substrate and exposed to EDOT vapor for a fixed time at a fixed temperature. EDOT VPP was carried out under primary vacuum by heating liquid EDOT monomers that evaporate and polymerize on the oxidant solution. The EDOT VPP was followed by the final heat treatment for mPEG polymerization/crosslinking (3 h at 50°C) to obtain PEDOT/PEO composite electrodes. The resulting electrode can be either i) washed in methanol to remove unreacted oxidant solution and weakly bonded PEDOT chains, or ii) left as it is for subsequent trilayer fabrication, which is described in the next section. This PEDOT electrode was swollen in ionic liquid (EMITFSI) for further characterization. It is worth noting that introducing the PEO into PEDOT electrodes helps to increase the specific capacitance, the cycling stability, and flexibility of the electrodes [52], which improves the strain and the life time of the actuator.

The final properties (thickness, electronic conductivity and volumetric charge density) of the PEDOT electrodes were studied and optimized [51] as a function of: composition of oxidant solution (content of mPEG), rotation speed of spin-coater for deposition of oxidant solution, as well as EDOT VPP time and temperature. The optimization of the PEDOT electrodes performed by K. Rohtlaid [51] in a cooperating project with our group is detailed in the Appendix A.2.1. Briefly, it can be concluded that to obtain PEDOT electrodes with high electronic conductivity and high electroactivity using VPP, it is necessary to add PEO precursors to the oxidant solution while not increasing their concentration above 20%. The rotation speed can be chosen according to the desired CP thickness. In addition, the polymerization time and temperature must not exceed 90 min and 50°C, respectively, in order to maintain both, high electronic conductivity and good electrochemical properties. The optimal parameters resulted in good electronic conductivities (around 200 S/cm) and high electroactivity (between 2.3 x 10^7 C/m^3 and 1.0 x 10^8 C/m^3). This conductivity is much lower than the previous conductivity value reported by Maziz [50] (before the PEDOT electrode is swollen in EMITFSI), which is equal to 805 S/cm - corresponding to an mPEG content of 30%, a rotational speed of the spin coater of 1000 rpm, a duration of 30 s, and the VPP duration of 30 min, producing a PEDOT electrode thickness of 0.34 µm. This decrease in the electronic conductivity is attributed to different factors. At first, in our case, a thicker PEDOT layer was fabricated by the VPP process. This was performed in a Sawatec vacuum hot plate instead of a bell jar, providing a higher density of EDOT vapor - resulting in a higher PEDOT density than

is achievable in the bell jar. Thicker PEDOT layers show a lower electronic conductivity than thinner ones [53]. Secondly, the PEO content in oxidant solution was below 20 % in order to maintain a high volumetric charge density - at the cost of low electronic conductivity.

To fabricate samples for further characterization, the synthesis parameters are selected as follow: mPEG content: 10%; EDOT VPP time: 50 min; EDOT VPP temperature: 40 °C; acceleration: 1000 rpm s^{-1}, duration: 30 s to obtain a high electronic conductivity and volumetric charge density. With those parameters, the relation between the rotational speed of the spin coater and the PEDOT thickness is determined as in Fig. 16, where the oxidant solution was deposited on the silicon wafer. Finally, the rotational speed is chosen as 2000 rpm and the expected thicknesses of the PEDOT electrodes are 2.2 µm providing experimentally highest bending strain in the trilayer configuration.

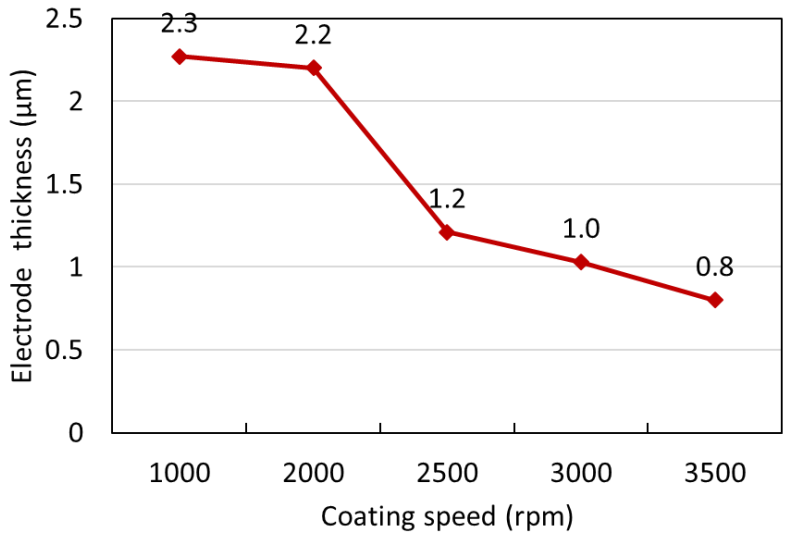


Fig. 12. Relation between the rotational speed of the spin-coater for deposition of the oxidant solution on a silicon wafer and the thickness of the PEDOT electrode, where the mPEG content is 10% of oxidant solution

2.5 PEDOT-based trilayer fabrication process

2.5.1 Trilayer fabrication process

In this section, the fabrication process of the CP-based trilayer actuators will be described. As mentioned earlier, this process was developed from the LbL method reported by Maziz [43]. However, some noticeable changes have been made, such as the optimization of the PEDOT electrodes described in the previous section, resulting in the increase of VPP time from 30 min to 50 min, a different vacuum hotplate (Sawatec HP-200) allowing a more precise temperature and vacuum control, replacing the vacuum bell during the VPP. The fabrication process was performed in a clean room environment (Class 100), which, given the potential effects of humidity and temperature on the process, should ensure a higher reproducibility.

The trilayer fabrication process is summarized as in Fig. 13. This process includes multiple steps where a trilayer structure was first coated and synthesized on a silicon wafer, followed by the heat treatment during three hours and femtosecond laser patterning to produce a cantilever beam shape. Lastly, the patterned beams were swollen in ionic liquid for approximately one week. The details of each step will be described below.

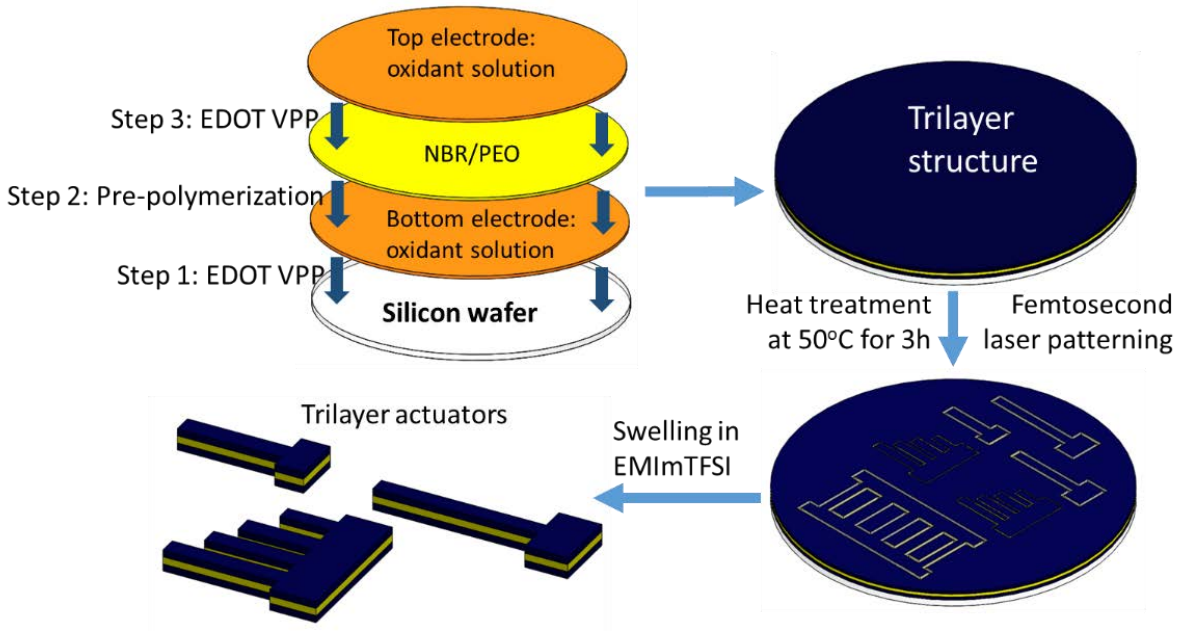


Fig. 13. Microactuator fabrication process showing the multilayer process followed by laser micromachining

The trilayer actuator was synthesized using the LbL method. In this process, all the layers are spin-coated on top of the previous layers and the thickness can be controlled extremely accurately by adapting the speed of rotation. The oxidant solution was prepared by adding PEO precursors (50 wt% PEGM and 50 wt% PEGDM) into a commercial $Fe(OTs)_3$ solution. The PEO precursors (mPEG) were added to each layer and polymerized at the end of the process throughout the trilayer structure to improve adhesion between the layers using the same ratios as described above. The solution was then stirred for 10 min and spin-coated onto a two-inch silicon wafer. The EDOT VPP was carried out in the same manner as in the PEDOT electrode fabrication section - during 50 min and at a 40˚C.

During the next step, the SPE layer, based on a semi-IPN architecture according to a procedure described in [43], was prepared: The NBR solution (20wt% NBR and 80wt% cyclohexanone) was mixed with PEO precursors (75 wt% PEGM and 25 wt% PEGDM vs. NBR). A free radical initiator DCPD (3 wt% vs PEO precursors) was then added to the solution, stirred for 15 min and degassed. A homogeneous mixture was obtained and spin-coated on top of the first PEDOT electrode layer. The relationship between the spin coating speed and the thickness of the NBR/PEO was investigated and shown in Fig. 14, which is similar to the results reported

by Maziz [39]. A rotational speed of 2000 rpm, 1000 rpm s^{-1}, 30 s was chosen to fabricate the SPE layer in this step. The pre-polymerization was carried out under a continuous supply of N_2 at 50°C during 45 min to enable the formation of the PEO network and to improve the adhesion between the first two layers.

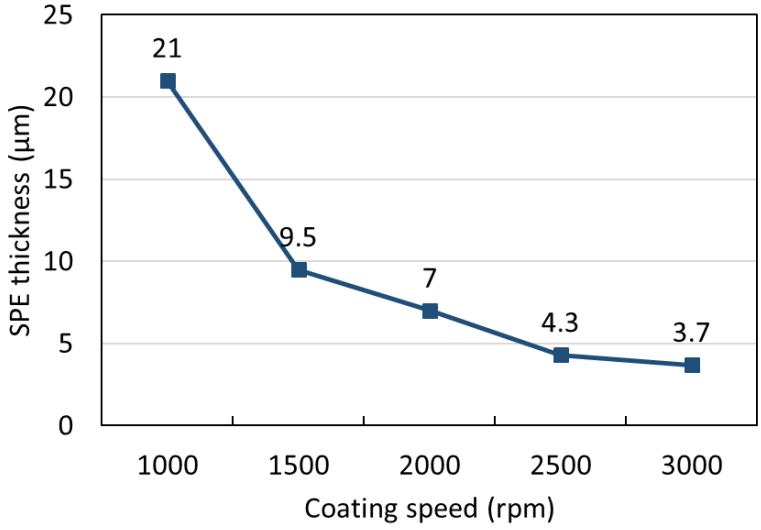


Fig. 14. Relationship between rotation speed of spin-coater for deposition of NBR/PEO and its resulting thickness

The second PEDOT electrode layer was synthesized in the same way as the first one. The oxidant solution was prepared, spin coated on top of the PEDOT/SPE bilayer, and EDOT VPP was carried out under the vacuum in the same way as for the first electrode. During this step, DCPD (3 wt% vs PEO network) was also added to the oxidant solution to initiate the polymerization of the PEO network.

After EDOT VPP of the second electrode layer, the trilayer was placed under a continuous flow of N_2 for a final heat treatment step (3 h at 50°C) [43] in order to polymerize the PEO precursors in every layer. This step provides a final intralayer cross-linking and interlayer cobonding [5]. It is worth mentioning that there is no DCPD in the first PEDOT layer as it would result in the early polymerization of the PEO precursors thus reducing the final cross-linking with the SPE layer during the final heat treatment. However, during the final heat treatment, the initiator from the second and third layers is assumed to initiate the polymerization of the PEO precursors in the first layer to improve adhesion between all three layers. Finally, the actuator was washed in methanol to remove any unreacted oxidant solution and any weakly polymerized PEDOT. Depending on the thickness of the oxidant solution, the washing solution can turn different shades, shown in Fig. 15. As shown previously, a thick oxidant solution produces a thick and dense PEDOT electrode layer. However, a lot of short dimers, trimers and short chains of PEDOT exist in this case and they are removed during the washing process, resulting a blue color of methanol. As the thickness of oxidant solution is reduced, the number

of short dimers, trimers and such are reduced significantly leading to a more transparency of methanol solution.

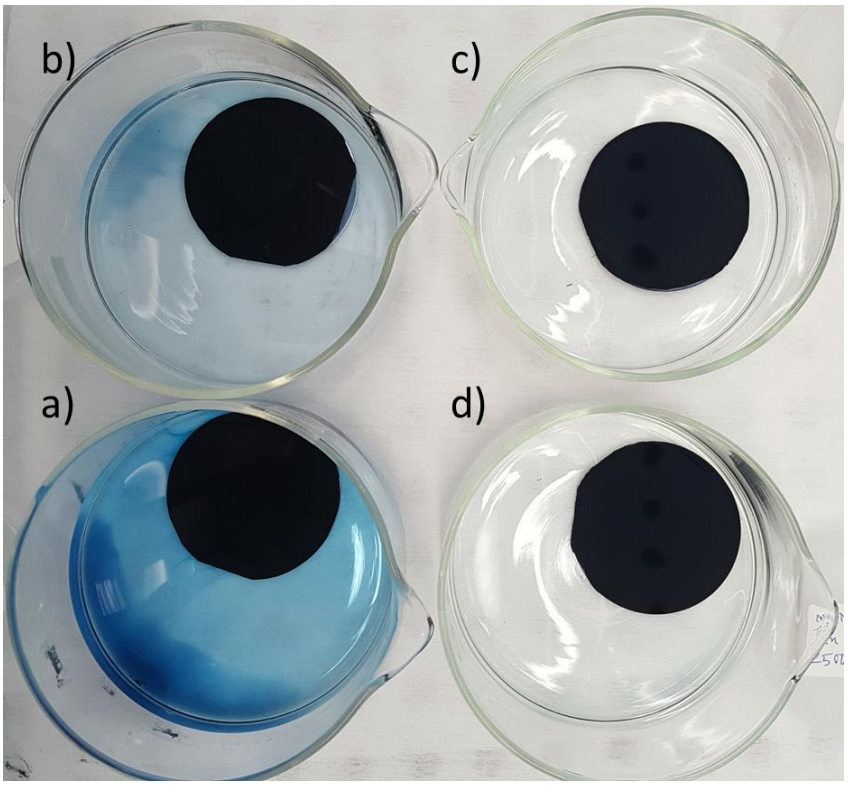


Fig. 15. Trilayer structures during washing step in methanol, the rotational coating speeds of PEDOT:NBR/PEO:PEDOT are a) 1000:2000:1000 b) 1500:2000:1500 c) 2500:2000:2500 d) 3000:2000:3000; the acceleration and coating duration are constant at 1000 rpm s^{-1} and 30 s, respectively. Les coloration is seen during washing for the fast spun, thin layers of oxidant solution, indicating less weakly polymerized EDOT.

In conclusion the following parameters for the fabrication of the trilayer actuators using LbL synthesis were chosen in order to obtain a thick, highly conductive and electroactive electrode: mPEG content of 10 wt%, oxidant solution applied with a coating speed, acceleration, and duration of 1500 rpm, 1000 rpm s^{-1}, and 30 s, respectively; and EDOT VPP at 40°C for 50 min producing a 2.2 µm in thickness of PEDOT layer (on silicon). And a rotational speed of 2000 rpm, 1000 rpm s^{-1}, 30 s was chosen to fabricate the SPE layer producing a 7 µm in thickness of the NBR/PEO layer.

2.6 PEDOT-based trilayer patterning

In the past, various techniques have been investigated to pattern the CP-based trilayer membrane into the desired beam shape at the micro-/nanoscale. Electropolymerization of the CP materials onto a patterned metal electrode such as gold or platinum was used to fabricate bilayer or trilayer structures, however the poor adhesion between gold layer and CP as well SPE layer substantial reduced the life-time of the actuator, and the gold layer also increases the total Young's modulus of the actuator, resulting in a strain decrease [54-56].

Reactive-ion etching (RIE) was used to remove unwanted area on a CP-based membrane to create high precision actuators [57, 58], however, this process involves the photolithography process to deposit a sacrificial layer (poly(vinyl alcohol)), and photoresist (Megaposit SPR 220 7.0 photoresist) as locally protective layer, and so is considered to be a long and costly process. Recently, a new patterning method has been introduced, where the oxidant solution is printed using a syringe-based printing or microcontact printing followed by laser ablation to cleanly cut the final device structures including the printed patterns [59]. This method allows a versatile deposition of CP layer and can be used in mass productive process. However, the resolution of the printing devices limits the precision of the resulting actuators. Ultrafast laser micromachining was employed to pattern PPy-based actuators [60-63], which works well. Use of electrical discharge machining is effective, but can be slow [64].

Among these patterning methods, contactless material processing by laser ablation micromachining is chosen in our study enabling a mask-less, top-down, and flexible machining technique. The trilayer structures are micro-patterned into microbeams using laser cutting (Oxford Lasers, a THG crystal (Third Harmonic generation) give the wavelength at 343 nm and 300 femtosecond diode-pumped (DPSS) lasers at 1030 nm (in IR), pulse length: 400 fs, spot size: 10 µm, galvanometric mirror resolution: 1 µm, maximum power 2 W with frequency rate at 200 kHz, the sample stage up to 300 × 300 mm^2 with linear accuracy +/- 0.5 µm, repeatability +/- 0.2µm; patterning conditions: power: 10%, cutting speed: 10 mm/s, cut passes: 30 passes) and a resulting beam is shown in Fig. 16b. Femtosecond laser patterning offers a high precision, small heat-affected zone, high reproducibility, short patterning time in comparison to other patterning methods, and can be applied before or after swelling of the trilayer structure. In this study, beams are designed with various geometries, where the length and the width are varied from 4 mm to 7 mm and 0.8 mm to 1 mm, respectively. Here, the ratio between the length and the thickness is from 200 to 350, which is high enough to assume this is a thin beam. In addition, all the characterizations later are manually handled, the beam size then must be big enough to facilitate the experiments. The rectangular contact pad (*length x width = 3 mm x2 mm*) is added at one end of the beam in order to allow a large clamping area, which is used to fix the beam and create the electrical contact to supply the voltage.

A trilayer coated wafer, after the drying process, is shown in Fig. 16a. And in Fig. 16b, a cut out trilayer actuator is seen in top view. After cutting, microbeams were then swollen in ionic liquid (EMITFSI) until they reached swelling saturation point (around one week [39, 43]) enabling the incorporation of the ions necessary for the redox process (Fig. 16c). SEM images (similar to those in Fig. 16c) show that the beam does not increase its length and width after the swelling.

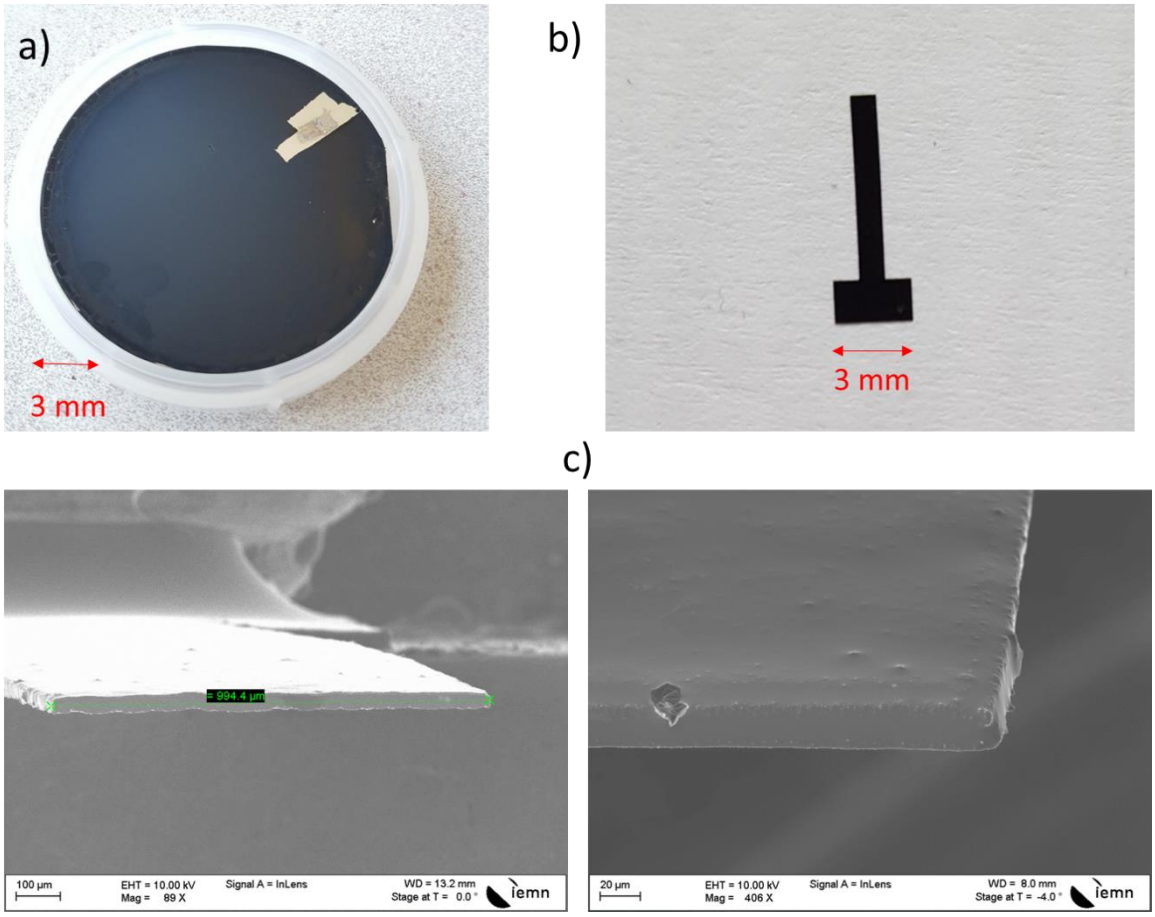


Fig. 16. a) The wafer after drying process, the white trace on the top right indicating the area has been peeled off for characterization: EDX and SEM, b) the resulting trilayer actuator after laser patterning process, the dimensions of the trilayer are length x width = 5 mm x 1 mm c) SEM images of the trilayer after swollen in EMITFSI

2.6.1 Fabrication of samples for the characterization process

In the previous section, the LbL fabrication process used to produce the trilayer actuators has been introduced. To characterize the electrochemomechanical properties of this resulting device, samples corresponding to different measurements have been fabricated, as summarized in Table 2.

Table 2. Summary the sample configuration for different characterizations

	Single layer PEDOT	Single layer NBR/PEO	Top PEDOT on NBR/PEO	Bottom PEDOT: NBR/PEO	PEDOT:NBR/PEO:PEDOT
Surface Roughness	x			x	x
Ionic conductivity		x	x	x	
Electronic conductivity			x	x	

Volumetric capacitance					x
Possible short circuit					x
Strain-to-charge ratio					x
Young's modulus		x			x
Damping ratio					x
Beam density					x
Strain difference					x
Linear strain					x
Blocking force					x

A single sIPN of NBR/PEO (50/50) was fabricated for the ionic conductivity, and Young's modulus measurement.

To investigate the electronic and ionic conductivities of the PEDOT electrodes and their asymmetric properties, a top bilayer (NBR/PEO coated with PEDOT/PEO) and bottom bilayer (PEDOT coated with NBR/PEO) were manufactured, where the thickness of NBR/PEO is increased to more easily distinguish between the ionic conductivity of PEDOT and of NBR/PEO alone

The volumetric capacitance, the possible short circuit between two PEDOT electrodes, the Young's moduli, the damping ratio, and the linear strain of the trilayer structuring of PEDOT-PEO/NBR-PEDOT were all measured on a fabricated trilayer produced as described in the previous section.

It is worth of noticing that during the fabrication of a single PEDOT layer, the NBR/PEO, and the bilayer, the initiator PCDP was added to each layer to polymerize the PEO. However, in the trilayer configuration, the initiator was added into the membrane and the second PEDOT layer only. This may lead to some differences in their properties.

2.7 Analysis of the texture of the trilayer structure

A trilayer sample was analyzed on EDX to confirm the three-layer structure, shown in Fig. 17a. The green color represent sulfur, which is only present in PEDOT, and the red the carbon, dominating in the NBR region

The sIPN morphology of the trilayer is described in Fig. 17b, where the PEO is covalently crosslinked through all the trilayer improving the adhesion between the electrodes and the

SPE layer. The PEDOT chains are synthesized by VPP on the top and the bottom electrodes and do not either crosslink to each other or inter-crosslink with PEO. The linear NBR chains are only available in the middle layer.

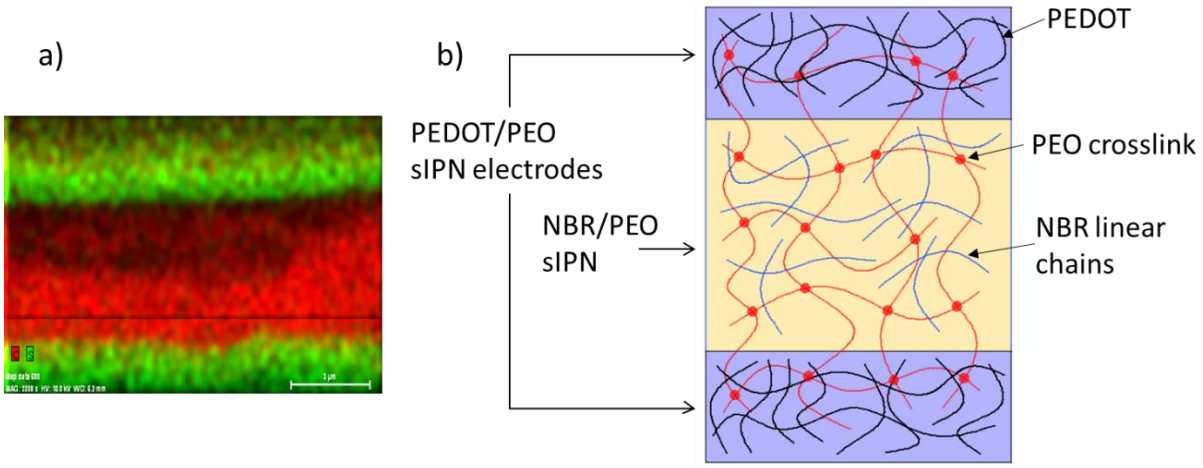


Fig. 17. a) The EDX of the trilayer structure, b) The anticipated morphology of the trilayer structure PEDOT:NBR/PEO:PEDOT

Table 2. Thicknesses of each layer before and after swelling in EMITFSI.

Trilayer	**Thickness before swelling (µm)**	**Thickness after swelling (µm)**
Bottom PEDOT electrode	2.1±0.3	3.5±0.5
SPE layer	7.0±0.3	10±0.5
Top PEDOT electrode	2.1±0.3	3.5±0.5

The thicknesses of each layer before and after immersion in EMITFSI are listed in Table 2. The thickness measurements have been performed on a set of five different trilayer samples prepared with the same fabrication process and the consistency of the thickness values in the table demonstrate the reproducibility of the fabrication process.

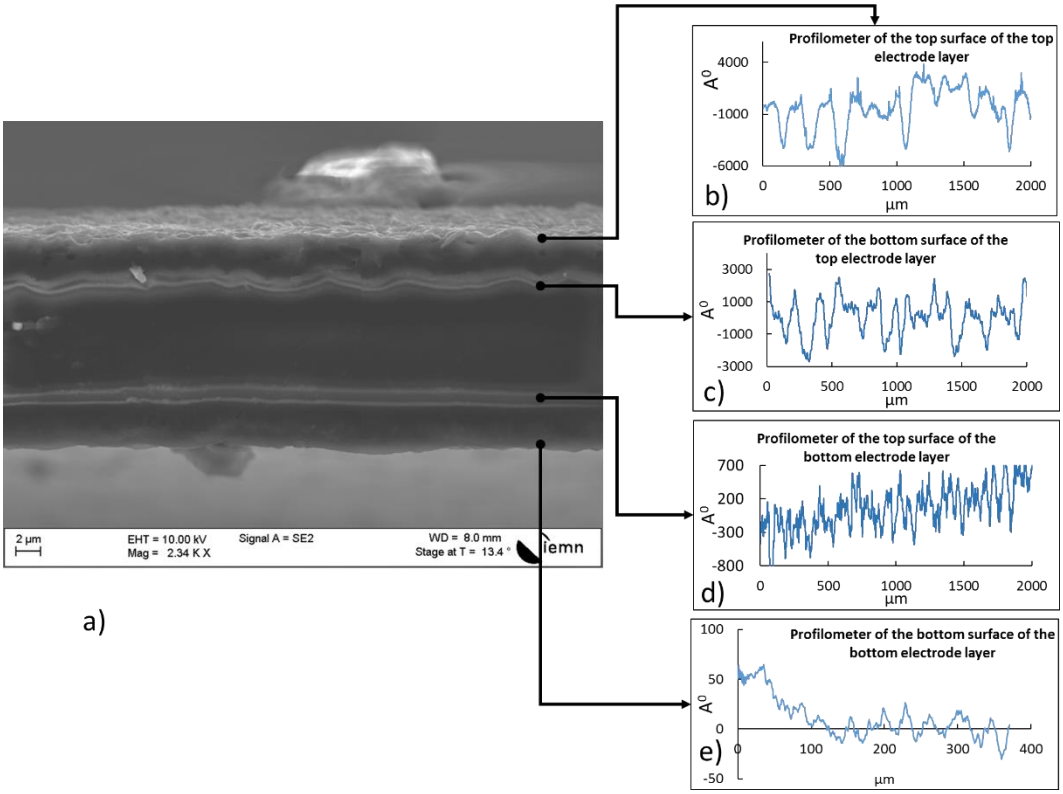


Fig. 18. a) SEM image of the trilayer cross section in dry state, profilometer surface roughness of the b) top surface of the top electrode layer, c) top surface of the SPE of a bilayer PEDOT/SPE, d) top surface of the bottom electrode layer, e) bottom surface of the bottom electrode layer

It is important to note that after swelling in EMITFSI, the total thickness of trilayer actuator can be easily verified by SEM (Fig. 18a) but the thickness change of each layer is impossible to determine directly on the trilayer either by SEM or EDX because the ionic liquid covers the cross section of the trilayer. Therefore, a single SPE layer was fabricated using the same parameters in comparison with the SPE layer in trilayer structure. This single layer was then swollen in EMITFSI during one week. It has been found that SPE layer increases by 43% its thickness after swelling. From this increasing percentage and the total thickness of the trilayer, the thicknesses of two conducting polymer electrode layers can be estimated. The error is calculated based on five measurements made at different position along the sample. The swollen percentage of SPE layer shown here is quite consistent with the results reported by Maziz [39] for the same type of SPE.

Despite the fact of sharing the same fabrication parameters, differences between the bottom and top PEDOT layers were observed with the roughness measurements conducted when the layers were still dry. It is worth noticing that the profilometer measurements in Fig. 18c and d were performed on the top surface of the SPE of a bilayer PEDOT/SPE and on the top surface of a single bottom PEDOT layer, respectively. The roughness was measured here while the layers were still on a silicon wafer and the average values obtained are 0.5 µm and around 0.1 µm respectively. The surface roughness of the top surface of the top electrode seen Fig.

18b is also measured as the actuator is still fixed on the silicon wafer and the average value obtained (0.7 µm) is similar to that measured on PEDOT/SPE. The average roughness on the bottom surface of the bottom electrode is measured after lift-off and once it has been flipped on over onto a new silicon wafer. The value obtained in this case is very small, around 0.06 µm (Fig. 18e) (refer to Appendix A.2.2 for the surface roughness measurement method on different samples). The average roughness of the top PEDOT electrode surface is then ten times higher than for the bottom electrode.

The LbL fabrication method may explain this roughness difference. The SPE layer is spin-coated on the bottom PEDOT layer and the pre-heat treatment (for evaporating the solvent and crosslinking PEO precursors) may result in a slight contraction of this layer, producing a slight and relatively regular folding on its surface. This folding depends on the thickness of the SPE layer and the way in which the heat treatment is performed. The top PEDOT layer only reproduces the shape of the SPE surface. The average roughness of the PEDOT surface in contact with open-air (top PEDOT electrode) (Fig. 18d) is, quite logically, greater than the one in contact with silicon substrate (Fig. 18e). The supposed contraction of the SPE layer during the trilayer fabrication process is visible once the microbeams are lifted off and swollen in EMITFSI. A slight curvature of the beam often appears which extends systematically the bottom layer of PEDOT previously in contact with the silicon wafer, and contracts the top layer of PEDOT. This indicates the presence of a weak stress inside the microbeam.

Another possible contribution to the roughness difference may come from the bottom-up forming mechanism of PEDOT during the VPP of EDOT. Brooke *et al.* [65] and Evans *et al.* [66] have shown that during the VPP of EDOT, PEDOT growth is via a bottom-up forming mechanism, where the oxidant solution is transported up to the surface to form a new PEDOT layer. This mechanism suggests that a denser PEDOT distribution is expected at the bottom PEDOT surface in contact with silicon, while the top PEDOT surface is less dense.

2.8 Conclusion

In this chapter, I have described the fabrication of a trilayer structure of a semi-NBR/PEO sandwiched between two PEDOT electrodes, produced by stacking LbL. By introducing the PEO into all three layers, the ionic conductivity and the mechanical adhesion among these layers increases. This fabricating method enabled us to obtain a thin, controllable thickness. From previous work, noticeable changes have been made, such as the optimization of the PEDOT electrodes resulting in the increase of VPP time from 30 min to 50 min, a different vacuum hotplate (Sawatec HP-200) allowing a more precise temperature and vacuum control replaced the vacuum bell during the VPP, and all the fabrication process was performed in the clean room environment, which ensures a higher reproducibility -ten batches of trilayer samples were fabricated and the bending experiment shown that the trilayer actuators in four batches were working. The percentage of the PEO in the PEDOT layer is also changed to 10%

in comparison with the 20 % used in the work of A. Maziz [67]. This percentage ensures a balance between high electronic conductivity (around 200 S/cm) and high volumetric charge density (between 2.3 x 10^7 C/m^3 and 1.0 x 10^8 C/m^3) of the PEDOT layer. Moreover, we have highlighted a slight asymmetry in surface roughness between the top and the bottom PEDOT layers which might have consequences on the electrical properties of the PEDOT electrodes and finally on the mechanical properties (displacement, force …) of the actuator.

The VPP process in this thesis has used the conventional oxidant solution consisting of 55% $Fe(TOs)_3$ in butanol. However, literature has shown that this high percentage produces a highly acidic and reactive oxidant solution, resulting in uncontrollable polymerization and structural defects in the deposited film [53]. Investigation on optimizing the percentage of oxidant solution, or adding base inhibitors such as pyridine to control the reaction rate are suggested to further improve the electrochemical properties of the PEDOT electrode. This is left to future work.

It is quite possible to think in the future to have a wider choice of trilayers. Indeed, the work of K. Rotlaid and F. Ribeiro go in this direction. In the case of K. Rotlhaid, the PEDOT electrodes are replaced by PEDOT: PSS with incorporated PEO, which allows for thicker actuators (around 30µm) - thereby producing more force (this work has not been published yet). In the case of F. Ribeiro, the possibility of incorporating the ionic liquid into the SPE at the time of manufacture is a promising innovation (this work is still unpublished). In fact, the swelling phase of our actuators modifies the total thickness by 160%, which potentially can have consequences on the transfer of electrodes in a complete integration step – where the metal electrodes in contacting with the PEDOT layers will be expanded leading to the facture of the electrode after the actuator is swollen. The manufacturing characteristics of these future materials will have to be taken into account to have the necessary elements for a good interpretation of the modeling and their experimental mode of operation.

The electrical and mechanical properties of each layer and the three-layer structure must also be evaluated experimentally in order to bring the parameters of interest to the model. This characterization process will be described in the next chapter.

[1] R.H. Baughman, L.W. Shacklette, R.L. Elsenbaumer, E.J. Plichta, C. Becht, Micro Electromechanical Actuators Based on Conducting Polymers, in: P.I. Lazarev (Ed.) Molecular Electronics: Materials and Methods, Springer Netherlands, Dordrecht, 1991, pp. 267-89.
[2] T. Sendai, H. Suematsu, K. Kaneto, Anisotropic strain and memory effect in electrochemomechanical strain of polypyrrole films under high tensile stresses, Japanese Journal of Applied Physics, 48(2009) 0515061-4.
[3] K. Kaneto, H. Hashimoto, K. Tominaga, W. Takashima, Shape retention in polyaniline artificial muscles, Japanese Journal of Applied Physics, 50(2011).
[4] D. Mecerreyes, Applications of Ionic Liquids in Polymer Science and Technology, Berlin, Heidelberg: Springer; 2015.
[5] D. Mecerreyes, Applications of ionic liquids in polymer science and technology, Heidelberg ; New York: Springer; 2015.
[6] K. Asaka, H. Okuzaki, SpringerLink (Online service), SpringerLINK ebooks - Chemistry and Materials Science (2014), Soft Actuators Materials, Modeling, Applications, and Future Perspectives, S.l.: Springer Japan; 2014.
[7] J. Citerin, A. Kheddar, M. Hafez, F. Vidal, C. Plesse, D. Teyssie, C. Chevrot, Characterization of a new interpenetrated network conductive polymer (IPN-CP) as a potential actuator that works in air conditions, Intelligent Robots and Systems, 2004 (IROS 2004) Proceedings 2004 IEEE/RSJ International Conference on2004, pp. 913-8 vol.1.
[8] U.L. Zainudeen, M.A. Careem, S. Skaarup, PEDOT and PPy conducting polymer bilayer and trilayer actuators, Sensors and Actuators, B: Chemical, 134(2008) 467-70.
[9] C. Plesse, F. Vidal, H. Randriamahazaka, D. Teyssié, C. Chevrot, Synthesis and characterization of conducting interpenetrating polymer networks for new actuators, Polymer, 46(2005) 7771-8.
[10] J. Tanguy, N. Mermilliod, M. Hoclet, Capacitive Charge and Noncapacitive Charge in Conducting Polymer Electrodes, Journal of The Electrochemical Society, 134(1987) 795-802.
[11] T. Yeu, K.M. Yin, J. Carbajal, R.E. White, Electrochemical Characterization of Electronically Conductive Polypyrrole on Cyclic Voltammograms, Journal of The Electrochemical Society, 138(1991) 2869-77.
[12] Y. Naka, M. Fuchiwaki, K. Tanaka, A micropump driven by a polypyrrole-based conducting polymer soft actuator, Polymer International, 59(2010) 352-6.
[13] Y. Fang, X. Tan, A novel diaphragm micropump actuated by conjugated polymer petals: Fabrication, modeling, and experimental results, Sensors and Actuators A: Physical, 158(2010) 121-31.
[14] K. Ikushima, S. John, A. Ono, S. Nagamitsu, PEDOT/PSS bending actuators for autofocus micro lens applications, Synthetic Metals, 160(2010) 1877-83.
[15] S. McGovern, G. Alici, V.T. Truong, G. Spinks, Finding NEMO (novel electromaterial muscle oscillator): A polypyrrole powered robotic fish with real-time wireless speed and directional control, Smart Materials and Structures, 18(2009).
[16] E.W. Jager, Immerstrand, C., Peterson, K.H. et al. , The Cell Clinic: Closable Microvials for Single Cell Studies, Biomedical Microdevices, 4(2002) 10.
[17] W.H.J. Edwin, Ingan, xe, O. s, Lundstr, xf, I. m, Microrobots for Micrometer-Size Objects in Aqueous Media: Potential Tools for Single-Cell Manipulation, Science, 288(2000) 2335-8.
[18] E.W.H. Jager, N. Masurkar, N.F. Nworah, B. Gaihre, G. Alici, G.M. Spinks, Patterning and electrical interfacing of individually controllable conducting polymer microactuators, Sensors and Actuators B: Chemical, 183(2013) 283-9.
[19] T. Göttsche, S. Haeberle, Integrated Oral Drug Delivery System with Valve Based on Polypyrrole, Biomedical Applications of Electroactive Polymer Actuators, John Wiley & Sons, Ltd2009, pp. 301-16.
[20] C.A. Cutler, M. Bouguettaya, J.R. Reynolds, PEDOT polyelectrolyte based electrochromic films via electrostatic adsorption, Advanced Materials, 14(2002) 684-8.
[21] J.D.W. Madden, N.A. Vandesteeg, P.A. Anquetil, P.G.A. Madden, A. Takshi, R.Z. Pytel, S.R. Lafontaine, P.A. Wieringa, I.W. Hunter, Artificial muscle technology: Physical principles and naval prospects, IEEE Journal of Oceanic Engineering, 29(2004) 706-28.

[22] A. Mazzoldi, A.D. Santa, D. De Rossi, Conducting Polymer Actuators: Properties and Modeling, in: Y. Osada, D.E. De Rossi (Eds.), Polymer Sensors and Actuators, Springer Berlin Heidelberg, Berlin, Heidelberg, 2000, pp. 207-44.
[23] E. Smela, Conjugated Polymer Actuators for Biomedical Applications, Advanced Materials, 15(2003) 481-94.
[24] A. Khaldi, C. Plesse, C. Soyer, E. Cattan, F. Vidal, C. Legrand, D. Teyssié, Conducting interpenetrating polymer network sized to fabricate microactuators, Applied Physics Letters, 98(2011).
[25] A. Khaldi, A. Maziz, C. Plesse, C. Soyer, D. Teyssié, F. Vidal, E. Cattan, Patterning innovative conducting interpenetrating polymer network by dry etching, IEEE/ASME International Conference on Advanced Intelligent Mechatronics, AIM2014, pp. 1424-9.
[26] L. Groenendaal, F. Jonas, D. Freitag, H. Pielartzik, J.R. Reynolds, Poly(3,4-ethylenedioxythiophene) and Its Derivatives: Past, Present, and Future, Advanced Materials, 12(2000) 481-94.
[27] F. Vidal, C. Plesse, G. Palaprat, A. Kheddar, J. Citerin, D. Teyssié, C. Chevrot, Conducting IPN actuators: From polymer chemistry to actuator with linear actuation, Synthetic Metals, 156(2006) 1299-304.
[28] F. Vidal, C. Plesse, D. Teyssié, C. Chevrot, Long-life air working conducting semi-IPN/ionic liquid based actuator, Synthetic Metals, 142(2004) 287-91.
[29] S.C. Kim, D. Klempner, K.C. Frisch, H.L. Frisch, Polyurethane Interpenetrating Polymer Networks. II. Density and Glass Transition Behavior of Polyurethane-Poly(methyl methacrylate) and Polyurethane-Polystyrene IPN's, Macromolecules, 9(1976) 263-6.
[30] G.M. Yenwo, L.H. Sperling, J. Pulido, J.A. Manson, A. Conde, Castor oil based interpenetrating polymer networks, IV. Mechanical behavior, Polymer Engineering & Science, 17(2004) 251-6.
[31] M.-J. Lee, Y.S. Choi, Y.S. Kang, J.-H. Choi, M.-S. Kang, All-solid-state proton conductive membranes prepared by a semi-interpenetrating polymer network (semi-IPN), Journal of Materials Chemistry, 22(2012) 18522-7.
[32] L.J. Goujon, A. Khaldi, A. Maziz, C. Plesse, G.T.M. Nguyen, P.-H. Aubert, F. Vidal, C. Chevrot, D. Teyssié, Flexible Solid Polymer Electrolytes Based on Nitrile Butadiene Rubber/Poly(ethylene oxide) Interpenetrating Polymer Networks Containing Either LiTFSI or EMITFSI, Macromolecules, 44(2011) 9683-91.
[33] F. Nicolas, M. Ali, P. Cédric, T. Dominique, C. Claude, V. Frédéric, Robust solid polymer electrolyte for conducting IPN actuators, Smart Materials and Structures, 22(2013) 104005.
[34] D. Mecerreyes, Springer-Verlag (Berlin), Applications of ionic liquids in polymer science and technology, Heidelberg: Springer; 2015.
[35] P. Verge, F. Vidal, P.-H. Aubert, L. Beouch, F. Tran-Van, F. Goubard, D. Teyssié, C. Chevrot, Thermal ageing of poly(ethylene oxide)/poly(3,4-ethylenedioxythiophene) semi-IPNs, European Polymer Journal, 44(2008) 3864-70.
[36] C. Plesse, F. Vidal, C. Gauthier, J.-M. Pelletier, C. Chevrot, D. Teyssié, Poly(ethylene oxide)/polybutadiene based IPNs synthesis and characterization, Polymer, 48(2007) 696-703.
[37] C. Plesse, A. Khaldi, Q. Wang, E. Cattan, D. Teyssié, C. Chevrot, F. Vidal, Polyethylene oxide–polytetrahydrofurane–PEDOT conducting interpenetrating polymer networks for high speed actuators, Smart Materials and Structures, 20(2011) 124002.
[38] F. Vidal, C. Plesse, G. Palaprat, J. Juger, C. Gauthier, J.-M. Pelletier, K. Masenelli-Varlot, C. Chevrot, D. Teyssié, Influence of the poly(ethylene oxide)/polybutadiene IPN morphology on the ionic conductivity of ionic liquid, European Polymer Journal, 49(2013) 2670-9.
[39] A. Maziz, C. Plesse, C. Soyer, C. Chevrot, D. Teyssié, E. Cattan, F. Vidal, Demonstrating kHz Frequency Actuation for Conducting Polymer Microactuators, Advanced Functional Materials, 24(2014) 4851-9.
[40] Retraction notice to "Differential impact of diabetes and hypertension in the brain: adverse effects in grey matter" [Neurobiol. Dis., 44 (2011) 161-173, http://dx.doi.org/10.1016/ j.nbd.2011.06.005], Neurobiol Dis, 68(2014) 229.

[41] M. Armand, F. Endres, D.R. MacFarlane, H. Ohno, B. Scrosati, Ionic-liquid materials for the electrochemical challenges of the future, Nat Mater, 8(2009) 621-9.
[42] G. Petroffe, L. Beouch, S. Cantin, P.-H. Aubert, C. Plesse, J.-P. Dudon, F. Vidal, C. Chevrot, Investigations of ionic liquids on the infrared electroreflective properties of poly(3,4-ethylenedioxythiophene), Solar Energy Materials and Solar Cells, 177(2018) 23-31.
[43] A. Maziz, C. Plesse, C. Soyer, E. Cattan, F. Vidal, Top-down Approach for the Direct Synthesis, Patterning, and Operation of Artificial Micromuscles on Flexible Substrates, ACS Appl Mater Interfaces, 8(2016) 1559-64.
[44] J.F. Hulvat, S.I. Stupp, Liquid-crystal templating of conducting polymers, Angew Chem Int Ed Engl, 42(2003) 778-81.
[45] B. Winther-Jensen, D.W. Breiby, K. West, Base inhibited oxidative polymerization of 3,4-ethylenedioxythiophene with iron(III)tosylate, Synthetic Metals, 152(2005) 1-4.
[46] C. Largeot, C. Portet, J. Chmiola, P.L. Taberna, Y. Gogotsi, P. Simon, Relation between the ion size and pore size for an electric double-layer capacitor, J Am Chem Soc, 130(2008) 2730-1.
[47] J.P. Lock, S.G. Im, K.K. Gleason, Oxidative Chemical Vapor Deposition of Electrically Conducting Poly(3,4-ethylenedioxythiophene) Films, Macromolecules, 39(2006) 5326-9.
[48] S. Kirchmeyer, K. Reuter, Scientific importance, properties and growing applications of poly(3,4-ethylenedioxythiophene), Journal of Materials Chemistry, 15(2005) 2077-88.
[49] K.H. Skorenko, A.C. Faucett, J. Liu, N.A. Ravvin, W.E. Bernier, J.M. Mativetsky, W.E. Jones, Vapor phase polymerization and mechanical testing of highly electrically conductive poly(3,4-ethylenedioxythiophene) for flexible devices, Synthetic Metals, 209(2015) 297-303.
[50] A. Maziz, C. Plesse, C. Soyer, E. Cattan, F. Vidal, Top-down Approach for the Direct Synthesis, Patterning, and Operation of Artificial Micromuscles on Flexible Substrates, ACS Applied Materials & Interfaces, 8(2016) 1559-64.
[51] T.N. Nguyen, K. Rohtlaid, C. Plesse, G.T.M. Nguyen, C. Soyer, S. Grondel, E. Cattan, J.D.W. Madden, F. Vidal, Ultrathin electrochemically driven conducting polymer actuators: fabrication and electrochemomechanical characterization, Electrochimica Acta, 265(2018) 670-80.
[52] K.D. Fong, T. Wang, H.-K. Kim, R.V. Kumar, S.K. Smoukov, Semi-Interpenetrating Polymer Networks for Enhanced Supercapacitor Electrodes, ACS Energy Letters, 2(2017) 2014-20.
[53] W. Shi, Q. Yao, S. Qu, H. Chen, T. Zhang, L. Chen, Micron-thick highly conductive PEDOT films synthesized via self-inhibited polymerization: roles of anions, Npg Asia Materials, 9(2017) e405.
[54] E. Smela, O. Inganas, I. Lundstrom, Controlled folding of micrometer-size structures, Science, 268(1995) 1735-8.
[55] E.W. Jager, O. Inganas, I. Lundstrom, Microrobots for micrometer-size objects in aqueous media: potential tools for single-cell manipulation, Science, 288(2000) 2335-8.
[56] E.W. Jager, E. Smela, O. Inganas, Microfabricating conjugated polymer actuators, Science, 290(2000) 1540-5.
[57] A. Khaldi, C. Plesse, C. Soyer, E. Cattan, F. Vidal, C. Legrand, D. Teyssié, Conducting interpenetrating polymer network sized to fabricate microactuators, Applied Physics Letters, 98(2011) 164101.
[58] A. Khaldi, A. Maziz, C. Plesse, C. Soyer, D. Teyssié, F. Vidal, E. Cattan, Patterning innovative conducting interpenetrating polymer network by dry etching, 2014 IEEE/ASME International Conference on Advanced Intelligent Mechatronics2014, pp. 1424-9.
[59] A. Khaldi, D. Falk, K. Bengtsson, A. Maziz, D. Filippini, N.D. Robinson, E.W.H. Jager, Patterning Highly Conducting Conjugated Polymer Electrodes for Soft and Flexible Microelectrochemical Devices, ACS Applied Materials & Interfaces, 10(2018) 14978-85.
[60] K.K. Lee, P.R. Herman, T. Shoa, M. Haque, J.D. Madden, V.X. Yang, Microstructuring of polypyrrole by maskless direct femtosecond laser ablation, Adv Mater, 24(2012) 1243-6.
[61] N. Bityurin, 8[space][space]Studies on laser ablation of polymers, Annual Reports Section "C" (Physical Chemistry), 101(2005) 216-47.

[62] A. Gursel, D. Valerie, R. Philippe, S. Geoff, Conducting polymer microactuators operating in air, Journal of Micromechanics and Microengineering, 19(2009) 025017.
[63] M. Farajollahi, Fabrication and non-linear modeling of conducting polymer-based actuators : toward catheter and tactile display applications: University of British Columbia; 2016.
[64] M. Anwar Mohammed, T. Saleh, D.W. Madden John, K. Takahata, Micropatterning Polypyrrole Conducting Polymer by Pulsed Electrical Discharge, Macromolecular Materials and Engineering, 299(2013) 198-207.
[65] R. Brooke, M. Fabretto, P. Hojati-Talemi, P. Murphy, D. Evans, Evidence for 'bottom up' growth during vapor phase polymerization of conducting polymers, Polymer, 55(2014) 3458-60.
[66] D. Evans, M. Fabretto, M. Mueller, K. Zuber, R. Short, P. Murphy, Structure-directed growth of high conductivity PEDOT from liquid-like oxidant layers during vacuum vapor phase polymerization, Journal of Materials Chemistry, 22(2012) 14889-95.
[67] A. Maziz, Microactionneurs à base de polymères conducteurs électroniques : Vers l'intégration aux microsystèmes par de nouveaux procédés d'élaboration, France: Université de Cergy Pontoise; 2014.

Chapter 3: Electrochemomechanical characterization of the trilayer structure

Contents

3.1 Introduction 46
3.2 Electro-chemical properties 48
3.2.1 Ionic conductivity of the SPE and PEDOT layers 49
3.2.2 Electrical conductivity of the PEDOT electrodes 52
3.2.3 Volumetric capacitance of the PEDOT electrodes 55
3.2.4 Possible short circuit between two PEDOT layers 58
3.3 Mechanical properties 59
3.3.1 Young's moduli of the SPE layer and of the trilayer actuator 59
3.3.2 Damping ratio 62
3.3.3 Blocking force characterization 63
3.4 Empirical strain-to-charge ratio 64
3.4.1 Strain to charge ratio 64
3.4.2 Linear strain 67
3.5 Conclusion 69

3.1 Introduction

In the previous chapter, a layer-by-layer method, combined with a vapor phase polymerization process, were employed to fabricate a thin trilayer structure. In order to most effectively exploit this process in actuators, having good models that predict response is useful. For this reason, characterization of the actuator's properties was done to gain knowledge and identify the important parameters affecting actuation performance. In this chapter, the geometric, electrochemical, mechanical and electrochemomechanical properties of these trilayers are determined. This includes measuring thicknesses of the conducting polymer containing layers and the separators, before and after swelling in ionic liquid. Stiffness, resistances (ionic and electronic), capacitance and active deflection under applied voltage are among the properties determined. From these measurements, key properties are extracted for use in modeling: Young's modulus, volumetric capacitance, ionic and electronic conductivities and strain to charge ratio – in some cases as a function of oxidation. These characteristics are then used to simulate polymer actuator and sensor responses (Chapters 4 and 5).

The characteristics of the resulting actuators, which were fabricated following the process mentioned in chapter 2, are studied in detail, as reported in the sections that follow. Before proceeding to the details, a typical device response is described. Fig. 1a shows the current response of the actuator under a step voltage. As can be seen, the output current quickly drops when the PEDOT electrodes approach their fully charged state. The equivalent displacement (Fig. 1b) is quite fast for first few seconds before it gets to a steady state. Fig. 1c shows the polarity of the applied voltage and the corresponding displacement direction of the trilayer. The positive potential induces a contraction in one PEDOT electrode and expansion of the other electrode. The amplitude of displacement is 3 mm of bending. The output current and the displacement can be used later to extract the information about the charge and strain.

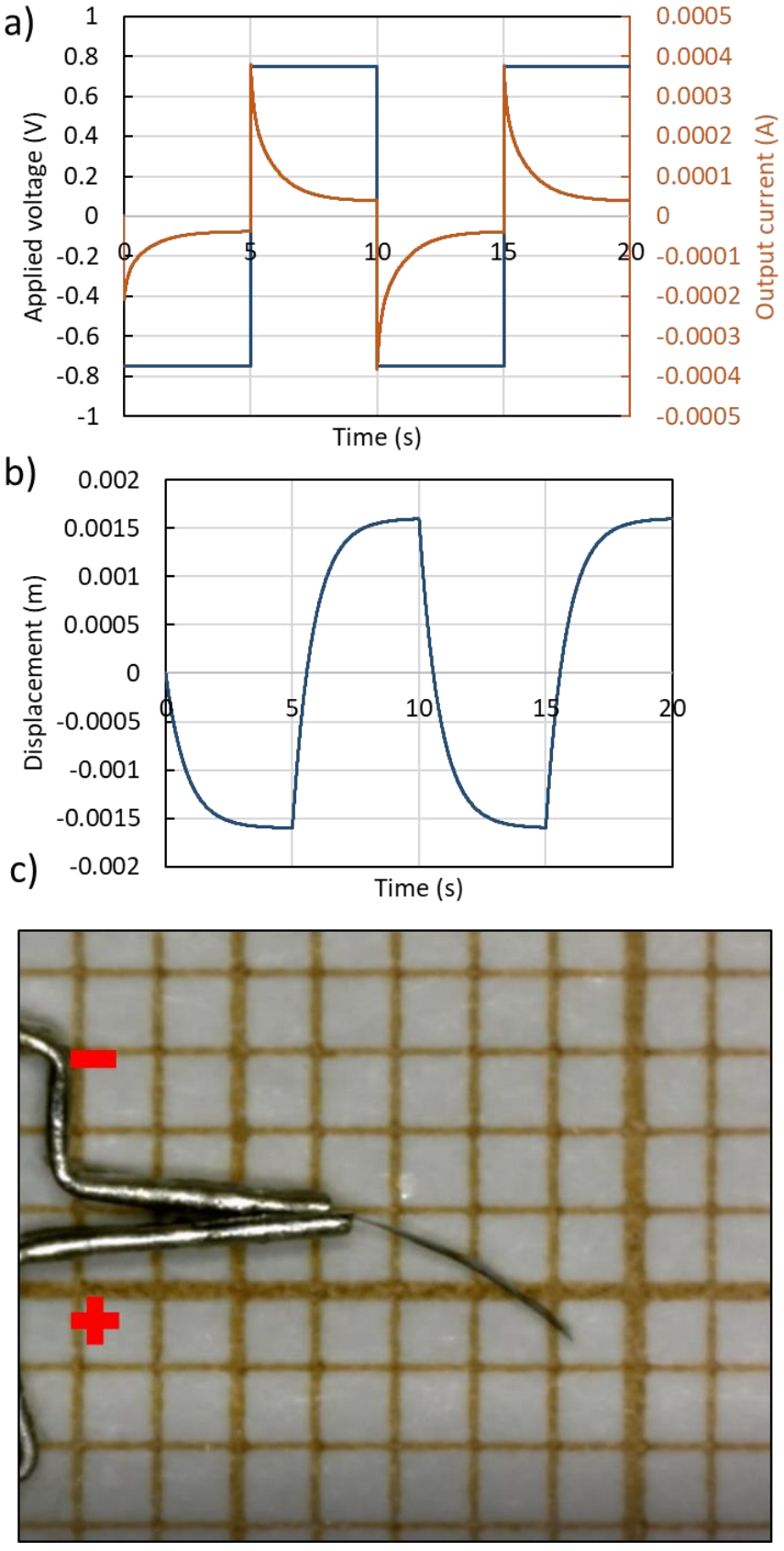


Fig. 1. Actuator behavior under a step voltage a) The applied step voltage and the response current, b) Bending response of the actuator, c) A picture of the bending actuator (length x width x thickness = 4 mm x 1 mm x 0.017 mm), the + and – indicate the polarity of the applied voltage.

Lots of factors can affect the strain, strain rate, and the blocking force of these actuators: for example ionic conductivity of the CP electrodes and the SPE layer can limit the strain rate and the bending speed of the actuator [1]. The electronic conductivity of the CPs can affect the circularity of the curvature of the beam during its actuation and is a function of the oxidation state, as demonstrated by Feldman [2-4]. The volumetric capacitance of the CP material assesses the ability to accommodate the ions under a voltage excitation. This value had been shown to vary with the scanning rate and the magnitude of the applied voltage [5, 6]. Since the trilayer structure is thin and PEDOT is grown in from the two opposing surfaces, there is a possible short circuit between the two CP electrodes. This can affect the the efficiency, sensor signal decay rate and the self-heating of the actuator, and so is important to know. The Young's modulus of the CP material determines the blocking force of the actuator (for a given strain). The Young's modulus was shown to be dependent on the oxidation state of the CP electrodes [4, 7].

In this chapter, the affecting factors discussed above will be taken into account during the investigation on the ultrathin PEDOT:NBR/PEO:PEDOT structure. The electrochemical properties of the actuators including ionic conductivity of the PEDOT electrodes and the NBR/PEO, the electronic conductivity and the volumetric capacitance of the PEDOT electrodes, as well as the possible short circuit between two PEDOT electrodes will be investigated. The coupling between the electrochemical and the mechanical part, representing by an empirical strain-to-charge ratio, is measured. The Young's moduli of the SPE, the PEDOT electrode as the function of the oxidation state, the damping ratio and the linear strain of the actuator will be studied. These resulting parameters provide an insight the actuator performance as well fulfilling the required values to establish the model predicting actuator's behavior.

3.2 Electro-chemical properties

Before beginning the full characterization, different sample configurations were fabricated to adapt for different measurements (refer to section 2.6.1 for list of fabricated samples).

It is worth noting that trilayers of varying thickness were fabricated and tested in actuation, to find a dimension range where significant bending actuation is achieved, for easy characterization. Ten trilayer membranes were fabricated on ten separate silicon wafers, in which the thicknesses of PEDOT electrodes were adjusted from 0.8 µm to 2.3 µm to investigate the effect of the PEDOT's thickness on the strain output of the trilayer actuator. Bending actuation experiments were observed on 4 samples, where the thicknesses of PEDOT electrodes vary from 1.2 µm to 2.3 µm. These exhibit bending under a voltage excitation. The biggest displacement was seen in a sample having a thickness of PEDOT:NBR/PEO:PEDOT = 2.2 µm:7 µm: 2.2 µm (pre-swelling dimensions). After swelling in ionic liquid, the thicknesses of the PEDOT electrodes and of the NBR/PEO layer are approximately 3.5 µm and 10 µm,

respectively. Therefore, this thickness ratio (PEDOT:NBR/PEO:PEDOT = 3.5 µm:10 µm:3.5 µm after swelling in ionic liquid) is chosen for further investigation on the volumetric capacitance, the possible short circuit between two PEDOT electrodes, the Young's moduli, the damping ratio, and the linear strain as well as the bending strain.

3.2.1 Ionic conductivity of the SPE and PEDOT layers

Ionic conductivity is one of a number of properties that limit current, and, as a result, charging speed. [8]. Therefore, it is a factor that can limit strain rate and bending speed of the trilayer actuator. PEDOT ionic conductivity was determined using an Electrochemical Impedance Spectroscopy (EIS) measurement according to a procedure described previously [8, 9] and summarized in Fig. 2a. A Solartron 1287A Potentiostat/Galvanostat combined with a Solartron 1260A frequency response analyzer was used to obtain the frequency responses. A 4-point measurement across the ionic liquid and the membrane (a bilayer or a trilayer) is used. We impose current between the working electrode (W.E) and the counter electrode (C.E) and detect a local potential drop between two reference electrodes (R.Es) (Fig. 2a). The W.E and the C.E are made of two pieces of glassy carbon, and the R.Es are the classic Ag/AgCl wire filled 4M NaCl.

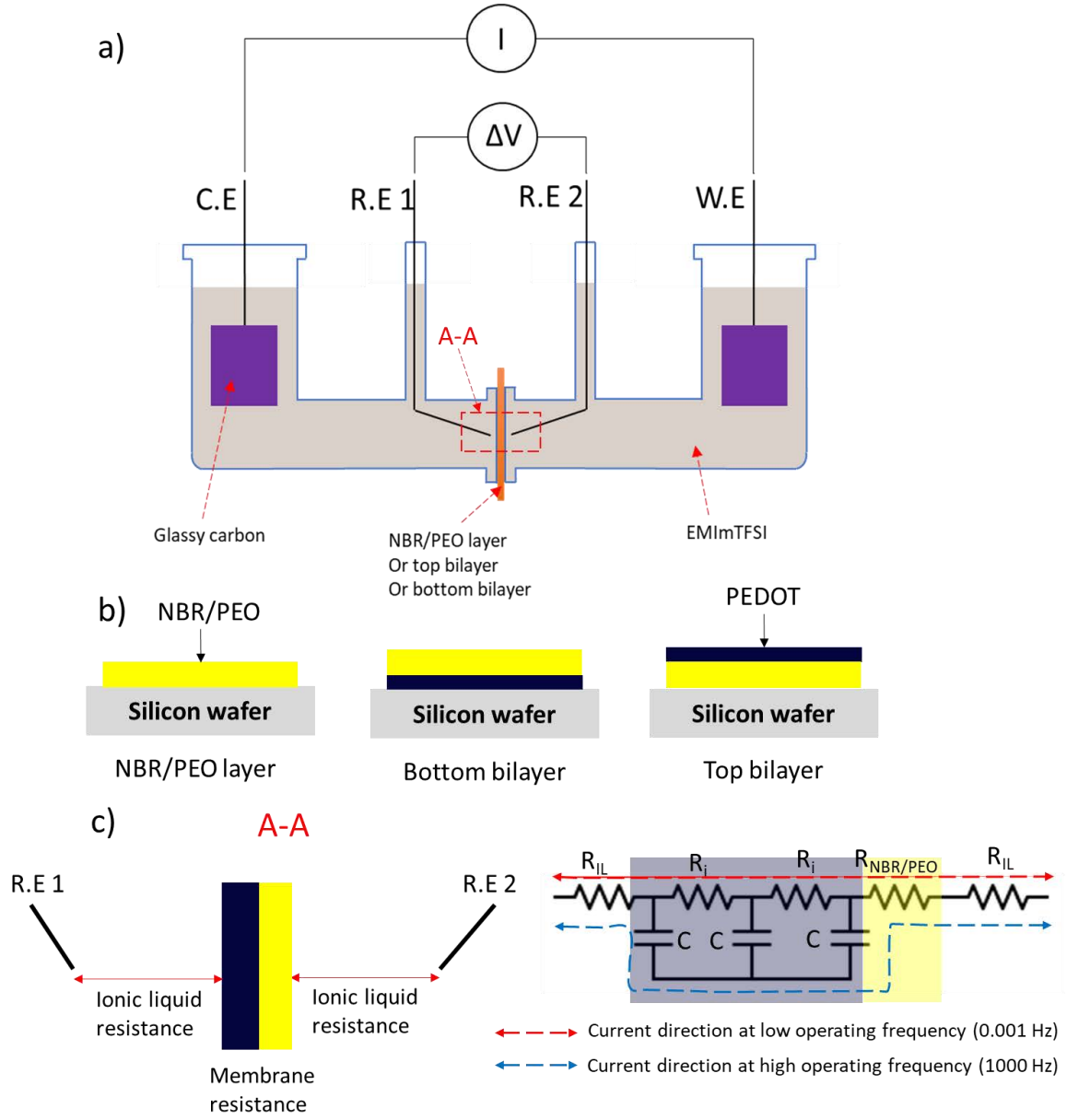


Fig. 2. a) EIS measurement using 4-point setup, b) NBR/PEO layer, bottom bilayer, and top bilayer configuration, and c) a zoomed image of an area in the red rectangular A-A and its equivalent circuit showing the current direction at low and high operating frequency.

It has been shown that there is an asymmetry between the top and the bottom PEDOT electrodes in a trilayer actuator fabricated by layer-by-layer method (chap. 2, section 2.7) [10]. As demonstrated, the roughness of the top PEDOT electrode is ten times higher than that of the bottom PEDOT electrode. This fact may lead to asymmetric properties between these two electrodes. Therefore, there is a need to characterize separately each electrode. A top bilayer (PEDOT electrode is polymerized on the top of NBR/PEO) and a bottom bilayer (PEDOT electrode is polymerized on a silicon wafer followed by a NBR/PEO layer) were investigated to find out the variation in PEDOT ionic conductivity, shown in Fig. 2b. Before the measurement, an NBR/PEO membrane, as well as the top bilayer and the bottom bilayer samples were immersed into EMITFSI for one week [11], to ensure a full uptake of ions.

Because the resistance of each layer depends on their thickness, to separate the PEDOT ionic resistance from other sources of resistance such as NBR/PEO resistance and ionic liquid resistance, the thickness of specimens including the thickness of NBR/PEO and PEDOT (Table 1) was increased during the fabrication process. It is worth of noticing that the thickness of swollen PEDOT layers were not measured directly but it was determined by SEM in its dry state and then multiplied by 1.66, which is the swelling factor in EMITFSI deriving from chapter 2 (section 2.7).

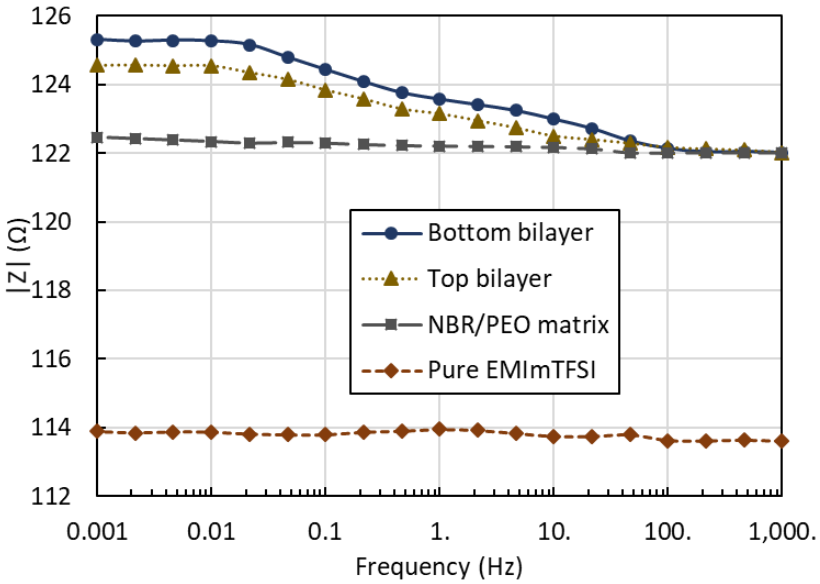


Fig. 3. Impedance values obtained from EIS measurements of a pure EMImTFSI, a top bilayer of NBR/PEO-PEDOT, a bottom bilayer of PEDOT-NBR/PEO, and a single NBR/PEO layer.

The EIS experimental results are shown in Fig. 3. The resistance between the cannulas of the ionic liquid alone (no film present) is 114 Ohms. The NBR/PEO matrix without PEDOT adds another 8 Ohms. The PEDOT containing layers add another 2 to 3 Ohms, as can be seen from the low frequency impedance. At high frequencies the effect of the conducting PEDOT layer disappears completely as its parallel electronic conductivity bypasses the ionic resistance [8] (as shown in Fig. 3c). Clearly the impedance is dominated by the ionic resistances of the sample, and of the electrolyte. The ionic conductivity (δ) of the PEDOT and NBR/PEO layers is determined by:

$$\delta = \frac{h}{R \times A}$$

where h is the thickness of either the PEDOT or the NBR/PEO layer (Table 1), and A is the sample surface area in contacting with the electrolyte, which is equal to 0.78 cm^2. Resistance R, is calculated by a subtraction between NBR/PEO containing cell resistance and pure EMImTFSI resistance (Fig. 3) to estimate the resistance of the NBR/PEO alone. To find the ionic resistances of the PEDOT layers, the difference in resistance between low EIS frequency

(1 mHz – representing the resistance of all layers) and high EIS frequency (resistance at 1 kHz – representing the resistance of NBR/PEO plus EMImTFSI) is calculated, for the same bilayer.

Table 1. Thickness in swollen state and ionic conductivity of the NBR/PEO alone, top bilayer, and bottom bilayer

	Thickness (swollen) (μm)	**Resistance (Ω)**	**Ionic conductivity (S/m)**
Ionic liquid	-	-	0.9 (provided by supplier)
NBR/PEO layer	25.3	8.3	0.038±0.005
Top PEDOT layer of the bilayer	5.0±0.4	2.6	0.025±0.002
Bottom PEDOT layer of the bilayer	7.7±0.4	3.3	0.030±0.002

In the Table 1, the resistance of the NBR/PEO layer is obtained by subtracting the impedance value of the "NBR/PEO matrix" data shown in Fig. 4a from the "pure EMITFSI". Similarly, the resistance of the PEDOT layer of the top and bottom bilayer is derived from the difference in their impedance at low and high frequency (Fig. 4). The ionic conductivity values for the top and bottom layers are similar to and slightly lower than the 0.04±0.002 S/m measured by Dobashi *et al.* [8], in that case using aqueous LiTFSI as the electrolyte. As can be seen from table 1, there is a slight difference between the ionic conductivity of the top and the bottom PEDOT electrodes, perhaps indicating a small effect of the asymmetry on the ionic conductivity. This difference is contributed by three main factors, an uncertainty of the thickness measurement, a slight fluctuation (representing in the error bar in the table) of the impedance at low and high frequencies, and an asymmetry in PEDOT electrodes themselves. The ionic conductivity of the NBR/PEO (0.038 S/m) membrane is though lower than the values reported by Vidal [12] (0.1 S/m) and Maziz [13] (0.13 S/m). These obtained values were measured for a thick full IPN membrane (thickness>200 μm, where NBR is crosslinked) but not a very thin sIPN as in our case.

3.2.2 Electrical conductivity of the PEDOT electrodes

Researchers have demonstrated that the electronic conductivity of PEDOT depends on the potential applied [2-4]. Feldman *et al.* [2] shown that a conductivity of a 13.9 μm thick PPy film in 0.1 M Et_4NClO_4/CH_3CN quite constant at approximately 3 x 10^{-1} S/cm as the potential of the film is decreased from 0.4 V to 0 V. When the potential continues to decrease to -0.6 V, the conductivity enormously drops to 10^{-6} S/cm. Warren *et al.* [3] and Farajollahi *et al.* [4, 14] found a similar trend where the conductivity of a 25 μm thick PPy film increases from 0.64 S/cm to 270 S/cm when the applied potential raises from -0.8 V to 0.4 V. This drop with decreasing voltage can be explained: the PPy electrode is indeed reduced and the doping level is decreased which reduces the charge carrier concentration, the mobility, and in turn the

conductivity. In my work, the electrical conductivities of the thin sIPN PEDOT/PEO electrodes will be characterized to explore their dependences on the potential applied.

Fig. 4 presents a three-electrode system (Solartron potentiostat, ModuLab XM ECS) for cyclic voltammetry analysis. The counter electrode was a platinum foil with a surface area greater than that of the trilayer actuator electrode (at the working electrode). The reference electrode was a standard wire Ag/AgCl filled with 4M NaCl solution. The potentiostat was connected to both trilayer electrodes using platinum clamps and then fully immersed in EMITFSI. This scheme is used to reduce or oxidize the specimens to a certain potential (compared to Ag/AgCl reference electrode).

To measure the electrical conductivity as a function of oxidation state, a potential (versus Ag/AgCl reference electrode) was applied to both sides of a trilayer structure in solution (Fig. 5). The dimensions of the specimen are *length (L) x width (b) x total thickness (h) = 10 mm x 3 mm x 0.017 mm* in the swollen state, the thickness of the PEDOT layers is $h_P = 3.5\ \mu m$ and the thickness of NBR/PEO is $h_S = 10\ \mu m$. The length and width of the sample were increased to adapt them to the 4-line measurement setup in Fig. 5.

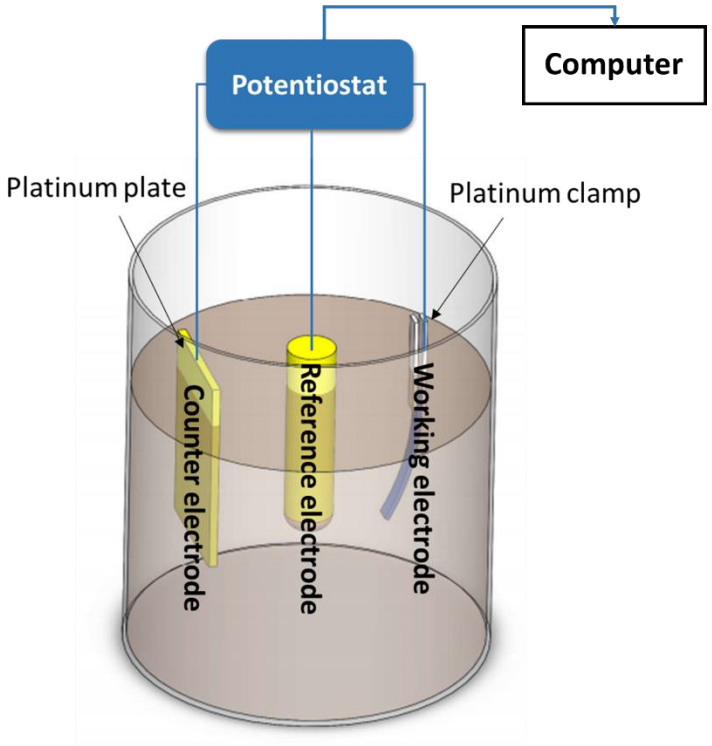


Fig. 4. Three-electrode system for setting the oxidation state of the PEDOT and for cyclic voltammetry analysis.

To drive the sample to the desired potential using the setup in Fig. 4, the voltage is applied and hold for 10 min, until the response current decays to 0 from its original position. The potential of the sample is then measured to confirm its oxidation (reduction) state. After reaching the desired potential, the sample is taken out the ionic liquid and laid down on the

four-line probe (Fig. 5) to measure its electrical conductivity. When the applied voltage is larger than +1 V or smaller than -1 V, the potential of the PEDOT electrodes is not stable and drops very quick once the sample is being taken out for measurement. This is the reason why I choose the range of applied potential between -1 V and 1 V.

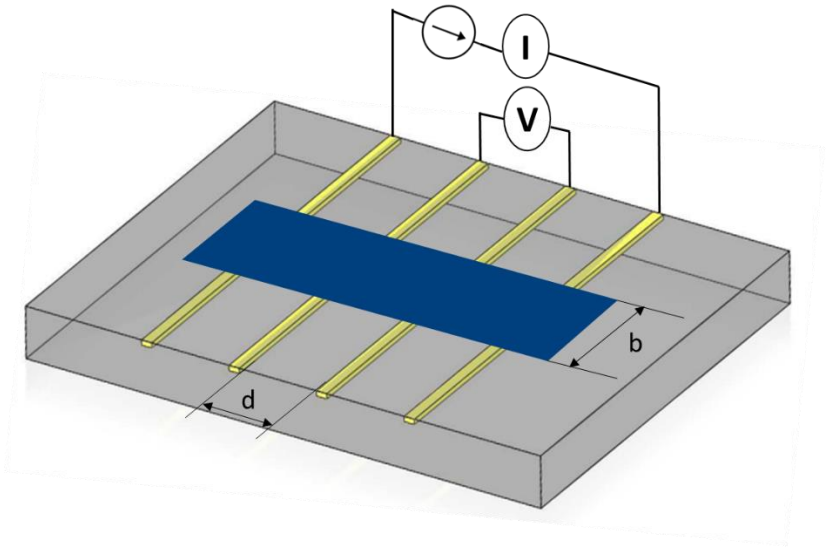


Fig. 5. A built in-house four-line probe to measure the electronic conductivity of the PEDOT electrodes, where the distance between two copper lines is d = 2 mm.

A 4-point probe is commonly used to measure the electronic conductivity of a surface. However, in the case of ultrathin polymer films, this device could damage the measurable layer due to its sharp probes. A four-line probe built in-house made from copper foil, a low resistance material, deposited on a glass slide to measure the electronic conductivity of a surface is presented in Fig. 5. In this setup, a constant current is applied between two external copper lines and the voltage between the two internal lines is then measured. The distance between the two internal lines, the thickness of the electrode layer and its geometry, the current applied, and the voltage measured are known and, therefore, the electronic conductivity can be derived. The measurement was performed on the top and bottom surfaces of the trilayer structure.

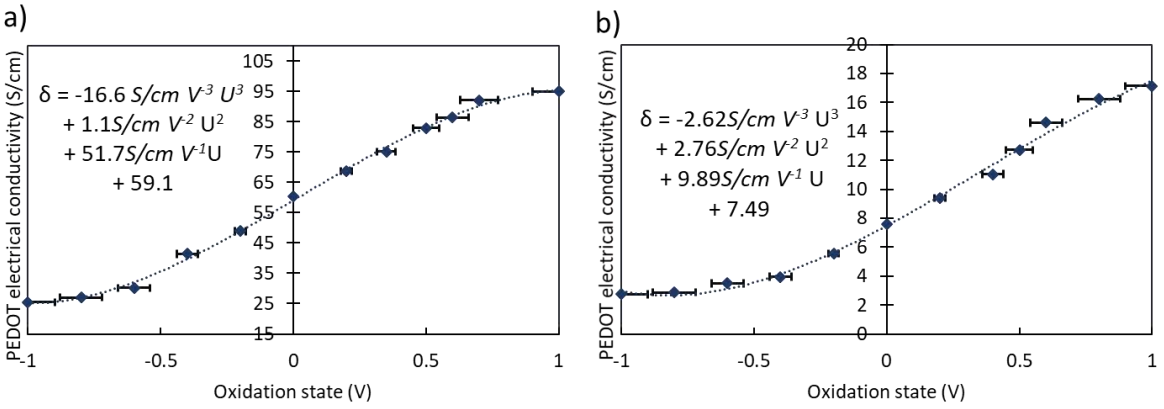


Fig. 6. PEDOT electrical conductivity as a function of oxidation state: a) on the bottom PEDOT surface of the trilayer structure, b) on the top PEDOT surface of the trilayer structure

Fig. 6. shows the electrical conductivities of the bottom and the top PEDOT electrodes in a trilayer configuration. At neutral state (the applied voltage U = 0 V), the electronic conductivity of the bottom PEDOT layer is 59 S/cm, which is comparable to 200 S/cm obtaining for a single PEDOT described in chapter 2 (section 2.4). As expected, the electrical conductivity drops markedly - by a factor of 5 (Fig. 6a) and 9 (Fig. 6b) in this case - as the PEDOT electrodes approach their reduced states (-1 V) from their oxidized states (1 V). This dropping value is smaller in comparison to the value reported by Farajollahi *et al.* [14] (dropped by factor of 24) for a 35 µm thick of PEDOT electrode in a 240 µm thick of trilayer actuator. This change fits a third order function, which will later be used in the model. The electrical conductivity of the bottom PEDOT electrode is about eight times higher than that of the top PEDOT electrode, confirming the asymmetry of the top and the bottom electrodes. This asymmetry stems from the actuator fabrication process, which is based on the layer-by-layer method, where the bottom PEDOT layer in contact with a silicon wafer has a smoother surface and a longer heat treatment period, while the top PEDOT layer formed on the NBR/PEO surface is rougher and treated for a shorter period.

3.2.3 Volumetric capacitance of the PEDOT electrodes

The volumetric capacitance describes the amount of charge per volume of electrode that is stored in response to a change of applied voltage. It also describes the ability to accommodate ions of the conducting polymer film during its actuation, since all electronic charge is balanced by ionic charge. Researchers have recently tried to determine the volumetric capacitance of pure PEDOT or PEDOT:PSS thin films [15, 16]. They found that this capacitance not only depends on the thickness and the density of PEDOT - determined by the VPP time and the coating speed - but also on the type of dopant, as smaller dopants increase the volumetric capacitance to a certain extent. In addition, Madden *et al.* [17, 18] have demonstrated a variation in the volumetric capacitance value of the polypyrrole as a function of applied voltage. Since the trilayer structure works as an actuator, a variation in the applied voltage is expected. For our measurement, the working electrode in Fig. 5 was connected to both electrodes of the trilayer actuator using platinum clamps and then fully immersed in EMImTFSI. The dimensions of the trilayer are *length (L) x width (b) x total thickness (h) = 5 mm x 1 mm x 0.017 mm* in the swollen state, and the thickness of each layer is $h_P = 3.5\ \mu m$ *and* $h_S = 10\ \mu m$.

In the first experiment, the volumetric capacitance of the PEDOT electrodes was investigated as a function of the scanning rate while the potential window was held constant. The potential was swept from U_1 = -0.6 V to U_2 = 0.7 V vs. Ag/AgCl reference electrode at scan rates, ϑ, varying from 0.005 V/s to 1 V/s (Fig. 7a). This potential window is carefully chosen to cover the oxidation and reduction peaks of the PEDOT electrodes during the redox process, but not

too high to accelerate other reactions due to the presence of impurity substances inside ionic liquid.

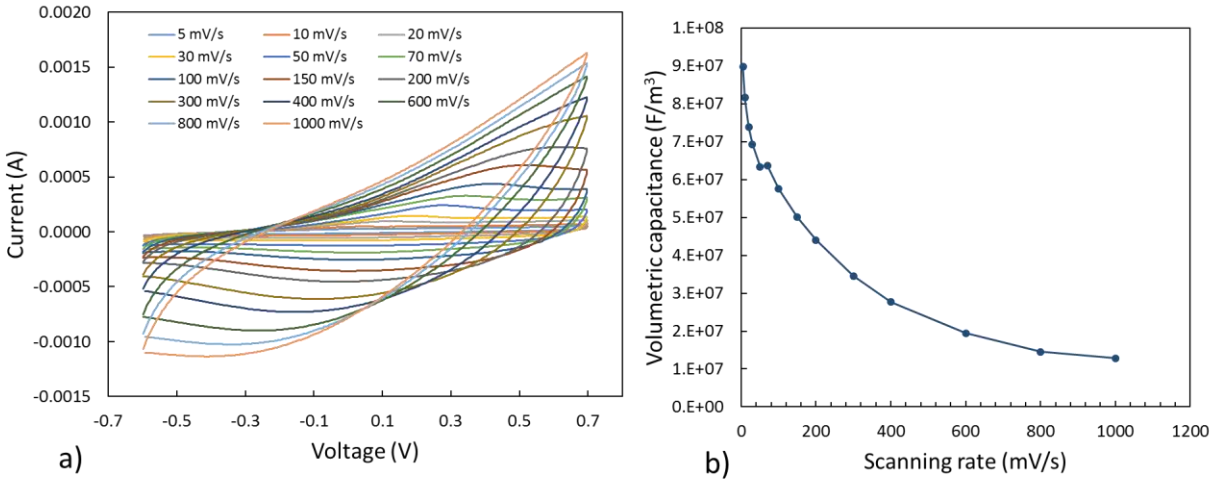


Fig. 7. a) Cyclic voltammograms of PEDOT electrodes obtained in neat EMImTFSI within a potential window of -0.6 V to +0.7 V with different scan rates: b) Volumetric capacitance of PEDOT electrodes as function of the scanning rate.

The effective capacitance was derived from the expression [19]:

$$C_{PEDOT} = \frac{\int_{U_1}^{U_2} i(U)dU}{\vartheta(U_2 - U_1)} \text{ (F)} \qquad (1)$$

Effective volumetric capacitance was calculated from:

$$C_V = \frac{C_{PEDOT}}{2Lbh_P} \text{ (F/m}^3\text{)} \qquad (2)$$

Here, h_P is the thickness of the one PEDOT electrode.

As described in Fig. 7b, the accessible volumetric capacitance varies with the scan rate. This value drops gradually from 90x10^6 F/m^3 at low scanning rate of 5 mV/s to 57 x 10^6 F/m^3 at the fairly quick scanning rate of 0.1 V/s. This value decreases steadily to 12 x 10^6 F/m^3 when the scan rate increases to 1 V/s. We attribute the ability of the PEDOT samples in this case to charge relatively rapidly in the presence of PEO pores, enabling faster ion transport [20]. Previous work has shown a value of volumetric capacitance of 145 x 10^6 F/m^3 for PEDOT-paper [5], between 49 x 10^6 F/m^3 and 67.3 x 10^6 F/m^3 for PEDOT:PSS [6], and 1 x 10^8 F/m^3 [14] for the PEDOT electrodes in a thick trilayer actuator. They have also observed a decrease in this capacitance value with an increasing scan rate. Fig. 8b suggests that the volumetric capacitance is still increasing as scan rate is decreasing, which could be due to long time constants associated with ion insertion. In my study, the volumetric capacitance measurement was conducted at even lower scanning rate of 0.5 mV/s, 1 mV/s, and 2 mV/s.

However, at these extremely low scan rates, the Pt clamp which is used to hold the trilayer as the working electrode and the surface of the PEDOT electrodes also provide an apparent capacitance behavior (another possibility to explain this increase is detailed in Appendix A.3.1). This apparent capacitance is significant compared to that of PEDOT electrodes making estimates of PEDOT volumetric capacitance difficult at these low scan rates.

In a second experiment, the potential window was varied from 0.5 Vpp to 3.3 Vpp while the scanning rate is held at 20 mV/s, as depicted in Fig. 8.

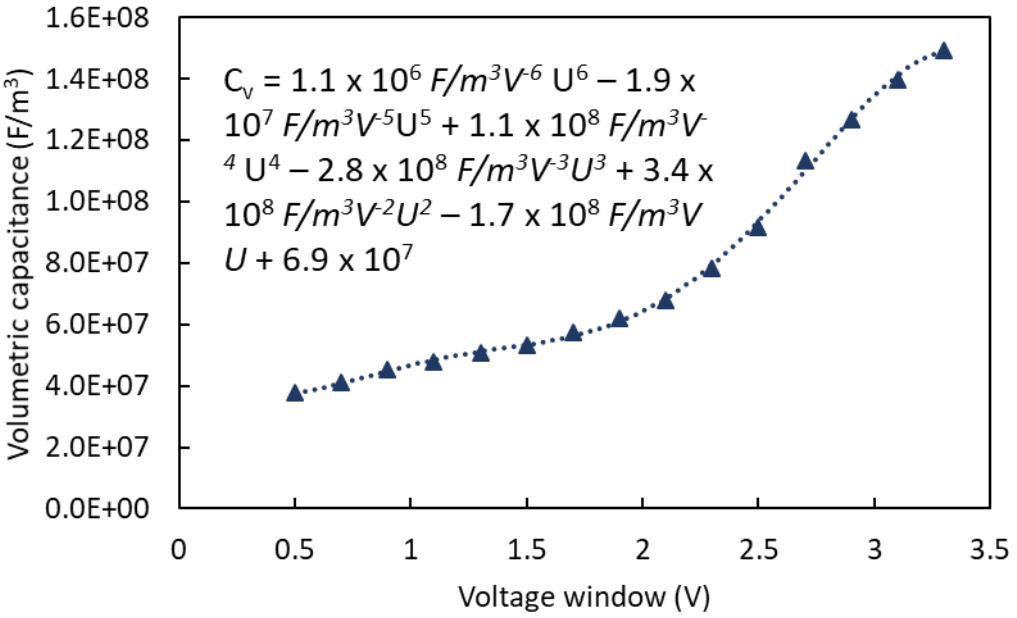


Fig. 8. Volumetric capacitance as a function of the voltage window from 0.5 Vpp to 3.3 Vpp.

As can be seen in Fig. 8, the volumetric capacitance increases gradually when the potential window increases from 0.5 Vpp to 2.2 Vpp. One way of picturing this enlargement is, as the voltage increases, more and more holes or electrons are created in or supplied to the PEDOT backbone chain leading to a gain in the number of ions inserted or extracted. This increment approaches a state of complete oxidation (or reduction) state as the voltage window reaches to 2.2 Vpp. The first possible contribution to this dependent is that at the oxidation state is extreme at a specific potential indicating by a positive peak potential during the cyclic voltammetry. Below this potential, the PEDOT electrodes are not fully oxidized and the volumetric capacitance is small. When the potential goes beyond this potential, the volumetric capacitance increases at higher speed.

Another possible explanation for this increment comes from the complex structure of PEDOT/PEO electrodes, which contains PEDOT chains with different length. At low potential, only long chains of PEDOT are oxidized while a larger voltage window will oxidize both long and shorter chains. This results in a higher volumetric capacitance.

The dependence of the volumetric capacitance on the potential window is approximated by a high order function. The order is continuously added until the resulting function fits within experimental uncertainty and the following sixth-order function is obtained:

$$C_V = 1.1 \times 10^6 F/m^3 V^{-6} U^6 - 1.9 \times 10^7 F/m^3 V^{-5} U^5 + 1.1 \times 10^8 F/m^3 V^{-4} U^4 - 2.8 \times 10^8 F/m^3 V^{-3} U^3 + 3.4 \times 10^8 F/m^3 V^{-2} U^2 - 1.7 \times 10^8 F/m^3 V^{-1} U + 6.9 \times 10^7 \ (F/m^3). \quad (3)$$

It is worth of noticing that this approximated function is only valid for the value of voltage staying in the range of the potential window from 0.5 Vpp to 3.3 Vpp. A capacitance value between two measured voltage window values can be interpolated from the equation (3). The values are averaged over the potential range, and take into account changes in both electrodes simultaneously.

To our knowledge, the voltage dependence of the specific capacitance of PEDOT material has not been reported yet. However, this voltage dependence of other supercapacitor materials such as manganese oxide/activated carbon in 2 mol/L KNO_3 electrolyte has already been studied [21] showing an increase in the capacitance as the operating voltage increases. Equation (3) is to some extent agreed with the trend observed by Stoller [21].

The volumetric capacitance allows the extent of charge transferred to be estimated, since its value is proportional to total charge transferred and the actuator volume. Along with the resistance, the total capacitance also determines the rate of charging and the rate of actuation. When multiplied by internal resistance, this *RC* product gives an estimate of response time of the actuator – which will be investigated in the chapter 4, section 4.3.

3.2.4 Possible short circuit between two PEDOT layers

To investigate the possible short circuit between two PEDOT electrodes, an input step voltage of *Upp* = 2 V, *f* = 0.005 Hz was applied to the trilayer actuator using a potentiostat with two-electrodes connected. As shown in Fig. 9, at this low frequency the response current at first reaches a peak and then quickly decays as the redox reactions in the electrodes is completed and the actuation approaches its maximum bending state. The current is expected to decrease to zero, which means no current passes through the trilayer. However, in this case a small current (-15.75 µA) is still observed after 100 s. When the voltage is switched to the other direction, the similar trend of the current is shown and the leakage current is 16.67 µA.

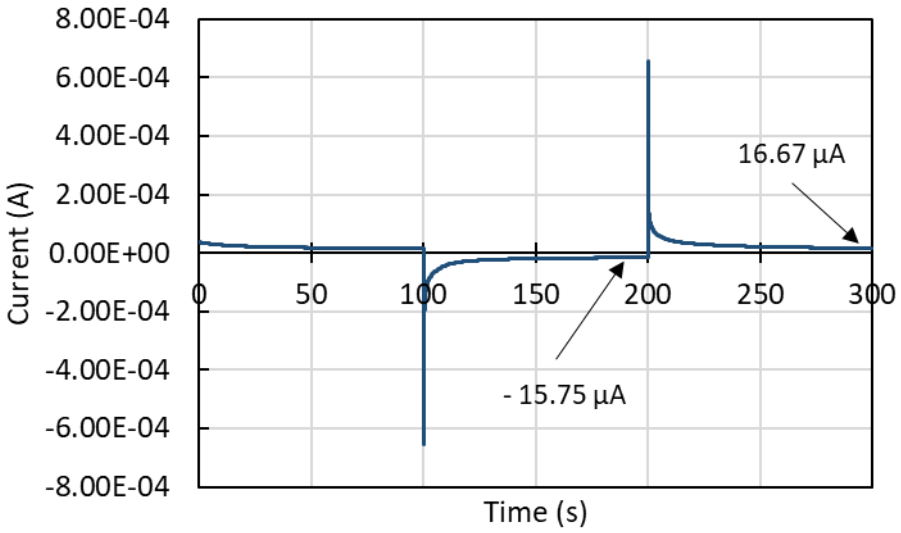


Fig. 9. The current response to an input step voltage at low frequency (f = 0.005 Hz)

A rough estimation on the short resistance of the trilayer gives: $R_{short} = \frac{U_{pp}}{i_{leak}} = \frac{2}{16\times10^{-6}} \approx 124\ k\Omega$. The leakage per area is then equal to: $R = \frac{R_{short}}{A} = \frac{62\times10^{3}\Omega}{(3\times2+5\times1)cm^{2}} = 11.2\ k\Omega/cm^{2}$, where *A* is the total area of the actuator, including the rectangular shape (*3 x 2* mm) fitting in the clamping area and the beam area (*5 x 1* mm). The thickness of the trilayer tested was 17 µm.

3.3 Mechanical properties

In this section, the Young's moduli of the SPE layer alone and of the trilayer actuator as a function of the oxidation state were measured in a swollen state.

3.3.1 Young's moduli of the SPE layer and of the trilayer actuator

A specimen of the SPE layer with the following dimensions of *length (L) x width (b) x thickness (h_S) = 10 mm x 6 mm x 0.07 mm* was tested using a Bose Electroforce 3000 dynamic mechanical analyzer. Both ends of this thin film are attached using the Bose Electroforce 3000 dynamic mechanical analyzer. Then, a longitudinal displacement at a rate of 0.1 mm/s is applied to the NBR/PEO sample and the force is recorded.

The relationship between the force *F* and the displacement *ΔL* gives a Young's modulus E_{SPE} for the SPE material of $E_{SPE} = \frac{F}{\Delta L}\frac{L}{bh_s} = 329 \pm 50\ kPa$. This value is consistent with the value reported by Festin [22] and Woehling [23] for the same type of material.

It must be recalled that Bahrami-Samani and Spinks [24, 25] have shown changes in shear modulus of a polypyrrole thin films at various applied potentials, whereas Farajollahi [4] also demonstrated the dependence of the Young's modulus of a penetrated PEDOT layer on the

applied voltage. Consequently, we have decided to measure the variation of the Young's modulus of trilayer actuators versus the applied voltage. The trilayer actuator (*length (L) x width (b) x thickness (h_t) = 10 mm x 6 mm x 0.017 mm*) was subjected a Bose Electroforce 3000 dynamic mechanical analyzer and a potentiostat.

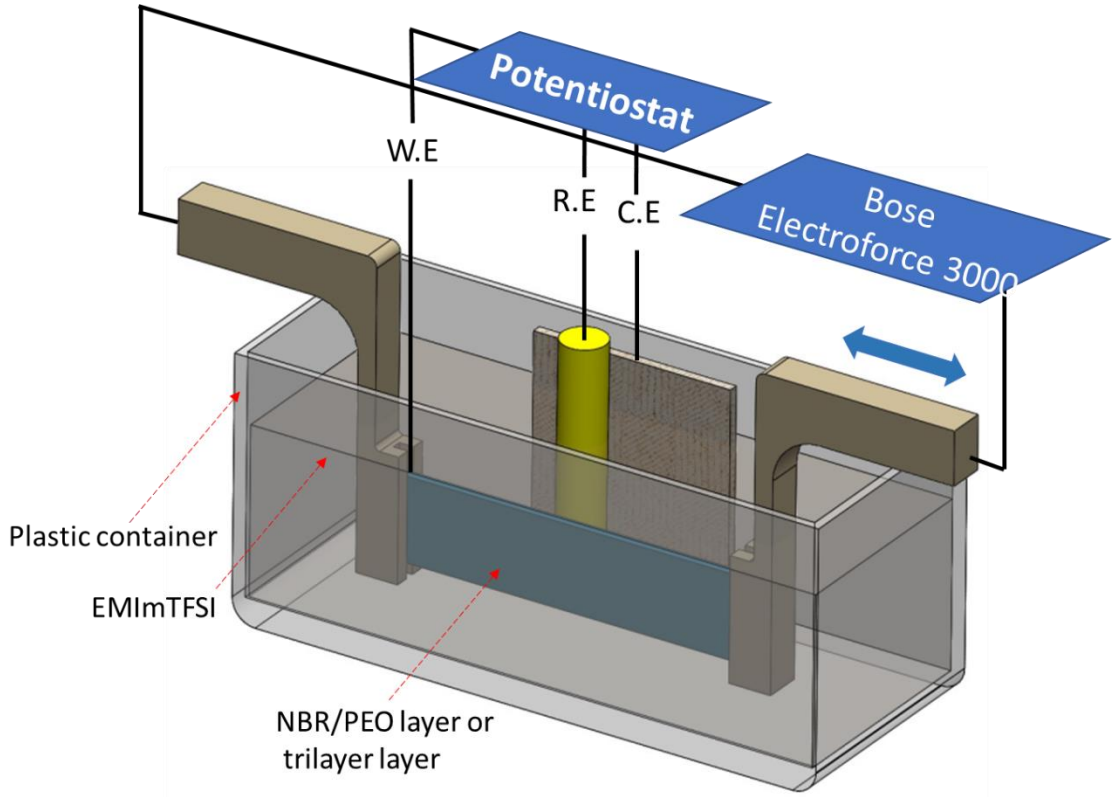


Fig. 10. Young's moduli of the NBR-PEO layer alone - and of a trilayer structure as a function of oxidation state - were measured using a Bose Electroforce 3000 dynamic mechanical analyzer

Fig. 10 describes the experimental setup used to measure the Young's moduli of the trilayer structure under voltage excitation, in a swollen state. The trilayer actuator is held in a Bose Electroforce 3000 dynamic mechanical analyzer using a platinum clamp at one end and a plastic clamp at the other end. The clamps and the trilayer actuator were immersed in EMImTFSI ionic liquid. Different positive and negative potentials (vs. Ag/AgCl reference electrode) (± 1.5, ± 1, ± 0.5 V) were applied to the specimens to oxidize or reduce the both PEDOT electrode at the same time. After applying a voltage, the open circuit potential (vs. Ag/AgCl) was measured to confirm the trilayer reached the desired voltage. The trilayer was then subjected to a controlled displacement/load. The Young's modulus was determined from the slope of the force/displacement curve and the dimensions of the specimen. The advantage of this experimental setup is that the Young's modulus measurement can be immediately performed after the trilayer reaches its oxidized (or reduced) state. Consequently, the measurement can be carried out at low (-1.5 V) or high (1.5 V) potential without an issue of the fast decaying voltage of the sample.

The Young's moduli of the trilayer actuators are measured and the Young's moduli of the PEDOT layer is deduced in Fig. 7.

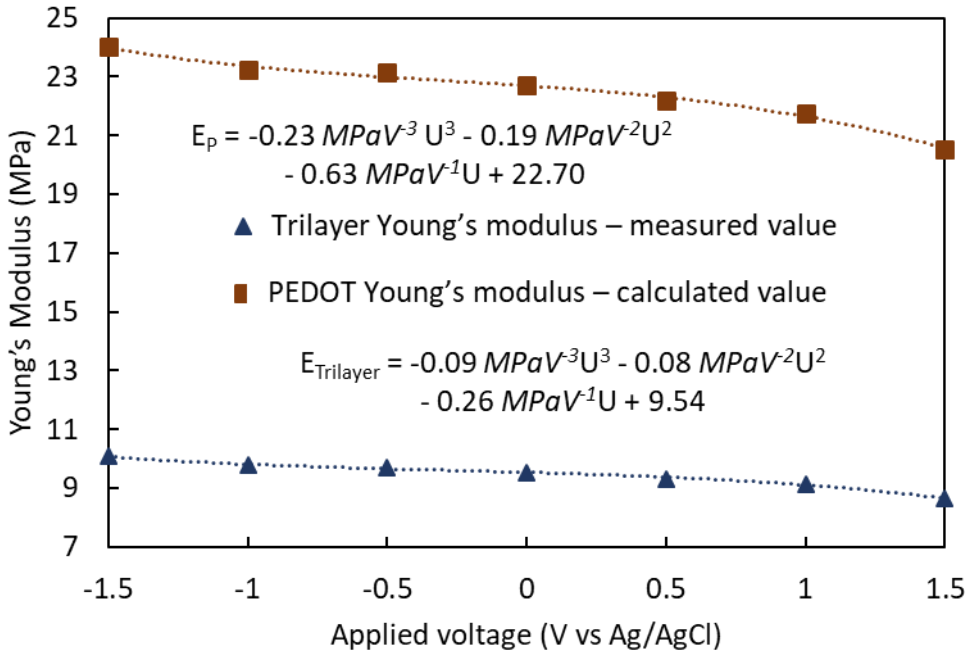


Fig. 11. Young's modulus of the trilayer actuator and the PEDOT layer as a function of applied voltage.

From the SPE Young's modulus and the trilayer Young's modulus, the Young's modulus of the PEDOT electrodes can be derived from the following equation [26] $E_P = \frac{(E_t h_t - E_S h_S)}{2h_P}$ (h_t, h_S, and h_P are the total thickness of the trilayer, the thickness of the NBR/PEO, and the thickness of PEDOT electrode, respectively) and plotted on the same graph in Fig. 11. As we can see, the Young's modulus of both the trilayer and the PEDOT layer decreases slightly by 14 % from 10 MPa to 8.6 MPa and from 24.0 MPa to 20.5 MPa, respectively, when they are switched from reduced state (- 1.5 V) to oxidized state (1.5 V).

A possible explanation for this reduction in modulus with increasing potential comes from the ion insertion and extraction from the PEDOT electrodes. A negative potential initiates a reduction of the polymer, leading to an insertion of EMI^+ cations into PEDOT electrodes. These ions balance the charge of the largely immobile $TFSI^-$ ions present in the matrix. This reduction may induce a tight coupling between the PEDOT chains and would account for the increase in Young's modulus at negative potentials. In contrast, a positive potential may increase the separation between the PEDOT chains and reduce the force between them leading to a decrease in Young's modulus. The observation here is consistent with the results reported by Zheng [27] and Shoa [28]. In addition, this percentage reduction is quite consistent with the value reported by Farajollahi [4].

3.3.2 Damping ratio

In the mechanical model, the natural frequency and damping coefficient are useful for determining response at frequencies where inertia is important. These were determined using a vibration experiment. In this experiment, the actuator was fixed at one end and free at the other end. This actuator was then deflected using a 3 axis motorized stage with a mounted by a force/displacement sensor (FT-RS1002 Microrobotic System, three degrees of freedom, maximum speed: 5 mm/s coupled with an FT-S100 microforce sensing probe with a measurement range of ±100 µN, resolution: 5 nN) and quickly released for free vibration. Oscillation was measured directly using a Keyence laser sensor (Keyence LK-G32, measurement range: ±4.5 mm, resolution: 0.05 µm), shown in Fig. 12.

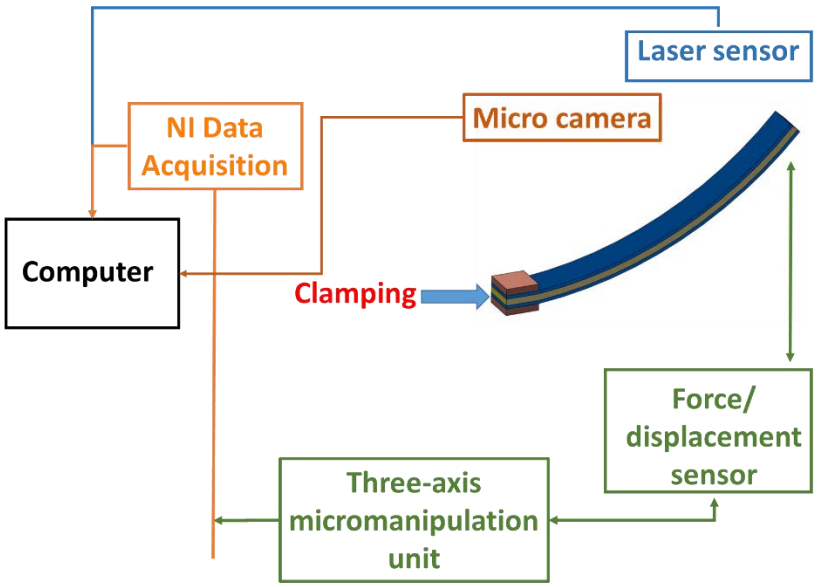


Fig. 12. Experimental setup to measure the damping ratio of the trilayer actuator and the blocking force

Damped oscillation is shown in Fig. 13.

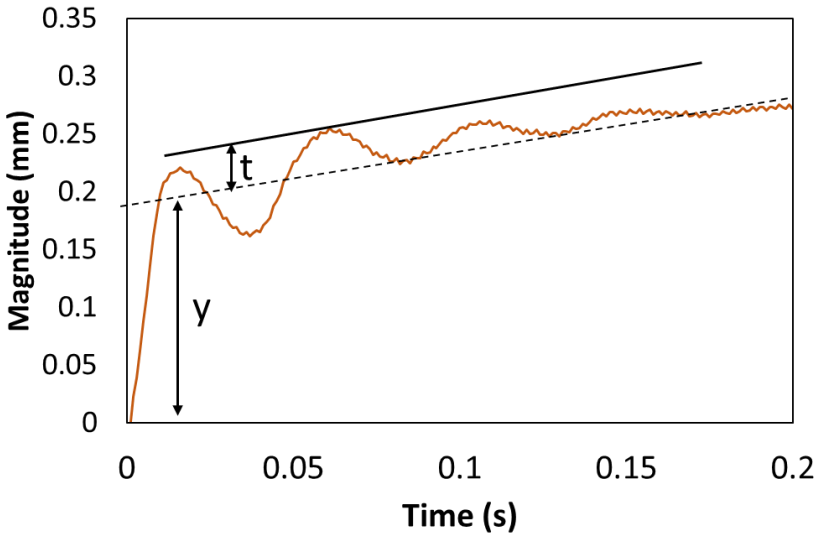


Fig. 13. Beam vibrating as function of time.

This response suggests that the actuator is well represented as a second-order system [29]. After subtracting the damping coefficient was calculated using the formula below:

$$\zeta = \frac{1}{\sqrt{\left(\frac{\pi}{ln\left(\frac{t}{y}\right)}\right)^2 + 1}} = 0.39 \quad , \tag{4}$$

where *t* is overshoot amplitude, which is the distance from middle line of sinusoidal part to highest peak and *y* is total displacement. There may be a second, longer time response, given the longer rise time to steady state. This was not included in the model.

3.3.3 Blocking force characterization

The force generated at the tips of the actuator of *length x width x thickness: 6 mm x 1 mm x 0.017 mm* at various magnitudes and frequencies of a square wave applied voltage were conducted using the setup described in Fig. 13, where the clamping is connected to a source of voltage.

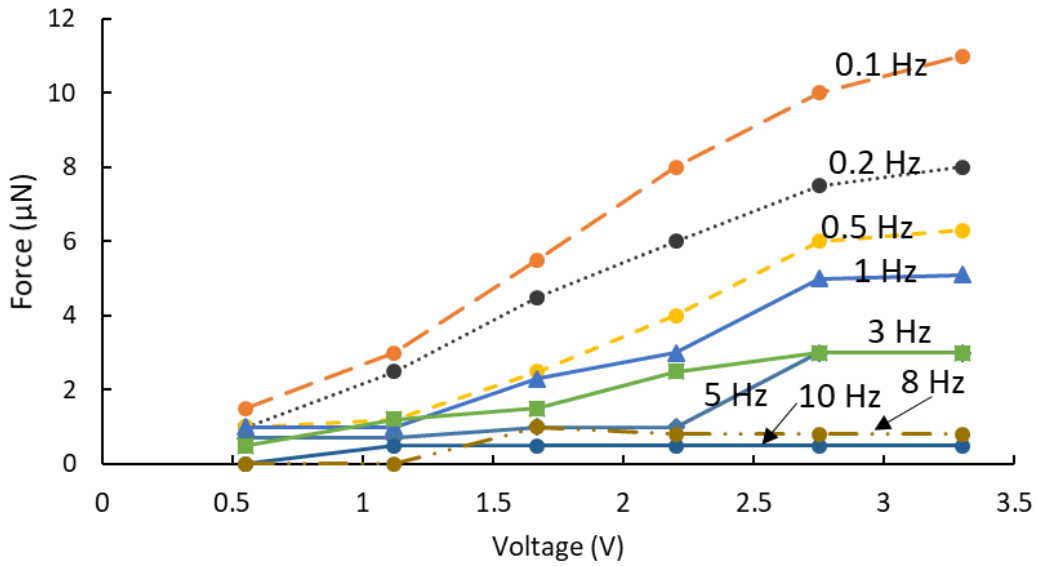


Fig. 14. Force generated as a function of the magnitude and the frequency of the applied voltage from a trilayer actuator of length x width x thickness: 6 mm x 1 mm x 0.017 mm.

Fig. 14 shows an upward trend in the force generated at the tip of the beam as the applied voltage is raised. This force decreases when the frequency increases. The blocking force can be calculated as the following equation [30]: $F = \frac{E_P \alpha \rho}{L} b \left(\frac{h_S}{2}\right)^2 \left[\left(1 + \frac{2h_P}{h_S}\right)^2 - 1\right]$, where $\rho = \frac{Q}{2Lbh_P}$ is the charge density. All the parameters in this equation are assumed to be constant except for the total charge Q is a function of time. A high frequency gives a small value of charge Q and in turn reduces the blocking force F. The force reaches zero or the reading is inaccurate due to background noise when the frequency is 10 Hz. In this experiment, the maximum force obtained at the tip of the trilayer was 11 µN at 0.1 Hz and 3.3 Vpp. It is worth of mentioning that over 2.75 Vpp, the generated force almost reaches saturation despite the increase in voltage, indicating that the two PEDOT electrode layers have been fully oxidized and reduced.

3.4 Empirical strain-to-charge ratio

3.4.1 Strain to charge ratio

The coupling effect between strain and charge was first proposed by Baughman *et al.* [31] to describe the change in polyacetylene thin film length corresponding to the insertion of ions. Della Santa [32] and Madden [18] suggest a strain-to-charge ratio on the order of 10^{-10} m^3/C for polypyrrole-based CP actuators. In this work, we have determined the strain-to-charge ratio of a PEDOT-based actuator. The experimental setup was to apply a triangular wave voltage to the trilayer actuator allowing actuator to bend at slower speed and then to record the output current and the bending response (Fig. 12).

From the actuator bending data, the strain difference produced by one PEDOT electrode (ε_{actual}) can be derived via the following equation $\varepsilon_{actual}\ (t)\% = \frac{h_t}{2}\left(\frac{1}{r_t(t)} - \frac{1}{r_0}\right)$, where r_0 and r_t are the radius of the actuator in neutral and stimulated state, respectively, and h_t is the thickness of the trilayer actuator. Fig. 15 gives an example of how r_0 and r_t are obtained from the bending measurement.

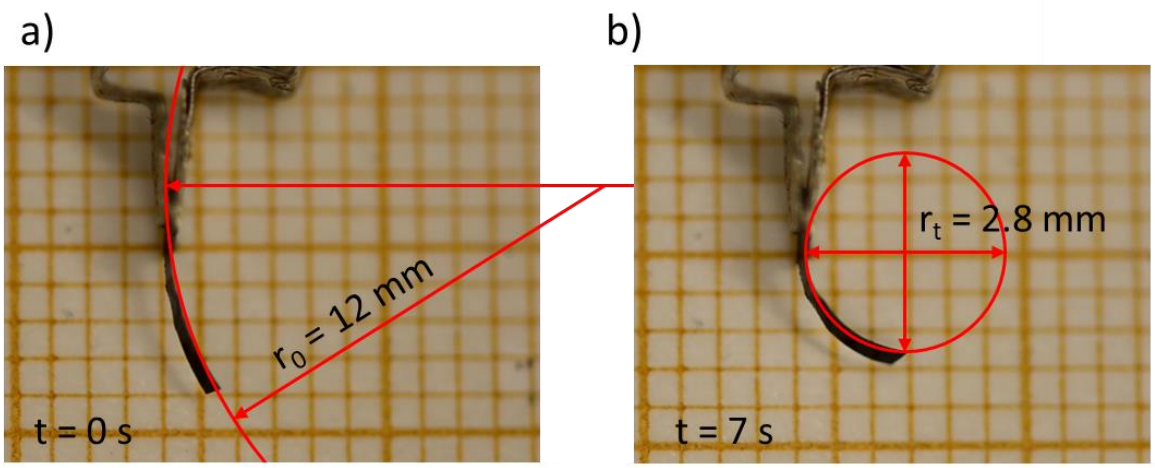


Fig. 15. Actuator at the a) neutral state where the bending radius is equal r_0 = 12 mm, and b) excited state where the bending radius is r_t = 2.8 mm. The orange square on the background of the pictures has the dimension of 1 x 1 mm.

Note that the strain difference equation above is used instead of the equation $\varepsilon = \frac{2h_t w}{L^2+w^2}$. The reason for this is that the latter is only valid for the case where the actuator is straight at its initial position and is symmetrically bent under a voltage excitation. In our case, since the actuator is initially curved, the resulting strain difference can be over or under estimated (depending on whether the trilayer is initially bent with the same or the opposing curvature).

From this bending strain, the active strain of the PEDOT electrode, which is the linear strain of a single PEDOT layer, is derived as following equation [33]:

$$\varepsilon_{active}\ (t) = \varepsilon_{actual}\ (t) \times \frac{h_P\left(h^4E^2+8h^3E+12h^2E+8hE+24h+12E^2+16\right)}{6h_t(h+1)(hE+2)} = 1.61 \times \varepsilon_{actual}\ (t), \quad (5)$$

where $h = \frac{h_S}{h_P}$ and $E = \frac{E_S}{E_P}$. An error bar of 5 % obtained from the bending strain measurements has been added.

Moreover, the volumetric charge density ($\Delta Q(t)/V_{PEDOT}$, where V_{PEDOT} is the one PEDOT electrode volume) (Fig. 17), resulting from the total insertion or extraction of ions per volume, is calculated by integrating the current over time (Fig. 17).

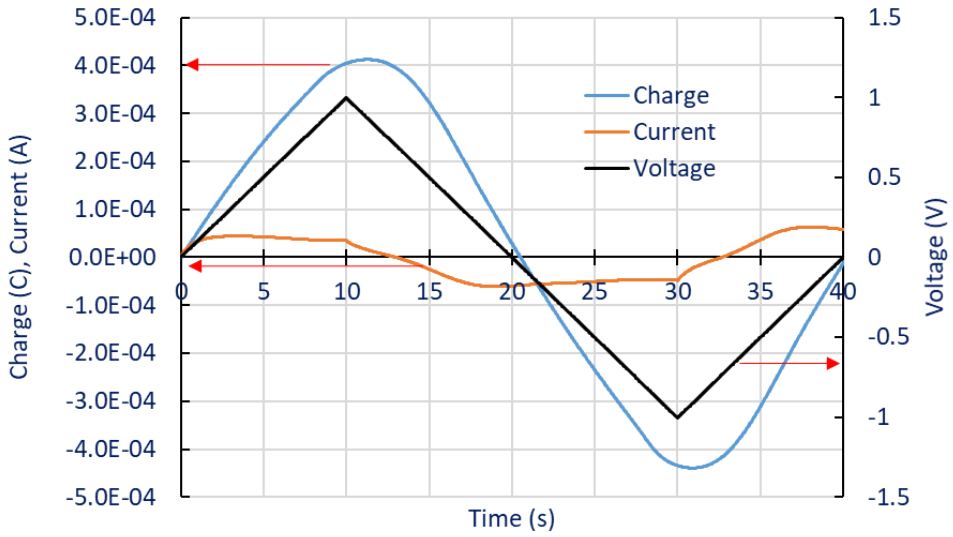


Figure 16. Current and charge response to a triangular input voltage.

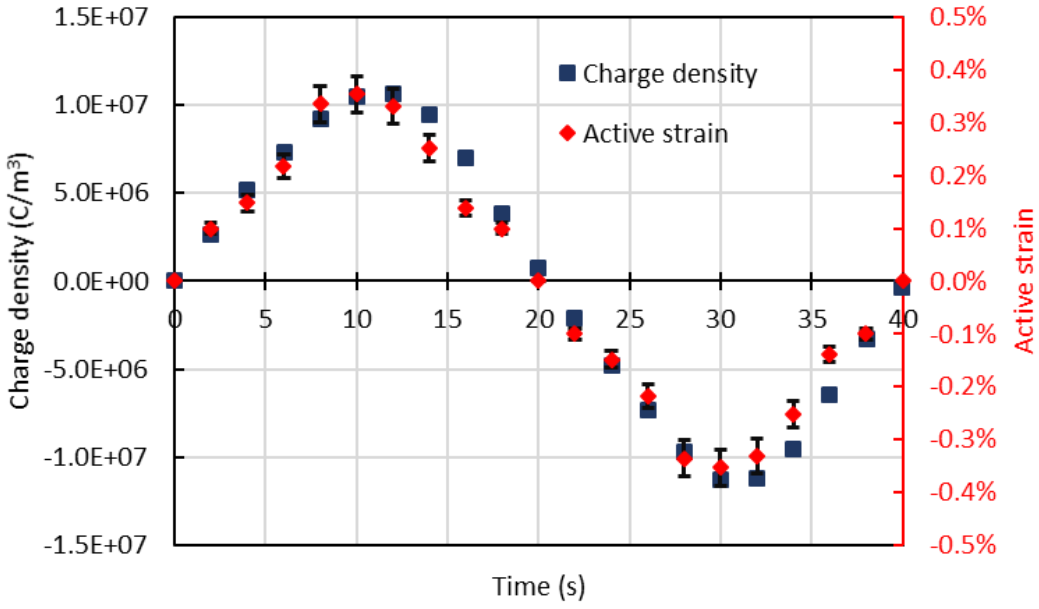


Fig. 17. Charge density and strain of the trilayer actuator as a function of time under a triangular wave voltage excitation

The strain-to-charge ratio is finally obtained by the ratio: $\alpha = \frac{\varepsilon_{active}(t)V}{\Delta Q(t)}$. The Fig. 17 shows a quite constant ratio of the active strain to charge density giving a constant value of the train-to-charge of 3.6 ± 0.5 x 10^{-10} (m^3/C). The value is in the same range as other measurements made in polypyrrole and PEDOT, as summarized in table 2. The strain to charge ratio will be used in the model developed in Chapter 4.

Table 2. Summary strain-to-charge ratio for different materials and actuator configuration

Material	Structure	Dopant	Solution	Strain-to-charge ratio value (m^3C^{-1}) x 10^{-10}	
PPy	linear actuator	DBS^-	NaDBS	1.7	[18]
		PF_6^-	$(C_2H_5)_4NPF_6$	5.3	[18]
		BS^-	NaBS	0.3	[32]
	trilayer	$TFSI^-$	LiTFSI	5	[34]
		PF_6^-	$TBAPF_6$	19.4	[35]
PEDOT	a single layer				
	a trilayer	$TFSI^-$	EMITFSI	2 - 4.56	[36, 37]
		$TFSI^-$	LiTFSI	1.7 - 12	[37, 38]

DBS = Dodecylbenzene sulfonate, TBA: tetrabutylammonium, PF_6: hexafluorophosphate

3.4.2 Linear strain

The relationship between the linear strain and the strain difference of the actuator is shown in equation (5). In this section, the linear strain of the trilayer actuator is investigated by applying a step voltage to a trilayer specimen to confirm this established relation. The trilayer actuator (*length (L) x width (b) x thickness (h_t) = 10 mm x 6 mm x 0.017 mm – this length is the part of the beam between clamps*) was subjected a prestress of 1.5 gf by the Bose Electroforce 3000 dynamic mechanical analyzer. This constant load is applied to one end of the beam, corresponding to a stress of 0.15 MPa, to keep the beam straight in the ionic liquid, as described in Fig. 10. A step voltage of 2 Vpp vs. Ag/AgCl at f = 0.001 Hz was then applied to both electrodes of the trilayer actuator. The uniaxial deformation of the beam was then recorded as in Fig. 18. L_2 and L_1 are the length of the beam in its expanding and shrinking state, respectively. A rough estimation gives us the value of linear strain of the trilayer actuator $\varepsilon_{active} \approx \frac{0.1mm}{10mm} = 1\%$, which is higher than the strain difference (0.56 %) between two PEDOT electrodes obtaining in the previous section. Given the relation between the linear strain and the strain difference is $\varepsilon_{active}\ (t) = 1.61 \times \varepsilon_{actual}\ (t)$, this fits quite well with the experimental results here: $1\% \approx 1.61 \times 0.56\%$

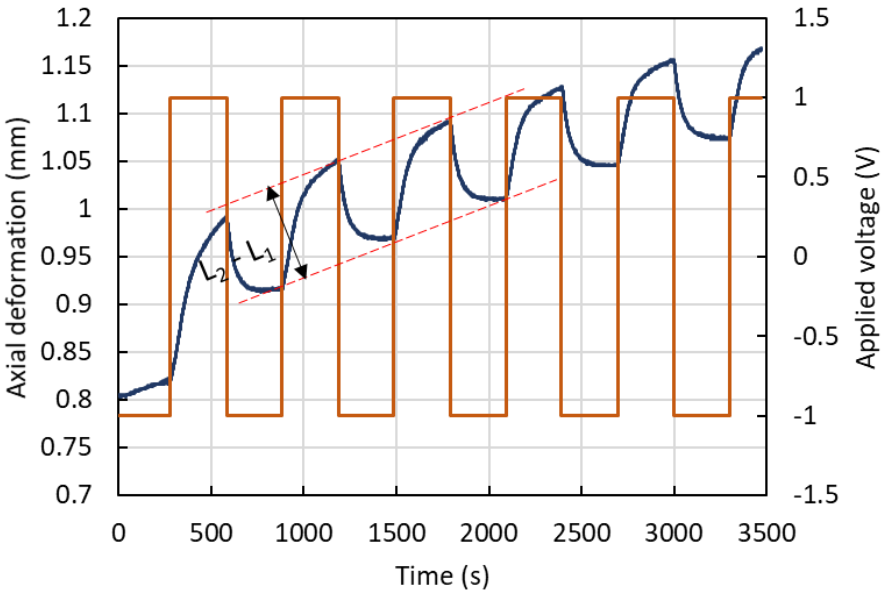


Fig. 18. Uniaxial deformation of the trilayer actuator under a step voltage

3.5 Conclusion

In this chapter, the new electrochemomechanical system has been characterized. Its electrochemical properties including the ionic conductivity of the PEDOT electrodes and SPE layer, the PEDOT electronic conductivity as a function of oxidation state, and the dependent PEDOT's volumetric capacitance on the potential window and the scanning rate were all study. In addition, the mechanical properties such as Young's modulus of the PEDOT as a function of the oxidation state, Young's modulus of the SPE layer, the damping ratio were also measured. Finally, the coupling between the electrochemical and the mechanical representing via an empirical strain-to-charge ratio was determined.

Table 3 Summary of measured parameters of the ultrathin trilayer actuator

PEDOT electrodes electrical conductivity (S/cm)	Top PEDOT electrode: $-2.62U^3 + 2.76U^2 + 9.89U + 7.49$ Bottom PEDOT electrode: $-16.6U^3 + 1.1U^2 + 51.7U + 59.1$
PEDOT electrodes ionic conductivity (S/m)	Top PEDOT electrode: 0.025 Bottom PEDOT electrode: 0.030
PEDOT electrodes' volumetric capacitance (F/m³)	$1.1 \times 10^6 U^6 - 1.9 \times 10^7 U^5 + 1.1 \times 10^8 U^4 - 2.8\ 10^8 U^3 + 3.4 \times 10^8 U^2 - 1.7 \times 10^8 U + 6.9 \times 10^7$
NBR/PEO ionic conductivity (S/m)	0.038
Strain-to-charge ratio (m³/C)	$\alpha = 3.6 \pm 0.5 \times 10^{-10}$
NBR/PEO Young's modulus (kPa)	329 ± 50
Trilayer actuator Young's modulus (MPa)	$-0.09U^3 - 0.08U^2 - 0.26U + 9.54$
PEDOT Young's modulus (MPa)	$-0.23U^3 - 0.19U^2 - 0.63U + 22.70$
Damping ratio	0.39
Beam density (kg/m³)	2000
Maximum strain difference (%)	0.56
Linear strain (%)	1

Table 3 summarizes the critical electrical, electrochemical, and mechanical properties of the trilayer actuators. These obtained values allow to evaluate the non-linear dynamic model established and will be discussed in the next chapter.

Besides, these obtained parameters provide us an inside on the physical structure of the system and the working mechanism of the actuator. Most important, the key factors affecting

actuation behavior are all determined providing us a best guideline to improve actuator's performance.

In the future perspective, there are different key points needed to be improve. At first, to study the optimum thickness of the PEDOT electrodes providing highest bending strain output, we have varied the PEDOT electrode thickness in the trilayer configuration from 0.8 µm to 2.7 µm by changing the rotational speed of depositing the oxidant solution of the spin coater from 3500 rpm to 1000 rpm, while the thickness of the SPE layer is constant at 7 µm. However, the strain measurement showed only four out of ten samples were working, where each sample is taken from one wafer. And the strain measurement is processed on the sample with the total thickness of 17 µm. Nevertheless, emerging work is required to improve the reproducibility of the fabrication process.

Moreover, the properties of the PEDOT and the SPE layers have been measured, however, each property was investigated on one specific thickness of the sample. Though, there is a need to confirm the obtained value by remeasuring on various thickness.

In addition, the unwanted asymmetric property between the top and the bottom PEDOT in the electronic conductivity measurement can be reduced by adjusting the heat treatment period during the fabrication of top bilayer and bottom bilayer.

[1] J.D. Madden, P.G. Madden, I.W. Hunter, Polypyrrole actuators: modeling and performance, 2001, pp. 72-83.
[2] B.J. Feldman, P. Burgmayer, R.W. Murray, The potential dependence of electrical conductivity and chemical charge storage of poly(pyrrole) films on electrodes, Journal of the American Chemical Society, 107(1985) 872-8.
[3] M.R. Warren, J.D. Madden, A structural, electronic and electrochemical study of polypyrrole as a function of oxidation state, Synthetic Metals, 156(2006) 724-30.
[4] F. Meisam, S. Farrokh, N. Naser, F. Adelyne, P. Cédric, T.M.N. Giao, V. Frédéric, D.W.M. John, Characterization and dynamic charge dependent modeling of conducting polymer trilayer bending, Smart Materials and Structures, 25(2016) 115044.
[5] J.A. Lee, M.K. Shin, S.H. Kim, H.U. Cho, G.M. Spinks, G.G. Wallace, M.D. Lima, X. Lepró, M.E. Kozlov, R.H. Baughman, S.J. Kim, Ultrafast charge and discharge biscrolled yarn supercapacitors for textiles and microdevices, Nature Communications, 4(2013) 1970.
[6] Y. Liu, B. Weng, J.M. Razal, Q. Xu, C. Zhao, Y. Hou, S. Seyedin, R. Jalili, G.G. Wallace, J. Chen, High-Performance Flexible All-Solid-State Supercapacitor from Large Free-Standing Graphene-PEDOT/PSS Films, Scientific Reports, 5(2015) 17045.
[7] G. Alici, P. Metz, G.M. Spinks, A mathematical model to describe bending mechanics of polypyrrole (PPy) actuators, Proceedings, 2005 IEEE/ASME International Conference on Advanced Intelligent Mechatronics2005, pp. 1029-34.
[8] Y. Dobashi, A. Fannir, M. Farajollahi, A. Mahmoudzadeh, A. Usgaocar, D. Yao, G.T.M. Nguyen, C. Plesse, F. Vidal, J.D.W. Madden, Ion Transport in Polymer Composites with Non-Uniform Distributions of Electronic Conductors, Electrochimica Acta, 247(2017) 149-62.
[9] D.S. Yoo, A. Mahmoudzadeh, E.C.W. Fok, K. Walus, J.D.W. Madden, Multiple time constant modelling of a printed conducting polymer electrode, Electrochimica Acta, 56(2011) 4711-6.
[10] T.N. Nguyen, K. Rohtlaid, C. Plesse, G.T.M. Nguyen, C. Soyer, S. Grondel, E. Cattan, J.D.W. Madden, F. Vidal, Ultrathin electrochemically driven conducting polymer actuators: fabrication and electrochemomechanical characterization, Electrochimica Acta, 265(2018) 670-80.
[11] D. Mecerreyes, Applications of Ionic Liquids in Polymer Science and Technology, Berlin: Springer; 2015.
[12] G. Petroffe, L. Beouch, S. Cantin, P.-H. Aubert, C. Plesse, J.-P. Dudon, F. Vidal, C. Chevrot, Investigations of ionic liquids on the infrared electroreflective properties of poly(3,4-ethylenedioxythiophene), Solar Energy Materials and Solar Cells, 177(2018) 23-31.
[13] A. Maziz, C. Plesse, C. Soyer, C. Chevrot, D. Teyssié, E. Cattan, F. Vidal, Demonstrating kHz Frequency Actuation for Conducting Polymer Microactuators, Advanced Functional Materials, 24(2014) 4851-9.
[14] M. Farajollahi, Fabrication and non-linear modeling of conducting polymer-based actuators : toward catheter and tactile display applications: University of British Columbia; 2016.
[15] N. Kurra, R. Wang, H.N. Alshareef, All conducting polymer electrodes for asymmetric solid-state supercapacitors, Journal of Materials Chemistry A, 3(2015) 7368-74.
[16] C.M. Proctor, J. Rivnay, G.G. Malliaras, Understanding volumetric capacitance in conducting polymers, Journal of Polymer Science Part B: Polymer Physics, 54(2016) 1433-6.
[17] M. Farajollahi, G. Alici, M.S. Sarwar, J.D.W. Madden, Conducting Polymers as EAPs: Physical Description and Simulation, in: F. Carpi (Ed.) Electromechanically Active Polymers: A Concise Reference, Springer International Publishing, Cham, 2016, pp. 353-83.
[18] J.D.W. Madden, Conducting polymer actuators: Massachusetts Institute of Technology; 2000.
[19] M. Ghidiu, M.R. Lukatskaya, M.-Q. Zhao, Y. Gogotsi, M.W. Barsoum, Conductive two-dimensional titanium carbide 'clay' with high volumetric capacitance, Nature, 516(2014) 78.
[20] J. Xi, X. Qiu, J. Li, X. Tang, W. Zhu, L. Chen, PVDF–PEO blends based microporous polymer electrolyte: Effect of PEO on pore configurations and ionic conductivity, Journal of Power Sources, 157(2006) 501-6.

[21] M.D. Stoller, R.S. Ruoff, Best practice methods for determining an electrode material's performance for ultracapacitors, Energy and Environmental Science, 3(2010) 1294-301.
[22] N. Festin, Conducting interpenetrating polymer network actuator sensor for biomimetic perception system: Université de Cergy Pontoise; 2012.
[23] V. Woehling, New Developments in electroactive materials based on electronic conductive polymers : Towards integration into biomedical systems: Université de Cergy Pontoise; 2016.
[24] M. Bahrami-Samani, C.D. Cook, J.D. Madden, G.M. Spinks, P.G. Whitten, Quartz crystal microbalance study of volume changes and modulus shift in electrochemically switched polypyrrole, Thin Solid Films, 516(2008) 2800-7.
[25] G.M. Spinks, L. Liu, G.G. Wallace, D. Zhou, Strain Response from Polypyrrole Actuators under Load, Advanced Functional Materials, 12(2002) 437-40.
[26] G. Alici, B. Mui, C. Cook, Bending modeling and its experimental verification for conducting polymer actuators dedicated to manipulation applications, Sensors and Actuators A: Physical, 126(2006) 396-404.
[27] W. Zheng, Analysis of high performance polypyrrole actuators: University of Wollongong; 2011.
[28] T. Shoa, T. Mirfakhrai, J.D.W. Madden, Electro-stiffening in polypyrrole films: Dependence of Young's modulus on oxidation state, load and frequency, Synthetic Metals, 160(2010) 1280-6.
[29] H. Jack, Engineer On A Disk, 2010.
[30] P.G.A. Madden, Development and Modeling of Conducting Polymer Actuators and the Fabrication of a Conducting Polymer Based Feedback Loop: MASSACHUSETTS INSTITUTE OF TECHNOLOGY; 2003.
[31] R.H. Baughman, L.W. Shacklette, R.L. Elsenbaumer, E.J. Plichta, C. Becht, Micro Electromechanical Actuators Based on Conducting Polymers, in: P.I. Lazarev (Ed.) Molecular Electronics: Materials and Methods, Springer Netherlands, Dordrecht, 1991, pp. 267-89.
[32] A.D. Santa, D.D. Rossi, A. Mazzoldi, Characterization and modelling of a conducting polymer muscle-like linear actuator, Smart Materials and Structures, 6(1997) 23.
[33] P. Du, X. Lin, X. Zhang, A multilayer bending model for conducting polymer actuators, Sensors and Actuators A: Physical, 163(2010) 240-6.
[34] C.H. Nguyen, G. Alici, G.G. Wallace, Modelling trilayer conjugated polymer actuators for their sensorless position control, Sensors and Actuators, A: Physical, 185(2012) 82-91.
[35] A.D. Price, Fabrication, Modelling and Application of Conductive Polymer Composites: University of Toronto; 2012.
[36] M. Bentefrit, S. Grondel, C. Soyer, A. Fannir, E. Cattan, J.D. Madden, T.M.G. Nguyen, C. Plesse, F. Vidal, Linear finite-difference bond graph model of an ionic polymer actuator, Smart Materials and Structures, 26(2017) 095055.
[37] A. Fannir, Actuators based on conducting polymers with a linear deformation in open air and compatible with a space environment: Université de Cergy Pontoise; 2017.
[38] M. Farajollahi, A. Usgaocar, Y. Dobashi, V. Woehling, C. Plesse, F. Vidal, F. Sassani, J.D.W. Madden, Nonlinear Two-Dimensional Transmission Line Models for Electrochemically Driven Conducting Polymer Actuators, IEEE/ASME Transactions on Mechatronics, 22(2017) 705-16.

Chapter 4: Linear dynamic and nonlinear dynamic model to predict PEDOT-based trilayer actuation behavior

Contents

4.1 Motivation....74
4.1.1 Objectives....74
4.1.2 Proposed methodology....74
4.2 State of art....74
4.2.1 A summary of Black box, white box, grey-box models for CP actuators....75
4.2.1.1 Black-box model....75
4.2.1.2 Grey-box model....75
4.2.1.3 White-box model....78
4.2.2 Why the choice of the Bond Graph language?....80
4.3 Dynamic Bond Graph modeling....84
4.3.1 Actuation description....84
4.3.2 Word Bond Graph model....86
4.3.3 BG submodels....87
4.3.3.1 Electrical model....87
4.3.3.2 Electromechanical coupling....91
4.3.3.3 Mechanical model....92
4.3.4 BG global models....98
4.4 Simulation tests....100
4.4.1 Software implementation....100
4.4.2 Comparison between the linear and nonlinear simulations....101
4.5 Comparison to experimental tests....104
4.5.1 Time domain responses....105
4.5.2 Frequency responses....108
4.6 Parameter sensitivity and power performance analysis....111
4.7 Conclusion....115

4.1 Motivation

4.1.1 Objectives

The goal of this chapter is to develop an electrochemomechanical model to simulate the performance of trilayer actuators. This model must on one hand, be able to predict the dynamic behavior under a voltage excitation, and on the other hand allow an evaluation of the critical parameters affecting actuation and the power performance.

4.1.2 Proposed methodology

In order to establish a suitable model having an ability to describe the CP-based trilayer actuators, a critical literature review on the modeling of CP actuators is the first step. From an engineering point of view, a grey-box model based on Bond Graph language [1, 2] was selected, as I expected these selections can provide a visual view for the reader and later on facilitate the control of the trilayer actuators.

In a second step, a nonlinear dynamic model to predict the nonlinear mechanical behavior and the complexity of the structuring materials of ultrathin trilayer actuators is established. The nonlinear mechanical behavior of these trilayer actuators stems from changes that occur as the voltage is increased [3-5]. During operation, oxidation in one PEDOT electrode layer and reduction in the other electrode, accompanied by a drop in potential along the length of the electrodes, are observed. These changes in state modify the electrical, coupling, and mechanical properties. Here, the nonlinear properties, including electrical conductivity, volumetric capacitance of the PEDOT-based electrodes, and Young's modulus, were all characterized and incorporated into the model. At the same time, a simpler version - a linear model - to predict small beam displacement, is derived from the nonlinear model. This linear model includes (1) an RC electrical circuit to represent the device charging, (2) an electromechanical coupling matrix that is based on the accepted relationship between the strain and the volumetric charge density, and (3) a mechanical model based on the modal superposition method to treat Euler-Bernoulli dynamic beam equations for beam displacement. A comparison of the simulation results with the nonlinear model shows the limitations of such an approach. A number of experimental validations have been conducted in both the time and frequency domains, highlighting the predictive properties of the nonlinear model. Finally, from the proposed model, an evaluation of the sensitivity of the actuator parameters and of the power performance helps to improve the understanding of actuator efficiency and its crucial properties.

4.2 State of art

Within this section, different approaches on the modeling of CP actuators will be reviewed from the perspective of black-box, grey-box, and white-box approaches. Languages used in these modeling will also be classified.

4.2.1 A summary of Black box, white box, grey-box models for CP actuators

Models are hypotheses that can be used to help describe, explain and/or predict the phenomena in a novel technology. Therefore, models are proposed and simulations are compared with experiments on a laboratory – scale. The agreement between the simulations and corresponding experimental data on one hand confirms the hypotheses proposed earlier and improves our understanding on the investigated technology on the other hand. A successful model can be a powerful tool for designer, since it allows prediction, in advance, of the behavior of the device under design [6, 7]. Once this step is solved, the model may also to be used to control the performance of the systems.

The literature review on the past and current status of the CP actuator modeling theory is divided into three sections: black-box or data-driven models [8], white-box or principle models [7], and grey-box models [6] - which are a trade-off between the white-box and the black-box models.

4.2.1.1 Black-box model

In order to facilitate the real-time control of the CP polypyrrole-based actuator positioning, Fang *et al.* [8] have proposed a simplified model, based on the knowledge of the actuation bandwidth as well as on typical values of the physical parameters, from the full infinite-dimensional model which was proposed by Madden [9, 10]. In this reduced third-order transfer function, the author assumed that the trilayer operates at low frequency, and diffusion coefficient will decay overtime due to solvent evaporation. However, this model is a purely empirical model which is obtained via output-input data, and must be re-identified for different samples. John *et al.* [11] proposed another transfer function approach by fitting the experimental data of polypyrrole-based actuator displacement as a function of frequency and applied voltage. This model was validated under a dynamic input voltage signal in both time and frequency domains. However, these models are a purely empirical model which is obtained via output-input data, and must be re-identified for different samples.

4.2.1.2 Grey-box model

The grey-box model of CP actuators relies on the idea of using strain-to-charge ratio and was first introduced by Della Santa *et al.* [12] for the case of a single layer of PPy doped with benzensulphonate anions (BS^-) in solvent of sodiumbenzensulphonate and in a mixture of acetonitrile and de-ionized distilled water. The actuator model was divided into three sub-models, where the electrochemical model is simply the total amount of charge exchanged during a stimulation cycle and the coupling between electrochemical part and mechanical part is denoted by α_{ech}. This electrochemical expansion coefficient is obtained from fitting a straight line to observed isotonic (constant force) length changes as a function of exchanged charge. It has the units of % C/mm. The mechanical sub model is based on the parallel

combination of two Maxwell elements (composed of an elastic and a viscous body in series [12]) and one elastic body. These models are intended to describe the viscoelastic properties of the conducting polymer films. The author has experimentally confirmed that the proposed model was able to predict the producing stress as well as the strain of PPy film in an electrolyte bath. However, this model only validated for a small deformation.

Madden [10] introduced the diffusive elastic model, which again uses the strain to charge ratio to describe actuation, but adds to it by considering the factors that limit the rate of charging. The idea proposed is that diffusion of ions into the polymer film is a major rate limiting factor, in addition to the resistances of the electrolyte and of the conducting polymer itself. This model contains an RC transmission line to describe the diffusion of ions through the thickness of the CP electrode. The electrical equivalent circuit is shown in Fig. 1a, where Z_D is the total impedance of the RC transmission line.

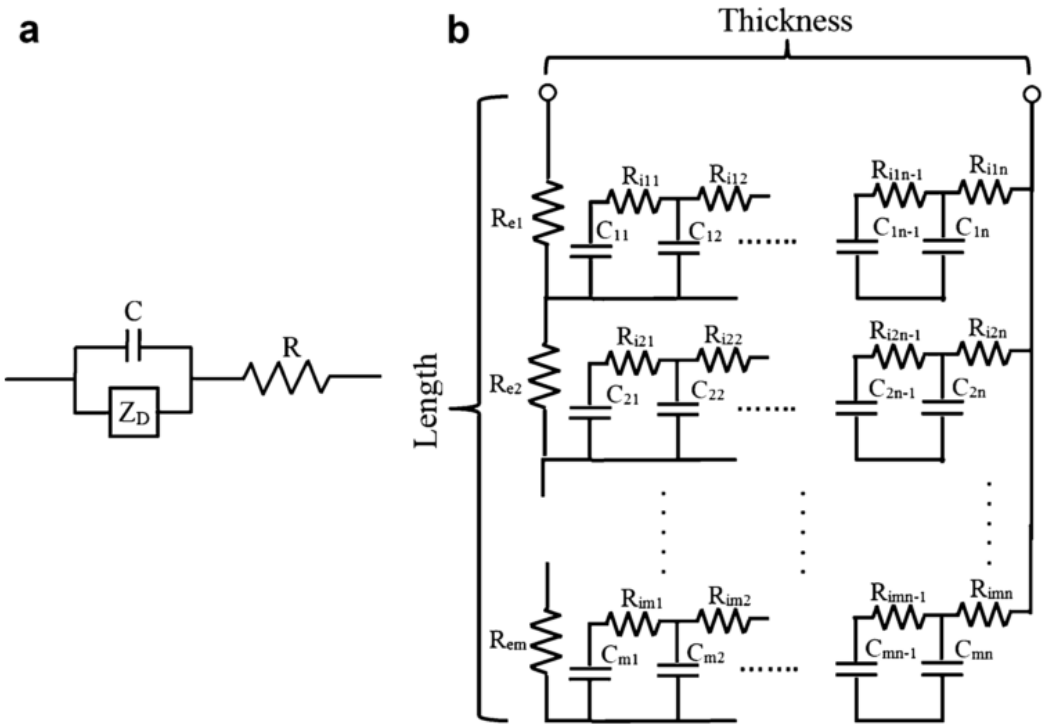


Fig. 1. a) The equivalent electrical circuit of the diffusive elastic model, which includes: a double layer capacitance C, electrolyte resistance R, and the impedance associated with ionic charge transport dominated by diffusivity Z_D, b) Example of an equivalent electrical circuit including a finite diffusion element C_{jk} and R_{ijk}, a resistance R_{ej}, and capacitance at the interface between the solution and the polymer

The model was later expanded to consider the distributed nature of charging in two dimensions, with a circuit model describing this situation shown in Fig. 1b. In this model, the distributed charge storage is represented by capacitances, C_{mn}. Their rate of charging (and hence the local rate of strain) is determined by electronic resistances, R_{em}, of the conducting

polymer film along its length (up the page), and ionic resistance, R_{imn}, representing ion transport within the conducting polymer. The rightmost column of capacitors and resistors describe the double layer capacitance between the electrolyte and the polymer and the ionic resistance of the electrolyte, respectively. The model is designed to describe a polymer films in electrolyte. In the case of a trilayer, the circuit diagram is reflected about the right hand edge. When the electrical resistance, R_{ej}, representing the electrical resistance along the length of the CP electrodes, is negligible, a two-dimensional transmission line is used as in Fig. 1b [13, 14]. In this model, the RC transmission lines extends from left to right to model the effective diffusion of ions through polymer thickness by capacitive coupling with ionic resistance of CP. The electrical resistance is considered to be negligible in comparison to ionic resistance through the thickness of the conducting polymer film. Each horizontally oriented one dimensional RC transmission line is separated from the next one by an CP electrical resistance R_{ej}, that accounts for the voltage drop that occurs as current passes along the length of the conducting polymer film. This discrete model is useful in that each element represents the properties of the device at a particular location, and each can be given a voltage dependent value.

Madden [10] incorporated electromechanical coupling based on the concept that the volumetric charge density is proportional to the induced material strain. The relation is given as following equation:

$$\varepsilon = \alpha C_V V + \frac{\sigma}{E},$$

where ε is the induced strain, α is the strain-to-charge ratio, C_V is the volumetric capacitance, and the applied stress and Young's modulus are σ and E, respectively. The terms on the right describe strain due to application of an external load, while the middle term describes the electromechanical coupling.

Madden's model was at first implemented in a linear, 1D configuration. However, conducting polymers have long been known to show changes in electronic and ionic conductivity as a function of oxidation state (see e.g. [15, 16]). Farajollahi *et al.* [3, 17] integrated the electronic and ionic conductivities of conducting polymers, and Young's modulus of the PEDOT-based trilayer actuator as a function of oxidation state into the 2-D RC transmission line model using a state-space representation. The model has the ability to predict dynamic response of the beam via radius of bending curvature at specific positions through time. However, the model is not suited to predict actuation strain as a function of the frequency of applied voltage, and generally needs to be rewritten for non-step voltage inputs.

Alici [18, 19] proposed several variations of a bending curve model to predict force and bending output of CP actuators. The key commonality in these models are the electromechanical coupling, α, determined experimentally at each operating voltage by

observing the actuator bending curvature of an unloaded beam. The determined α can be used to predict maximum blocking force and establish a nonlinear second-order differential equation relating the displacement of the beam and the applied voltage, as well beam mechanical properties. To a certain extent, the model showed a good agreement with experimental results, but it was not able to predict the tip excursions exceeding 90^0, and the transient actuation response.

In Moghadam *et al.*'s [20, 21] model, while the electrical model and the electromechanical coupling were derived from a linear transmission line model [13], the mechanical model was either based on Euler-Bernoulli beam theory and Hamilton's principle, or the dynamic rigid finite element method, to predict bending actuation. These approaches offer efficient methods in case of large displacement and complex shapes. However, the use of a linear electrical model limits their advantage.

In a recent study, C.H. Nguyen *et al.* [14] showed an advanced mathematical model including a 2D transmission line extracting from the Madden's model, the mechanical, and viscoelastic properties of a CP trilayer actuator that is a the Kelvin–Voigt model. The proposed model was experimentally validated in both frequency and time domains of a linear displacement. Afterwards, the authors implemented the model into an inversion-based feedforward controller intended for biomedical applications and proved the ability to control the actuator's displacement of the proposed controlling system.

4.2.1.3 White-box model

In the white box model, the nature of the actuation mechanism including the movement of charge under a potential and ions concentration is related via thermodynamic and transport/kinetic theories. Thermodynamics helps predict the final equilibrium state, while ion transport, reaction kinetics and the dynamics of motion determine the time it takes to reach equilibrium. There is no conducting polymer actuator model that is completely white box as they do not describe how volume changes from first principles. In this section, some aspects of the charging and actuation that have been treated from a fundamental perspective are discussed.

On the transport side the Wang and Smela [22] developed a finite element model for charge transport by diffusion and migration in a single layer of polypyrrole in electrolyte, based on transport equations for ionic and electronic charge coupled with the Nernst-Planck equation in term of reaction time *t*, as follows:

$$\frac{\partial \boldsymbol{C}_i}{\partial \boldsymbol{t}} = -\nabla \cdot \vec{\boldsymbol{J}}_i = -\nabla \cdot (-\boldsymbol{D}_i \nabla \boldsymbol{C}_i - z_i \boldsymbol{\mu}_i \boldsymbol{C}_i \nabla \phi), \quad (1)$$

where *i* indicates the species under consideration, which can be anionic, cationic species, or the electronic charge distribution in CP chains. C_i is the concentration, z_i is valence charge number, μ_i is the ionic mobility of species *i*, and ϕ is the local electric potential. The two terms on the right represent diffusion and migration. In this equation, convection is neglected as it is assumed that the charge concentration is diluted and there is no interaction among the charge carriers. Therefore, convection flux can be separated from diffusion flux. Poisson's equation is used to couple net charge density Q (C/cm^3) and the concentration C_i:

$$\epsilon_0 \nabla \cdot (\epsilon_r \nabla \emptyset) = Q = \sum_{i=1}^{n} z_i C_i. \quad (2)$$

Here ϵ_0 is the permittivity of a vacuum, and ϵ_r is the dielectric constant of the material. The model allowed to answer several important questions: the migration does contribute to ion transport at extreme potential, and the presence or the absence of a net charge in the polymer does not make any change to the concentration. However, this model does not link the local net charge density to mechanical behavior and neither does it consider any actuation phenomena. A number of gray box models are able to incorporate similar models of transport. For example, the transmission line model in Fig. 1b incorporates the responses of Equations 1 and 2 for the special cases that migration is dominating transport, and that charge storage is capacitive. In the limit as the elements in Fig. 1b are reduced in size, the response becomes diffusive.

Otero [23] has introduced a first-principle model based on the electrochemical and polymeric principles as applied to conducting polymers. He combined the theory of reaction rate for oxidation processes, the kinetic relations among the activation energy, and the increment of the mechanical work. The model describes the evolution of the potential under flow of a constant current, as follows:

$$U = U_0 + i_a Z + \Delta U(n-1) - \frac{\Delta(PV)}{(1-\alpha)nF} + \frac{RK}{(1-\alpha)nF} \times \left\{ \ln\left(\frac{i_a}{FV}\right) - d \ln[A^-] - e \ln\left([Pol^*]_{initial} - \frac{i_a t}{FV}\right) - \ln k_{a0} \right\}, \quad (3)$$

where i_a is the anodic current, $[Pol^*]$ is the evolution concentration of the active centers of the polymeric chains storing a positive charge after oxidation in the film during the time of current flow (starting at $[Pol^*]_{initial}$), *Z* is electrochemical cell impedance, R is the universal gas constant, *F* is the Faraday constant, *n* is the number of charges involved in a chain reaction, *V* is the volume of the reduced and dry reactive CP film inside the electrolyte, k_a is the rate constant. The voltage across the cell, *U*, from left to right, is the sum of the initial potential, U_o, a voltage drops due to the internal impedance, a shift due to work done on the sample, and finally terms resulting from the over potential needed to drive the reaction away from the equilibrium potential, resulting from the shift in oxidation state. Since the equilibrium electrochemical response of PPy and other conducting polymers is known to be more complicated than one described by a single redox reaction with one equilibrium

potential, the response in Equation 3 is considered instead to be the sum of many closely spaced redox reactions, indexed by integer *n*, representing the many oxidation states of the polymer. In the end, these many states are often accounted for by fitting factors (in this case an assumed separation between states of ΔU), greying the model. The model includes both actuating and sensing magnitudes, as any change through mechanical work (ΔPV), temperature K, and electrolyte concentration [A^-] can be sensed via the potential evolution U. The authors confirmed the predicting ability of the model in both actuating and sensing using a polypyrrole-based bilayer in $LiClO_4$ electrolyte. A close correlation has been observed between the simulation and experiment at low frequency of 0.01Hz, however it is not experimentally validated for the intermediate and high frequencies yet. A difference between this work and the grey box work of Madden and Farajollahi is that the thermodynamics of the conducting polymer are instead accounted for by a capacitance in the work of those authors, rather than related to standard reduction potentials. The end effect though is the same, as the reduction potentials are fit, rather than being known. Another difference is the explicit incorporation of the mechanical work done into the electrochemical model.

Venugopal *et al.*[24] introduced a thermodynamic chemomechanical constitutive model that they used to describe polypyrrole doped with dodecylbenzene sulfonate incorporated into a bilayer actuator in aqueous NaCl solution. The model is developed from work and energy formulations for chemomechanical actuation, given by:

$$\begin{Bmatrix} \Delta\varepsilon \\ \Delta\mu_i \end{Bmatrix} = \begin{bmatrix} 1/E & \xi_c \\ \xi_m & \left(\frac{RK}{C_i^0}\right)(1 - y_i^0) \end{bmatrix} \begin{Bmatrix} \Delta\sigma \\ \Delta C_i \end{Bmatrix}, \tag{4}$$

where $\Delta\varepsilon$ is mechanical strain, $\Delta\mu_i$ is the chemical potential resulting from electrochemical gradients of ionic species, σ is the applied stress, and C_i is moles/molar concentration of diffusing species '*i*'. ξ_m and ξ_c represent chemomechanical coupling coefficients due to chemical gradients and an applied mechanical stress, respectively, which are calculated under the assumption of zero dead space in CP layers, indicating a tight packing of polymer chains. ξ_c is akin to the strain to charge ratio, α, introduced above. It is a strain per molar change in concentration that in this case is computed based on the occupied volume of species inserted into the conducting polymer. ξ_m is the inverse coefficient with the same units, describing the change in potential energy due to the application of a stress. *E* is the Young's modulus, and y_i^0 is mole fraction of species '*i*' contained originally in the system. Two hypotheses were stated: the actuation parameters are regulated by the finite number of redox sites in the CP chains, and the strain developed is limited by saturation concentration of electrolyte. The experimental strain presented in this paper showed a correlation with the modeling data, however the relative error is considerable and may not suitable for actuation behavior prediction.

4.2.2 Why the choice of the Bond Graph language?

Table 1. Summarize on various model approaches of CP-based actuators

Ref.	Box model	Model characteristic	Lumped/distributed/continuous	Model presentation	Model validation
Fang *et al.* [8]	Black box	Robust self-turning regulator allowing highly adaptive prediction the bending	-	3rd order transfer function	Experimentally validated at low operating frequency f < 1Hz during 4h of continuously operating
John *et al.* [11]	Black box	-	-	6th order transfer function	Experimentally validated in frequency domain up to 100 Hz during 4 seconds of operation
Della Santa *et al.* [12]	Grey box	For a thin PPy film Electrochemical model: charge density as a function of time Electrochemomechanical coupling: empirical strain-to-charge Mechanical model: Maxwell elements in parallel	Lumped approach		Experimentally validated in time domain
Madden [10]	Grey box	For a thin PPy film Electrochemical model: elastic diffusive model Electrochemomechanical coupling: empirical strain-to-charge Mechanical model: Elastic material	Distributed	Transfer function	Experimentally validated in time and frequency domains
Alici [18, 19]	Grey box	For a PPy-based trilayer Electrochemical model: simplified elastic diffusive model Electrochemomechanical coupling: empirical strain-to-charge	Lumped in electrochemical model Continuous in mechanical model	Second-order differential equation	Experimentally validated for actuation at steady state and small displacement

		Mechanical model: second order differential equation			
Moghadam *et al.* [20, 21]	Grey box	For a PPy-based trilayer Electrochemical model: simplified elastic diffusive model Electrochemomechanical coupling: empirical strain-to-charge Mechanical model: rigid finite element method	Lumped in electrochemical model Distributed in mechanical model	Second-order differential equations	Experimentally validated for time and frequency domain for a linear displacement
C. Nguyen *et al.* [14]	Grey box	For a PPy-based trilayer Electrochemical model: simplified elastic diffusive model Electrochemomechanical coupling: empirical strain-to-charge Mechanical model: beam bending equation	Lumped	Transfer function	Experimentally validated for time and frequency domain
Wang and Smela [22]	White box	For a PPy film Electrochemical model: charge transport by diffusion and migration	Distributed	Partial differential equations	Simulation validated for electrochemical model
Otero [23]	White box	For a PPy bilayer film Electrochemical model: reaction rate for oxidation process Electrochemomechanical coupling: thermodynamic equations	Lumped	Derivation of Buttler–Volmer equation	Experimentally validated for time domain at low operating frequency. Not fully white as redox potentials are fit.
Venugopal *et al.*[24]	White box	For a PPy bilayer film A chemomechanical constitutive model based thermodynamics	Lumped	2x2 coupling matrix	Experimentally validated with considerable error in strain prediction

As summarized in table 1, modeling can be based on white, grey and black box models depending on the understanding and the ability to describe a system. In the case of the black box model, a transfer function is usually built from experimental data, whereas the white box models are generally constituted from partial differential equations, which allow the research and development of analytical solutions in space and time of continuous systems.

Between these two extremes, there are many other methods that can be proposed and that are well adapted to the grey-box model. They are usually divided in two categories: the lumped element approach and the distributed element approach [2], both methods being considered as an approximation of the continuous problem since they are represented by ordinary differential equations and depend only of the time. The distributed model is more accurate and complex as it uses infinitesimal elements to represent the system along the space. In contrast, the lumped approach concentrates the properties of the systems at singular points. Among the possible elements, one can cite, either the physical elements as the equivalent circuit, the mass-spring-damping system, the transmission line, or the numerical elements as in the finite element, finite difference, and the finite volume method… Of course, in case of multi-domain analysis, the modeling can be hybrid and based on a combination of these different methods depending on which aspects one emphasizes: mathematical or physical, accurate or not complex.

Since ionic EAP actuators inherently involve mechanical and electrical energy flow, combined with the chemical domain, a thorough model for explaining the behavior of this actuator class must include coupling between these multiple energy domains. BG (Bond Graph) methodology is well suited for describing coupled domains [2, 25]. It allows easy access to the magnitudes of energy transformed (e.g. between electrical and mechanical), stored power, and dissipated power inside these actuators. The BG language has shown also its flexibility in working with different energy domains and feasibility to describe interactions between systems. These characteristics provide an approach for design of actuators and further, the design of complete actuated robots, while retaining the physical structure of the model [26].

There are few works in modeling ionic EAP actuators using a BG. Among these, Byung-Ju Yi concentrated on the diffusion in the separator and electrode layers of ionic polymer-metal composites (IPMCs), but not on describing the mechanical response. The model was not verified by experiments [27]. Nishida *et al.* [26] demonstrated a model of IPMCs by using Bond Graphs to describe distributed port-Hamiltonian (DPH) systems on multiple spatial scales. The coupling among different energy domains in IPMC can be modeled by DPH systems with unidirectional energy flows without calculating analytic solutions. The advantage of this approach is that it is a powerful tool in optimizing the design and control method of the investigated system. However, the disadvantages of the distributed port-Hamiltonian is that it normally requires understanding on mathematical model and currently, there is no commercial software to simulate the port-Hamiltonian model. Bowers [28] built a BG model

of bilayer actuators operating in a liquid environment. Recently, Bentefrit *et al.* [29] presented a finite-difference BG model of a trilayer actuator. However, this model focuses on linear behavior and therefore can only predict the mechanical displacement of the actuator when the applied voltage is relatively small. In this work, the aim is to extend the BG modeling of conducting polymer actuators to nonlinear systems, and to incorporate both actuation (Chapter 4) and sensing (Chapter 5). The models are applied to actuators developed using the new layer-by-layer process.

4.3 Dynamic Bond Graph modeling

In this section, a nonlinear model and its simplification – a linear model to predict trilayer actuator behavior - are proposed. The nonlinear model represents an application and substantial extension of the linear transmission line model developed by Madden [10]. The nonlinear model is intended to predict the nonlinear behavior of the actuator. It consists of a 1D RC electrical sub-system that is simplified from a 2D transmission line. Complex processes such as diffusion-like transport of ions through the internal PEDOT nano-structure, the redox process in the polymer, and the formation of a double layer between the interface of the PEDOT and electrolyte, are all considered. An empirical coupling ratio relating the instantaneous charge input and the output moment is implemented. The deformation of the polymer is converted to bending using a mechanical model based on the rigid finite element method. This approach is valid for large displacement and takes mass of the actuator into account.

The proposed linear model comprises a capacitor in series with a resistor to represent the electrical response. This is a simplification of the 1D RC transmission line circuit used in the full model. An electromechanical coupling coefficient then relates the amount of charge input to the free strain of the polymer. The beam geometry and mechanical properties are used to estimate deflection and the total force applied to the free end of the beam as the output. The mechanical model in this simplified case is based on a linear dynamic Euler-Bernoulli beam.

4.3.1 Actuation description

An ultrathin trilayer configuration operating in air [30] is studied here. In this configuration, a solid polymer electrolyte (SPE), made of nitrile butadiene rubber (NBR) /poly(ethylene oxide) (PEO), accommodates cations 1-Ethyl-3-methylimidazolium ($EMIm^+$) and anions bis(fluorosulfonyl)imide ($TFSI^-$) and is sandwiched between two PEDOT containing CP electrodes. When an excitation voltage is applied between the two electrodes, the positive potential extracts electrons (oxidation process) from the one PEDOT electrode [31]. Cations leave the electrode to balance charge. At the other electrode, cations are injected by a diffusion-like process into the CP layer, neutralizing the reduced polymer backbone [32, 33]. In addition, a voltage drop is expected along the trilayer due to the existence of the electrical resistance along the length of the PEDOT electrodes. The ion transfer leads to swelling of one

of the conducting layers and contraction of the other, resulting in bending of the sandwich structure up or down (Fig. 2b).

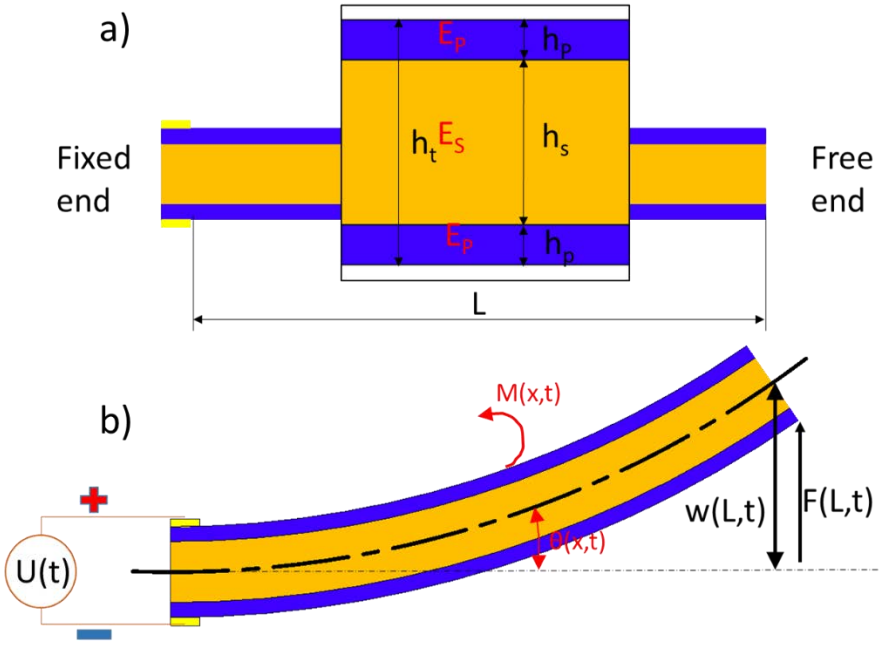


Fig. 2. a) a CP actuator in neutral state and its dimensions (shown in the magnified section in the middle), and b) a voltage excitation induces a tips displacement w(L, t) and an angular rotating angle $\theta(x,t)$ of the actuator, which is equivalent to an external force F(L, t) or a moment M(x, t), respectively. The Young's moduli of the PEDOT electrodes and the NBR/PEO layer are E_P and E_S, respectively.

Fig. 2a describes the actuator dimensions, where *L*, h_p, h_s, h_t, and *b* are the length of the actuator, the PEDOT electrode's thickness, the NBR/PEO's thickness, the total thickness, and the width of the actuator, respectively.

Table 2. Notations for continuous, lumped, and distributed modeling approaches

	Continuous	**Lumped**	**Distributed**
Voltage input	$U^C(x,t)$	$U^C(t)$	$U_i^C(t)$
Current input	$i^C(x,t)$	$i^C(t)$	$i_i^C(t)$
Charge	$Q^C(x,t)$	$Q^C(t)$	$Q_i^C(t)$
Capacitance	$C(x,t)$	$C(t)$	$C_i(t)$
Force	$F(x,t)$	$F(t)$	$F_i(t)$
Displacement	$w(x,t)$	$w(t)$	$w_i(t)$
Rotating angle	$\theta(x,t)$	$\theta(t)$	$\theta_i(t)$
Angular velocity	$\dot{\theta}(x,t)$	$\dot{\theta}(t)$	$\dot{\theta}_i(t)$
Moment	$M(x,t)$	$M(t)$	$M_i(t)$

A voltage excitation *U(t)* induces a displacement *w(L, t)* at the tips of the beam and a rotating angle $\theta(x,t)$ at position *x* away from the clamping point. From the tips displacement value, the curvature *K(t)*, the strain difference $\varepsilon_{actual}(t)$, and the linear strain $\varepsilon_{active}(t)$ can be derived (refer to chapter 3, section 3.4 for the detail derivation on the strain difference and the linear strain). Three modeling approaches are now discussed: continuous, lumped and distributed. To facilitate the modeling process later on, I distinguish the notations among three cases in table 2. The continuous variables are both time, *t*, and position, *x*, dependent, while in the distributed case position is replaced by an element index, *i*. The lumped elements have no spatial dependence.

4.3.2 Word Bond Graph model

Creation of a bond graph, like other models, often starts with a block diagram known as a word bond graph. The proposed "word BG" model of this actuator consists of three sub-systems: the electrochemical subsystem, the electrochemomechanical coupling, and the mechanical sub-system. The application of a voltage and current leads to charge accumulation and current, which are passed to the electro-chemo-mechanical subsystem, where the insertion of charge is converted to strain and stress. The resulting stresses and strains then produce a moment and a bending of the device. The connections between these subsystems are shown in Fig. 3 and are represented by "half arrows" indicating the assumed instantaneous positive flow of energy in the actuator. Chapter 5 treats the reverse case for the sensor and produces a combined model.

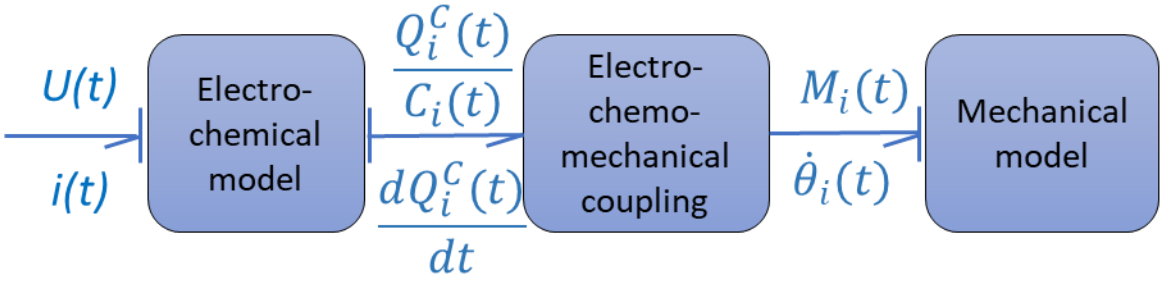


Fig. 3. Trilayer actuator Words BG model.

In the nonlinear model, the global system input is voltage, $U(t)$, whereas the outputs are current $i(t)$, and beam angular velocity $\dot{\theta}_i(t)$. The electrochemical model inputs the time and space variation in charge of the actuator during the operation, $\frac{dQ_i^C(t)}{dt}$. Local charging is then related to strain and mechanical deformation through the electrochemomechanical coupling system described below. The mechanical system is driven by the modal actuation moment $M_i(t)$ generated from coupling. In addition, each pair of input and output variables provides information about power transmission, described as follows:

$$(\ voltage,\ current\ ) = \left(\ U(t), i(t)\right);\ \left(\frac{Q_i^C(t)}{C_i(t)}, \frac{dQ_i^C(t)}{dt}\right),\ \text{and}$$

$$(moment,\ rotational\ angular\ velocity\ )\ =\ (\ M_i(t), \dot{\theta}_i(t)\ ).$$

In the linear model, angular velocity $\dot{\theta}_i(t)$ and actuation moment $M_i(t)$ are replaced by beam displacement $w(x,t)$ and actuation force $F(L,t)$, respectively. Other elements remainthe same as in the nonlinear model.

4.3.3 BG submodel descriptions

Once the word BG is obtained, the BG describing each sub-system can be derived from the equations involving in the electrical, the coupling, and the mechanical variables.

4.3.3.1 Electrochemical model

As reported in section 4.2.1.2, a grey-box electrochemical model is used in this study. An RC equivalent circuit was proposed to explain the diffusion through the electrode thickness and the electrical resistance of PEDOT was added along the length of the electrodes, leading to a 2D transmission line model of a trilayer actuator [10, 34]. The transmission lines here present a combination of storage and migration. The effect of ion diffusion due to a difference in concentration is neglected. In a recent research [15], nuclear magnetic resonance (NMR) spectroscopy has been used to determine the diffusion coefficient of the ions PF_6^- in PPy. The result found ($5x10^{-9}$ cm^2/s) is an order of magnitude smaller than the value extracted from the EIS measurement. This suggests that field driven ion migration is dominant in the impedance spectroscopy case.

The diffusion transmission line (Fig. 4a) is described by capacitors C_{ij}, i = 1,3, j = 1, …, m, and R_{ij} are the ionic resistances of the electrode layer. R_{1ie}, R_{3ie} are the electrical resistances along the length of the PEDOT electrodes. R_{Sj} are the ionic resistances of the SPE layer, R_{short} is the possible short circuit resistance between the electrodes (1st and 3rd layers), and C_{dli} are the double layer capacitances formed at the interface between the PEDOT electrodes and the SPE layer.

Conducting polymers store substantial charge. Getting the charge in and out is typically the rate limiting factor (though inertia can also limit rate of deformation at high frequencies, as will be seen). The capacitors in the model represent charge storage, and the resistors act to slow charging. The model in Figure 4a can be simplified substantially because not all rate limiting factors are significant, in part since the ratio between the thickness and the length of the electrodes is small ($<1/10^3$). The magnitudes of the polymer *RC* charging time constant along the length, the diffusion time constant through the thickness of the electrodes, the

double layer charging time, and the *RC* time constant determined by ionic transport through the SPE layer – are now estimated to determine which factors dominate.

Estimates are based on time constants that are the product of a resistance and an effective capacitance [35]. The more important factors are selected and the 2D transmission line model is simplified, with a small effect on the accuracy. These rate limiting factors are calculated for a beam having a typical geometry of *length (L) x width (b) x total thickness (h) = 5 mm x 1 mm x 0.017 mm* in the electrolyte swollen state, and thicknesses of a PEDOT electrode: h_P*= 3.5 µm* and of SPE layer h_S*= 10 µm*.

The double layer charging time constant is determined by:

$$\tau_{dl} = R_S \times C_{dl} = \frac{h_S}{\delta_S \times b \times L} b \times L \times C_A = \frac{10^{-5} m \times 0.2\ F/m^2}{(0.038\ S/m)} = 53\ \mu s, \qquad (5)$$

where R_S and h_S are the resistance and the thickness of the SPE layer, respectively, *b* is the width of the actuator, *L* is the length of the actuator, C_A (F/m^2) is the double layer capacitance per area [36], and δ_s (*S/m*) is the ionic conductivity of the SPE layer, which is characterized in chapter 3 (section 3.2). This time is very short compared to typical actuation response times as the double layer capacitance are tiny compared to the bulk storage, and so the double layer capacitances can be neglected.

'Effective diffusion time through electrodes' thickness is calculated using the following formula:

$$\tau_D = \frac{h_P^2}{D} = \frac{(3.5 \times 10^{-6} m)^2 \times (52 \times 10^6 F/m^3)}{0.025\ S/m} = 0.0073\ s, \qquad (6)$$

where h_P is the thickness, and *D* is the effective diffusion coefficient which is determined by δ_i (*S/m*), the ionic conductivity within the electrode, divided by C_V (F/m^3), the volumetric capacitance of the electrode (the values of δ_i and C_V are referred to chapter 3 (section 3.2)), in the common case that it is the ionic resistance that limits the charging rate [10]. The time is quite short, so we shall see that this effect does not dominate for this particular electrode thickness, and so simplifications can be made.

The resistance to ion transport through the SPE layer R_S is another rate limiting factor to be considered:

$$\tau_S = R_S \times C = \frac{h_S}{\delta_S \times b \times L} \frac{C_V \times L \times b \times h_P}{2} = \frac{(10^{-5} m) 52 \times 10^6 F/m^3 (3.5 \times 10^{-6} \mathrm{m})}{2 \times (0.038\ S/m)} = 0.0240\ s, \quad (7)$$

where the factor of "two" accounts for the two capacitors in series.

The polymer charge time constant resulting from the electronic resistance along the length of the electrodes is:

$$\tau_L = R_P \times C_V \times L \times b \times h_P = \frac{L}{\delta_e h_P b} C_V \times L \times b \times h_P = \frac{(5\times10^{-3}m)^2 52\times10^6 F/m^3}{2500 S/m} = 0.52\ s, \quad (8)$$

where R_P is the electrical resistance, V_P is the volume of the PEDOT electrode, δ_e is the PEDOT electrical conductivity (refer to chapter 3, section 3.2). This time constant is relatively large, indicating that the resistance along the length is important and should be included in the model.

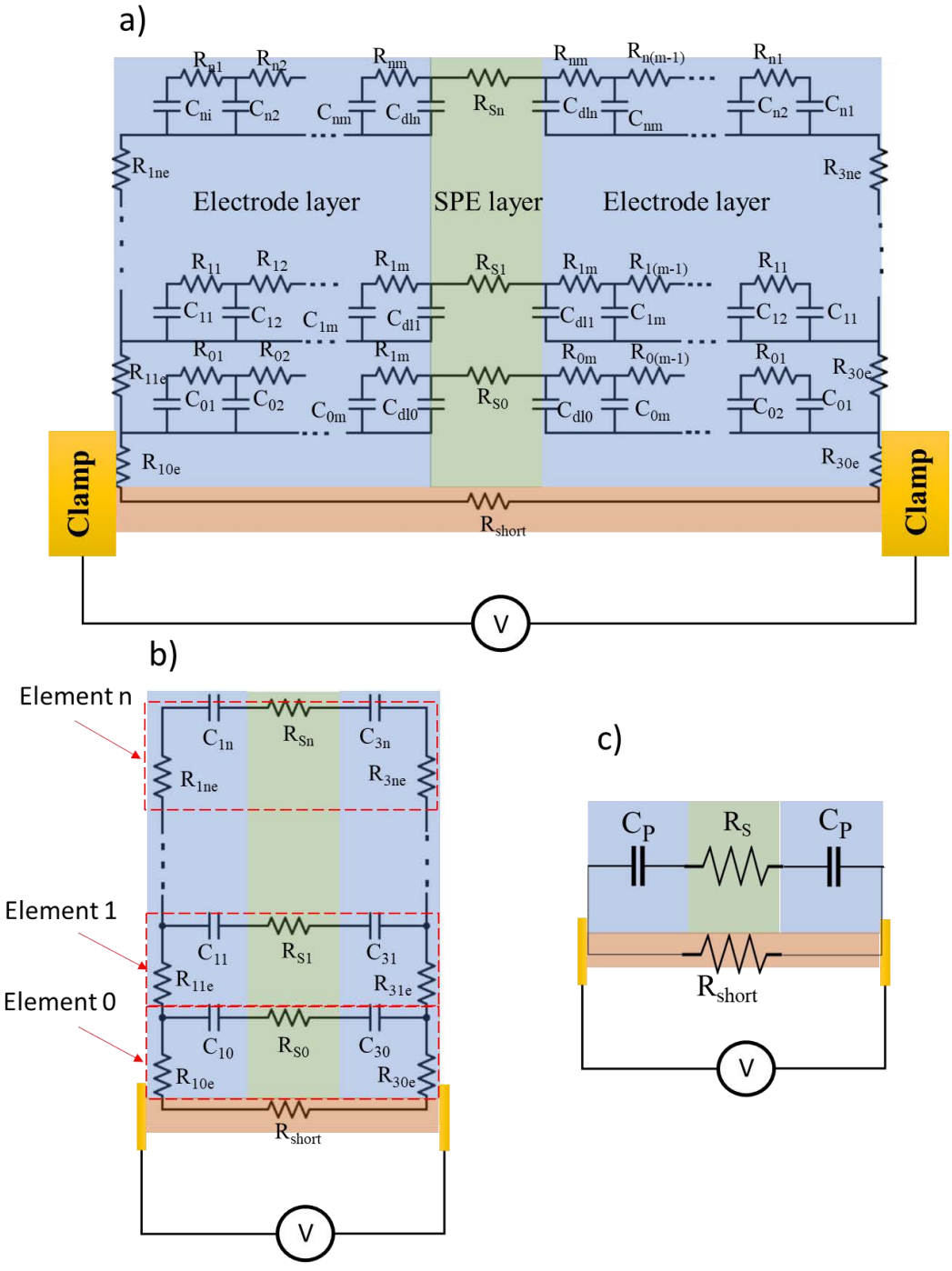


Fig.4. a) 2D diffusion transmission line across the thickness and the length of a trilayer actuator, and simplified electrochemical model of the trilayer actuator for b) nonlinear model, and c) linear model

As can be seen from four values above, the polymer charge time constant (0.52 s) and the resistance to ion transport through the SPE layer (0.024 s) play important roles in comparison to the diffusion time through the thickness (0.0073 s) and the double layer charging time constant (53 µs). The 2D transmission line model shown in Fig. 4a can then be simplified to the 1D transmission line shown in Fig. 4b. The investigated trilayer actuator is divided into *(n + 1)* elements corresponding to the space discretization.

To establish even a simpler electrochemical model, we could also assume in the same case that the electronic conductivity of the PEDOT electrodes is high resulting in a small τ_L (equation 4). The transmission line in Fig. 4b is reduced to only two capacitors in series with a resistor and all in parallel with a resistor, as shown in Fig. 4c.

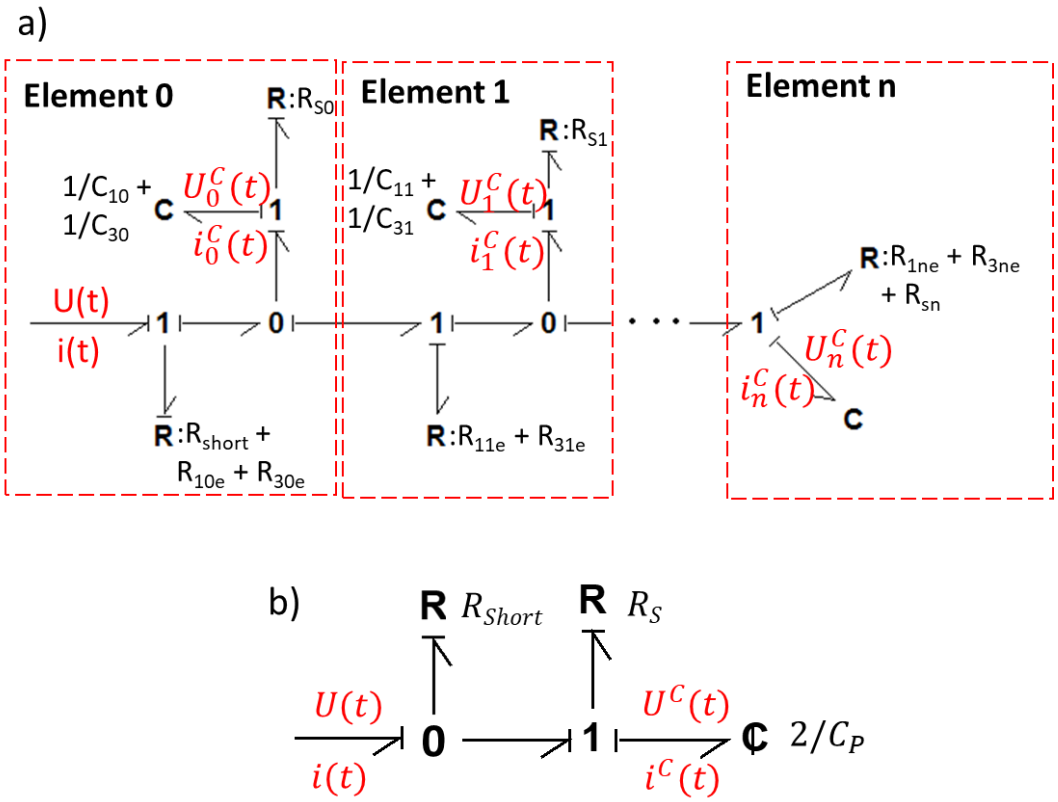


Fig. 5. BG representation of a) the nonlinear electrochemical model, b) the linear electrochemical model.

The BG representations shown in the Fig. 5a and 5b are used to describe the electrochemical model of the 1D transmission line shown in Fig. 4b and 4c, respectively. Resistance and capacitance are described by the one-port R-elements and the one-port C-elements in the

electrochemical system, respectively. The one-port C elements are shown for simplicity, - but in the full electrochemomechanical model, these are two-port ¢-elements in which the charge state of the capacitor is coupled to the stress-strain state of the actuator. As defined in all BG models, 0-junctions behave such that all the voltage, force or torque values are equal across the bonds, and total current values in and out of the junction are equal zero. In the 1-junctions, the current, speed or angular velocity is the same through each bond and the sum of voltages is equal to zero. These are equivalent to parallel (0) and series (1) electrical circuit configurations.

4.3.3.2 Electrochemomechanical coupling

BG language is especially advantageous for modeling the coupled electrochemical - mechanical effects compared to equivalent circuits [37] since it is possible to develop a new element depending on the physical laws. The electrochemical-mechanical coupling effects are represented by two-port ¢-elements in BG having the ability to describe both energy transfer between different domains and energy storage in the electrodes.

In Fig. 6, the electromechanical coupling effect of the nonlinear model is depicted by a two-port ¢-element with current dQ_i/dt and total moment M_i(including an external mechanical moment and a moment generated by an input current) implemented on both sides. Based on the relationship between total moment M_i and charge per volume ρ [38], the coupling matrix of a 2×2 element is established as follows:

$$\begin{bmatrix} U_i^C \\ M_i \end{bmatrix} = \begin{bmatrix} \frac{1}{C_i} & 0 \\ \frac{\alpha E_P (h_S + h_P)}{2L_i} & \frac{4bsin(\theta_i)}{3L_i\theta_i} E_P \left(\frac{h_S}{2}\right)^3 \left[\left(1 + \frac{2h_P}{h_S}\right)^3 - 1 + \frac{E_S}{E_P}\right] \end{bmatrix} \begin{bmatrix} Q_i^C \\ \theta_i \end{bmatrix}, \quad (9)$$

where, α is an empirical strain-to-charge ratio [39], and θ_i is the rotational angle of the i^{th} element relative to the direction of $(i\text{-}1)^{th}$ element. L_i is the length of element i. In this coupling matrix, the bottom left element describes the effect of charge on output moment, via the strain-to-charge ratio, while the bottom right element relates the beam bending angle to the output moment. The relation on the bottom left stems from the simple relationship that active free strain is proportional to charge density, with the strain to charge ration being the constant of proportionality. The strain is then scaled by modulus of the polymer layer to find stress. The bottom right term has been derived from the equations for force generation, F, by a cantilever beam [38]: $F = \frac{E_P \alpha \rho}{L} b \left(\frac{h_S}{2}\right)^2 \left[\left(1 + \frac{2h_P}{h_S}\right)^2 - 1\right] + \frac{2bE_P K}{3L} \left(\frac{h_S}{2}\right)^3 \left[\left(1 + \frac{2h_P}{h_S}\right)^3 - 1 + \frac{E_S}{E_P}\right]$, where $\rho = \frac{Q}{2Lbh_P}$ is the charge density, and $K = \frac{2w}{L^2 + w^2}$ is the curvature of the actuator (refer to Appendix A.4.1 for the detail derivation).

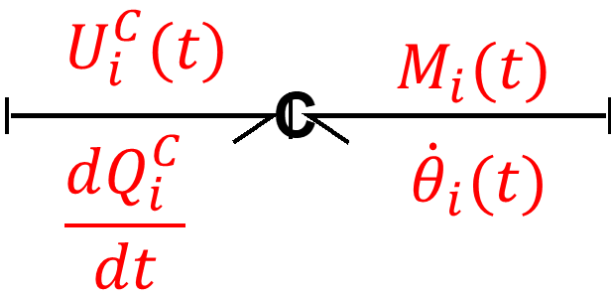


Fig. 6. Coupling between electrical sub-system and mechanical sub-system.

To obtain a simple electrochemomechanical coupling description for the linear model, where we only have a single capacitor and two capacitors, the discretized voltage U_i^C, moment M_i, rotation angle θ_i, and charge Q_i^C are replaced by total voltage across the capacitor U_C, force at the tips of the beam $F(L,t)$, the tips displacement $w(L,t)$, and total charge on the capacitor $Q_C(t)$, respectively. This coupling matrix is described below:

$$\begin{bmatrix} U^C(t) \\ F(L,t) \end{bmatrix} = \begin{bmatrix} \frac{1}{C(t)} & 0 \\ \frac{\alpha E_P(h_S+h_P)}{2L} & \frac{4bE_P}{3L}\left(\frac{h_S}{2}\right)^3\left[\left(1+\frac{2h_P}{h_S}\right)^3 - 1 + \frac{E_S}{E_P}\right]\frac{1}{L^2+w^2} \end{bmatrix} \begin{bmatrix} Q^C(t) \\ w(L,t) \end{bmatrix}, \quad (10)$$

A common property of the coupling matrix in equation (9) and (10) is that the factor of "0" on the top right of the coupling matrix represents the sensing coupling. An input displacement or stress induce an output voltage. Literature [40-43] has shown that the trilayer transducer used in our study shows bidirectional operation. An applied voltage can induce a bending output and an input displacement can produce a voltage output. Since the electromechanical coupling is small, the influence of the sensing part on actuation is small and is therefore neglected here. Sense voltages are in the range of 1 mV while actuation voltages applied are typically 1 V or more. Within the scope of this chapter the focus is on actuation and for now the sensing aspect is ignored. However, this aspect can easily be introduced, as is done in Chapter 5.

The bottom right factors of the coupling matrix in equation (9) and (10) provide feedback, which changes the total moment/force based on the output rotating/displacement value.

4.3.3.3 Mechanical model

The generated moment from coupling effects is then applied to the trilayer actuator resulting in the bending. Since the ratio between thickness and length of the ionic EAP actuator is small $\left((2h_P + h_S)/L \ll 1\right)$, this actuator can be considered as a thin beam.

In addition, evidence of the large displacement of the trilayer actuator used in this study and shown in Fig. 16 (section 4.5.1) suggests that a nonlinear model should be developed to describe the mechanical system. Several beam modeling methods exist, such as, for a small

displacement: the Euler-Bernoulli beam theory [44], the Timoshenko beam theory, and the Rayleigh-Ritz beam theory [45], and for a large displacement such as the Galerkin finite element method to solve second order nonlinear differential equations [46], as well as the rigid finite element method (RFEM) [47]. RFEM allows us to take into account the nonlinear dynamic mechanical behavior of the actuator easily, and to account for inertia [25, 48, 49]. Effects of mass have been left out of previous models [50, 51] since conducting polymer actuators have historically been slow. However the PEDOT-NBR/PEO trilayer similar to those presented in this work have been shown to be fast in their responses [52], so inclusion of inertial effects in the proposed model is important to predict the actuation at high operating frequencies.

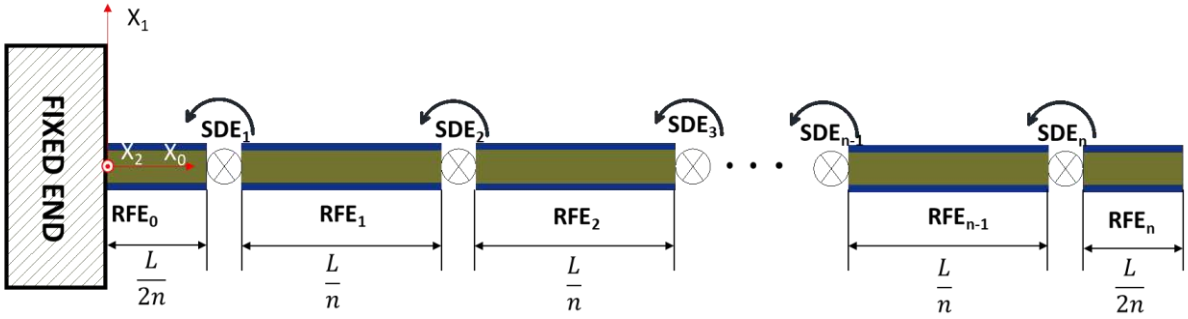


Fig. 7. Rigid Finite Element Model (RFEM) of a trilayer actuator, in which it is divided into (n+1) rigid elements: from RFE_0 to RFE_n, the elements each have a mass and are linked by a spring-damper element SDE_1 to SDE_n, shown in their initial positions. The integrated coordinator includes X_0 axis along the length of the actuator, X_1 axis perpendicular to the X_0 and X_2 axis perpendicular to the X_0X_1 surface.

So, if we consider RFEM, the actuator is divided into $(n+1)$ rigid elements from RFE_0 to RFE_n, where the length of each element is calculated according to the following rule: $L_i = L/n$, $i = 1, \ldots, n-1$ and $L_0 = L_n = L/2n$. Each element is rigid and has a mass. Consecutive elements are linked together by a torsional spring-damping element (SDE), which allows a rotation around its axis X_2 (perpendicular to X_0X_1 surface) (Fig. 7). The general Lagrange principle at each SDE is written as follows:

$$\frac{d}{dt}\left(\frac{\partial T}{\partial \dot{\theta}_i}\right) - \frac{\partial T}{\partial \theta_i} + \frac{\partial G}{\partial \theta_i} + \frac{\partial D}{\partial \dot{\theta}_i} = M_i, \qquad (11)$$

where $i = 1, \ldots, n$, and T, G, and D are the kinetic energy, potential energy, and dissipation energy, respectively, of the system of $(n+1)$ elements. The terms in the equation are now described mathematically, following the treatment presented by Wittbrodt *et al.* [49] and Moghadam *et al.* [53] [54].

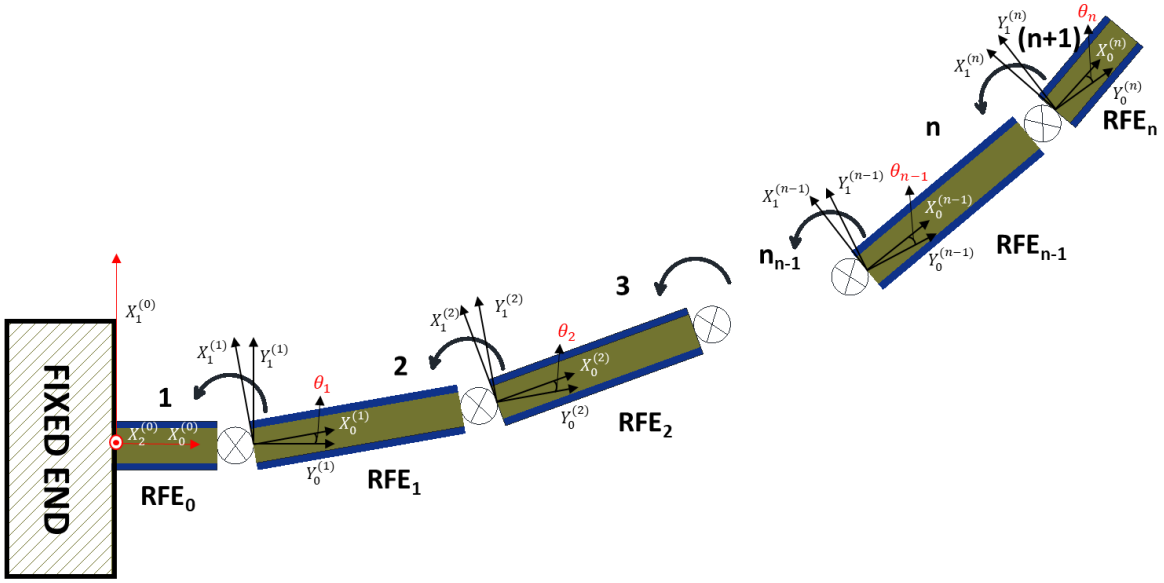


Fig. 8. Trilayer actuator in a bent state. The bending angle between the element (i-1) and the element i is θ_i.

Considering a differential element dm_i on RFE_i, the kinetic energy of this element is:

$$dT_i = \frac{1}{2} tr\{\dot{r}_i \dot{r}_i^T\} dm_i \quad , \tag{12}$$

where $r_i = \begin{bmatrix} X_0^{(i)} & X_1^{(i)} \end{bmatrix}^T$. $X_0^{(i)}$, and $X_1^{(i)}$ are the components of displacement in two axes of the i^{th} element, in the local coordinates, as depicted in Fig. 8. The total kinetic energy of the system is then:

$$T_i = \frac{1}{2} \int_{m_i} tr\{\dot{r}_i \dot{r}_i^T\} dm_i = \frac{1}{2} tr\{\dot{B}_i H_i \dot{B}_i^T\}, \tag{13}$$

where pseudo-matrix $H_i = \int_{m_i} \check{r}_i \check{r}_i dm_i = \begin{bmatrix} m_i {L_i}^2/3 & 0 & m_i L_i/2 \\ 0 & m_i h^2/12 & 0 \\ m_i L_i/2 & 0 & m_i \end{bmatrix}$, (14)

m_i is the mass of the RFE_i, h is the thickness of the actuator, and L_i is the length of the RFE_i.

The matrix $B_i = \check{B}_1 \check{B}_2 \dots \check{B}_i$, enables the description of the total rotation of an element and its position as a function of time. Here, $\check{B}_i = \begin{bmatrix} Cos\,\theta_i & -Sin\,\theta_i & L_i \\ Sin\,\theta_i & Cos\,\theta_i & 0 \\ 0 & 0 & 1 \end{bmatrix}$, which represents the rotational matrix of the element the RFE_i, expressed in terms of angles, θ_i, relative to the previous beam segment RFE_{i-1}, and the length of each segment, L_i (Fig. 24).

Then the total kinetic energy of the system is obtained by the sum of T_i:

$$T = \sum_{i=1}^{n} T_i. \tag{15}$$

The total potential energy of the system is $G = \frac{1}{2}\sum_{i=1}^{n} k_i \theta_i^2$ (16), where $k_i = \frac{EI}{L_i}$, which is the stiffness of each RFE_i element [55].

The total dissipation energy is $D = \frac{1}{2}\sum_{i=1}^{n} c_i \dot{\theta}_i^2$ (17), where $c_i = \frac{\eta I}{L_i}$, η is the normal damping material constant, *I* is the inertial moment, and *E* is the Young's modulus of the trilayer actuator.

The external moment is determined by the electrochemomechanical coupling established from equation (5).

The final Lagrange equation is obtained by inserting equations (17), (16), and (15) into (11).

In order to describe the Lagrange principle in a BG, the component $\frac{d}{dt}\left(\frac{\partial T}{\partial \dot{\theta}_i}\right)$ needs to be rewritten as the following chain:

$$\frac{d}{dt}\left(\frac{\partial T}{\partial \dot{\theta}_i}\right) = \sum_{j=1}^{n}\left[\frac{\partial}{\partial \theta_j}\left(\frac{\partial T}{\partial \dot{\theta}_i}\right)\frac{\partial \theta_j}{\partial t} + \frac{\partial}{\partial \dot{\theta}_j}\left(\frac{\partial T}{\partial \dot{\theta}_i}\right)\frac{\partial \dot{\theta}_j}{\partial t}\right], \tag{18}$$

and the component $\dot{B}_i$ is described as:

$$\dot{B}_i = \frac{dB_i}{dt} = \sum_{j=1}^{i}\left[\frac{\partial B_i}{\partial \theta_j}\frac{\partial \theta_j}{\partial t}\right]. \tag{19}$$

This set of Lagrange equations can be rewritten in the following form:

$$\begin{aligned} \ddot{\theta}_1 &= f(\dot{\theta}_1, \dot{\theta}_2, \dots, \dot{\theta}_n, \theta_1, \theta_2, \dots, \theta_n, t) \\ \ddot{\theta}_2 &= f(\dot{\theta}_1, \dot{\theta}_2, \dots, \dot{\theta}_n, \theta_1, \theta_2, \dots, \theta_n, t) \\ &\vdots \\ \ddot{\theta}_n &= f(\dot{\theta}_1, \dot{\theta}_2, \dots, \dot{\theta}_n, \theta_1, \theta_2, \dots, \theta_n, t) \end{aligned}, \tag{20}$$

or in a compact form:

$$\hat{\mathrm{I}}(\theta, \ddot{\theta}).\ddot{\theta} + \mathrm{R}\dot{\theta} + C\theta + e(\theta, \dot{\theta}) = M \tag{21}$$

In our case, since the actuator is initially curved, the initial condition can be provided by setting the vector of the rotational angles of the RFEs at the time $t = t_0$: $\theta(t_0) = [\theta_1(t_0) \quad \theta_2(t_0) \quad \dots \quad \theta_n(t_0)]^T$. Assuming that the actuator is stationary at the time $t = t_0$: $\dot{\theta}(t_0) = \left[\dot{\theta}_1(t_0) \quad \dot{\theta}_2(t_0) \quad \dots \quad \dot{\theta}_n(t_0)\right]^T = [0 \quad 0 \quad \dots \quad 0]^T$. Finally, the results form a matrix of rotational angles at each SDE during the time span $t = t_0, \dots, t_m$, where time has been divided into *m*:

$$\begin{bmatrix} \theta(t_0) \\ \theta(t_1) \\ \vdots \\ \theta(t_m) \end{bmatrix} = \begin{bmatrix} \theta_1(t_0) & \theta_2(t_0) & \cdots & \theta_n(t_0) \\ \theta_1(t_1) & \theta_2(t_1) & \cdots & \theta_n(t_1) \\ \cdots & \cdots & \cdots & \cdots \\ \theta_1(t_m) & \theta_2(t_m) & \ldots & \theta_n(t_m) \end{bmatrix}. \quad (22)$$

Knowing the rotational angles as a function of time, the position of the RFEs and the actuator shape can be easily derived.

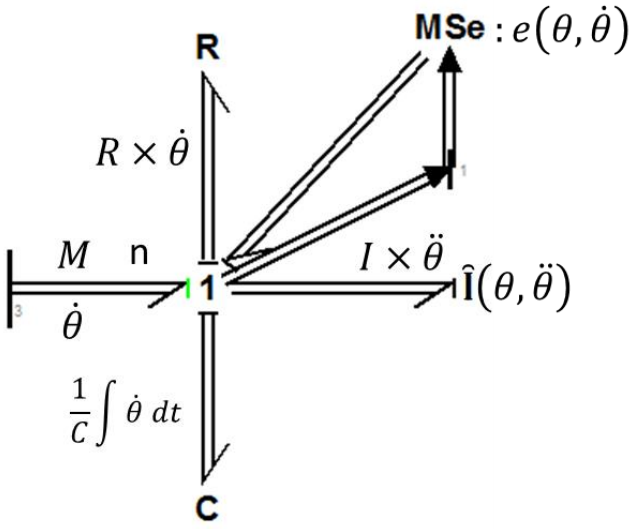


Fig. 9. Mechanical BG model.

Based on equation (21), the mechanical BG model is described as in Fig. 9. Here, the input power, represented by the applied moment, *M*, and the angular velocity $\dot{\theta}$, is divided among n-port R-elements, n-port C-elements,n-port Î-elements, and a multiport source element MSe, which indicates the damping constant, the inverse of the spring constant, the mass, and nonlinear dynamic rotation $e(\theta, \ddot{\theta})$. The *multi-BG* notation (*n* bonds) is used here since it turns out to be a natural and a concise way of representing the power behavior of macroscopic multiport systems.

For a simple linear model, the Euler-Bernoulli dynamic beam theory is selected to present the mechanical model instead of the rigid finite element method used in the nonlinear describing previously. The Euler-Bernoulli theory provides an accurate model, low-order, lumped-parameter representation of distributed elements to predict the small displacement of a bending beam.

The Euler-Bernoulli equation (21) can be also derived from the Lagrange principle (equation 7) by assuming that the dissipation energy is equal to zero (*D = 0*). The potential energy of a single beam element is then calculated as below:

$$G = EI\left(\frac{\partial^2 w(x,t)}{\partial x^2}\right)^2, \tag{23}$$

and its kinetic energy is given by:

$$T = \rho A\left(\frac{\partial w(x,t)}{\partial t}\right)^2. \tag{24}$$

Yielding equation (23) and equation (24) into equation (11) gives equation (25).

Karnopp [56] introduced the first model BG to describe results of solving Euler-Bernoulli beam equation using the separation of variables method. A similar method can be used to derive the CP actuator model in this paper, but with different boundary conditions. The Euler-Bernoulli equation for a dynamic beam is developed as follows:

$$EI\frac{\partial^4 w(x,t)}{\partial x^4} + \rho A\frac{\partial^2 w(x,t)}{\partial t^2} = F(L,t). \tag{25}$$

Here E_S is SPE layer's Young's modulus, while A and b are cross section and width of the beam, respectively.

The set of boundary conditions for a CP beam with clamping at one end are:

$$w(x,t)|_{x=0} = 0; \frac{\partial w(x,t)}{\partial x}\Big|_{x=0} = 0 \quad . \tag{26}$$

In the case of an applied point force at the other free end:

$$\frac{\partial^2 w(x,t)}{\partial x^2}\Big|_{x=L} = 0\ ; -EI\frac{\partial^3 w(x,t)}{\partial x^3}\Big|_{x=L} = F(L,t)\ . \tag{27}$$

The separation of variables method [56] begins by assuming the displacement $w(x,t)$ can be separated into a function of x only , $Y(x)$ and a function of time, t, $\mu(t)$:

$$w(x,t)\ =\ Y(x)\,\mu(t). \tag{28}$$

Substituting (7) into (5), the solution for this equation is in form of mode shape functions:

$$Y_n(x) = \big(cos\ (r_nL) - cosh(\ r_nL)\big)\big(sin(\ r_nx) + sinh(\ r_nx)\big)$$
$$-\big(sin(\ r_nx) - sinh(\ r_nx)\big)\big(cos\ (r_nL) + cosh(\ r_nL)\big), \tag{29}$$

and the contribution of n^{th} mode is:

$$m_n\ddot{\mu_n}(t) + 2\zeta_n\omega_n m_n\dot{\mu_n}(t) + m_n\omega_n^2\mu_n(t) = F(t)Y_n(L), \tag{30}$$

where r_nL yields equation: $cos\ (r_nL)cosh(\ r_nL) = 1$, mode frequencies $\omega_n^2 = \frac{EI}{\rho A}\frac{(r_nL)^4}{L^4}$, mode mass $m_n = \int_0^L \rho A Y_n^2\,dx$, and model damping $b_n = 2\zeta_n\omega_n m_n$ in which damping ratio ζ_n is found by experiment. The model stiffness is given by: $k_n = m_n\omega_n^2$.

Once mode shape functions $Y_n(x)$ and contribution functions $\mu_n(t)$ have been determined, equation (28) can be rewritten as: $w(x,t) = \sum_{n=1}^{\infty} Y_n(x)\mu_n(t)$, or in differential form:

$$\dot{w}(x,t) = \sum_{n=1}^{\infty} Y_n(x)\dot{\mu}_n(t). \quad (31)$$

From the equations (26), (27), (30), the BG representation of the mechanical model can be established as in the Fig. 10. It is worth noticing that the value of $Y_i(0)$ and $Y_i(L)$ obtaining from the equation (29), together with the model mass m_i and model stiffness k_i can be all calculated once the dimensions, Young's modulus, and density of the trilayer actuator are determined.

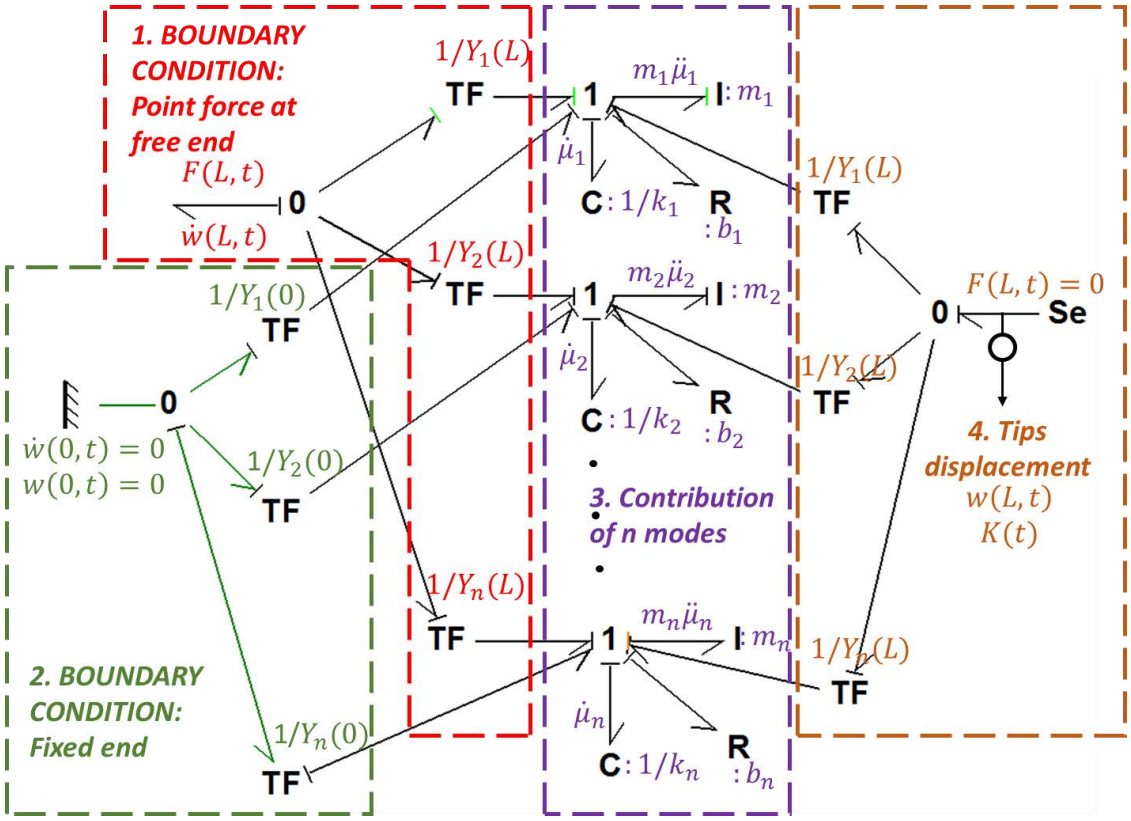


Fig. 10. BG representation of the mechanical model of the trilayer actuator, the block 1 (red color) indicates the point force F(L, t) obtaining from the electromechanical coupling matrix applying to the free end of the beam, the block 2 (green color) presents the boudary condition where one end of the beam is fixed, the block 3 (pink color) is a BG presentation of the equation (25), and finally the block 4 (orange color) introduces the method to extract the tips displacement of the beam w(L, t).

4.3.4 BG global models

In previous sections, the electrochemical model, the electrochemomechanical coupling, and the mechanical model have been established. To form the global model, the electrochemical

model is combined with the electrochemomechanical coupling in BG. The moment is exported from the coupling, and then transmitted into the mechanical model. For simplicity, the elements in the model are organized and divided into small sub-systems as depicted in Fig. 11.

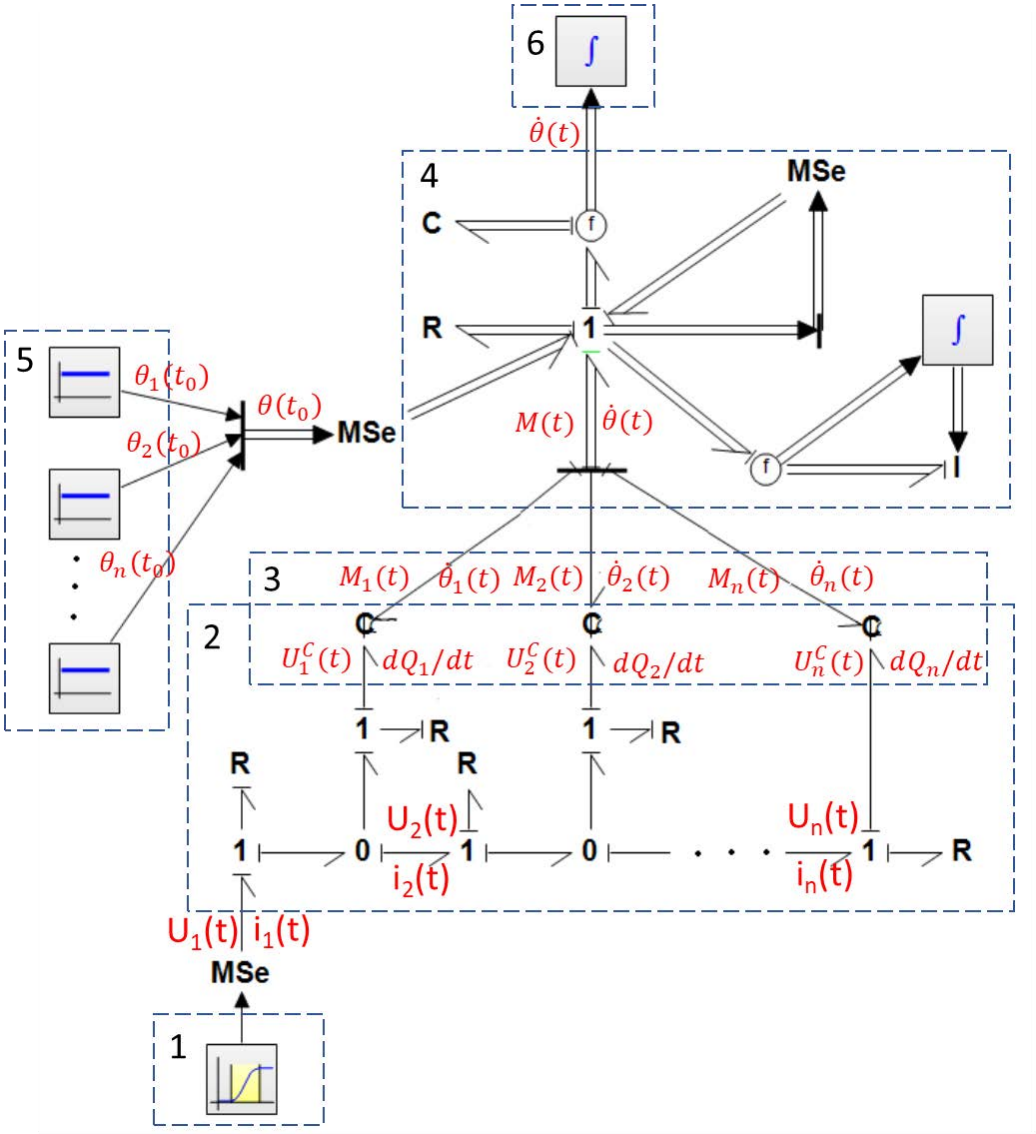


Fig. 11. CP actuator global model: 1. Voltage source, 2. Electrochemical model, 3. Coupling between electrochemical and mechanical part, 4. Mechanical model, 5. Boundary conditions: initial stress, 6. Displacement output.

It is worth noticing that the number of the RFE elements is (*n + 1*) whereas the SDE elements is *n*. Theoretically, the higher the number of RFE elements is, the more precise the simulation will be in comparison with the analytical method but at the expense of computational time. A rough estimation has shown that the relative error is 1.14 % and 0.41 % at first resonant frequency [47] with respect to the analytical method solution when the number of RFE is 4 (*n*

= 3) and 6 (*n = 5*), respectively. Within our proposed model, we have chosen two cases where 4 RFEs and 6 RFEs are used to investigate the accuracy of our model.

To establish the global linear model, the physical model, the electromechanical coupling, and the mechanical model obtained in previous section are connected. The elements in the model are organized and divided into small sub-systems as depicted in Fig. 12. The power transmitted through the different sub-system is followed which proves one advantage of the BG approach.

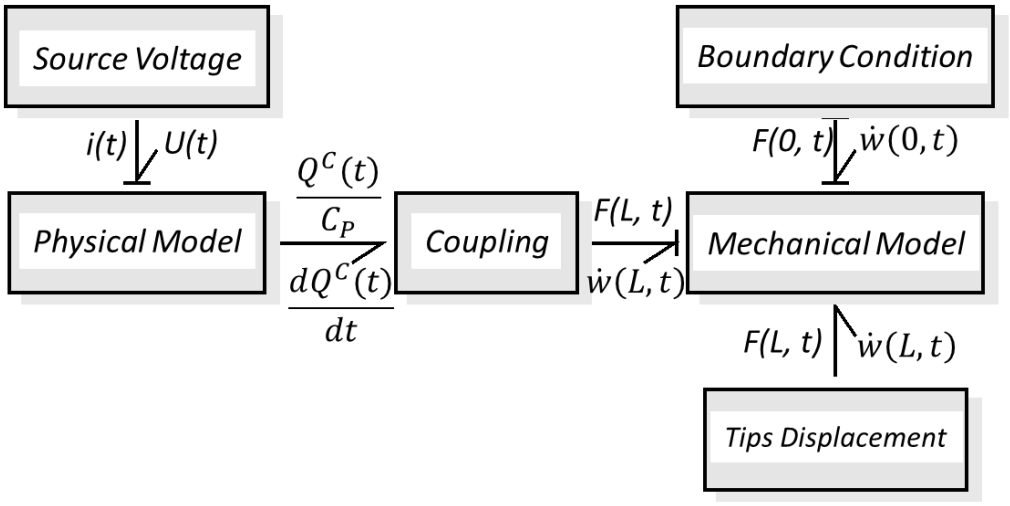


Fig. 12. Linear BG global model of CP actuators, where a source of voltage is employed as the input and the tips displacement of the beam is the output of the model.

Dissipation during one cycle is 12 µJ, which includes both electrochemical and mechanical dissipation. If all of this heat remains in the sample, the resulting increase in temperature is approximately 0.02 ^{0}C. As the actuator is operated continuously during 100 cycles, the increasing temperature would have reached up to 2 ^{0}C. However, since the trilayer is small and thin, the heat convection between the interface of the actuator and surrounding air is assumed to be sufficient to cool down the actuator and thermal effects are ignored.

However, in Bond Graph language, the coupling between thermal dissipation and thermal expansion could be modeled by introducing an electro-thermal-mechanical element. Continuing in this sense, another coupling in parallel to electro-chemo-mechanical coupling will be added into the current model.

4.4 Simulation tests

4.4.1 Software implementation

To implement the BG models, the 20-sim mechatronic modeling package, version 4.6 (Student License), was employed. This commercial software provides a simple method to graphically

build, simulate, and analyze the model behavior in multiple domains, and create control systems.

20-sim offers various toolboxes such as block diagrams, physical components, and BGs, and flexible links among others, enabling a quick and intuitive design.

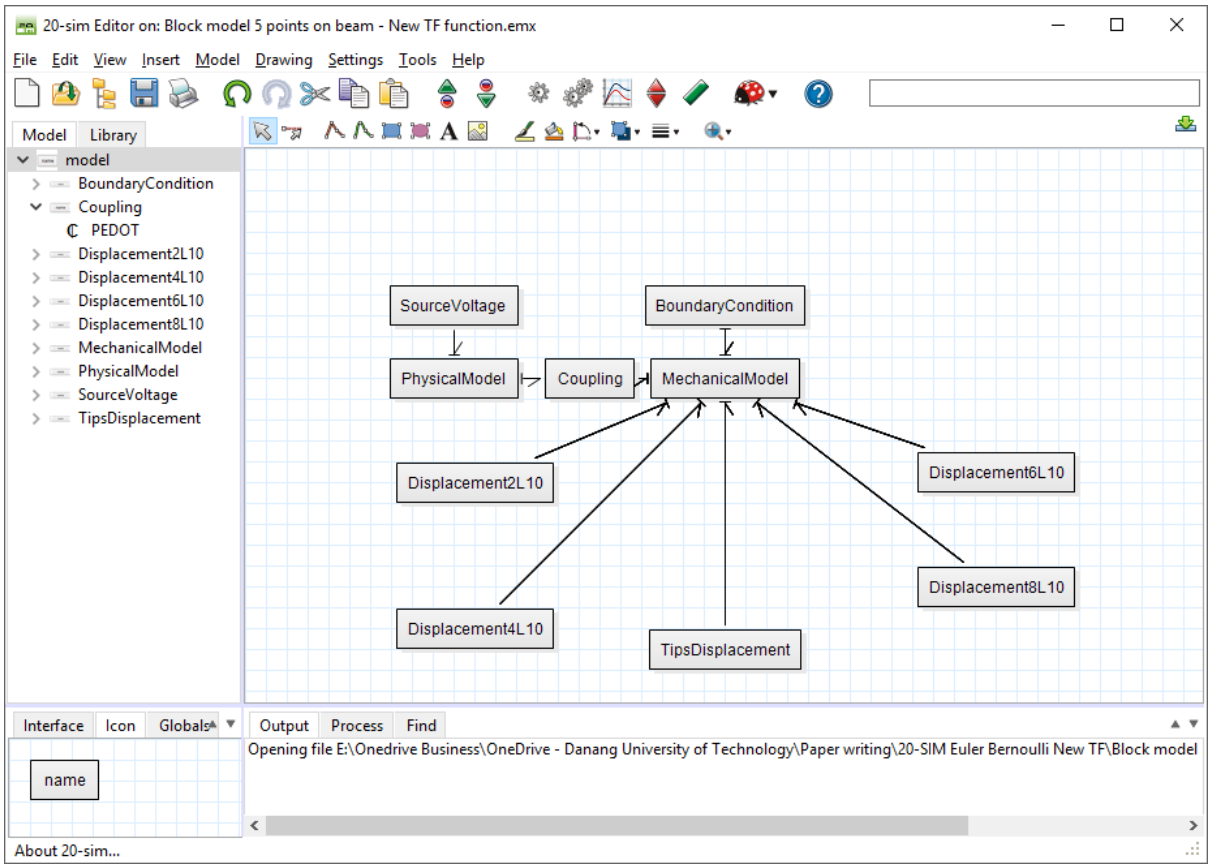


Figure 13. Interface of 20-sim simulation software

An example of 20-sim user interface is shown in Fig. 13, where the linear model of the trilayer actuator is organized into submodels.

4.4.2 Comparison between the linear and nonlinear simulations

In the previous section, two models, including a linear model and a nonlinear model, were built to predict the actuation behavior of the trilayer actuators. This section will deal with the advantages and disadvantages of both models by comparing simulations.

It is worth noting that to simulate the nonlinear model, parameters obtained from chapter 3 (section 3.5) are employed and processed into the built model. These also include the potential dependence of the electrical conductivity, the volumetric capacitance, and the Young's modulus of the PEDOT electrodes. For the linear model, by assuming the potential is V = 0, the required values can be extracted and described in table 3.

Table 3 Summary of derived parameters for the linear model

Length x width x PEDOT's thicknesses x NBR/PEO thickness (mm)	5 x 1 x 0.0035 x 0.01
PEDOT electrodes' volumetric capacitance (F/m³)	6.8×10^7
NBR/PEO ionic conductivity (S/m)	0.038
Strain-to-charge ratio (m³/C)	$\alpha = 3.6 \pm 0.5 \times 10^{-10}$
NBR/PEO Young's modulus (kPa)	329 ± 50
Trilayer actuator Young's modulus (MPa)	9.54
PEDOT Young's modulus (MPa)	12.98
Damping ratio	0.39
Beam density (kg/m³)	2000

In the first step, the output currents from the linear model and the nonlinear model (with 6 RFEs) under a step voltage of 2 V_{pp} and 0.1 Hz are compared (Fig. 14). Considering half cycle of the applied voltage, it is clear that during the first few seconds (< 2s) the current output from the 6 RFEs decays quicker than the linear model. An inspection on the nonlinear model shows that this quicker decay is due to the incorporation of PEDOT electronic resistance into the model, as a higher PEDOT electronic resistance induces a faster decay. At a longer response (>2s), the output currents from two models match quite well.

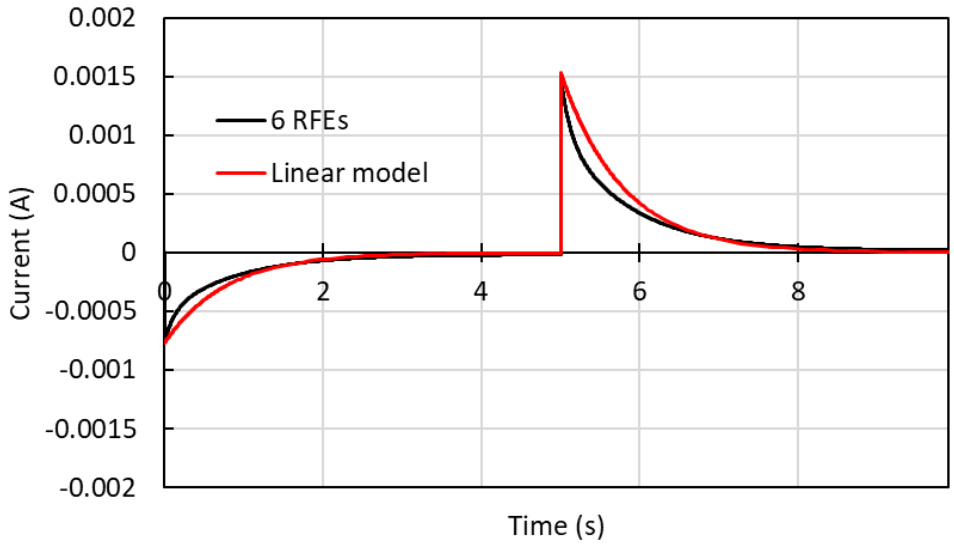


Fig. 14. Comparison between the output current of the linear model and nonlinear (6 RFEs) responses to a step voltage of 2 V_{pp} at f = 0.1 Hz

In next step, the bending displacement simulations of two models are compared (Fig. 15). At a small magnitude of the applied voltage (V_{pp} = 0.5 V, 1 V), these models show a similar actuation behavior, as expected. When the magnitude is increased (V_{pp} = 1.5 V, 2 V) the difference between two models is getting bigger. This can be explained as the Euler – Bernoulli beam theory cannot predict the beam displacement (*w (x, t)*) in *x* direction but only in *y* direction. The fact that the linear model cannot predict the large displacement is clearly shown in this comparison. However, the nonlinear model (with only 6 RFEs) can better accommodate large bending.

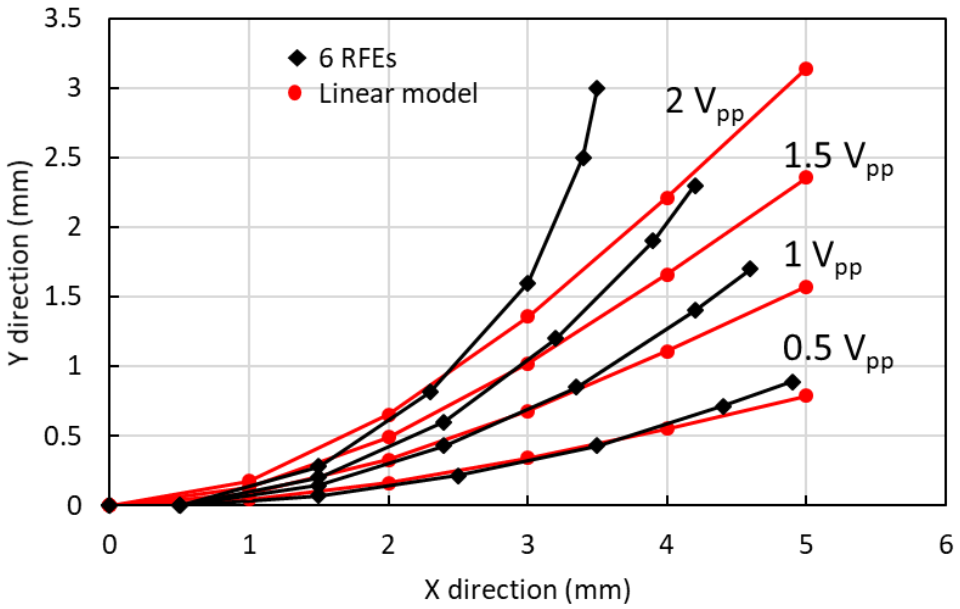


Fig. 15. Comparison between the linear model and the nonlinear model in bending displacement of the actuator in response to the step input voltage with various magnitudes

Two comparisons above visually show the disadvantages of the linear model against the nonlinear one. A full comparison between these two models is summarized in the table 4.

Table 4. Pros and cons of the linear model in comparison to the nonlinear model

Criterion	Linear model	Nonlinear model
Model establishing	Easy	Difficult
Required parameters	9	13 (3 are potential dependent) - much longer characterization
Time needed to run the model	Short time (30 s)	Long time (10 min)
Ability to implement nonlinear properties of materials	Impossible	Possible
Ability to implement asymmetric properties between the PEDOT electrodes	Impossible	Possible
Large displacement prediction	Impossible	Possible with high accuracy
Ability to predict voltage drop along the length of the beam	Impossible	Possible
Dynamic behavior prediction	Possible	Possible
Accessibility to information on energy and efficiency	Possible	Possible
Ability to implement for a complex structure	Possible (but may become complex in the process)	Possible

In general, the proposed nonlinear model is an advance relative to the linear model as it overcomes all the weaknesses available in the linear model. However, establishing and characterizing the necessary parameters for the nonlinear model requires much more time. The linear can be considered to use i) where a small displacement is expected, and ii) a small voltage magnitude is applied.

In this study, since the electrochemomechanical properties of PEDOT depend on its oxidation state, as demonstrated, and the trilayer actuator shows a large displacement responding to a voltage excitation, the proposed nonlinear model is selected for further study in the next sections.

4.5 Comparison to experimental tests

In the previous section, a nonlinear BG model was proposed to predict actuation behavior and the parameters required for the proposed model were characterized. To evaluate the agreement between the BG model and the experimental results, a set of experiments has

been performed. The geometry of the trilayer actuator used in these characterizations is equal to *length x width x thickness = 5 mm x 1 mm x 0.017 mm*, unless otherwise is stated. First, the simulation and experimental current outputs will be compared, followed by the mechanical responses. Then an analysis of performance is made to identify the critical parameters affecting it. Finally, the energy efficiency will be investigated.

4.5.1 Time domain responses

Fig. 16 shows a trilayer actuator under a square wave voltage excitation. The asymmetry between the top and the bottom PEDOT electrode layers is demonstrated via an initial curved beam state (Fig. 16b). This curved state is due to stresses inside the trilayer. To account for this bending in the neutral state in comparisons with model preditions below, the model was used to find the relative change in curvature, which is added to the initial curvature of in the simulation response.As seen in Fig. 16a, beam deflects leftwards when -1.1 V is applied to the left side (bottom) electrode and +1.1 V is applied to the right side top PEDOT electrode layer. As the voltage direction is reversed, the beam bends back until it is straight (Fig. 16c).

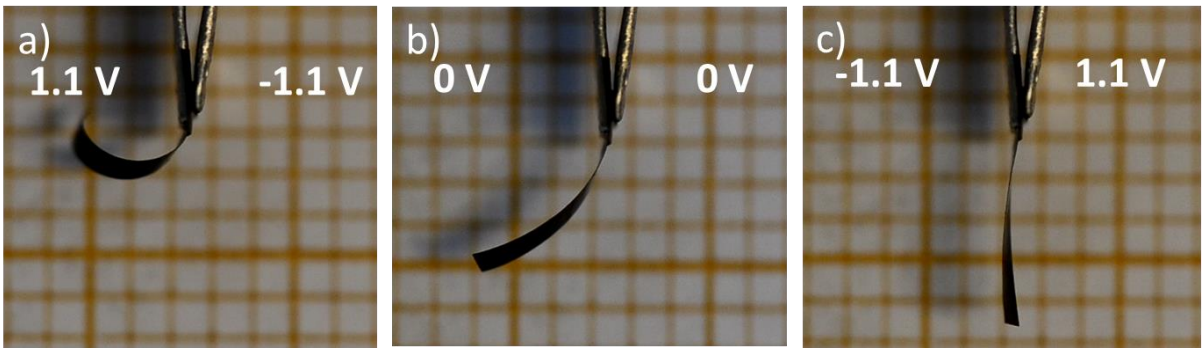


Fig. 16. Trilayer actuator under voltage excitation: a) Top PEDOT electrode voltage: -1.1 V, Bottom PEDOT electrode: 1.1 V, b) neutral state, c) Top PEDOT electrode: 1.1 V, Bottom PEDOT electrode: -1.1 V.

The input current and displacement of the beam were captured and compared with model predictions. As demonstrated in the previous section, the PEDOT electrical conductivity, the PEDOT volumetric capacitance, and the Young's modulus of the trilayer actuator are dependent on the applied potential, and this dependence was fitted with a polynomial to improve the convergence when solving the BG model. All voltage dependencies were incorporated into the proposed BG model.

A triangular wave allowing more precise position control followed by a square wave voltage providing a fast actuation response was applied to the trilayer actuator (Fig. 17a). The recorded current was then compared with the output current from the electrochemical sub-model.

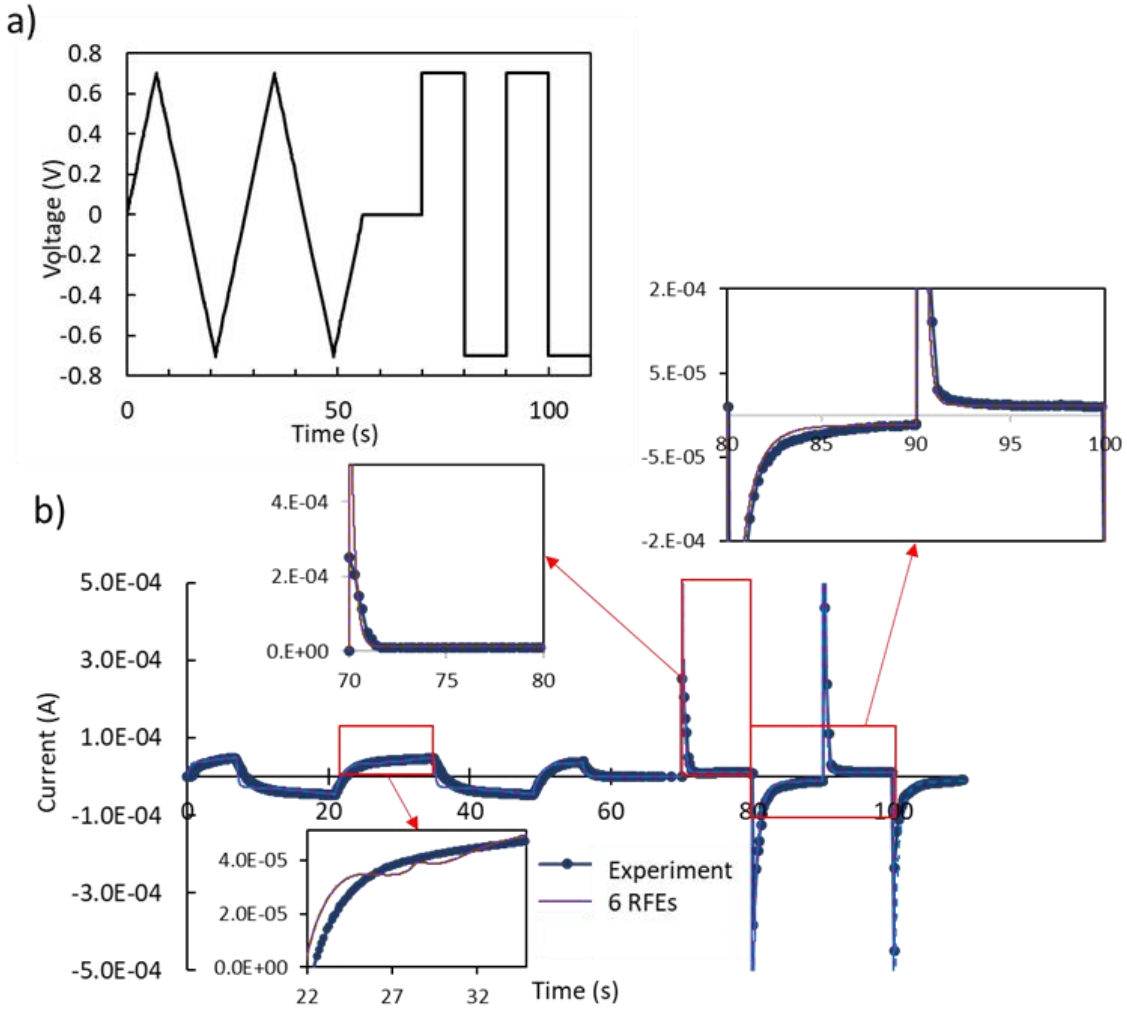


Fig. 17. a) Triangular wave and rectangular wave applied voltage, b) Measured and simulation current response

As shown in Fig. 17b, the simulated current (4 RFEs and 6 RFEs simulated current are indistinguishable, so only the result of 6 RFEs is plotted) matched the experimental results quite well, and there is an asymmetry in the output current between two halves cycles of the applied voltage. This asymmetry is due to the dependence of the electronic conductivity of the PEDOT electrodes on the applied potential. In the case of a step voltage, the response time and the amplitude of the current of the models were slightly faster than in the experiment. This is due to the limited sampling rate (5 points/s) of the device used to measure the current.

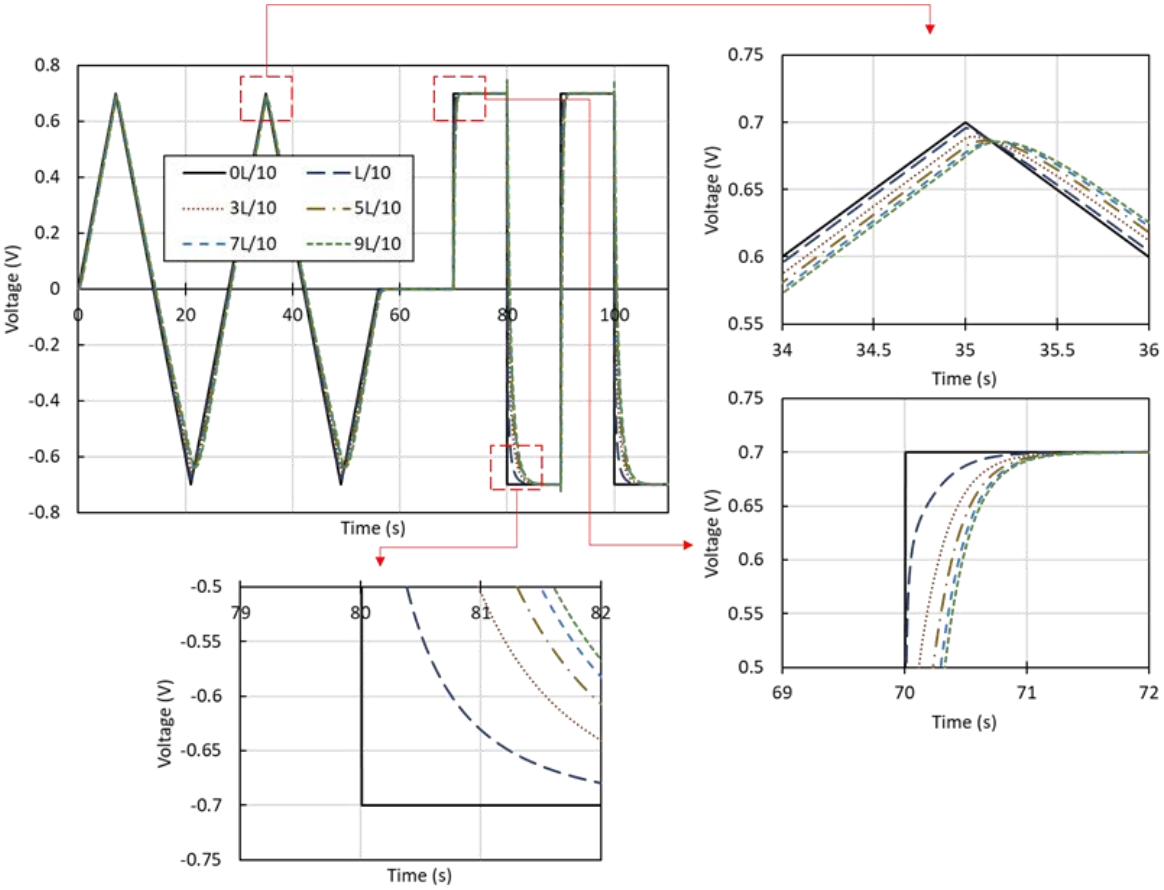


Fig. 18. Modeled voltage drops along the length of the beam due to the existence of electrical resistance of PEDOT electrodes. The black curve is the voltage seen at the fixed end of the cantilever where electrical contact is made. The dashed green line is the predicted voltage as seen at 0.9 of the length, and the others are in between.

Fig. 18 depicts the modeled drop in voltage along the length of the beam. In the step response, a significant reduction in the voltage is observed at the position x = L/10 in comparison with the applied voltage (at the position x = 0), close to the clamping point, at short times (< 0.3 s). For longer times (> than half a second), the drop becomes negligible. The drop increases further away from the clamping point, as expected. However, in the ramp response, it is clear that the reduction in voltage is not significant (around 7% at the tip of the beam), and the maximum voltages are shifted to the right showing a delay or a slower actuation response as we go further away from the clamping point. An asymmetric voltage between the two half cycles of the applied voltage is also observed, which is due to the variation in PEDOT electronic conductivity following the change in voltage.

To evaluate the ability of the model to track the mechanical behavior of the trilayer actuator, the beam displacement was recorded using a camera to determine the radius of curvature and the bending strain as a function of time and position along the length of the beam. The bending induced strain was determined from the radius of curvature, which is calculated from

the rotation angle θ_i of each RFE. In the first set of experiments, the magnitude of the square wave voltage was varied from 0.5 Vpp to 3 Vpp, while the frequency was held at 0.1 Hz. Fig. 19 shows quite good agreement between the measured and the theoretical strain in both cases (where the beam was divided into 4 RFEs (3 SDEs) or 6 RFEs (5 SDEs)), except for the point where the voltage is 3 Vpp. This difference is due to a change in the electrical and the mechanical properties of the trilayer actuator as a result of the irreversible degradation in polymer chains inside the electrodes [57]. However, this change was not considered in the proposed model. Continuously operating the actuator at this high voltage will significantly decrease its lifetime. As it has been observed by the authors, after tens of cycles of deflection at this high applied voltage, the magnitude of displacement will quickly decrease to zero.

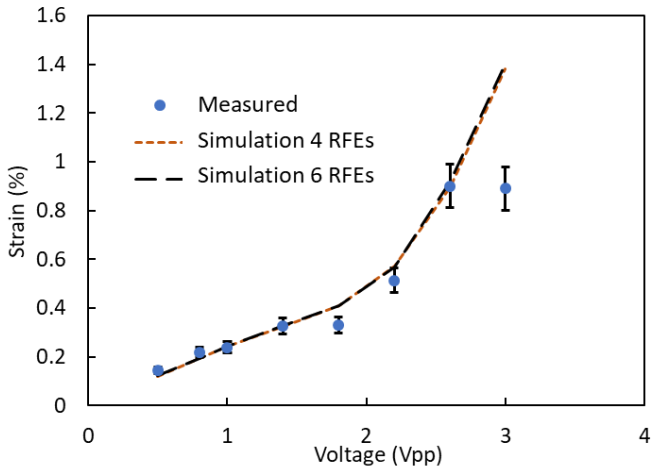


Fig. 19. Comparison between the simulations and the experiments on the strain as a function of the magnitude of applied voltage at a constant frequency of 0.1 Hz

4.5.2 Frequency responses

An advantage of the proposed model is the ability to incorporate the damping coefficient and the mass of the actuator. This becomes particularly important at high frequencies and short times, as is now shown.

In a second set of experiments, the frequency of the applied square wave voltage was varied between 0.05 Hz and 15 Hz while the magnitude was constant at 2.2 Vpp (Fig. 20a). Fig. 20a shows the magnitude of the error between the model and the simulation as a function of frequency. In the simulations, the damping coefficient was varied to study its effect on the goodness of fit. The value measured in Chapter 3 is 0.39, which also gives the best match to the data. To simplify these two figures, the 4 RFEs curves have been removed from the graph as they are very similar to the 6 RFEs curves. Once again, a good agreement between the simulations (indicated by "Simulation 6 RFEs: η = 0.39" curve in Fig. 20a, b and experiments is observed. It is worth noting that this damping ratio η = 0.39 was obtained via a vibration

measurement [58]. However, when the frequency increases to over 5 Hz, a difference can be seen (a relative error of approximately 15%). This inaccuracy may come from the method used to measure the strain based on capturing actuation (limited frame rate: 24fps) and imaging analysis which is not very accurate at high frequency.

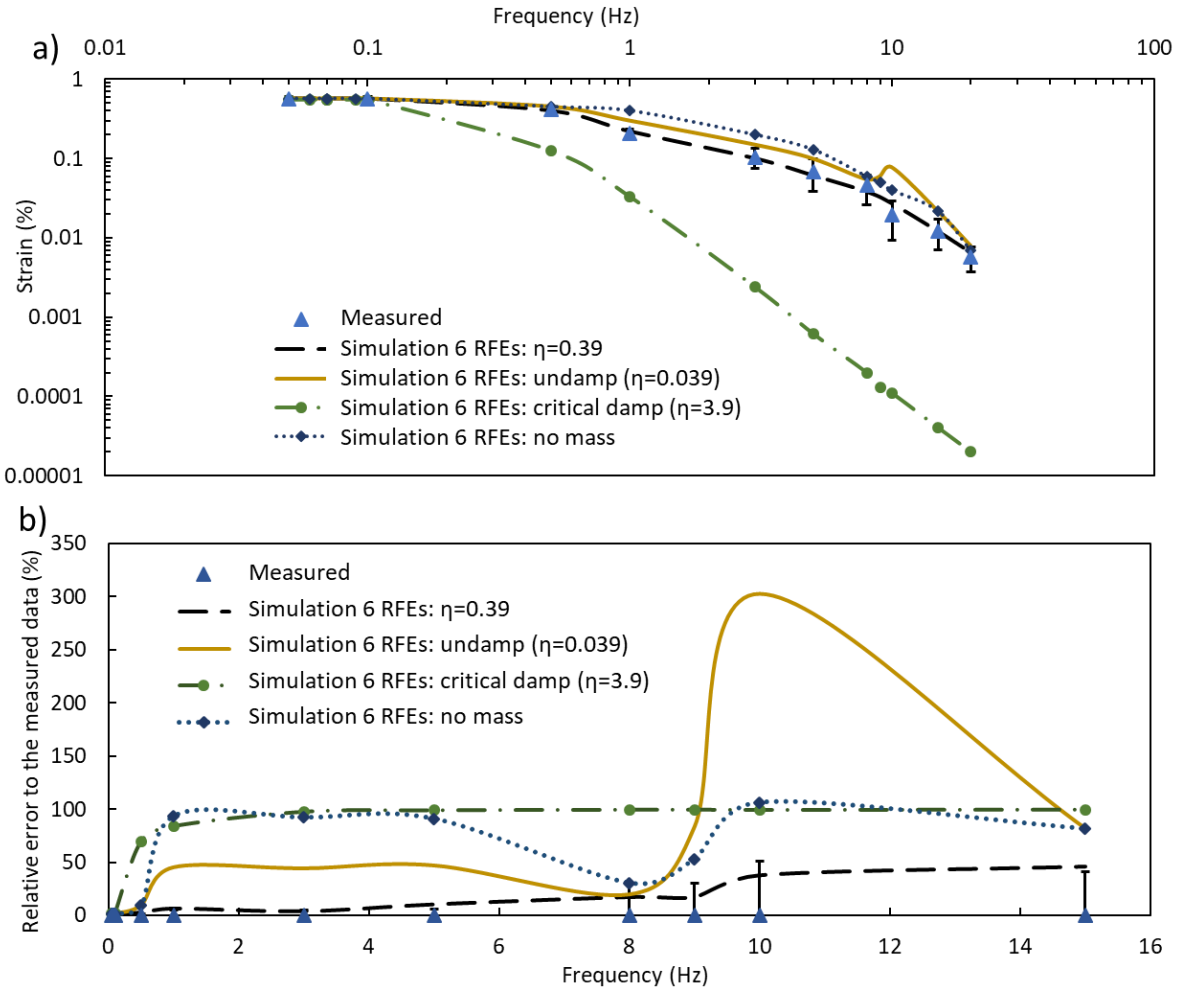


Fig. 20. a) Comparison between the simulations and the experiments on the strain as a function of the frequency of applied voltage at a constant magnitude of ±1.1 V, b) The relative error of the simulations compared to the measured data.

Damping shows a significant effect on the strain of the actuator at intermediate and high frequency (> 0.5 Hz). In the case of overdamping, where the assumed damping ratio (η = 3.9) is ten times higher than the measured value [58], the strain drastically drops as the frequency is increased and the relative error is around 100%. A small increase in strain is seen when the damping ratio is assigned as a nearly undamped (η = 0.039) situation, and the first resonant frequency of the actuator is clearly visible in this case as there is an increase in strain around 10 Hz (Fig. 20a, b). When mass of the actuator is removed from the model, there is a clear

overestimation of strain by the simulation (by approximately 100%), demonstrating the importance of including mass in the simulations at moderate to high frequencies.

The model has the ability to predict the dynamic mechanical response of the beam. A voltage of 2.2 Vp at 0.1 Hz was applied to the trilayer. The beam was previously held at -2.2 V (top vs. bottom electrode) in the almost straight position depicted in Fig. 16c. At the time 0 s, the voltage reserved the direction (Fig. 16a) and the dynamic behavior of the beam was captured at time steps of 0 s, 1 s, 3 s, and 5 s, and then compared to the simulation results. As shown in Fig. 21, the predicted results follow the beam movement at those time points.

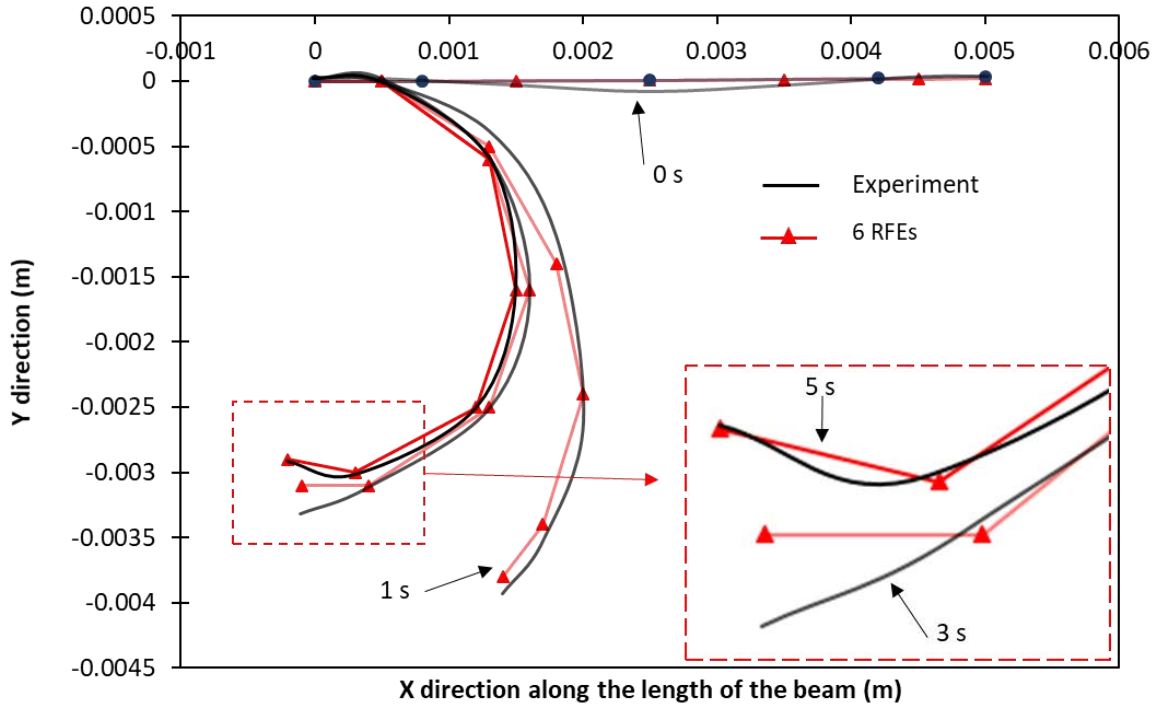


Fig. 21. Comparison between the experiment and the simulation in terms of the dynamic mechanical behavior of the beam subjected to a voltage excitation of 2.2 Vpp at 0.1 Hz.

In general, the nonlinear model shows a good agreement with the experimental results. In comparison with previous studies, the biggest advantage of our proposed model is the ability to implement the nonlinear behavior of the PEDOT electrical conductivity and volumetric capacitance and the Young's modulus of the trilayer actuator due to its dependence on the oxidation state. The integration of the mass and the damping effect into the proposed model allows prediction of the actuation behavior at high frequency – which has become important as high actuation rates are reached [52]. The ability to extract the nonlinear dynamic mechanical displacement of the beam is another benefit of the model, which allows us to track beam motion as a function of time.

4.6 Parameter sensitivity and power performance analysis

The previous sections have confirmed the ability to predict actuator performance of the model in both time and frequency domains. Another advantage of the model is that it can provide an insight into actuator performance as a function of its critical parameters, which have been characterized. For example, Fig. 22 gives an assessment of how sensitive the active strain difference (proportional to the deflection) is to Young's modulus, PEDOT electrical conductivity, SPE ionic conductivity, and the length of the actuator at both low (Fig. 22a) and high frequency (Fig. 22b). This result suggests that for the actuator geometry studied, reducing elastic modulus will have a significant effect on deflection, while the influence of the length is very important at high frequency. Not surprisingly, conductivity has little effect on strain at low frequencies of operation, but this effect becomes large at high frequencies.

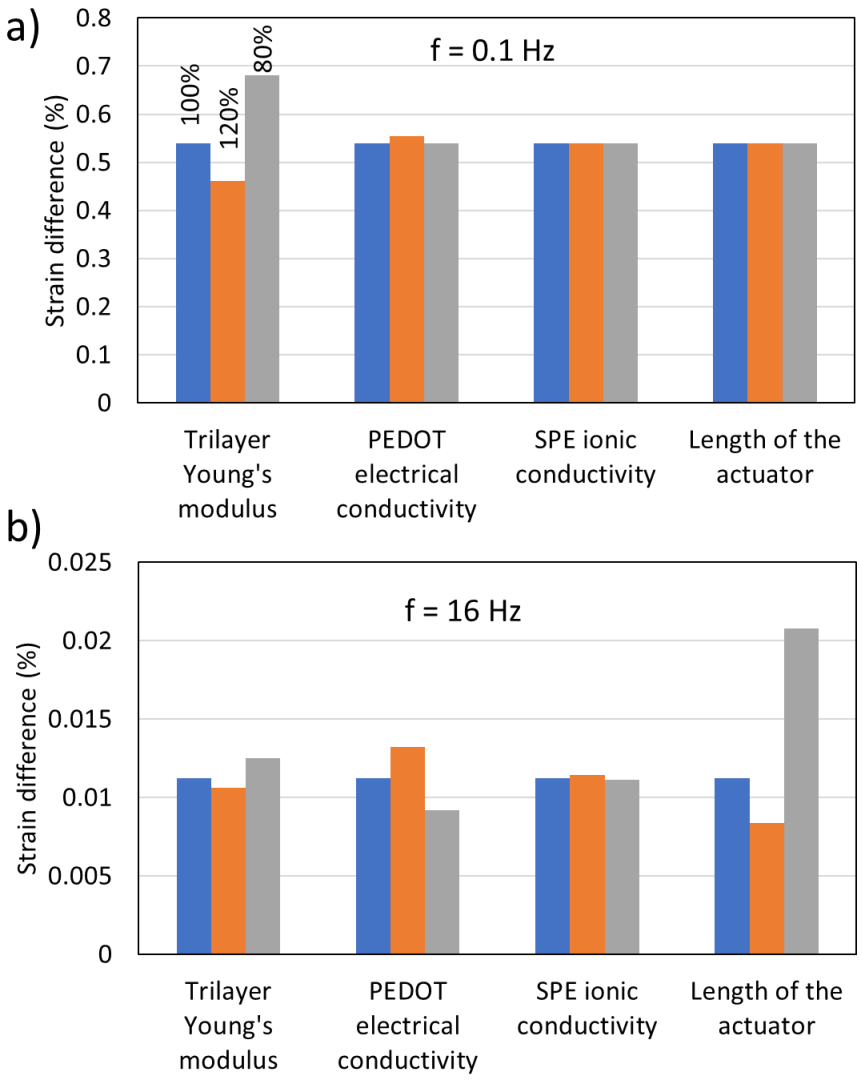


Fig. 22. Key factors affecting the actuator displacement under a square wave voltage (Vpp = 2.4 V), a) at low frequency f = 0.1 Hz, and b) at high frequency f = 16 Hz. For each parameter,

three columns from left to right represent for its real value (blue column), its value increased by 20% (orange column), and its value reduced by 20% (grey column).

The value of these parameters have been adjusted by ± 20% of their values while the others were maintained constant. It is clear that at low frequency (f = 0.1 Hz) of applied voltage, an increase of the PEDOT electrical conductivity would lead to very little increase in strain difference while a stiffer beam would reduce displacement. SPE ionic conductivity shows a small effect on the beam displacement, as expected. At high frequency (f = 16 Hz), while the effect of the Young's modulus remains similar, the PEDOT conductivity has a great influence on the strain difference, and the increase of length reduces deformation. The latter are expected due to the high currents seen by the trilayer at short times, and hence the large voltage drops along the length.

In addition, the proposed BG model allows ready access to information about the energy stored, dissipated, and transmitted – in this case electrochemical and mechanical energies. Considering half a period of the applied voltage (0.1 Hz at 2 Vpp), Fig. 23 shows the evolution of the electrochemical (left) and the much smaller mechanical (right) component energies with time, including both stored and dissipated contributions. As expected for a system composed of resistors with capacitors in series, the input energy increases with time until the energy storage is complete (Fig. 23a). Mechanical energy also rises and then saturates, with the same time constant (Fig. 23b).

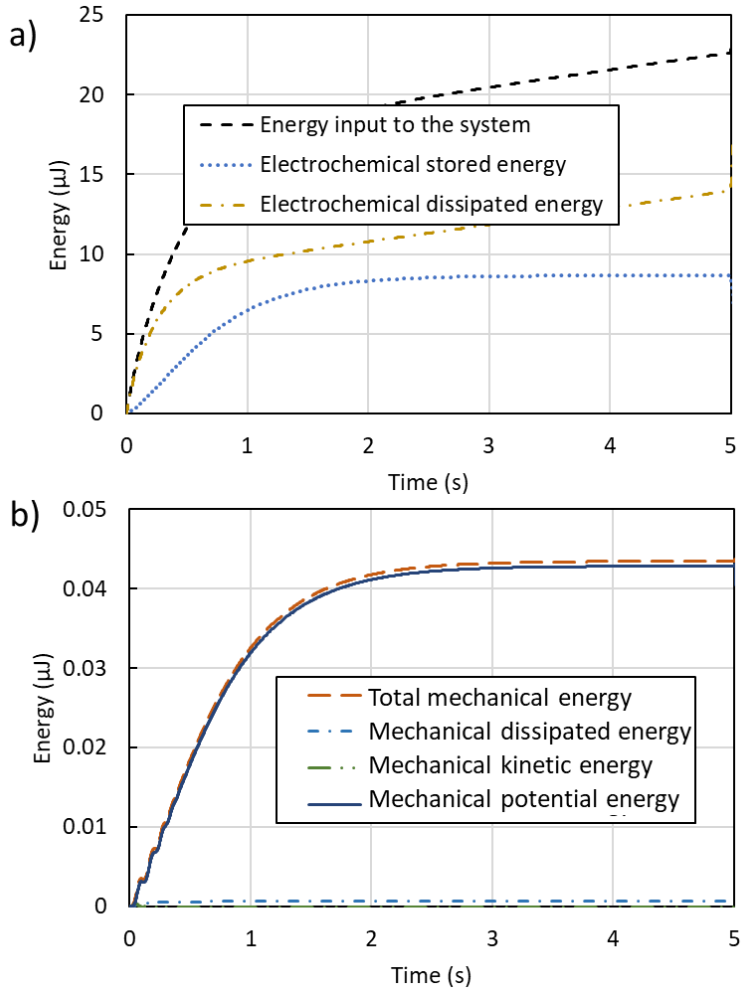


Fig. 23. Evolution of energy over half a period of applied voltage: a) In the electrochemical part, b) In the mechanical part.

Fig. 24 replots the stored and dissipated energy components of energy as fractions of the total input energy. From this plot it is evident that the mechanical energy represents about 0.2% of the total. 40 % of the input electrical energy is stored, which is not surprising since a 50:50 split is what would be expected from a simple series RC circuit that is charged with a step voltage input. A slow ramp input, in which currents are kept small to minimize iR drop, would lead to a significantly higher component of stored energy. On the mechanical side, kinetic energy and dissipation loss accounting for tiny portion, which depends on speed, rise quickly and then decays again as the actuator accelerates and then decelerates. The stored mechanical energy is elastic potential energy that accumulates as the beam bends, and is more than 99% of the total. Dissipation losses can even be reduced, once again, by actuating slower. The relatively small fraction of electrochemical energy converted to mechanical is consistent with previous reports showing a small electromechanical coupling coefficient [10, 41, 59]. The efficiency however need not be so small, especially in slow charging situations where much of the input electrical energy can be recovered during discharge. Previous work shows that overall efficiency can exceed 10 %, if electrical energy is recovered [10].

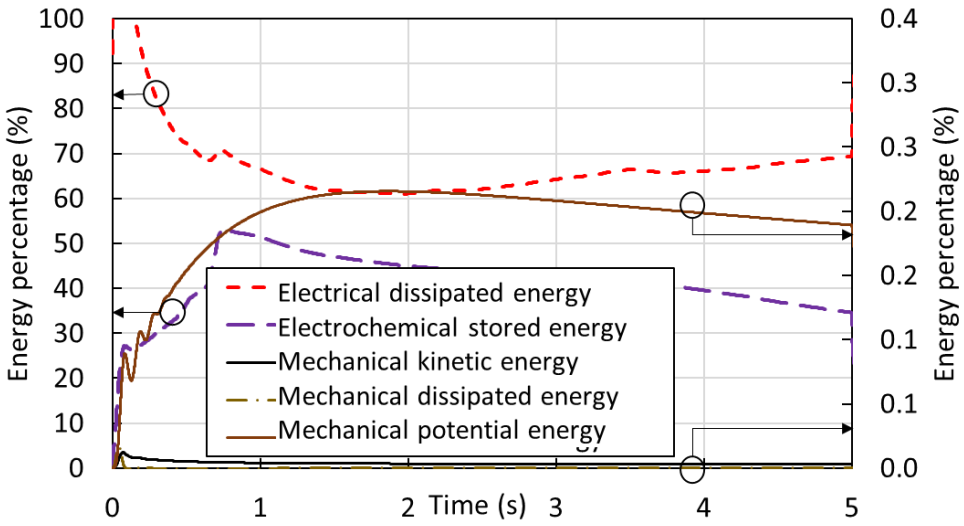


Fig. 24. Instantaneous electrical to mechanical coupling.

Using the proposed model, one can use to model to explore how to improve the energy conversion from electrical into mechanical. Here, a slow ramp voltage is used instead of the step voltage. The simulation results show that an input voltage of 100 mV/s with a frequency of f = 0.05 Hz increases the electrochemical stored energy and mechanical potential energy up to 60 % and 0.4 %, respectively. The switch from a step to a ramp doubles the coupling in much the same way as charging an RC circuit with a ramp rather than a step increases charging efficiency by reducing the ohmic losses. Furthermore, a slower ramp of 5 mV/s with a frequency f = 0.0025 Hz is predicted to increase the electrochemical stored energy to 90% and the mechanical potential energy to 3%.

The conversion to mechanical energy provides a value for the electrochemical internal coupling. In practice we want the mechanical work to be applied to an external load. The energy in the trilayer beam needs to be transferred to an external mass, spring or other type of load, which further reduces the overall electromechanical coupling, since not all of the elastic potential energy in the beam will be passed on.

Coupling is poor in these actuators. Most of the input energy is stored electrochemically, with only a small fraction converted to work. The good news is that, if we can recover the stored electrical energy in each charge/discharge cycle, the efficiency can be much higher than the electromechanical coupling. For example, in the full charge/discharge cycle at 5 mV/s, 90 % of energy is stored electrochemically. Assuming we can recover 90 % of this stored energy on discharge, then we have lost 14 % of the input energy. The upper bound on efficiency is then the output mechanical energy percent divided by the lost energy percent (3%/14%). This gives an overall electrical to mechanical efficiency of 21 %. This percentage will be reduced by the coupling between the beam and the external load, but nonetheless energy recovery dramatically improves efficiency.

Furthermore, the electrochemical lost can be reduced by increasing the thickness of the separator (NBR/PEO) to avoid the contact between two PEDOT electrodes. And an increase in the strain-to-charge ratio by investigating different materials for the electrodes and electrolyte will efficiently increase the electromechanical coupling.

4.7 Conclusion

In this chapter, a nonlinear dynamic model and a simpler dynamic linear model have been proposed to simulate the actuation of ultrathin trilayer actuators. A comparison between these two models has shown that the linear model is simple to build and easier to characterize all of its require parameters. However, it is most suitable to predict small displacements, and losses accuracy at large displacements and voltages.

The proposed nonlinear model showed advances to the existing work on trilayer actuators in that it can precisely predict a nonlinear dynamic actuation with an ability to implement nonlinear electrochemical and mechanical properties of the materials: PEDOT electrical and ionic conductivities; volumetric capacitance values; and Young's modulus variation. In addition, it accounted for the mass and damping associated with the beam. All physical characteristics used in the model were measured.

The concordance between the simulation and experimental results in both time and frequency domains confirms the ability to predict the bending of the trilayer actuator. Moreover, the approach is represented in Bond Graph language, providing a simple way to access the energy information, evaluate the critical parameters affecting the performance of the actuator, and allowing an insight into the phenomena occurring in the ionic actuator.

In addition, the model can also be used to optimize the design of the transducer before it is fabricated. The simulation software allows the input parameters such as dimensions, and material properties (conductivities, Young's modulus, …) to be varied over defined ranges to help define the range that will produce the desired response. These values will become a guideline for the designer to tune the transducer properties. The tool can also be used to determine which material properties most limit response in order to drive material development or enable the evaluation of emerging materials. For example, a new material may feature a higher strain to charge ratio, but also a lower ionic conductivity. The model is capable of exploring the implications of this change.

For the future perspective, the proposed nonlinear model is theoretically suitable to predict even higher frequency actuation. In addition, the model was built based on Bond Graph language, providing at first a possibility to integrate it into a real actuator controlling system and second, to develop a more complex model to control not only a single beam but also a complicated geometry. These possibilities can bring more power to the model.

[1] D. Karnopp, R.C. Rosenberg, Analysis and simulation of multiport systems; the bond graph approach to physical system dynamics, Cambridge, Mass.,: M.I.T. Press; 1968.
[2] D. Karnopp, System dynamics : modeling and simulation of mechatronic systems, Hoboken: Wiley; 2012.
[3] F. Meisam, S. Farrokh, N. Naser, F. Adelyne, P. Cédric, T.M.N. Giao, V. Frédéric, D.W.M. John, Characterization and dynamic charge dependent modeling of conducting polymer trilayer bending, Smart Materials and Structures, 25(2016) 115044.
[4] G.M. Spinks, L. Liu, G.G. Wallace, D. Zhou, Strain Response from Polypyrrole Actuators under Load, Advanced Functional Materials, 12(2002) 437-40.
[5] C.H. Nguyen, G. Alici, G.G. Wallace, Modelling trilayer conjugated polymer actuators for their sensorless position control, Sensors and Actuators A: Physical, 185(2012) 82-91.
[6] F. Carpi, E. Smela, Biomedical applications of electroactive polymer actuators, Chichester, West Sussex: John Wiley & Sons; 2009.
[7] F. Carpi, Electromechanically active polymers, 1st ed., Place of publication not identified: Springer; 2016.
[8] Y. Fang, X. Tan, G. Alici, Robust Adaptive Control of Conjugated Polymer Actuators, IEEE Transactions on Control Systems Technology, 16(2008) 600-12.
[9] J.D. Madden, P.G. Madden, I.W. Hunter, Polypyrrole actuators: modeling and performance, 2001, pp. 72-83.
[10] J.D.W. Madden, Conducting polymer actuators: Massachusetts Institute of Technology; 2000.
[11] S. John, G. Alici, C. Cook, Frequency response of polypyrrole trilayer actuator displacement, SPIE Smart Structures and Materials + Nondestructive Evaluation and Health Monitoring, SPIE2008, p. 8.
[12] A.D. Santa, D.D. Rossi, A. Mazzoldi, Characterization and modelling of a conducting polymer muscle-like linear actuator, Smart Materials and Structures, 6(1997) 23.
[13] J.D.M. Tina Shoa, Chi-Wah Eddie Fok, Tissaphern Mirfakhrai, Rate Limits in Conducting Polymers, Advances in Science and Technology, 61(2008) 7.
[14] C.H. Nguyen, G. Alici, G.G. Wallace, Modelling trilayer conjugated polymer actuators for their sensorless position control, Sensors and Actuators, A: Physical, 185(2012) 82-91.
[15] C.-H. Tso, J.D. Madden, C.A. Michal, An NMR study of PF6− ions in polypyrrole, Synthetic Metals, 157(2007) 460-6.
[16] M.J. Ariza, T.F. Otero, Ionic diffusion across oxidized polypyrrole membranes and during oxidation of the free-standing film, Colloids and Surfaces A: Physicochemical and Engineering Aspects, 270-271(2005) 226-31.
[17] M. Farajollahi, A. Usgaocar, Y. Dobashi, V. Woehling, C. Plesse, F. Vidal, F. Sassani, J.D.W. Madden, Nonlinear Two-Dimensional Transmission Line Models for Electrochemically Driven Conducting Polymer Actuators, IEEE/ASME Transactions on Mechatronics, 22(2017) 705-16.
[18] G. Alici, B. Mui, C. Cook, Bending modeling and its experimental verification for conducting polymer actuators dedicated to manipulation applications, Sensors and Actuators A: Physical, 126(2006) 396-404.
[19] G. Alici, N.N. Huynh, Predicting force output of trilayer polymer actuators, Sensors and Actuators A: Physical, 132(2006) 616-25.
[20] A.A.A. Moghadam, M. Majid, T. Keivan, T. Masoud, Analytical dynamic modeling of fast trilayer polypyrrole bending actuators, Smart Materials and Structures, 20(2011) 115020.
[21] A.A.A. Moghadam, W. Hong, A. Kouzani, A. Kaynak, R. Zamani, R. Montazami, Nonlinear dynamic modeling of ionic polymer conductive network composite actuators using rigid finite element method, Sensors and Actuators A: Physical, 217(2014) 168-82.
[22] X. Wang, B. Shapiro, E. Smela, Development of a Model for Charge Transport in Conjugated Polymers, The Journal of Physical Chemistry C, 113(2009) 382-401.
[23] J.G. Martinez, T.F. Otero, Mechanical awareness from sensing artificial muscles: Experiments and modeling, Sensors and Actuators B: Chemical, 195(2014) 365-72.

[24] V. Venugopal, H. Zhang, R. Northcutt, V.B. Sundaresan, A thermodynamic chemomechanical constitutive model for conducting polymers, Sensors and Actuators B: Chemical, 201(2014) 293-9.
[25] M. Szczotka, A modification of the rigid finite element method and its application to the J-lay problem, Acta Mechanica, 220(2011) 183-98.
[26] G. Nishida, K. Takagi, B. Maschke, T. Osada, Multi-scale distributed parameter modeling of ionic polymer-metal composite soft actuator, Control Engineering Practice, 19(2011) 321-34.
[27] B.J. Yi, I. Busch-Vishniac, Modeling of EAPs as multiple energy domain systems: A bond graph approach, Proceedings of SPIE - The International Society for Optical Engineering2006.
[28] T.A. Bowers, MSc thesis title: Modeling, Simulation, and Control of a Polypyrrole-Based Conducting Polymer Actuator: Massachusetts Institute of Technology; 2004.
[29] M. Bentefrit, S. Grondel, C. Soyer, A. Fannir, E. Cattan, J.D. Madden, T.M.G. Nguyen, C. Plesse, F. Vidal, Linear finite-difference bond graph model of an ionic polymer actuator, Smart Materials and Structures, 26(2017) 095055.
[30] T.N. Nguyen, K. Rohtlaid, C. Plesse, G.T.M. Nguyen, C. Soyer, S. Grondel, E. Cattan, J.D.W. Madden, F. Vidal, Ultrathin electrochemically driven conducting polymer actuators: fabrication and electrochemomechanical characterization, Electrochimica Acta, 265(2018) 670-80.
[31] G.A. Snook, P. Kao, A.S. Best, Conducting-polymer-based supercapacitor devices and electrodes, Journal of Power Sources, 196(2011) 1-12.
[32] F. Vidal, C. Plesse, D. Teyssié, C. Chevrot, Long-life air working conducting semi-IPN/ionic liquid based actuator, Synthetic Metals, 142(2004) 287-91.
[33] C.M. Proctor, J. Rivnay, G.G. Malliaras, Understanding volumetric capacitance in conducting polymers, Journal of Polymer Science Part B: Polymer Physics, 54(2016) 1433-6.
[34] T. Shoa, J.D. Madden, N.R. Munce, V. Yang, Analytical modeling of a conducting polymer-driven catheter, Polymer International, 59(2010) 343-51.
[35] J.D. Madden, P.G. Madden, I.W. Hunter, Conducting polymer actuators as engineering materials, SPIE's 9th Annual International Symposium on Smart Structures and Materials, SPIE2002, p. 15.
[36] J.C.E. Marin S. Halper, Supercapacitors: A Brief Overview, MITRE Nanosystems Group, 2006.
[37] I.J. Busch-Vishniac, H.M. Paynter, Bond graph models of acoustical transducers, Journal of the Franklin Institute, 328(1991) 663-73.
[38] P.G.A. Madden, Development and Modeling of Conducting Polymer Actuators and the Fabrication of a Conducting Polymer Based Feedback Loop: MASSACHUSETTS INSTITUTE OF TECHNOLOGY; 2003.
[39] J.D.W. Madden, PhD thesis title: Conducting Polymer Actuators, Massachusetts Institute of Technology2000.
[40] T.F. Otero, Biomimetic Conducting Polymers: Synthesis, Materials, Properties, Functions, and Devices, Polymer Reviews, 53(2013) 311-51.
[41] T. Shoa, J.D.W. Madden, T. Mirfakhrai, G. Alici, G.M. Spinks, G.G. Wallace, Electromechanical coupling in polypyrrole sensors and actuators, Sensors and Actuators, A: Physical, 161(2010) 127-33.
[42] N. Festin, C. Plesse, C. Chevrot, D. Teyssié, L. Josselin, P. Pirim, F. Vidal, Actuation and Sensing properties of Electroactive Polymer Whiskers, Procedia Computer Science, 7(2011) S4-S7.
[43] Y. Wu, G. Alici, J.D.W. Madden, G.M. Spinks, G.G. Wallace, Soft Mechanical Sensors Through Reverse Actuation in Polypyrrole, Advanced Functional Materials, 17(2007) 3216-22.
[44] S.A. Sina, H.M. Navazi, H. Haddadpour, An analytical method for free vibration analysis of functionally graded beams, Materials & Design, 30(2009) 741-7.
[45] A. Labuschagne, N.F.J. van Rensburg, A.J. van der Merwe, Comparison of linear beam theories, Mathematical and Computer Modelling, 49(2009) 20-30.
[46] G.R. Bhashyam, G. Prathap, Galerkin finite element method for non-linear beam vibrations, Journal of Sound and Vibration, 72(1980) 191-203.
[47] E. Wittbrodt, I. Adamiec-Wójcik, S.a. Wojciech, SpringerLink ebooks - Engineering (2006), Dynamics of flexible multibody systems : rigid finite element method, Berlin: Springer; 2006.
[48] A.A. Shabana, Flexible Multibody Dynamics: Review of Past and Recent Developments, Multibody System Dynamics, 1(1997) 189-222.

[49] I.A.-W. Edmund Wittbrodt, Stanislaw Wojciech, The Rigid Finite Element Method, Dynamics of Flexible Multibody Systems: Rigid Finite Element Method, Springer Berlin Heidelberg, Berlin, Heidelberg, 2006, pp. 35-82.
[50] G. Alici, B. Mui, C. Cook, Bending modeling and its experimental verification for conducting polymer actuators dedicated to manipulation applications, Sensors and Actuators, A: Physical, 126(2006) 396-404.
[51] C.H. Nguyen, G. Alici, G. Wallace, An Advanced Mathematical Model and its Experimental Verification for Trilayer Conjugated Polymer Actuators, IEEE/ASME Transactions on Mechatronics, 19(2014) 1279-88.
[52] A. Maziz, C. Plesse, C. Soyer, C. Chevrot, D. Teyssié, E. Cattan, F. Vidal, Demonstrating kHz Frequency Actuation for Conducting Polymer Microactuators, Advanced Functional Materials, 24(2014) 4851-9.
[53] A.A.A. Moghadam, W. Hong, A. Kouzani, A. Kaynak, R. Zamani, R. Montazami, Nonlinear dynamic modeling of ionic polymer conductive network composite actuators using rigid finite element method, Sensors and Actuators A: Physical, 217(2014) 168-82.
[54] A.A.A. Moghadam, A. Kouzani, R. Zamani, K. Magniez, A. Kaynak, Nonlinear large deformation dynamic analysis of electroactive polymer actuators, Smart Structures and Systems, 15(2015) 22.
[55] S. Wojciech, I. Adamiec-Wójcik, Nonlinear vibrations of spatial viscoelastic beams, Acta Mechanica, 98(1993) 15-25.
[56] D.C. Karnopp, Chapter 10: Distributed-parameter systems, SYSTEM DYNAMICS: Modeling, Simulation, and Control of Mechatronic Systems, JOHN WILEY & SONS2012, pp. 470-512.
[57] J. Ding, D. Zhou, G. Spinks, G. Wallace, S. Forsyth, M. Forsyth, D. MacFarlane, Use of Ionic Liquids as Electrolytes in Electromechanical Actuator Systems Based on Inherently Conducting Polymers, Chemistry of Materials, 15(2003) 2392-8.
[58] N.T. Nguyen, C. Plesse, F. Vidal, C. Soyer, S. Grondel, J.D.W. Madden, E. Cattan, Microfabricated PEDOT trilayer actuators: synthesis, characterization, and modeling, SPIE Smart Structures and Materials + Nondestructive Evaluation and Health Monitoring, SPIE2017, p. 13.
[59] J.D.W. Madden, N.A. Vandesteeg, P.A. Anquetil, P.G.A. Madden, A. Takshi, R.Z. Pytel, S.R. Lafontaine, P.A. Wieringa, I.W. Hunter, Artificial muscle technology: Physical principles and naval prospects, IEEE Journal of Oceanic Engineering, 29(2004) 706-28.

Chapter 5: Sensing ability and sensing model of the PEDOT-based trilayer actuators

Contents

5.1 Introduction 120
5.2 Theories on the mechanoelectrical effects 120
5.3 Sensing modeling 126
5.3.1 Mechanoelectrical coupling 126
5.3.2 Global model 128
5.4 Experimental setup 128
5.5 Results 130
5.5.1 Comparison between the model simulation and experimental results 131
5.6 Discussion 135
5.6.1 Force in response to a step displacement 137
5.7 Conclusion 138

5.1 Introduction

CP-based trilayer is an active material that exhibits an interesting bidirectional electromechanical coupling where an input voltage results in the displacement of the film and a voltage is produced when a displacement is applied to the film: mechanical deformation of the transducer by external mechanical loads causes movement of ions, and the generation of voltages. In this chapter, various theories on the mechanoelectrical effect will be reviewed and a sensing model for CP's will be described. The predictions of this model will then be compared with the experimental sensing results, showing that the complete electromechanical model represents an effective approach to describe both sensing and actuation. In conclusion, we will discuss the potential of the trilayer PC based as a sensor.

5.2 Theories on the mechanoelectrical effects

In general, the mechanism of mechanical sensing is based on the insertion and expulsion of ions into and out of the CP film. Researchers have developed two different configurations for CP – based sensor devices (Fig. 1). One is a free-standing film of CPs operating in electrolyte [1], and another one is the trilayer structure operating in open air where a polymer electrolyte is sandwiched between two CP electrodes [2].

The sensing ability of CPs has attracted some researchers to use them in few applications. A system containing two strips of trilayer structuring of CP - solid polymer electrolyte - CP is employed to mimic the whisker's functionality [3].

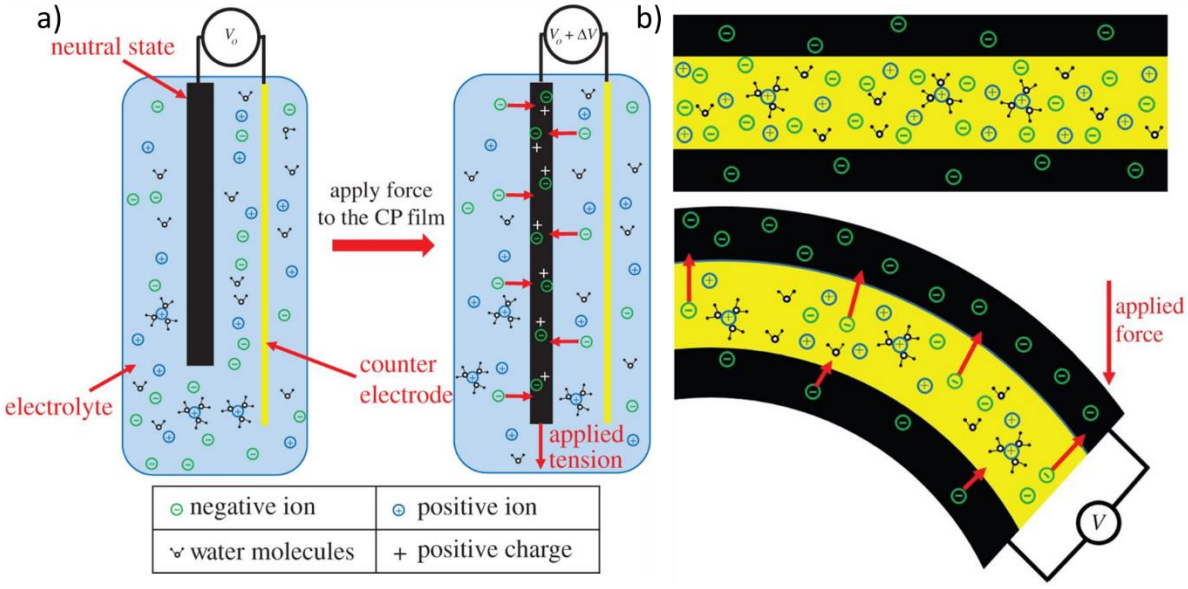


Fig. 1. a) Schematic of CP free-standing film sensing mechanism before and after subjected to a linear force, and b) Schematic of a bending trilayer sensor [4]

The mechanoelectrical effect of CP was first observed by Takashima *et al.* [5] in 1997, for a free standing film of polyaniline in 1 M HBF_4 aqueous solution. In his sensing approach, redox potential was maintained constant while a time varying tension was applied to the sample.

The authors demonstrated that the induced charge depends upon the magnitude of the tensioning load and the degree of doping. The energy conversion efficiency from mechanical to electrical was less than 0.01 %. One of the possible mechanisms proposed by the authors behind this induced charge is the stretching of the film resulting in the stretching of the main chain of the CP, and thus in the change of the density of states near the chemical potential induced redox current.

In 2007, Takashima *et al.* [1] performed a more intensive study on the sensing ability of polypyrrole composite films. A PPy film electrodeposited in dodecylbenzene sulfonic acid (DBS) and in bis(trifluoromethane sulfonyl)imide (TFSI) produced a negative and a positive current, respectively, when subjected to an increased tensile load. The switching polarity of the induced current agrees well with the film actuation polarity, indicating that the electromechanical actuation is the phenomenological counterpart of the mechanoelectrical sensing. The authors proposed a model based on Gibb's free energy theory and Fick's law to describe the flux of ions into and out of CP film. From this model, the authors claim that the maximum current is proportional to the concentration of mobile ion in the film and to the applied load. The re-establishing of Donnan's equilibrium is used to explain the current response.

At the same time, Wu *et al.* [2] introduced an experimental study on sensing ability of a trilayer structure of PPy/A – PVDF – PPy/A in open air in both reduced and oxidized states, where A is either DBS^- or ClO_4^-. Fig. 2 summarizes the results of experiments, where a sinusoidal voltage is obtained at open circuit in response to a sinusoidal displacement. The effect of small mobile ions ClO_4^- and large immobile ions DBS^- are clearly shown via the difference in the polarity of the output voltage. In this paper, authors have suggested two different mechanisms. In the first mechanism, so called "Deformation Induced Ion Flux" has been proposed to explain the phenomena observed in this experiment (Fig. 3). In this theory, a mechanical deformation affects the ion concentration within CP and, therefore, shifts the balance of the ions between the CP and the electrolyte. An ion flux results - with only smaller mobile ions displacing, while large dopants move at much lower speed. Consequently, the mechanical deformation results in a separation of ionic charge and causes a voltage difference.

The proposed model was confirmed via another set of experiments, where the authors used ionic liquid $BMI.PF_6$ (1-butyl-3-methyl-imidazolium hexafluorophosphate) and propylene carbonate (PC) mixtures as supporting electrolyte for the PPy/PF_6 – Pt/PVDF/Pt - PPy/PF_6 sensor. Depending on the ratio between $BMI.PF_6$ and PC, an "out of phase" voltage at amplitude of 0.07 mV (molar ratio $BMI.PF_6$: PC = 10 : 1) or an "in phase" voltage output at amplitude of 0.04 mV (molar ratio $BMI.PF_6$:PC = 1:10) is obtained.

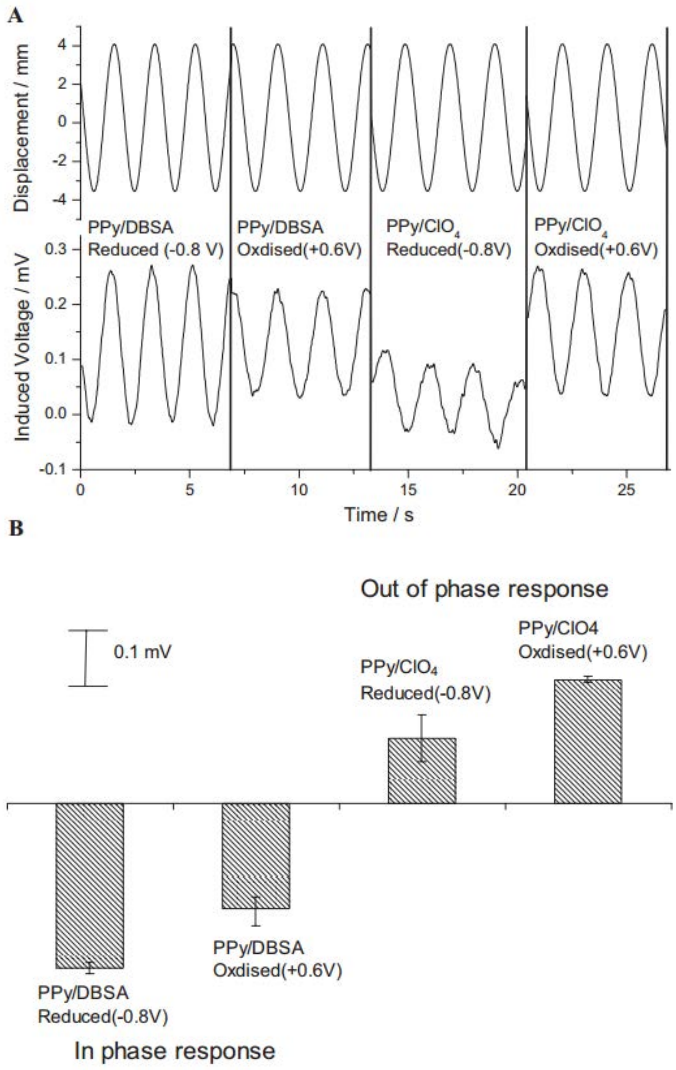


Fig. 2. Effect of counter-ion and redox state on the voltage output of polypyrrole mechanical sensor [2] (Reprinted with permission from John Wiley and Sons)

Based on the elastic energy change produced by inserting or removing an ion from the polymer by a change in stress, the input stress (σ) is proportional to the sensor voltage output (V) via an empirical strain-to-charge ratio (α): $U = \alpha \times \sigma$ [1,2].

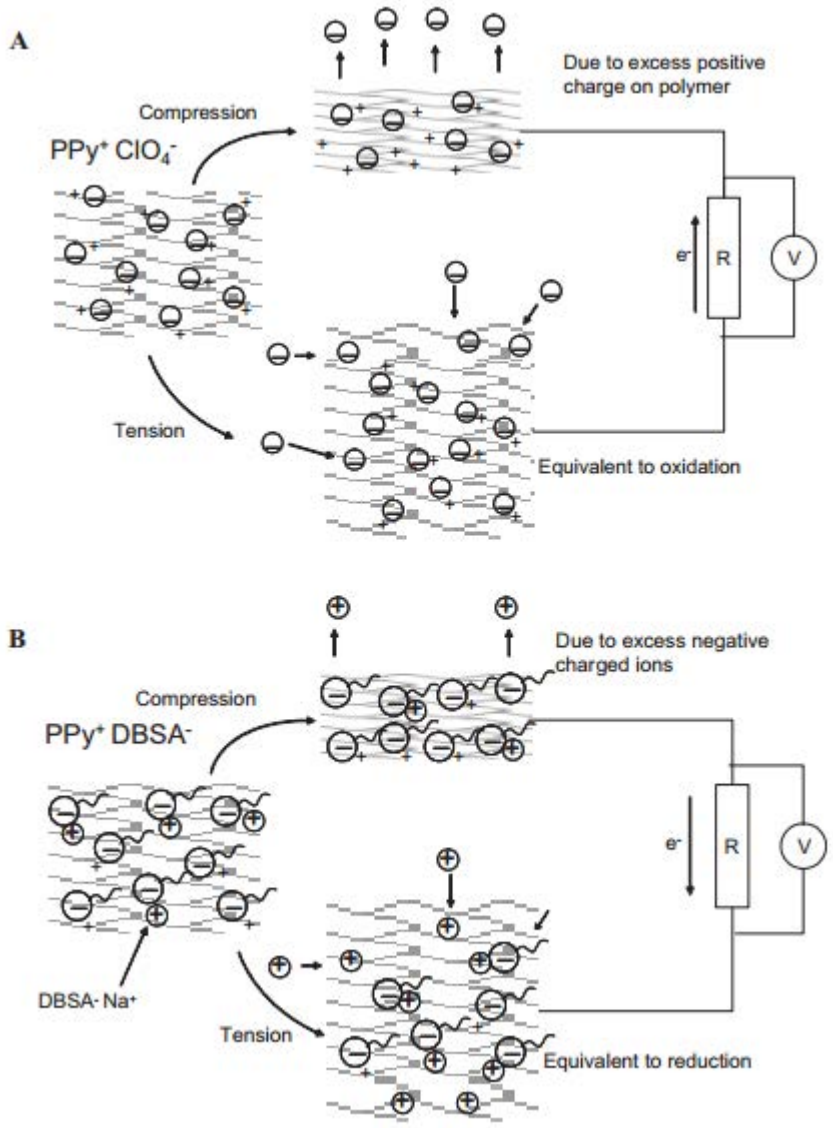


Fig. 3. Schematic diagram illustrating the net ion transport expected in both the "Deformation Induced Ion Flux" model and based on elastic energy considerations [2] (Reprinted with permission from John Wiley and Sons). In the first case compression of the polymer leads to an increase in ion concentration within the polymer, and a net flux of ions out. In the second, it is the compressive stress that squeezes ions out.

Shoa *et al.* [6] also observed a similar sensing behavior of a PPy thin film in an aqueous solution of $NaPF_6$, using a two electrodes experimental setup. The voltage generation in such a thin film is proposed to result from the tensile stress. This stress expands the PPy network, and thus reduces the force that required for ions to be inserted into the PPy network. The elastic insertion forces are key in this explanation. The authors have proposed a model to predict the magnitude and polarity of the output voltage, where the relationship between elastic modulus of the polymer, the capacitance, and the mechanical capacitance resulting from elastic energy stored during charging are all considered. The key input to the model is the strain to charge ratio, α, which is related to the amount of volume change per ion inserted. This in turn determines how much elastic energy is needed to insert ions – which is in addition

to any electrostatic and chemical potential energy added as the polymer is charged and the oxidation state is changed. The basic prediction of the model is that the voltage U change at open circuit resulting from a change in the applied stress, σ, is $U = \sigma\alpha$ [7].

In 2012, Festin [8] demonstrated the sensing response of 220 µm thick PEDOT-based trilayer actuators, where the PEDOT chains interpenetrate an IPN film made of NBR/PEO. The author has experimentally observed a linear relationship between the applied stress (mechanical strain) and the output voltage measured in open circuit state. A switch in the output voltage polarity was also reported when the ionic liquid EMITFSI is used instead of $LiClO_4$.PC.

Recently, Madden and his team [9, 10] have proposed a mechanism model for piezoionic effect. In their experimental setup, a thin film of ionic conducting polymer, such as polyacrylamide, poly(vinylidenefluoride - hexafluoropropylene) (PVDF-HFP), polar (polyurethane), highly polar poly(ethylene oxide) (PEO), charged poly(ethylene glycol) (PEG) or PEG derivatives, is placed between two rigid electrodes, in which the distance between those two is 1 cm. A voltage and a current ranges of 10^{-2} V and of 10^{-7} A, respectively, is observed when an externally applied local pressure at a portion of the layer (Fig. 4).

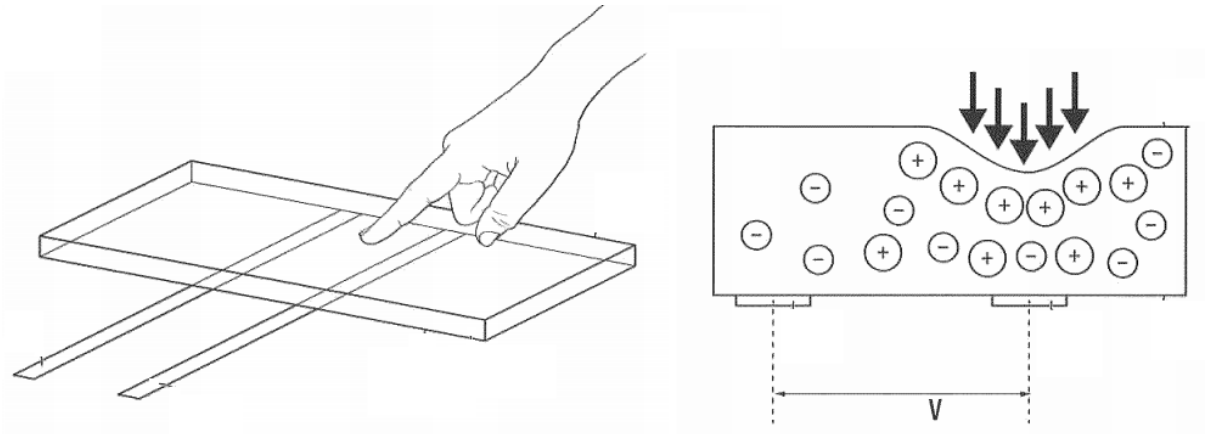


Fig. 4. Experimental scheme and induced voltage mechanism of a thin ionic conducting polymer film under an applied stress [10]

This induced voltage and current could be a result of the redistribution of mobile ions due to a change in the local ions concentration, based on the Donnan potential. A possible equation for predicting the electrical potential (U) due to the difference in local concentration ($\sum[C^+]$) is:

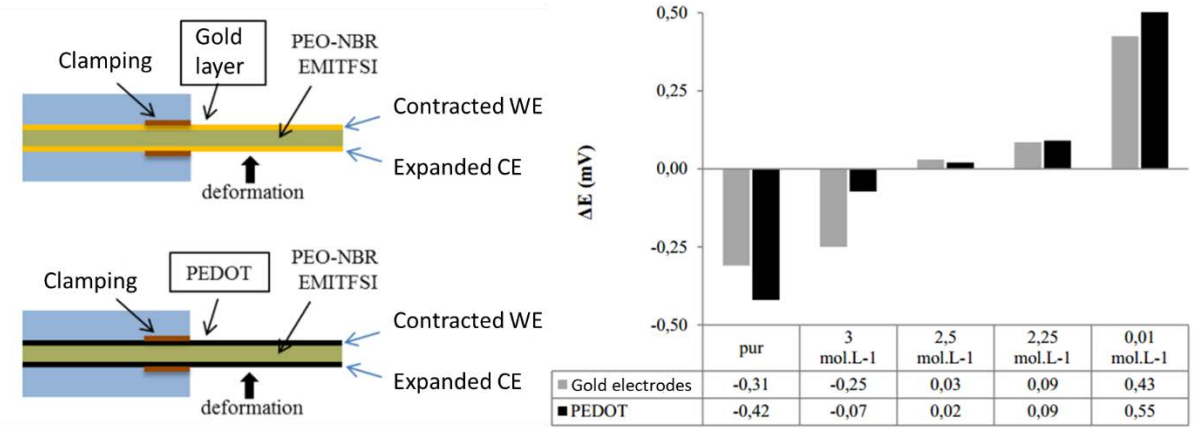
$$\Delta U = \frac{RG}{zF} \ln\left(\frac{[C^+]_x}{[C^+]_{x+\Delta x}}\right)$$

where G is the temperature, R is the ideal gas constant, z is the valence charge of the ion, F is the Faraday's constant, $[C^+]_x$ and $[C^+]_{x+\Delta x}$ are the concentration of the i^{th} mobile ions in the polymer at location *x* and (*x + Δx*). In this study, the speed of rising voltage and current, the

polarity and amplitude of the generated voltage are also discussed showing their dependent on type and size of mobile ions, and mechanical properties of the host polymer.

These results obtaining by Madden suggest that any single or interpenetrating polymer network, which is able conduct the ions – and does not necessary to conduct electrons, could produce a voltage and a current under a suitable mechanical excitation. In our case, since the fabricated NBR/PEO is a sIPN, which conducts ions as demonstrated previously via ionic conducting measurement, this NBR/PEO layer in the trilayer configuration plays an important role in the sensing ability of the trilayer.

In Woehling's study [11], the contribution of PEDOT electrodes in sensing ability of the trilayer was demonstrated. Fig. 5 shows that an input deflection induces an output voltage in both trilayer structures: Gold:NBR/PEO:Gold and PEDOT:NBR/PEO:PEDOT, swollen in EMITFSI or EMITFSI-PC at various concentration from 0.01 M to 3 M. In case of the pure EMITFSI and low concentration EMITFSI-PC, the magnitude of the output voltage from gold:NBR/PEO:gold is 25% smaller than that of second case. This suggests the output voltage of the trilayer structure composed of PEDOT:NBR/PEO:PEDOT includes the contribution of two factors: the voltage induced by NBR/PEO alone (similar to the voltage generated in an IPMC), and the voltage produced by conducting polymer electrodes [6].



	pur	3 mol.L-1	2,5 mol.L-1	2,25 mol.L-1	0,01 mol.L-1
Gold electrodes	-0,31	-0,25	0,03	0,09	0,43
PEDOT	-0,42	-0,07	0,02	0,09	0,55

Fig. 5. Schematic experiments and comparison of output voltage in two different trilayer configurations: Gold-NBR/PEO-Gold, and PEDOT-NBR/PEO-PEDOT with the dimension of L = 15mm, b = 5mm, h_t = 0.17 mm at various EMITFSI-PC concentrations, under a 2% applied strain [11] (Retrieved from https://tel.archives-ouvertes.fr/tel-01413677. By permission from author.). In this case a positive voltage suggests anion motion.

The results from Fig. 5 also show that the output voltage's polarity depends on the EMITFSI – PC concentration. The magnitude of output voltage is highest at the concentration extremes of pure EMITFSI and at the lowest (0.01 M) EMITFSI concentration. As the concentration of EMITFSI in PC is decreased, the magnitude is reduced. When the EMITFSI concentration is 2.5 M, the output voltage switched its polarity and increased as the concentration continues to decline.

Following this literature review, it can be concluded that there are three potential models that may explain sensing in conducting polymers: (1) an IPMC-like flux due to a pressure gradient within the ionically conductive separator; (2) a concentration (Donnan potential) mechanism, in which change in polymer volume induces a change in ion concentration and a resulting voltage generation, and (3) an elastic energy induced charge expulsion mechanism. All three predict that the more mobile ions will be involved in the transport, and hence result in voltage changes of the same sign. Whatever the mechanism, it does appear that the sensing and actuation mechanisms are related, as expected by microscopic reversibility. For this reason, I will choose to represent the sensing effect in section 5.2 via the empirical strain to charge ratio. Within this chapter, a simple sensing relation – which is the inverse of the actuation mechanism – will be implemented into the linear actuation model developed in chapter 4. Furthermore, a single model is developed for operating in both sensing and actuation modes. Then, a set of experiments will be performed and compared to a simulation in section 5.3 and 5.4 to confirm the ability of the model to predict the output voltage magnitude and polarity. Finally, several aspects on model limitations will be discussed in section 5.5.

5.3 Sensing modeling

In this section, a simple sensing model is developed, comprising three sub models: an electrochemical submodel containing a capacitor in series with a resistor (refer to section 4.2.2.1), a mechanoelectrical coupling (described in 5.2.1), and a mechanical model based on Euler-Bernoulli dynamic beam theory (refer to chapter 4.2.2.3). In order to follow the same methodology than in chapter 4, it is again represented using a Bond Graph formalism.

5.3.1 Mechanoelectrical coupling

As mentioned in the introduction, Shoa's model [6] and Wu's model [2] proposed a simple relation between the applied stress (σ) and the output voltage (U) via an empirical strain-to-charge ratio (α) $U = \sigma \times \alpha$. This ratio shows a bidirectional electrochemical effect. When the CP film is considered as an actuator, the strain to charge represents the relation between the volume change and the inserted charge density (units of m^3/C). Whereas for the sensor case, this ratio describes the amount of electrical potential produced by an applied stress (V/Pa – which is equivalent since a Volt is a Joule per Coulomb).

We demonstrate here the flexibility of two-port $\mathbb{C}$-element which is used to couple both electromechanical (actuation) and mechanoelectrical (sensing) relationships by a single matrix of 2 x 2 elements, shown in equation (1):

$$\begin{bmatrix} U_C \\ F \end{bmatrix} = \begin{bmatrix} \frac{1}{2C} & \frac{1.61\times(h_s+h_p)\alpha E_P}{L^2+w^2} \\ \frac{\alpha E_P(h_S+h_P)}{2\mathrm{L}} & \frac{4bE_P}{3L}\left(\frac{h_S}{2}\right)^3\left[\left(1+\frac{2h_P}{h_S}\right)^3-1+\frac{E_S}{E_P}\right]\frac{1}{L^2+w^2} \end{bmatrix}\begin{bmatrix} Q^C \\ w^2 \end{bmatrix}. \quad (1)$$

Here *Q* is the charge per volume applied to produce actuation and *w* is the displacement imposed externally on the trilayer (and that is being sensed). U^C is the sense voltage (change in open circuit potential) plus the voltage determined by the state of charge. *F* is the force needed to deflect the beam by *w* plus the force generated by the application of the charge. In the equation (1), the actuation side has been derived from chapter 4 (section 4.3.3.2), where $F = \frac{\alpha E_P(h_S+h_P)}{2\mathrm{L}} \times Q + \frac{4bE_P}{3L}\left(\frac{h_S}{2}\right)^3 \left[\left(1+\frac{2h_P}{h_S}\right)^3 - 1 + \frac{E_S}{E_P}\right]\frac{1}{L^2+w^2} \times w$. Here E_p and E_S are the elastic moduli of the conducting polymer and the separator layers, respectively. h_s and h_p are the thicknesses of the separator layer and the PEDOT electrode, respectively, and *L* is the length of the beam. On the sensing side from top row of the matrix in Equation 1, we start with the relationship:

$$U^C|_{Q=0} = \alpha \times \sigma_P = \alpha \times \varepsilon_{external} \times E_P \tag{2}$$

where $\varepsilon_{external}$ is the linear strain applied to the PEDOT electrodes as a result of displacement, w_{ext}.

From the chapter 3 (section 3.4.1), based on beam bending stiffness of a trilayer, the relation between the linear strain $\varepsilon_{external}$ and the strain difference (ε_{actual}) of one PEDOT electrode is:

$$\varepsilon_{active} = \varepsilon_{actual} \times \frac{h_P\left(h^4E^2+8h^3E+12h^2E+8hE+24h+12E^2+16\right)}{6h_t(h+1)(hE+2)} = 1.61 \times \varepsilon_{actual} \tag{3}$$

where $h = \frac{h_S}{h_P} = \frac{10\mu m}{3.5\mu m} = 2.9$ and $E = \frac{E_S}{E_P} = \frac{329kPa}{12.9MPa} = 0.0255$.

The relation between the strain difference (ε_{actual}) and the beam deflection (*w*) is:

$$\varepsilon_{actual} = \frac{2(h_s+h_p)w}{L^2+w^2} \tag{4}$$

Replace (4) and (3) into (2), we have:

$$U^C|_{Q=0} = 1.61 \times \alpha \times E_P \times \frac{2(h_s+h_p)w}{L^2+w^2} \tag{5}$$

We also have:

$$U^C|_{w=0} = \frac{Q}{C_P}, \tag{6}$$

From (5) and (6), we obtain the sensing relation as following:

$$U^C = U^C|_{Q=0} + U^C|_{w=0} = \frac{Q}{2C_P} + 1.61 \times \alpha \times E_P \times \frac{(h_s+h_p)w}{L^2+w^2} \tag{7}$$

It is worth noting that the output voltage (U_P) is the peak-to-peak voltage obtained between two PEDOT electrodes according to the strain difference also between two PEDOT layers.

From equation (2) and (3), the coupling matrix in equation (1) is derived.

5.3.2 Global model

From the electrochemical model containing a single capacitor in series with a single resistor, the two-port ℂ-element, and the mechanical model based on Euler-Bernoulli dynamic beam theory (refer to chapter 4), a unique Word BG model could be established and as shown in Fig. 6.

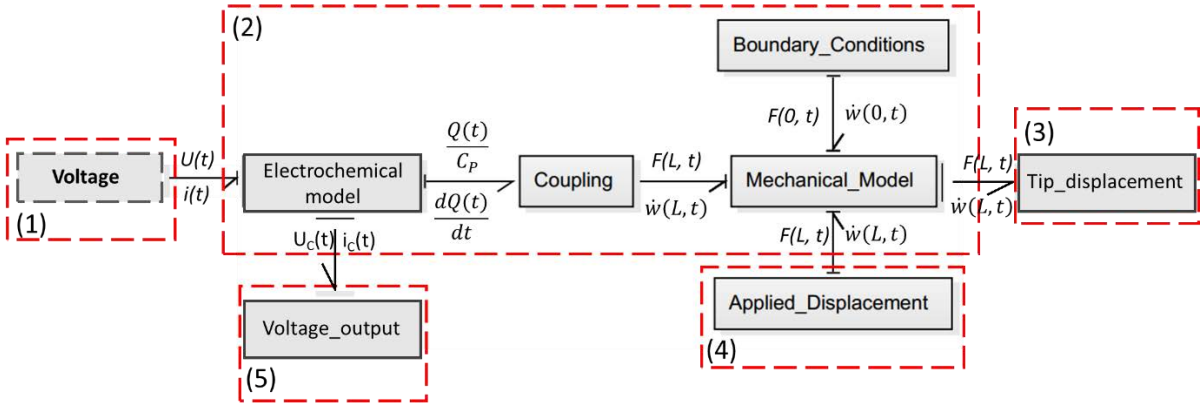


Fig. 6. Global Word BG model, where (1) and (3) represent the input voltage and the tip displacement, respectively, as the trilayer structure in actuation mode; the (4) and (5) are the input displacement and the voltage output, respectively, when the trilayer is operated as a sensor, (2) is the global BG model

It is worth noting that in comparison to the linear actuation model, in this sensing model an applied displacement (4) or a force is introduced as an input to the model instead of an input voltage (1), since we are investigating the mechanoelectrical ability of the trilayer structure. The bidirectional electromechanical coupling is described in the equation (1) and the detailed description of most of the global BG model (2) was established in chapter 4 (section 4.2.2). Only the parameters of the coupling ₵-element have been modified as shown in equation 1.

5.4 Experimental setup

The trilayers used in this measurement were fabricated following the procedure described in chapter 2 (section 2.5). The resulting trilayers were swollen in ionic liquid during one week before the experiment. To investigate the mechanoelectrical effect of the trilayer structure, an experimental setup is depicted as in Fig. 7a. One side of the trilayer sensor is placed on a thin plastic film – which has much higher stiffness than the trilayer. The film and trilayer stick together thanks to the tacky surface of the ionic liquid containing trilayer. The film forms a fourth layer (it is now a quadruple layer), adding stiffness, and increasing resonance frequency of the sensor to about 110 Hz calculated value (from as low as 2.5 Hz for the longer trilayer alone). One end of the trilayer is clamped between two metal electrodes which are connected to a National Instruments data acquisition system via a homemade amplifier (gain can tune between 1 and 1000, input impedance is 10 MΩ) to collect the voltage signal. At the other

end, it is held by the moving part of the Bose ElectroForce 3100 Series. The input displacement is precisely applied to the tip of the trilayer as depicted in Fig. 7a. The computer is programmed to apply a specified magnitude and frequency of a sinusoidal or a step displacement, and record the actual displacement from the feedback sensor on the Bose system. It simultaneously records the sensor voltage signal. An example of the resulting voltage responses to an input displacement of magnitude of 2 mm and frequency of 3 Hz is shown in Fig. 7b. Notice that the output voltage is more stable after few cycles of applying displacement.

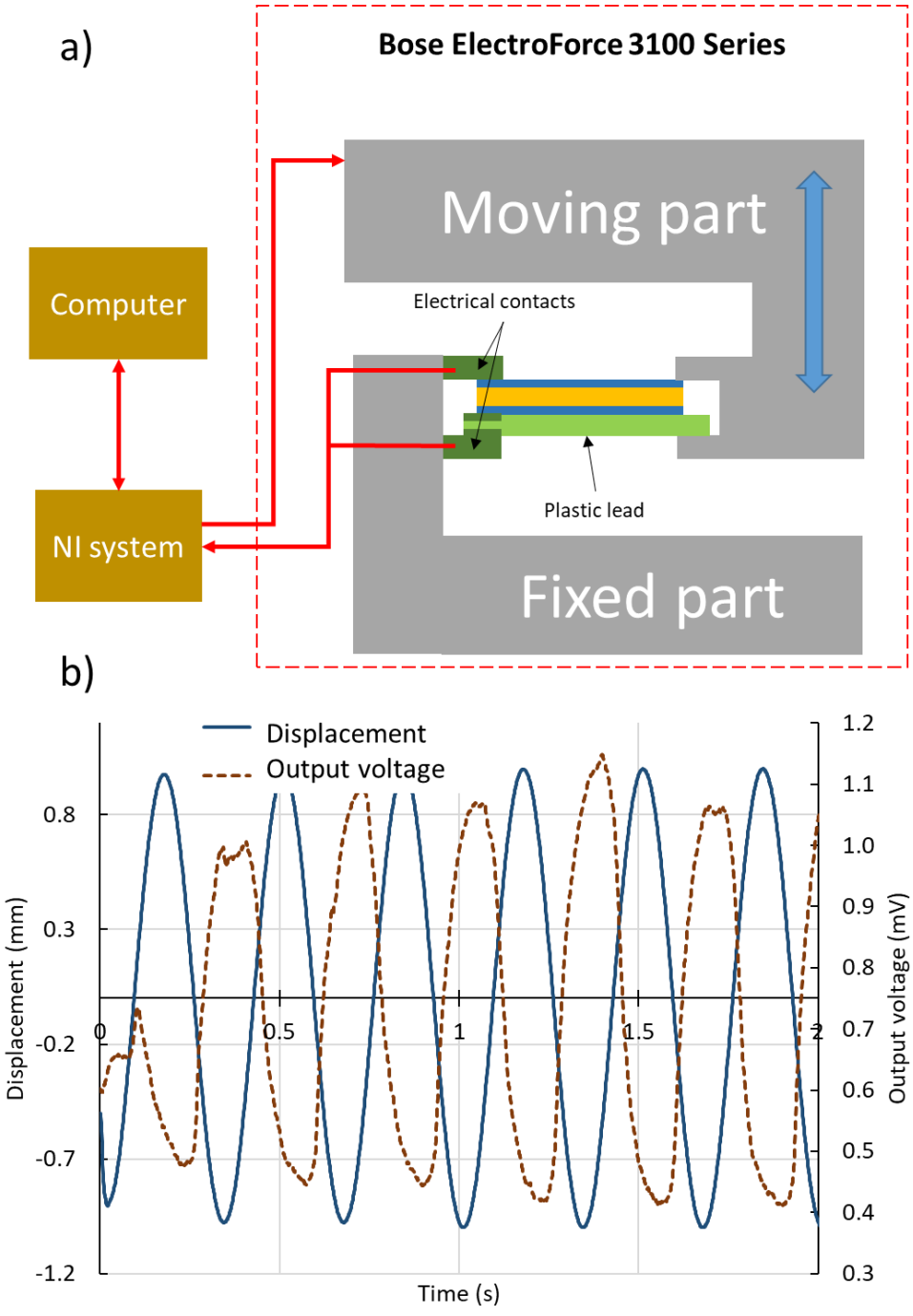


Fig. 7. a) Experimental setup to measure the voltage response to a sinusoidal displacement, and b) An output voltage response to an input displacement of the magnitude of 2 mm and frequency of 3 Hz on a trilayer of *7 mm x 1 mm x 0.017 mm*.

In my study, the trilayer structure containing ionic liquid can be seen as two separated phases: the sIPN as a porous phase, and ionic liquid as a fluid phase. Literatures have shown a poroelastic behavior of a gel network under a compression [12, 13]. Poroelasticity describes the relation between the porous scaffold and the fluid flow containing in this structure. When a mechanical load (a compression) is applied to this composite structure (solid and fluid), the porous part experiences a pressure changing leading to the fluid motion. As the applied displacement is kept constant, the responded force (as a function of time) is decreased before reached plateau. This phenomenon has been demonstrated via experiments and modeling by the authors.

Fig. 8 illustrates the experiment to measure the force response of a trilayer structure to a step displacement to evaluate the degree of ionic liquid flows through the trilayer structure – or a stress relaxation. A three–axis nanomanipulation unit is used to apply a step displacement, and a force/displacement sensor (FT-RS1002 Microrobotic System, three degrees of freedom, maximum speed: 5 mm/s coupled with an FT-S100 microforce sensing probe with a measurement range of ±100 µN, resolution: 5 nN) records the force response as a function of time, and a micro camera (Dino-Lite AM7000/AD7000, resolution: 5 MPX) is used to record the bending displacement of this trilayer.

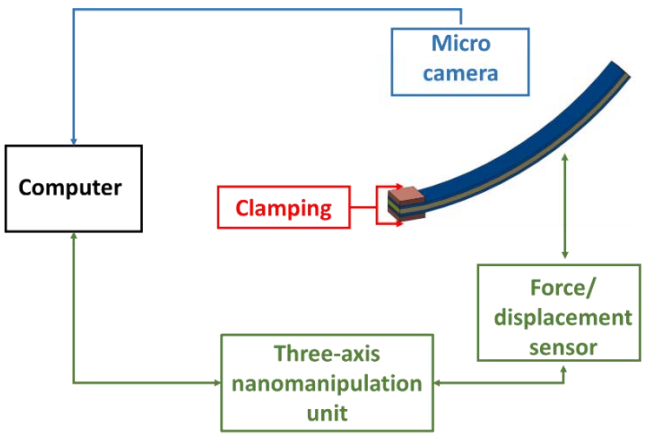


Fig. 8. Experimental setup to measure the decaying of blocking force of the actuator in response to a step displacement

5.5 Results

In order to confirm the agreement between the simulation results and the experiments on the output voltage, it is recorded as a function of the magnitude and the frequency of a sinusoidal displacement. The voltage response is also investigated in case of an input step displacement. Finally, the blocking force of a specimen is measured under a step displacement. All the measurements have been conducted on the trilayer structures with the

dimension of *length (L) x width (b) x total thickness (h) = 7 mm x 1 mm x 0.017 mm* in the swollen state, and the thickness of each layer: h_P *= 3.5 µm* and h_S *= 10 µm.* It is worth noting that the clamped area is a rectangular of *3 mm x 2 mm* and it is not taking into account in my calculation.

5.5.1 Comparison between the model simulation and experimental results

As discussed in the introduction, the mechanoelectrical mechanism is contributed from two factors: the movement of ions in the PEDOT electrodes and in NBR/PEO layer, could be distinguishes from the actuation mechanism. In order to evaluate the sensing model, the sense strain-to-charge ratio needs to be remeasured as we expect it is different from the value used in the actuation model, which is equal to 3.6 ± 0.5 x 10^{-10} m^3/C (refer to chapter 3, section 3.4.1).

A trilayer beam is subjected to a sinusoidal displacement. In the first case, the magnitude of the displacement is held at 2 mm while the frequency is varied between 0.5 Hz and 100 Hz. The polarity of the output voltage is determined as described in Fig. 9a, where the top (compressed) PEDOT electrode produces a negative potential relative to the bottom electrode. This suggests a motion out of this electrode by the cation. The magnitude of the measured voltage output and the estimated empirical strain-to-charge ratio are a steady 0.75 mV and 4.9 x 10^{-10} m^3/C, when the frequency increases from 0.5 Hz to 20 Hz, shown in Fig. 9b. These values gradually reduce to 0.14 mV and 7.4 x 10^{-11} m^3/C when the frequency reaches 100 Hz. The contribution of different factors could explain this reduction. At first, when the trilayer sensor is operating at the frequency higher than 30 Hz, the feedback displacement data showed a fluctuation in magnitude, which indicates this frequency approaches the resonant frequency of the Bose system and perhaps overestimates the displacement magnitude (the real magnitude is smaller than the set magnitude). Therefore, the output voltage is expected to reduce. The second possibility comes from the nature of the sensing mechanism, which is based on the flow of ions into and from the CP electrodes, and the ion mobility can be a limiting factor at this high frequency. Shoa *et al.* [6] also observed the drop in voltage at high frequency.

If voltage and displacement obtained in this measurement are normalized in term of thickness of the sensor, a coefficient can be calculated as below:

$$\Delta V = \alpha \times \sigma \rightarrow \frac{Q}{Volume} = \alpha \times C_V \times \sigma \rightarrow \frac{Q}{Area} = \alpha \times t \times C_V \times \sigma \quad (8)$$

In the PVDF piezoelectric [14], the coefficient d_{33} is derived as following:

$$Q = d_{33} \times F \rightarrow \frac{Q}{Area} = d_{33} \times \sigma \quad (9)$$

From (8) and (9), we have:

$$\frac{d_{33}}{\alpha \times t \times C_V} = \frac{2 \times 10^{-11} C/N}{3.6 \times 10^{-10} m^3/C \times 7 \times 10^{-6} m^3 \times 5 \times 10^7 F/m^3} = \frac{2 \times 10^{-2}}{126} = 1.5 \times 10^{-4}$$

This value suggests that the sensitivity of the trilayer at this thickness is better than that of piezoelectric.

A range of the strain-to-charge ratio obtaining from Fig. 9b is implemented into the model. The agreement between the simulation and experiments is confirmed via another set of experiments on a different sample with the same dimensions, shown in Fig. 9c.

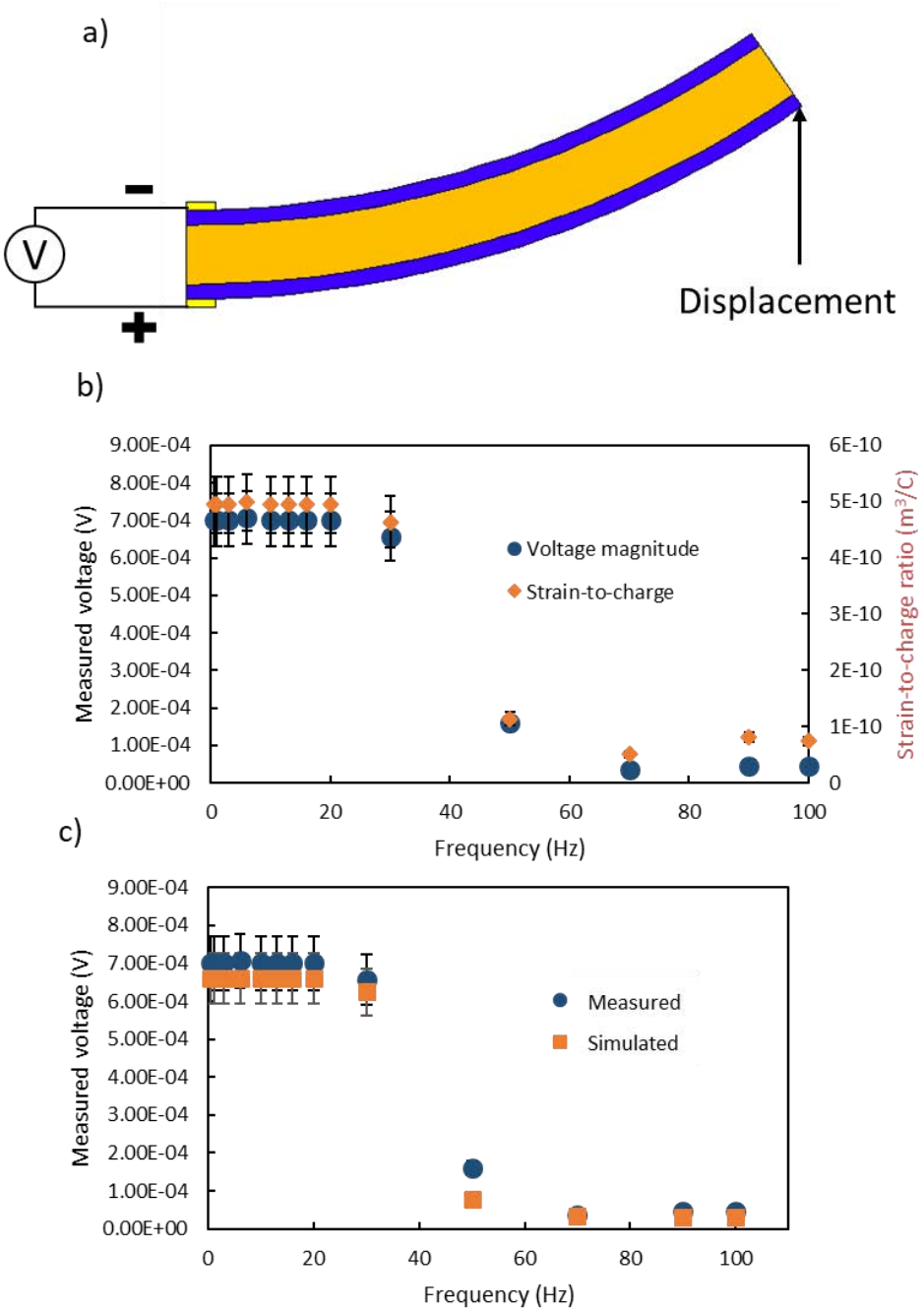


Fig. 9. a) Schematic of a trilayer transducer under a displacement excitation and the produced voltage polarity b) Voltage magnitude and the strain-to-charge ratio as a function of frequency when the magnitude of the sinusoidal displacement is constant at 2mm, c) Comparison between the simulation and the experiment of the magnitude of output voltage

In a second experiment, the frequency of the sinusoidal displacement is held constant at 3 Hz while the magnitude is changed between 0.04 mm and 3 mm. The linear relation between the output voltage and the magnitude of displacement, which was reported by Wu [2] and Woehling [11], is shown again in Fig. 10a, despite a small fluctuation. This voltage reaches the maximum at 0.76 mV when the magnitude approaches 2 mm, and then it decreases to 0.66 mV as the magnitude continues to increase. The strain-to-charge ratio has been derived in

this case and its average value is 4.76 x 10^{-10} m^3/C, which is similar to the previous experiment. A good fit between the simulation and experiment is demonstrated in Fig. 10b, despite the last point where the magnitude of displacement is biggest. There are few possibilities contributing to the decreasing voltage output at the largest displacement. Firstly, a large input displacement can induce a non-circular curvature of beam, in which the position closest to moving part (Fig. 7a) is more straight and the beam can show a wavy bending. In addition, the contacting area between the electrical contact and the electrodes can be changed under a large displacement because of a high stiffness of the plastic lead.

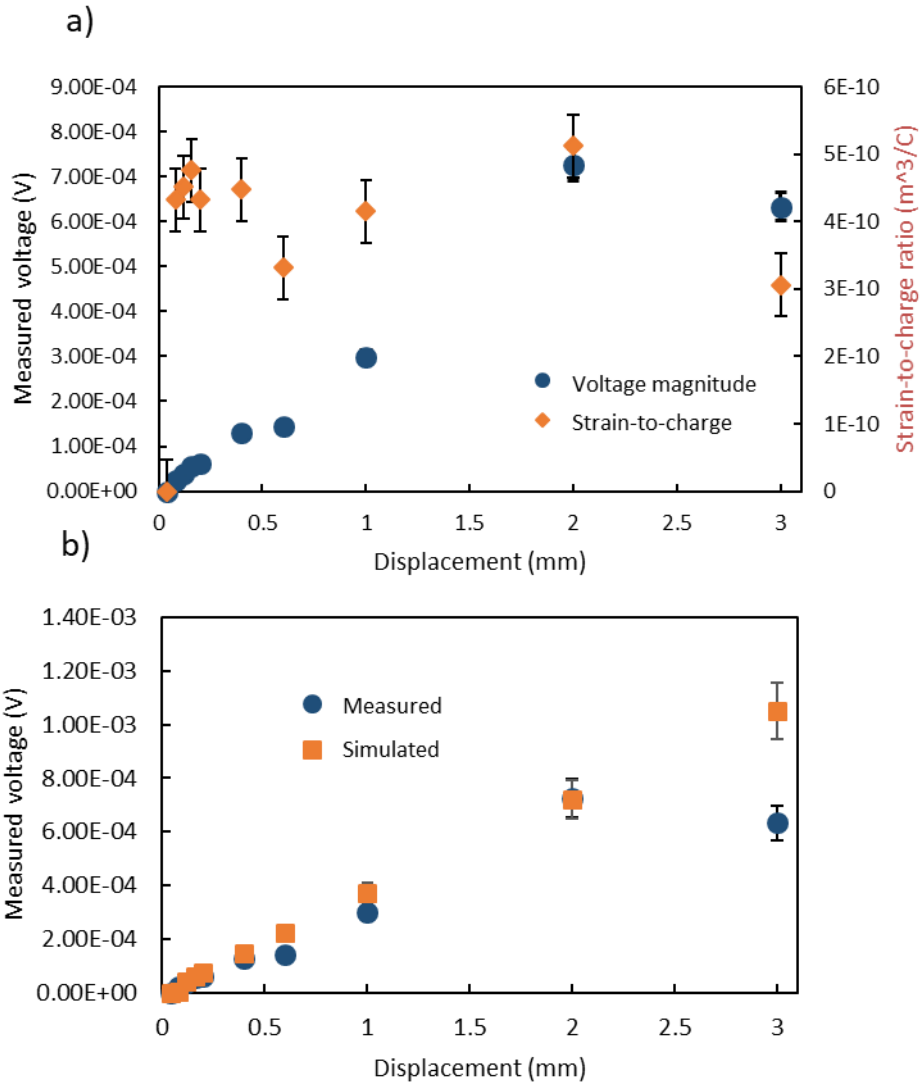


Fig. 10. a) Voltage magnitude and the strain-to-charge ratio as a function of magnitude when the frequency of displacement is constant at 3 Hz, b) Comparison between simulation and experiment of the magnitude of output voltage

Fig. 11 described another experiment where a step displacement was applied to the tip of the trilayer beam. The voltage output at first increases with the same speed as the step displacement and reaches the maximum value of 0.66 mV as the displacement peaks 3 mm

(induce an average strain difference of $\frac{(h_s+h_p)w_{ext}}{L^2+w_{ext}^2} = \frac{(10+3.5)10^{-6}m\times3\times10^{-3}m}{(7^2+3^2)10^{-6}m} = 0.069\%$ between two PEDOT electrodes). Immediately after the increase, the voltage quickly decays as the displacement remains constant. The simulation result follows quite well the experiment, though the decrease of the voltage in this case is the result of charging the capacitance or the PEDOT electrodes in other words. It is worth noting that the parameters used in the sensing model remain the same to those of the linear actuation model (chapter 4, section 4.2). These parameters include the strain-to-charge ratio obtained in previous characterization (8.45 x 10^{-10} m^3/C), the capacitance value (chapter 3, section 3.2.3), the leakage resistance (chapter 3, section 3.2.4), the NBR/PEO ionic resistance (chapter 3, section 3.2.1). A closer look to the model parameters shows that the speed of the decay depends on the level of the leakage resistance and the capacitance, where a smaller leakage and capacitance values induce a faster decay. In contrast, a bigger leakage resistance and capacitance result in a long decay of the voltage – or simply this is the decay in an RC circuit when the supplied voltage is cut off. Even though the model is able to predict the peak voltage and the shape of the decay, it does not reflect the real mechanism of the output voltage. A possible qualitative explanation will be proposed in the appendix A.5, where the flux of cations and anions through the trilayer is considered as a main contribution to the shape peak and the later decay of the output voltage.

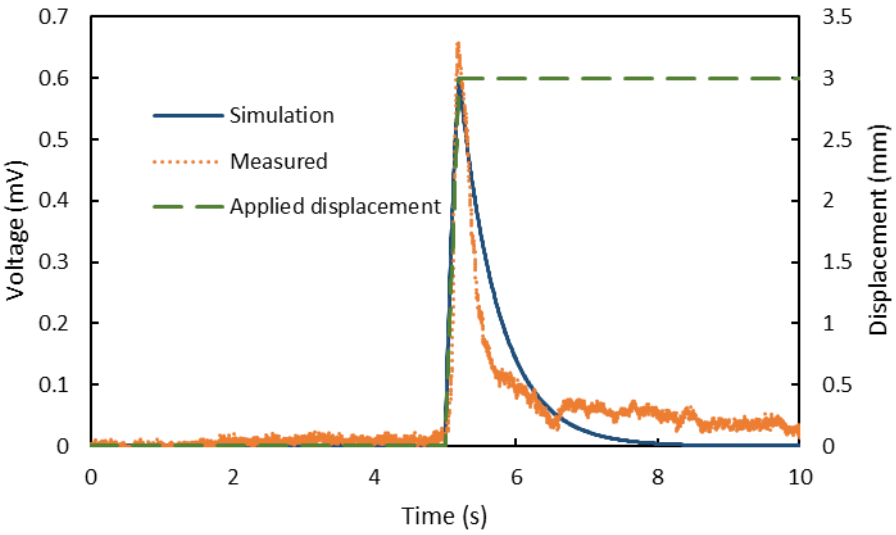


Fig. 11. Comparison between the simulation and measured voltage responding to an applied step displacement

It takes 1.7 s for the sensor to lose 90% of its maximum magnitude voltage, indicating the sensor cannot be used to measure a static or a low frequency (< 0.3 Hz) displacements. This is similar to piezoelectric sensors, which are inherently unable to measure static excitations [15]. In the case of the present sensor, the drop in sensor response is the result of a short between the two electrodes. The PEDOT is in contact across the separator. If this can be

removed, it should be possible to record displacements at much lower frequencies. There still may be some parasitic reactions that slowly lead to self-discharge, ultimately determining the low frequency limit of the device.

Recent work (not published yet) conducted by K. Rothlaid (U. Cergy-Pontoise 2018) has shown that the use of PEDOT doped with polystyrene sulfonate (PSS) results in a stable output voltage for at least for few minutes, with no decay observed. This alternative material can be a suitable selection for the sensing application in static and low frequency case.

5.6 Discussion

In the previous section, the strain-to-charge ratio (α) was estimated as the function of frequency and magnitude of the input sinusoidal displacement. The obtained value at the frequencies below 30 Hz and at strains smaller 0.23% is approximately 8.4×10^{-10} m^3/C. This value is bigger than the strain-to-charge value obtaining for the electromechanical effect, which equals to $3.6 \pm 0.5 \times 10^{-10}$ m^3/C.

There may be a contribution of different factors during the measurement resulting in a different strain-to-charge ratio. At first, in the experiments above, the input displacement is applied at the position of the tip of the trilayer. It is a point load. This leads to the fact that the stress distribution is not homogeneous along the length of the trilayer, in which the largest stress is induced at the position close to the fixed end and smallest stress is observed at the position close to the flexible end. A simple stress distribution along the length of the beam is derived as following:

$$\sigma(x) = \frac{w \times 3E_t I_t \times (L-x)}{L^3 S},$$

where w is the input displacement, E_t and I_t is the Young's modulus and inertial moment of the beam, respectively, x indicates the position along the length of the beam (L) away from the clamping point, and $S = bh^3/12$ is section modulus of the beam.

As a result, the strain to charge ratio should be considered as a function of position along the length of the beam. The use of constant value of the strain to charge ratio can be explained as an average of this value for a specific PEDOT volume.

The second contribution to the measurement error may come from the use of the plastic lead during the measurement. Even though this plastic foil is thinner than the trilayer structure, the presence of this foil will change the neutral axis of the trilayer during the bending, in which two PEDOT electrodes will not be induced a symmetric strain in opposite sign. Therefore, the derived strain from the input displacement is needed to be adapted. The plastic lead (Young's modulus ≈ 3GPa) is much stiffer than the trilayer sensor (Young's modulus ≈ 13MPa), therefore in this experiment, we assumed that the neutral axis of the four layers (the trilayer and the plastic lead) close to that of the plastic lead. The strain difference between two PEDOT

electrodes under an input bending can be derived as $\varepsilon_{actual} = \frac{(h_s+h_p)w}{L^2+w^2}$, this relation is used in equation (4).

Apart from these two measurement errors, this different strain to charge ratio – if it is real – suggests a possibility of existing a different operating mechanism in the mechanoelectrical effect of the trilayer structure.

In Appendix A.5.1, a model is proposed to explain for the sensing mechanism of the trilayer actuator, however without the experimental confirmation, this model becomes an opening conclusion.

5.6.1 Force in response to a step displacement

Here stress relaxation is investigated. Whatever the sensing working mechanism of the trilayer structure may be, the movement of ions inside the trilayer under a mechanical excitation (a displacement or a force) is essential for all the possibilities. One question is whether or not there is a substantial flow of ionic solution. If there is, this will lead to a reduction in force over time when a displacement is applied. Such a drop can also be due to stress relaxation in the film of course.

Fig. 12a shows a two-steps input displacement to a trilayer sample. The specimen is pushed forward and pulled backward by a silicon tip of a displacement/force sensor. The resulting force is recorded as a function of time, shown in Fig. 12b. The force increases to approximate 2 µN as the step displacement of - 0.5 mm is applied, and then it slowly reduces and reaches plateau after 30 s. The same trend is observed when a step of + 0.5 mm is applied, however a bigger voltage magnitude was recorded in this case. The force drop suggests the existence of ion flow upon an application of displacement or just simply the viscoelastic response of the material. The responding force reaches the plateau indicating this flow is getting slower and will stop at some point or again just the viscoelastic behavior after a certain amount of time that is bigger than the relaxation time constant of the material.

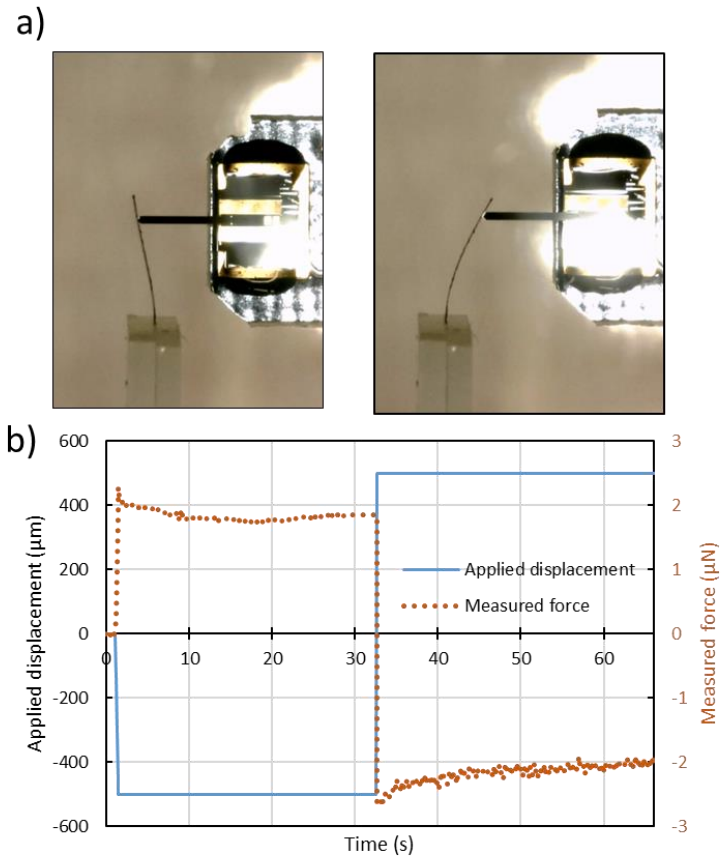


Fig. 12. a) Experiment of applying step displacement, and b) The decay of force response of the beam as a function of time.

5.7 Conclusion

In this chapter, a simple relation between the induced stress and the output voltage has been implemented in the linear actuation model with the purpose to build a unique linear model operating in both actuation and sensing modes. The strain-to-charge ratio was recharacterized and the concordance between the simulation and experiment of the output voltage has confirmed the ability to predict the sensing function of the trilayer, despite a small error. The model shows its advance in predicting quite well the voltage decay under a step displacement.

The future perpective of this chapter is to optimize the experimental design. Applying homogeneous stress along the length of the trilayer would reduce any variation in sense voltage along the length. The second is to reduce the asymetric strain between two PEDOT electrodes, which could be done by using a symmetric bending set-up. These improvements will ensure the reliablity of the experimental results and provide a clue on the existing of novel sensing mechanism.

[1] W. Takashima, K. Hayasi, K. Kaneto, Force detection with Donnan equilibrium in polypyrrole film, Electrochemistry Communications, 9(2007) 2056-61.
[2] Y. Wu, G. Alici, J.D.W. Madden, G.M. Spinks, G.G. Wallace, Soft Mechanical Sensors Through Reverse Actuation in Polypyrrole, Advanced Functional Materials, 17(2007) 3216-22.
[3] N. Festin, C. Plesse, C. Chevrot, D. Teyssié, L. Josselin, P. Pirim, F. Vidal, Actuation and Sensing properties of Electroactive Polymer Whiskers, Procedia Computer Science, 7(2011) S4-S7.
[4] T. Wang, M. Farajollahi, Y.S. Choi, I.T. Lin, J.E. Marshall, N.M. Thompson, S. Kar-Narayan, J.D.W. Madden, S.K. Smoukov, Electroactive polymers for sensing, Interface Focus, 6(2016).
[5] W. Takashima, T. Uesugi, M. Fukui, M. Kaneko, K. Kaneto, Mechanochemoelectrical effect of polyaniline film, Synthetic Metals, 85(1997) 1395-6.
[6] T. Shoa, J.D.W. Madden, T. Mirfakhrai, G. Alici, G.M. Spinks, G.G. Wallace, Electromechanical coupling in polypyrrole sensors and actuators, Sensors and Actuators, A: Physical, 161(2010) 127-33.
[7] J.D.W. Madden, Conducting polymer actuators: Massachusetts Institute of Technology; 2000.
[8] N. Festin, Conducting interpenetrating polymer network actuator sensor for biomimetic perception system: Université de Cergy Pontoise; 2012.
[9] M.S.u. Sarwar, Y. Dobashi, E. Glitz, M. Farajollahi, S. Mirabbasi, S. Naficy, G.M. Spinks, J.D.W. Madden, Transparent and conformal 'piezoionic' touch sensor, SPIE Smart Structures and Materials + Nondestructive Evaluation and Health Monitoring, SPIE2015, p. 9.
[10] M.S. John Madden, Yuta DOBASHI, Edmond Cretu, Shahriar Mirabbasi, Ettore Glitz,Meisam Farajollahi Method and sensor for pressure sensing based on electrical signal generated by redistribution of mobile ions in piezoionic layer, in: U.S.P. Application (Ed.) US Application Publication, University of British Columbia United State, 2015, p. 40.
[11] V. Woehling, New Developments in electroactive materials based on electronic conductive polymers : Towards integration into biomedical systems: Université de Cergy Pontoise; 2016.
[12] S. Cai, Y. Hu, X. Zhao, Z. Suo, Poroelasticity of a covalently crosslinked alginate hydrogel under compression, Journal of Applied Physics, 108(2010) 113514.
[13] W. Hong, X. Zhao, J. Zhou, Z. Suo, A theory of coupled diffusion and large deformation in polymeric gels, Journal of the Mechanics and Physics of Solids, 56(2008) 1779-93.
[14] F. Bernard, L. Gimeno, B. Viala, B. Gusarov, O. Cugat, Direct Piezoelectric Coefficient Measurements of PVDF and PLLA under Controlled Strain and Stress, Proceedings, 1(2017).
[15] G. Gautschi, Piezoelectric Sensorics: Force Strain Pressure Acceleration and Acoustic Emission Sensors Materials and Amplifiers: Springer-Verlag Berlin Heidelberg; 2002.

Chapter 6: Conclusion and outlook

Developments in conducting polymer transducers operating in air make them more effective in terms of generated force, displacement and frequency of operation, among others. Recently, they have been grown at acceptable scales for potential integration into microsystems. The ultimate goal is to have a material whose properties are well known and can be modeled in order to be predictive in the manufacture of a soft microsystem that includes flexible transducers. That is why this thesis was focused on their characterization, and modeling. To the best of my knowledge, this is the first effort to fully characterize and model such a very thin trilayer transducer, where the total thickness of the transducer is only 17 µm - after being swollen in ionic liquid, and it is the most complete combined effort at characterization and modeling yet undertaken for conducting polymer actuators.

The first step in this work was to improve on a recently developed clean room compatible microfabrication process for conducting polymer trilayers. Although the yield remains low with this process, the relevant physical characteristics of a successful device were fully characterized, including factors affecting ionic and electronic transport, coupling between charge and strain, material stiffnesses, and damping. In actuation a strain difference of approximately 1%, a blocking force of 12 µN, and a sensing voltage of 0.7 mV were obtained from a transducer of *length x width = 6 mm x 1 mm*. This deflection and sensing voltage match the expected response, as described by a non-linear model.

The conducting polymer PEDOT was used as the active material. Since the 3,4-ethylenedioxythiophene (EDOT) polymerization is a complicated and sensitive process and PEDOT is a complex material showing nonlinear electrochemomechanical properties, the fabrication, characterization, and modeling processes are confronted with various issues. Overcoming these technical challenges led to some main scientific and engineering contributions as listed here:

- The characterization and improvement of the trilayer fabrication process. In this trilayer configuration, a semi-NBR/PEO is sandwiched between two PEDOT/PEO electrodes, produced by stacking layer by layer. This fabrication technique allows us to tune the thickness of each layer as desired. In a departure from previous work, changes have been made, such as the optimization of the PEDOT electrodes, resulting from the increase in vapor phase polymerization time from 30 min to 50 min, switching to a vacuum hotplate (Sawatec HP-200) allowing more precise temperature and vacuum control than was achieved using a vacuum bell, and performing all the fabrication process in a clean room environment. The percentage of the PEO in the PEDOT layer was also changed to 10%, from 20 %, to ensure a balance between high electronic conductivity (around 200 S/cm) and high volumetric charge density (leading

to an increase from 2.3 x 10^7 C/m^3 to 1.0 x 10^8 C/m^3) of the PEDOT layer. In addition, I have investigated the asymmetry in surface roughness between the top and the bottom PEDOT layers, which might have consequences on the electrical properties of the PEDOT electrodes, and finally on the mechanical properties (displacement, force …) of the actuator.

- Full characterization of the critical electrochemomechanical properties of the trilayer transducers has been done. The electrochemical properties including the ionic conductivity of the PEDOT electrodes and of the SPE layer, the PEDOT electronic conductivity as a function of oxidation state, and the dependence of PEDOT's volumetric capacitance on the potential window were all studied. In addition, the mechanical properties such as Young's modulus of the PEDOT as a function of the oxidation state, Young's modulus of the SPE layer, and the damping ratio. Finally, the coupling between the electrochemical and the mechanical were represented via an empirical strain-to-charge ratio, the linear strain was determined and the blocking force measured as a function of applied potential. These obtained parameters provide us an insight into the physical structure of the system and the working mechanism of the actuator. Most importantly, the key factors affecting actuation behavior are all determined, providing us a best guideline to improve the actuator's performance.
- Development of a nonlinear dynamic model – and along with it a much simpler dynamic linear version of the model – capable of simulating the actuation of ultrathin trilayer actuators. A comparison between these two models has shown that the linear model is simple to build and it is easier to obtain all of its required parameters. However, it is most suitable to predict small displacements, providing a less precise prediction than the non-linear model for larger applied voltages and displacements. The nonlinear model showed advances over the existing work on trilayer actuators in that it can precisely predict a nonlinear dynamic actuation with an ability to implement nonlinear electrochemical and mechanical properties of material: PEDOT electrical and ionic conductivities; volumetric capacitance values; and Young's modulus variation. In addition, it accounted for the mass and damping associated with the beam. All physical characteristics used in the model were measured. The concordance between the simulation and experimental results in both time and frequency domains confirms the ability to predict the bending of the trilayer actuator. In addition, the approach is represented in a Bond Graph language, providing simple way to access the energy information, evaluate the critical parameters affecting the performance of the actuator, and allow an insight into the phenomena occurring in the ionic actuator.

- Development of a unique linear model operating in both actuation and sensing modes. A simple relation between the induced stress and the output voltage has been implemented in the linear actuation model. The strain-to-charge ratio was recharacterized in sensing mode and the concordance between the simulation and

experiment of the output voltage has confirmed the ability to predict the sensing function of the trilayer, despite a small error. Another advance of the model is its predictionof the sensing voltage decay rate under a step displacement.

Recommendations for future work

In addition to the contributions listed above, this thesis work also draws out some new challenges in all three domains including fabrication, characterization, and modeling.

- At first, a further optimization on the transducers' fabrication process can be performed to improve the yield and reproducibility. The VPP process in this thesis has used the conventional oxidant solution consisting of 55% $Fe(TOs)_3$ in butanol. However, literature[1] has shown that this high percentage produces a highly acidic and reactive oxidant solution, resulting in uncontrollable polymerization and structural defects in the deposited film. Investigation on optimizing the percentage of oxidant solution, or adding base inhibitors such as pyridine to control the reaction rate are suggested to further improve the electrochemical properties of the PEDOT electrode. In addition, an asymmetric geometry between the top and the bottom PEDOT electrodes was observed and resulted in an asymmetry in the electronic conductivity of PEDOT layers as well an initially curved state of the trilayer beam. This can be possibly overcome by fabricating PEDOT electrodes with different thicknesses to compensate for the pre-stress in the beam.
- Secondly, in the characterization, the properties of the PEDOT and the SPE layers have been measured, however, each property was investigated on one specific thickness of the sample. There is a need to confirm that the obtained values are consistent at other thicknesses. If they are unchanged with thickness, then one set of values can be used for all device geometries. It is also interesting to consider the extension of this model to other trilayer structures, whether conducting polymer-based or IPMC, as well as to other shapes. Even in IPMCs it is possible that the same characteristics can be used to understand their sensing and actuation responses.
- In addition, the nonlinear model is theoretically suitable to predict high frequency actuation ($f > 100$ Hz). In addition, the model was built based on Bond Graph language, providing at first a possibility to integrate it into a real actuator control system, and second to develop a more complex model to control not only a single beam but also a complex geometry. These possibilities can show the power of the model, which is not fully demonstrated here yet.
- Finally, in the bidirectional electromechanical model, there is need to optimize the experimental design. In the testing method used, in which the beam is bent using a point load applied near the tip, the moment is not uniform along the length, and so

the sensing voltage is expected to vary also. It would be useful to investigate the effect of this variation along the length on the time response of the sensor. The second is to reduce the asymmetric strain between two PEDOT electrodes, which could be done by using a symmetric bending setup. These improvements will ensure the reliability of the experimental results and provide a clue on the origins of the novel sensing mechanism.

This thesis proposes methods of characterization and modeling flexible transducers that should facilitate the engineering work to design microsystems for example micro-robotics.

1 W. Shi, Q. Yao, S. Qu, H. Chen, T. Zhang, L. Chen, Micron-thick highly conductive PEDOT films synthesized via self-inhibited polymerization: roles of anions, Npg Asia Materials, 9(2017)

A.2 Chapter 2: PEDOT-based trilayer fabrication process

A.2.1 Optimization of electrochemical properties of PEDOT electrodes

Optimization of LBL synthesized electrodes was carried out in order to obtain highly conductive and electroactive of conducting polymer electrodes (CPE) (PEDOT layers) which are critical parameters for obtaining efficient bending type trilayer microactuators. High electronic conductivity will be necessary to promote fast charge transport along the length of the device and will be involved in the curvature homogeneity of the final beam. Besides electronic conductivity, also volumetric charge density as an indicator of electroactivity, is a critical parameter since the electrode strain is directly proportional to the number of inserted/expelled ions [1]. In other words, if PEDOT chains are highly conductive but not accessible for insertion/expulsion of ions of the chosen electrolyte, the resulting deformation will be small. For this purpose, the volumetric charge density of each synthesized CPE has been minutely characterized and needs to be as high as possible.

Optimization on PEDOT/PEO electrode properties has been performed first as a function of mPEG content in the oxidant solution and in the present section all the results for the PEDOT electrodes are given in the swollen state (EMImTFSI), if not stated otherwise.

It was found that while increasing the mPEG content in the oxidant solution, the thickness of the electrodes (Fig. 1a) remained in the same range from 0% - 20% mPEG before a drastic increase. A possible reason for the increase in thickness is the pre-polymerization of mPEG in the flask. Indeed, peroxide based initiators, such as DCPD, and Fe^{3+} ions can react and generate radicals at room temperature [2]. The presence of radicals will lead to a non-desired polymerization of mPEG in the oxidant solution. While this phenomenon seems rather limited for a low content of mPEG, and a low content of DCPD, it becomes obvious for high content of mPEG, since it was found that the bulk polymerization occurs with 50 wt% of mPEG. As the mPEG and DCPD contents are increased in the oxidant solution, the concentration of monomers and generated radicals are both increasing the polymerization kinetics and promote an increase of viscosity in the flask. The thickness of spin-coated oxidant solution layer on the substrate is then higher and leads to the increase in thickness of PEDOT electrode layers.

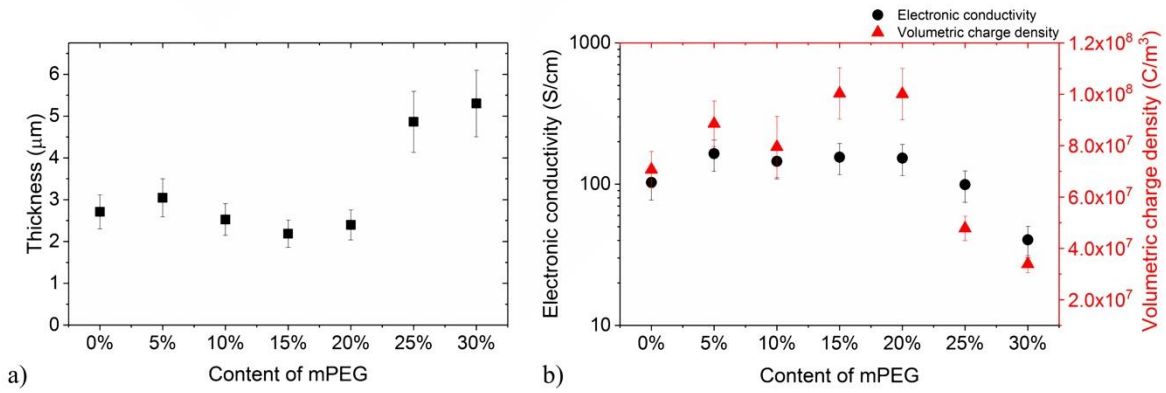


Fig. 1. Results of mPEG content in the oxidant solution: thickness (a-■), electronic conductivity (b-●), and volumetric charge density (b-▲) at a scan rate of 20 mV/s and a voltage window of 2 V. Spin coating speed/acceleration/duration of oxidant solution: 2500 rpm/1000 rpm s^{-1}/30 s; EDOT VPP time: 30 min; EDOT VPP temperature: 40 °C.

Adding up to 20 wt% mPEG into the oxidant solution leads also to an improvement of the electrical and electrochemical properties of the PEDOT electrodes (Fig. 1b). Adding only 5 wt% mPEG to the oxidant solution increases the electronic conductivity from 103 S/cm to 164 S/cm. These results are consistent with the literature indicating that adding glycol based additives [3-5] into the oxidant solution helps to affect positively the synthesis of highly conductive and electroactive PEDOT layers, so in our case, mPEG is behaving as a reactive additive. In contrast, the excess of PEG-based monomers (above 20 wt% mPEG) in the oxidant solution leads to a decrease of both electrical and electrochemical properties, probably due to the increase of non-electrically conducting phase (mPEG) in the electrodes. On the other hand, the reason for the decrease of electrical and electrochemical properties above 20 wt% mPEG in the electrodes can also be explained by the pre-polymerization of mPEG in the flask, which forms thicker and more disorganized electrodes and can result in the loss of charge transport along the electrodes.

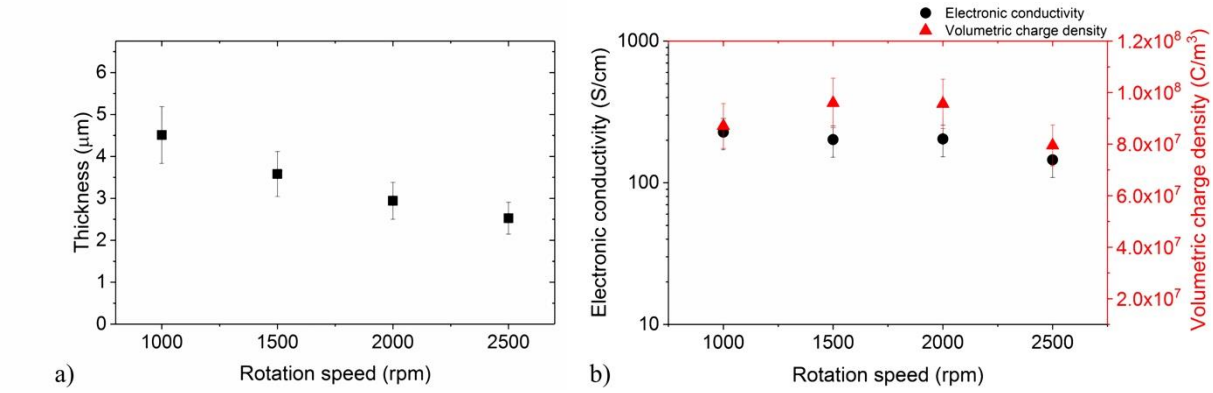


Fig. 2. Thickness (a-■), electronic conductivity (b-●) and volumetric charge density (b-▲) of PEDOT electrodes as a function of rotation speed of the spin coater. mPEG content: 10%; EDOT VPP time: 30 min; EDOT VPP temperature: 40 °C. Acceleration 1000 rpm s^{-1}, duration 30 s.

Decreasing the rotation speed of the oxidant solution during the spin coating step led to a thicker oxidant solution layer on the substrate and therefore thicker CPE layers (Fig. 2a). Changing the rotation speed did not have a tremendous effect on the electroactivity (Fig. 2b) of the electrode layers, which remain high at all speeds (between 7.9 x 10^7 C/m^3 and 9.6 x 10^7 C/m^3). A same behavior is also observed with the electronic conductivity i.e. the rotation speed in the range of 1000 rpm to 2000 rpm hardly influences the electronic conductivity values which remain high (around 200 S/cm). Depending on the desired electrode thickness, any rotation speed can be chosen while maintaining the same synthesis conditions (10% mPEG, EDOT VPP for 30 min at 40°C) to obtain highly conductive PEDOT electrodes with high electroactivity.

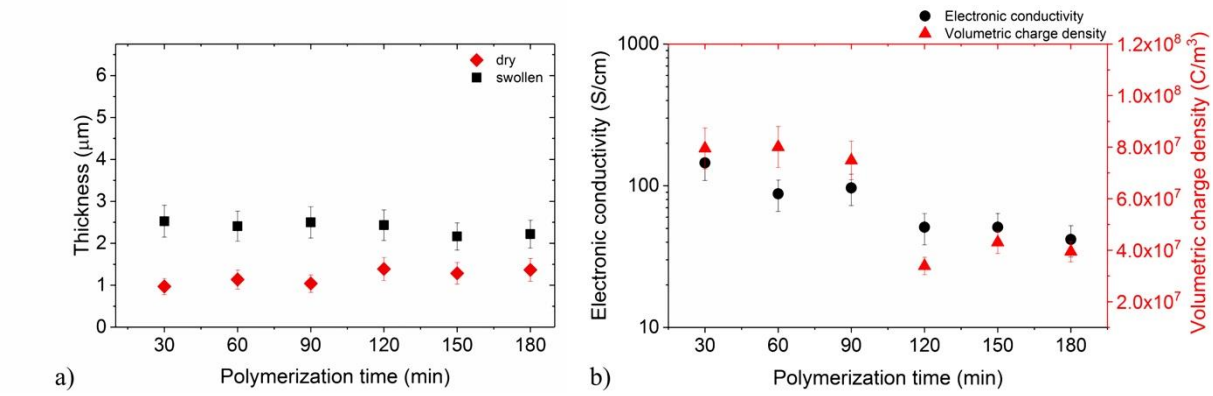


Fig. 3. Effect of EDOT VPP time on PEDOT electrode's thickness (a-■/♦), electronic conductivity (b-●), and volumetric charge density (b-▲). mPEG content: 10 wt%; spin coating speed/acceleration/duration of oxidant solution: 2500 rpm/1000 rpm s^{-1}/30 s; EDOT VPP temperature: 40 °C.

The effect of EDOT VPP time on PEDOT electrode properties is described in Fig. 3. While increasing the polymerization time, it can be seen that the thickness of the swollen electrodes (Fig. 3a) is decreasing. Those results were surprising but can be explained when measuring the thickness of dry/non-swollen electrodes. Indeed, the thickness of the dry electrodes is increasing as a function of VPP time as expected. This result points out a decrease of swelling ability of the electrodes while polymerization time is increased, probably related to higher stiffness of the CPE layer. At the same time, the electronic conductivity is decreasing gradually from 145 S/cm (30 min) to less than 50 S/cm (180 min) (Fig. 3b). This trend has already been described and explained by the fact that longer polymerization times lead to higher structural

disorder or randomly orientated disconnected islands in the polymer. These defects limit charge transport and result in higher resistance on the PEDOT layer [6, 7].

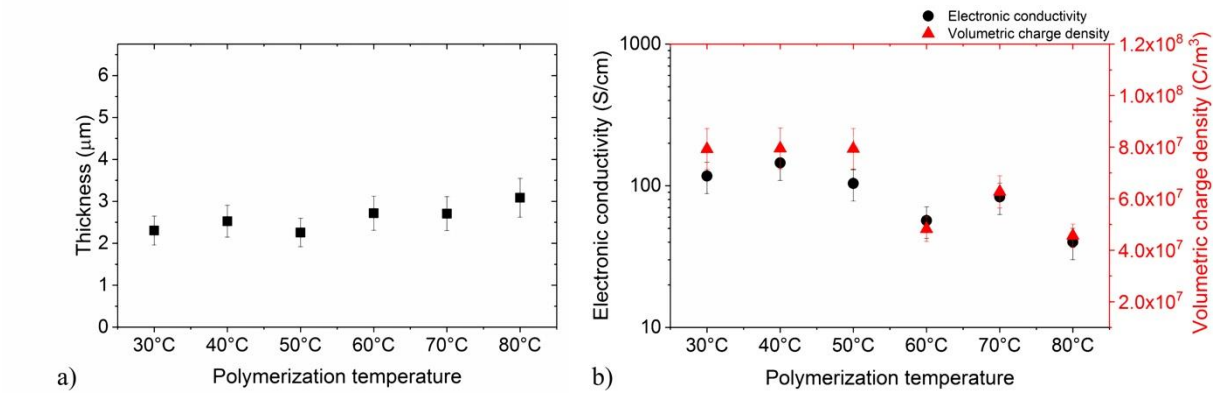


Fig. 4. Influence of EDOT VPP temperature on PEDOT electrode's thickness (a-■), electronic conductivity (b-●), and volumetric charge density (b-▲). mPEG content: 10 wt%; spin coating speed/acceleration/duration of oxidant solution: 2500rpm/1000rpm s^{-1}/30s; EDOT VPP time: 30 min.

Increasing the EDOT VPP temperature also increases the thickness of the PEDOT electrodes because of the higher concentration of EDOT vapor reacting with the surface of the oxidant solution (Fig. 4a). The higher temperature also allows partial polymerization of PEO during the VPP process which ensures the swelling ability of the electrodes in EMImTFSI, thus avoiding the decrease in thickness as observed while the VPP time was increased. Between 30°C and 50°C the electronic conductivity (Fig. 4b) lies around 100-150 S/cm and a significant decrease to 40 S/cm and 4.6x10^7 C/m^3 is observed when the temperature is increasing to 80°C. The VPP temperature has a great influence on the morphology and the lattice structure of the PEDOT layers. At higher temperature (above 50°C), the polymerization rate is faster, causing structural disorder in the electrode. It has been shown previously that the optimal VPP temperature for fabricating PEDOT layers is 46±1°C. Above this temperature the electronic conductivity of CPE layers decreased because the lattice structure of the PEDOT films had almost no orientation [8].

It can be concluded that to obtain PEDOT electrodes with high electronic conductivity and high electroactivity using VPP, it is necessary to add PEO precursors to the oxidant solution while not increasing their concentration above 20%. The rotation speed can be chosen according to the desired CPE thickness without affecting the electronic conductivity. In addition, the polymerization time and temperature must not exceed 90 min and 50°C, respectively, in order to maintain both, high electronic conductivity and electrochemical properties. The optimal parameters resulted in high conductivities (around 200 S/cm) and high electroactivity (between 2.3 x 10^7 C/m^3 and 1.0 x 10^8 C/m^3). PEDOT electrode thicknesses can be tuned between 0.8 and 5.3 µm. The optimization of the electrodes in this section

helped to determine the right parameters for fabricating highly conductive and electroactive PEDOT electrodes.

A.2.2 Surface measurement method

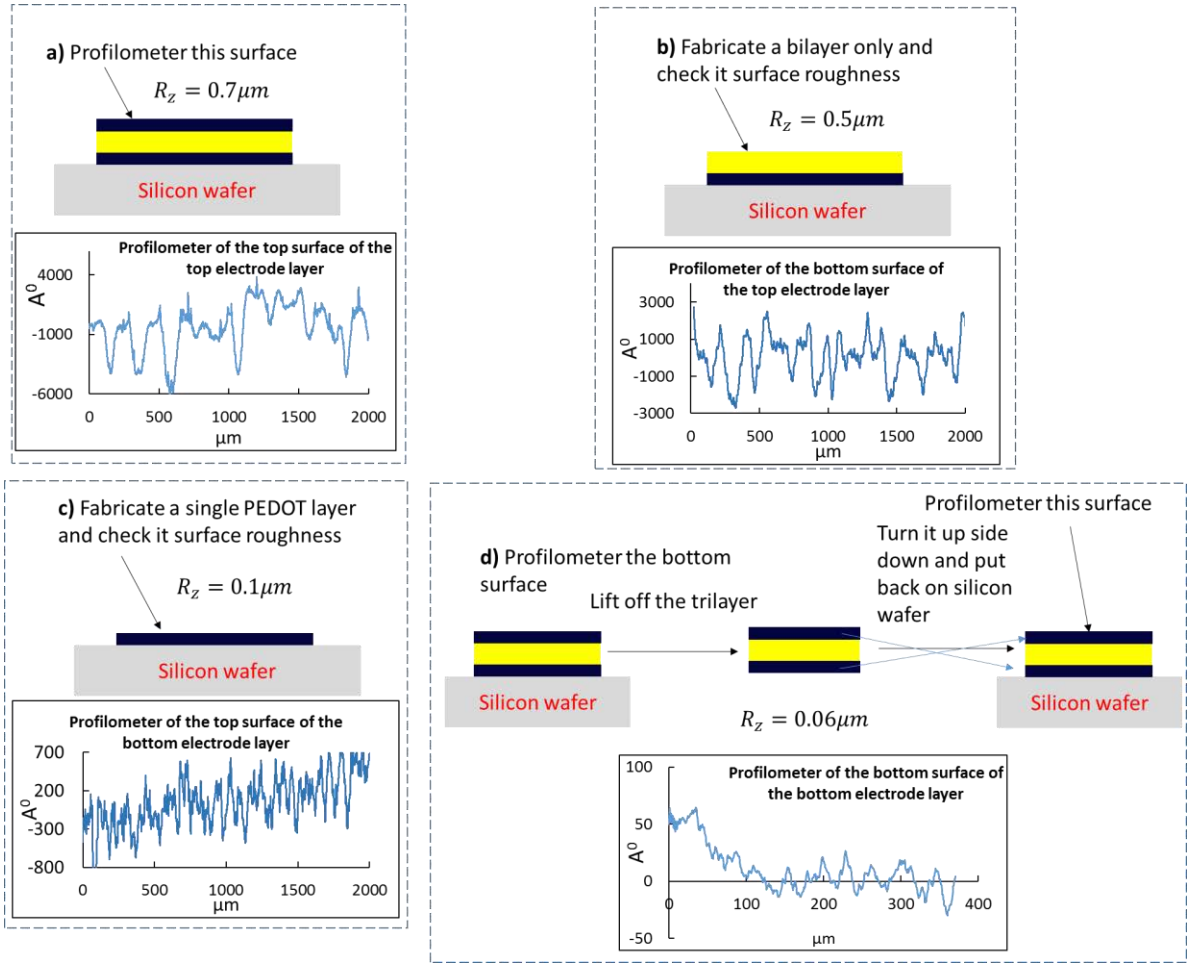


Fig. 5. Surface roughness measurement apparatus

The Fig. 5 depicts four different steps to measure the roughness on four surfaces. The first three surfaces (**Fig. 5 a, b, c)** were simply scanned as they were fabricated. In the last measurement (**Fig. 5 d**), the trilayer was flipped over and put back on a silicon wafer before scanned.

A.3 Chapter 3: Electrochemomechanical characterization of the trilayer structure

A.3.1 Qualitative explanation the apparent capacitance of the PEDOT electrodes at extreme low scan rate

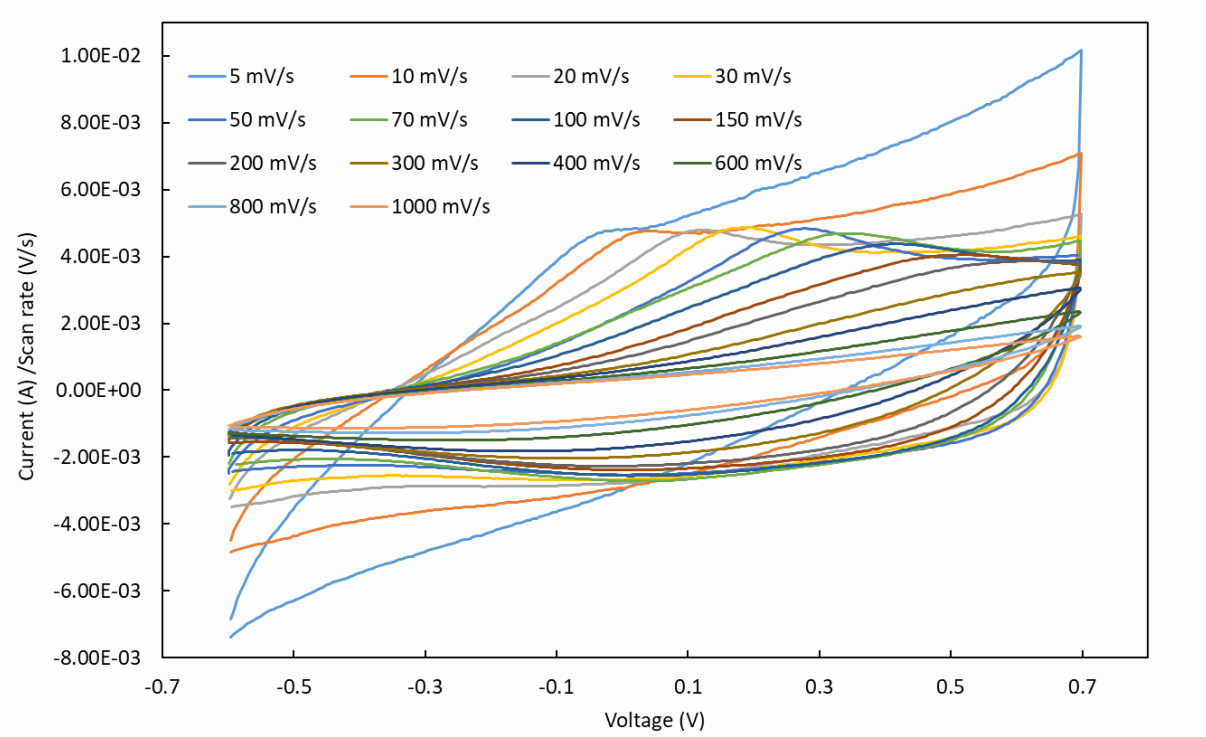


Fig. 6 Cyclic voltammograms of PEDOT electrodes obtained in neat EMImTFSI within a potential window of -0.6 V to +0.7 V with different scan rates. The vertical axis indicates the current (A) scaled by the scanning rate (V/s).

As a function of rate, there are three regions of response in the CVs above. In the first region, scan rate is so fast that we never see the full capacitance. The response looks more resistive with a loop representing capacitance (1000 mV/s to 300 mV/s). For the second region, scan rate is slow enough that we see the capacitance, but the time constant is still significant compared to the scan time. As a result, there is a rise time before reaching a constant current. Constant current is indicative of the full capacitance. This effect can be seen by looking at the curves in the positive scan direction. Curves from 200 mV/s down to 20 mV/s reach a fairly constant current at positive voltages on the upward scan (a constant 0.004 A/(V/s)). As the scan rate slows, the rise in current is shifted to a lower voltage, making the loop area larger, and increasing the apparent capacitance. And finally, the rate of charging eventually becomes so slow that we don't see a purely capacitive response any more. This is seen in the range of 10 mV/s down to 5 mV/s. The current is no longer flat as we approach 0.7 V. There is a rise in current that looks like that from a parasitic reaction (curving upwards with increasing potential). This shifts the entire curve upwards. We can also see this influencing the current at negative voltages also. To compensate for this, we can integrate over a full cycle (integrate

the current on the way up, then integrate it on the way down. Subtract the charge on the way down from the charge on the way up, and divide by scan rate and twice the voltage range).

A.4 Chapter 4: Linear dynamic and non-linear dynamic model to predict PEDOT-based trilayer actuation behavior

A.4.1 The coupling matrix derivation method

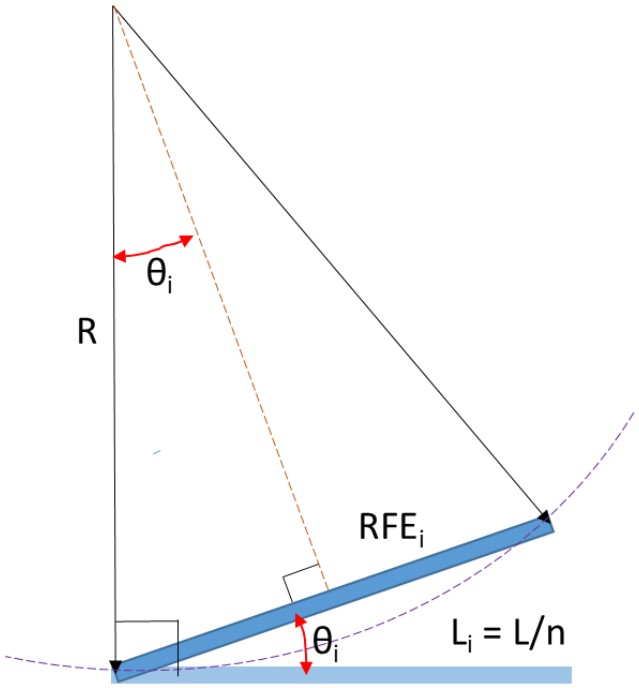
From [9], we have:

$$F = \frac{E_P \alpha \rho}{L} b \left(\frac{h_S}{2}\right)^2 \left[\left(1+\frac{2h_P}{h_S}\right)^2 - 1\right] + \frac{2bE_P K}{3L}\left(\frac{h_S}{2}\right)^3 \left[\left(1+\frac{2h_P}{h_S}\right)^3 - 1 + \frac{E_S}{E_P}\right], \quad (1)$$

where *F* is the total force produced by the trilayer actuator, $\rho = \frac{Q}{2Lbh_P}$ is the charge density, and $K = \frac{2w}{L^2+w^2}$ is the curvature of the actuator.

The first term of the equation (1) can derived as following:

$$\frac{E_P \alpha \rho}{L} b \left(\frac{h_S}{2}\right)^2 \left[\left(1+\frac{2h_P}{h_S}\right)^2 - 1\right] = \frac{E_P \alpha}{L}\frac{Q}{2Lbh_P} bh_P(h_P+h_S) = \frac{\alpha E_P (h_P+h_S)}{2L^2} Q \quad (2)$$



From the Figure above, we also have: $K = \frac{1}{R} = \frac{2\sin(\theta)}{L}$ (3)

The second term of the equation (1) can be derived:

$$\frac{2bE_P K}{3L}\left(\frac{h_S}{2}\right)^3 \left[\left(1+\frac{2h_P}{h_S}\right)^3 - 1 + \frac{E_S}{E_P}\right] = \frac{2bE_P}{3L}\frac{2\sin(\theta)}{L}\left(\frac{h_S}{2}\right)^3 \left[\left(1+\frac{2h_P}{h_S}\right)^3 - 1 + \frac{E_S}{E_P}\right] \quad (4)$$

Yield (4) and (2) into (1) and apply for RFE_i element, we obtained:

$$F_i = \frac{\alpha E_P(h_P+h_S)}{2L_i^2} Q_i^C + \frac{2bE_P}{3L_i} \frac{2\sin(\theta_i)}{L_i} \left(\frac{h_S}{2}\right)^3 \left[\left(1+\frac{2h_P}{h_S}\right)^3 - 1 + \frac{E_S}{E_P}\right] \quad (5)$$

Multiple the right and left term by L_i, we have:

$$M_i = F_i \times L_i = \frac{\alpha E_P(h_P+h_S)}{2L_i} Q_i + \frac{4bE_P}{3L_i} \frac{\sin(\theta_i)}{\theta_i} \left(\frac{h_S}{2}\right)^3 \left[\left(1+\frac{2h_P}{h_S}\right)^3 - 1 + \frac{E_S}{E_P}\right] \times \theta_i \quad (6)$$

The equation (6) represents the electrochemomechanical coupling matrix used in equation (9), section 4.3.3.2.

A.5 Chapter 5: Sensing ability and sensing model of the PEDOT-based trilayer actuators

A.5.1 A possible qualitative sensing model

Earlier experiments have suggested some facts that are:

- Sign of voltage in sensing suggests cations' movement is much faster in comparison to the negative charges' flow (section 5.4.1).
- Sign of actuation during application of a charge suggests the movement direction of the cations deciding the bending side of the actuator. No stress relaxation of the actuator is observed during the input voltage is being applied, indicating that only one type of ions involves in the actuation mechanism (section 3.1).
- Decay in voltage seen in step response suggests the existing of ion flow involving of both anions and cations in the mechanoelectrical phenomenon of the trilayer structure.
- Much higher strain to charge ratio in sensing may indicate multiple mechanisms.

These facts suggesting a possible sensing mechanism of the trilayer structure which is described in Fig. 8.

Since PEO is well known for its ionic conductivity, the penetration of the PEO through all three layers: PEDOT – NBR – PEDOT increases the mobility of both cations EMI^+ and anions $TFSI^-$ in the whole structure. PEO plays a role as a local tank to store the ions and a medium for the transport of the ions. In the other words, mobile anions and cations are available in NBR/PEO membrane as well in the PEDOT layer. In addition, relatively immobile anions ($TFSI^-$) exist in PEDOT electrodes in the doped state to balance charge on the PEDOT backbones. This is demonstrated in the electromechanical phenomenon, where, based on the direction of bending, it appears that anion flux dominates. Fig. 7 describes the 3D molecular structure of both EMI cation and TFSI anion, where the size of those two is comparable. However, in the pure form of the ionic liquid, EMI^- and $TFSI^-$ ions tend to form a cluster of positive and negative

charges whose net charge is "–" resulting in bigger negative charges and smaller positive ions [10-13].

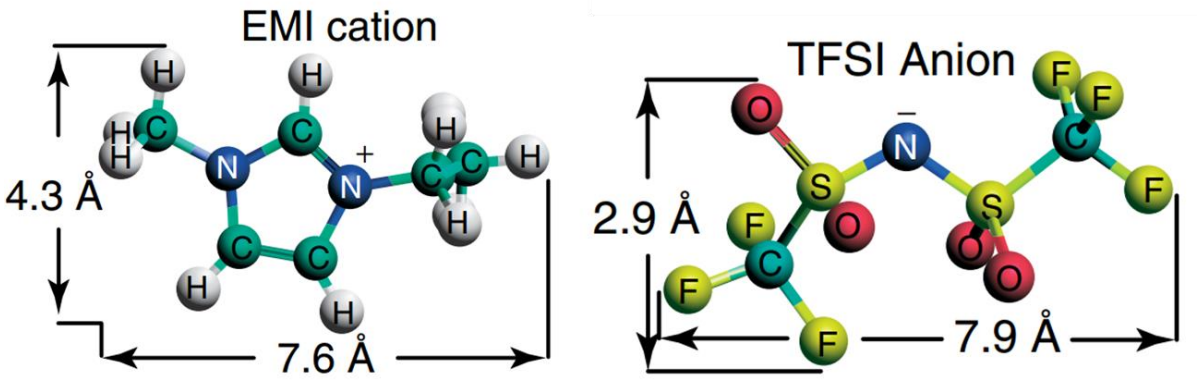


Fig. 7. 3D molecular structure and size of EMI cation and TFSI anion (Adapted with permission from Ref. [14]. American Chemical Society, 2008.)

An input step displacement makes the beam bend and creates a change in volume (Fig. 8). The upper side of the beam from the neutral axis suffers a negative strain and a reduction in volume leading to an increase in local ion concentration and an increase in elastic potential energy. To balance this change in concentration, the mobile charges start to migrate to lower concentration areas. Due to a possible interaction between the $TFSI^-$ and PEO backbones and the difference in size between the EMI^+ and negative ionic clusters, the negative charges tend to move slower than the cations, creating a total negative charge or a negative potential in the upper side. In contrast, the lower side increases its volume and produces a total positive charge or positive potential. These two simultaneous phenomena produce a sharp rise voltage at the beginning. In Fig. 8, negative ionic clusters are bigger and move slower, denoted by shorter velocity arrows. And also depending on the position away from the neutral axis, an increase in induced stress leads to an increase in diffusion speed when we go away from the neutral axis.

After a certain amount of time, due to the ion redistribution, the local difference in concentration of ions is reduced and leads to the decay of the voltage to zero. In term of thermodynamic, the rebalance decreases the energy of the trilayer system to a more stable state, which reduces the force of the trilayer.

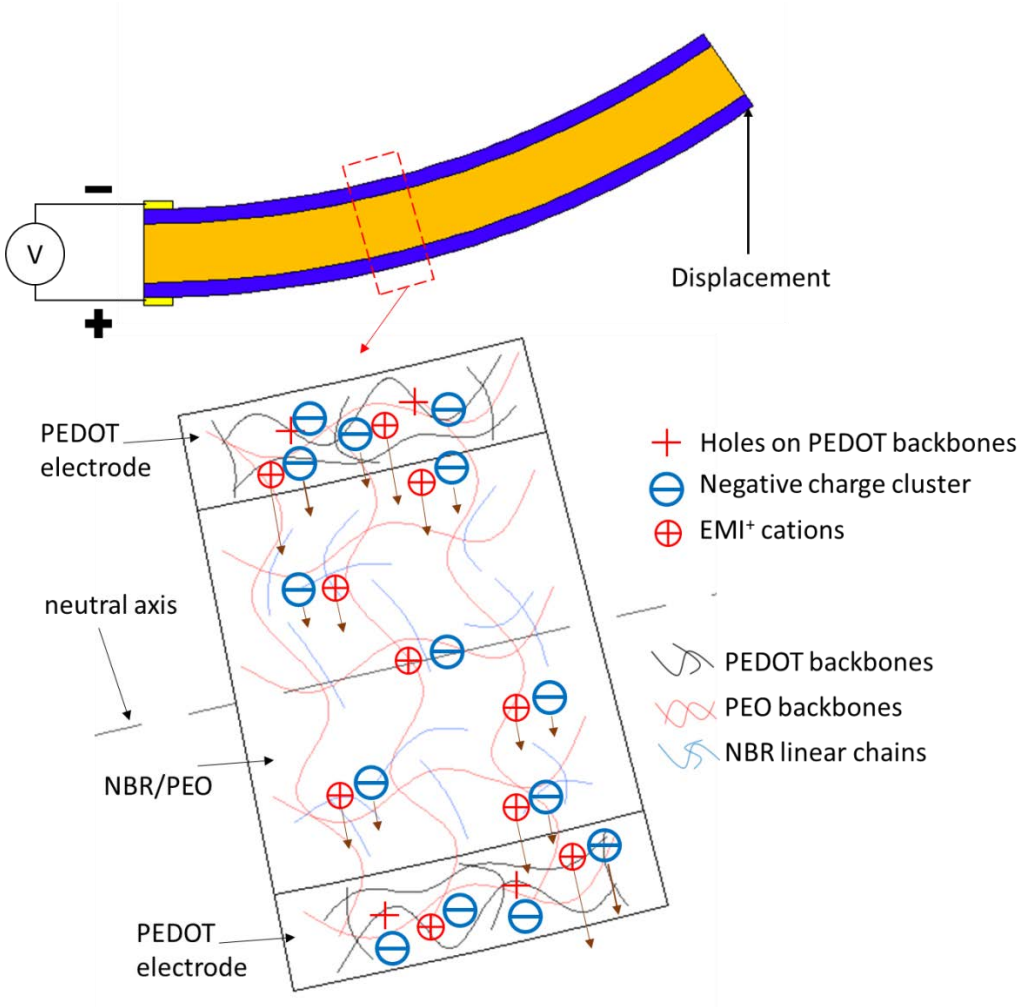


Fig. 8. A qualitative model on sensing mechanism of the trilayer structure: an input displacement causes a flux of cations and anion through the PEDOT electrodes and NBR/PEO layer, the direction of arrows indicates the moving direction while the length of arrows implies the ions velocity

In this sensing model, the strain is induced in all three layers - PEDOT electrodes and the NBR/PEO layers - when a displacement is applied to the trilayer, resulting in the ion flow all through the three layers. In other words, this displacement induces more charges to move resulting in a higher output voltage and finally higher strain to charge ratio in case of sensing.

However, in the actuation model, an input voltage only induces the strain on two PEDOT electrodes.

[1] J.D.W. Madden, Conducting polymer actuators: Massachusetts Institute of Technology; 2000.
[2] J.F. Perez-Benito, Iron (III)− Hydrogen Peroxide Reaction: Kinetic Evidence of a Hydroxyl-Mediated Chain Mechanism, The Journal of Physical Chemistry A, 108(2004) 4853-8.
[3] M. Mueller, M. Fabretto, D. Evans, P. Hojati-Talemi, C. Gruber, P. Murphy, Vacuum vapour phase polymerization of high conductivity PEDOT: Role of PEG-PPG-PEG, the origin of water, and choice of oxidant, Polymer, 53(2012) 2146-51.
[4] K. Zuber, M. Fabretto, C. Hall, P. Murphy, Improved PEDOT conductivity via suppression of crystallite formation in Fe (III) tosylate during vapor phase polymerization, Macromolecular Rapid Communications, 29(2008) 1503-8.
[5] M. Fabretto, C. Jariego-Moncunill, J.-P. Autere, A. Michelmore, R.D. Short, P. Murphy, High conductivity PEDOT resulting from glycol/oxidant complex and glycol/polymer intercalation during vacuum vapour phase polymerisation, Polymer, 52(2011) 1725-30.
[6] H. Kim, K. Jeong, C.-J. Yu, H.-S. Nam, H. Soh, J. Lee, The effects of the surface morphology of poly (3, 4-ethylenedioxythiophene) electrodes on the growth of pentacene, and the electrical performance of the bottom contact pentacene transistor, Solid-State Electronics, 67(2012) 70-3.
[7] A. Ugur, F. Katmis, M. Li, L. Wu, Y. Zhu, K.K. Varanasi, K.K. Gleason, Low-Dimensional Conduction Mechanisms in Highly Conductive and Transparent Conjugated Polymers, Advanced Materials, 27(2015) 4604-10.
[8] D. Wu, J. Zhang, W. Dong, H. Chen, X. Huang, B. Sun, L. Chen, Temperature dependent conductivity of vapor-phase polymerized PEDOT films, Synthetic Metals, 176(2013) 86-91.
[9] P.G.A. Madden, Development and Modeling of Conducting Polymer Actuators and the Fabrication of a Conducting Polymer Based Feedback Loop: MASSACHUSETTS INSTITUTE OF TECHNOLOGY; 2003.
[10] J. Hou, Z. Zhang, L.A. Madsen, Cation/Anion Associations in Ionic Liquids Modulated by Hydration and Ionic Medium, The Journal of Physical Chemistry B, 115(2011) 4576-82.
[11] B.A. Marekha, O.N. Kalugin, M. Bria, R. Buchner, A. Idrissi, Translational Diffusion in Mixtures of Imidazolium ILs with Polar Aprotic Molecular Solvents, The Journal of Physical Chemistry B, 118(2014) 5509-17.
[12] S. Katsuta, K. Imai, Y. Kudo, Y. Takeda, H. Seki, M. Nakakoshi, Ion Pair Formation of Alkylimidazolium Ionic Liquids in Dichloromethane, Journal of Chemical & Engineering Data, 53(2008) 1528-32.
[13] S. Katsuta, R. Ogawa, N. Yamaguchi, T. Ishitani, Y. Takeda, Ion Pair Formation of 1-Alkyl-3-methylimidazolium Salts in Water, Journal of Chemical & Engineering Data, 52(2007) 248-51.
[14] C. Largeot, C. Portet, J. Chmiola, P.L. Taberna, Y. Gogotsi, P. Simon, Relation between the ion size and pore size for an electric double-layer capacitor, J Am Chem Soc, 130(2008) 2730-1.